Sedimentation of circular and elliptical objects in a two-dimensional foam

by

Ioan Tudur Davies

Aberystwyth University
2009

THESIS
submitted to Aberystwyth University
by
Ioan Tudur Davies, M.Sc (Wales)
In Candidature for the Degree of
PHILOSOPHIAE DOCTOR

Declaration

This work has not previously been accepted in substance
for any degree and is not being concurrently submitted in candidature
for any degree.

Signed ..... (candidate)

Date .....

Statement 1

This thesis is the result of my own investigations, except
where otherwise stated.
Other sources are acknowledged by footnotes giving explicit
references. A bibliography is appended.

Signed ..... (candidate)

Date .....

Statement 2

I hereby give consent for my thesis, if accepted, to be made
available for photocopying and for inter-library loan, and for the
title and summary to be made available to outside organisations.

Signed ..... (candidate)

Date .....

Abstract

The rheology of a two-dimensional dry foam is probed with quasi-static bubble-scale simulations of the sedimentation of circular discs and elliptical objects. The sedimenting objects move in response to a combination of their weight and the forces exerted on them by the network of soap films and the pressures in the bubbles.

Viewed macroscopically, the plasticity and elasticity of the foam combine to determine the rate of descent of a circular disc. A critical disc weight is found that determines whether the disc is supported by the foam or not. This critical weight increases linearly with disc diameter and decreases with the liquid fraction of the foam with a power-law relation. Similarly, the drag force exerted on a disc increases linearly with its diameter and decreases with the liquid fraction of the foam with a power-law relation. An attractive force between a disc and a nearby wall is seen when the disc is further than two bubble diameters from the wall. Such wall effects are minimal when the disc sediments from a central position in a channel of sufficient width.

The interaction between two sedimenting discs is quantified by placing them in one of two configurations: one in which the discs are placed side by side and the other in which the discs are initially one above the other. The discs descend through the foam and move towards a stable orientation in which they are positioned directly above one another with a constant separation of one or two bubbles. Above a critical initial separation of the order of 5 bubble diameters, the discs do not interact. The existence of the critical separation is shown to be a result of the discrete nature of a dry foam.

The descent and rotational motion of an ellipse of similar size and weight to one of the circular discs is then considered. An ellipse rotates towards a stable orientation in which its major axis becomes parallel to gravity, driven by the local structure of the foam. This rotational motion is much slower than the downward motion.

Cyflwynir y gwaith hwn i

Dad a Mam am eu cefnogaeth trwy gydol fy addysg, i Lis a Dan, ac i Llinos am ei holl amynedd ac anogaeth!

This work is dedicated to

my parents for supporting me throughout my education as well as Lis, Dan and Llinos for their patience and encouragement!

Acknowledgements

I thank K. Brakke for developing, distributing and supporting the Surface Evolver. Thanks to participants at the Foam Mechanics Workshop held at Grenoble in 2007 for stimulating discussion. Also, thanks to Aled Wyn and Benjamin Dollet for stimulating discussion. Financial support is gratefully acknowledged from EPSRC (EP/D071127). Finally, I thank Dr. Simon Cox for his supervision for the past three years.

Contents

1 Introduction **1**

1.1 Foam Applications . . . 2
1.1.1 Personal Care Products . . . 2
1.1.2 Food and Drink Products . . . 4
1.1.3 Fire-Fighting . . . 5
1.1.4 Enhanced Oil-Recovery . . . 5
1.1.5 Mineral Flotation and Separation Processes . . . 6
1.1.6 Other Applications . . . 7
1.2 Foam as a Complex Fluid: A Continuum Approach . . . 8
1.3 2D *versus* 3D . . . 13
1.4 Foam Structure . . . 14
1.4.1 Laplace-Young Law . . . 14
1.4.2 Plateau's Law . . . 14
1.4.3 Euler's Law . . . 15
1.4.4 The Statistics of Foam Structure . . . 16
1.4.5 Foam Liquid Fraction . . . 16
1.5 Foam Rheology . . . 18
1.5.1 Elastic Response . . . 19
1.5.2 Plastic Response - T1s . . . 19
1.6 Foam Dynamics . . . 19
1.6.1 Coarsening . . . 20
1.6.2 Drainage . . . 21
1.6.3 Collapse . . . 22
1.7 The Classical Stokes Experiment . . . 23
1.8 Einstein's Particle Theory . . . 24
1.8.1 Small solid particles in a foam . . . 24
1.9 The Stokes Experiment for Fluids . . . 25
1.9.1 One Sphere . . . 26
1.9.2 Wall Effects . . . 27
1.9.3 Negative Wake . . . 29
1.9.4 Multiple Objects . . . 30
1.9.5 Long Objects . . . 33
1.10 The Stokes Experiment and Foams . . . 34

2 Methodology **42**
2.1 Review of Simulation Techniques . . . 42
2.1.1 Quasistatic Model . . . 43
2.1.2 The Large Q-Potts Model . . . 45
2.1.3 Hybrid Lattice Gas Model . . . 48
2.1.4 The Vertex Model . . . 50
2.1.5 The Bubble Model . . . 51
2.1.6 The Viscous Froth Model . . . 52
2.2 Surface Evolver Method for the Sedimentation of Objects . . . 55
2.2.1 Initial Structure . . . 55
2.2.1.1 Area Constraints of Bubbles . . . 56
2.2.1.2 T1 Events . . . 59
2.2.1.3 Structures Used . . . 60
2.3 Circular Discs . . . 60
2.3.1 Initial Placement . . . 61
2.3.2 Disc Motion . . . 61
2.4 Elliptical Object . . . 65
2.4.1 Area Constraint at Ellipse Boundary when $\phi = 0$ . . . 67
2.4.1.1 Singular Point in Content Integral . . . 72
2.4.2 Area Constraint at Ellipse Boundary when $\phi \neq 0$ . . . 72
2.4.3 Ellipse Motion . . . 80
2.5 Computational Time . . . 84

3 One Disc Sedimenting in a 2D Foam **86**
3.1 Introduction . . . 86
3.2 Maximum Disc Weight that a Foam Supports . . . 88
3.2.1 Variation of Disc Area . . . 90
3.2.2 Variation of Liquid Fraction . . . 91
3.3 A Reference Simulation . . . 93
3.4 Wall Effects on the Sedimentation Process . . . 98
3.5 Foam Fields . . . 104
3.5.1 Bubble Displacement Field . . . 104
3.5.2 T1 Positions . . . 106
3.5.3 Bubble Pressure . . . 114
3.6 Variation of the Bubble Area Dispersity . . . 116
3.7 Forces Exerted on the Disc during Sedimentation . . . 120
3.7.1 Drag Force Dependence on Disc Size . . . 120
3.7.2 Drag force Dependence on Liquid Fraction . . . 123
3.8 Does a “Negative Wake” Exist in a Dry Foam? . . . 127
3.9 Concluding Remarks . . . 130

4 Two Discs Sedimenting and Interacting in a 2D Foam: Configuration 1 **132**
4.1 Introduction . . . 132
4.2 Reference Simulation for Configuration 1 . . . 133
4.3 Variation of Initial Separation . . . 138

4.4 Foam Fields . . . 143
4.4.1 Bubble Displacement . . . 143
4.4.2 Position of T1s . . . 144
4.4.3 Bubble Pressure . . . 147
4.5 Variation of the Bubble Area Dispersity . . . 150
4.6 Wall Effects . . . 153
4.7 Variation of Disc Area . . . 158
4.8 Discussion . . . 160
4.8.1 Effect of Disc Weight on Interaction . . . 160
4.8.2 Variation of Liquid Fraction . . . 161
4.9 Concluding Remarks . . . 162

5 Two Discs Sedimenting and Interacting in a 2D Foam: Configuration 2 164
5.1 Introduction . . . 164
5.2 Reference Simulation for Configuration 2 . . . 165
5.3 Variation of Initial Separation . . . 170
5.4 Foam Fields . . . 173
5.4.1 Bubble Displacement . . . 174
5.4.2 T1 Position . . . 174
5.4.3 Bubble Pressure . . . 180
5.5 Variation of Disc Area . . . 180
5.6 Discussion . . . 186
5.6.1 Variation of the Disc Weight . . . 187
5.6.2 Variation of Liquid Fraction . . . 187
5.7 Concluding Remarks . . . 188

6 Sedimentation of an Elliptical Object in a 2D Dry Foam 190
6.1 Introduction . . . 190
6.2 Sedimentation of an Ellipse with Fixed Orientation . . . 194
6.2.1 Major Axis Parallel or Perpendicular to the y-axis . . . 194
6.2.1.1 Vary Ellipse Area . . . 197
6.2.1.2 Vary Ellipse Eccentricity . . . 201
6.2.2 Major Axis at a Acute Angle to the x-axis . . . 202
6.3 Sedimentation of a Freely Rotating Ellipse in a 2D Dry Foam . . . 209
6.3.1 Metastable to Stable Orientation . . . 209
6.3.2 Foam Fields . . . 213
6.3.2.1 Bubble Displacement . . . 213
6.3.2.2 Bubble Pressure Field . . . 215
6.3.2.3 T1 Positions . . . 218
6.3.3 Variation of the Initial Orientation of the Ellipse . . . 220
6.3.4 Varying the Ellipse Area . . . 221
6.3.5 Varying the Eccentricity of the Ellipse . . . 222
6.3.6 Varying the Weight of the Ellipse . . . 226
6.4 Discussion . . . 229
6.4.1 Varying the Liquid Fraction . . . 229

6.4.2 Variation of Bubble Area Dispersity 231
6.4.3 Time-Scales for Ellipse Motion 232
6.4.4 Concluding Remarks 233

7 Conclusions **234**
7.1 Outlook and Future Work 237

BIBLIOGRAPHY **240**

8 Appendix A - Published Work **248**

Chapter 1

Introduction

The work presented in this thesis aims to improve current prediction of foam response using two-dimensional simulations. The complex nature of foams is studied by looking at the sedimentation and interaction of objects descending under their own weight through a foam.

In this chapter, the well known concepts of foam structure and rheology are introduced. However, before explaining what is known of foam's behaviour, the reasons for studying foam in the first place need to be understood. The use of foam in everyday life and in industrial processes is reviewed in section 1.1. An understanding of a foam's rheology is required in order to improve the efficiency of many processes. This makes them more cost-effective, whence making their product more competitive within the market.

Foams can be used as a prototype to study other complex fluids as one can visualize the deformation and flow of the bubbles. In this case, we choose to work at the bubble scale. The motivation for choosing to work in this scale is given in section 1.2, where a continuum approach to describe foam response is presented. The benefits of working in 2D instead of 3D are discussed in section 1.3.

A detailed introduction to the structure, rheology and dynamics of a 2D dry foam is given in sections 1.4, 1.5 and 1.6 respectively.

The sedimentation of objects (which are large compared to a bubble) through a 2D

foam is a variation of the classical Stokes experiment which is described in section 1.7. The existing work using the experiment to probe the response of complex fluids in general is reviewed in section 1.9.

We are interested in the sedimenting motion of objects through an aqueous foam. The objects that we consider are larger than the average bubble within the foam. A brief review of work that considers the motion of small solid particles (that have typical length scale of the microstructure of the foam) through a foam is given in section 1.8.1. The variations of the Stokes experiment used in this work contribute to the more general increase in understanding of foam rheology in the foam research community. Existing work that probes the response of a foam using similar methods is reviewed in section 1.10.

Having introduced the physics involved in foam rheology in this chapter, we move on to describe how this is numerically implemented in simulation techniques in chapter 2. Then the results obtained in our simulations are presented and discussed in chapters 3, 4, 5 and 6. The conclusions and aims of future work are discussed in section 7.

1.1 Foam Applications

In this section the main reasons why physicists, mathematicians, chemists and chemical engineers are interested in understanding foam rheology is presented by demonstrating foam's vast range of applications. Liquid and solid foams are materials which are familiar to everybody as they are used in all kinds of domestic processes. They are also of importance in many industrial processes [1, 2, 3]. An overview of these applications and how the desirable properties of foam apply is given in this section.

1.1.1 Personal Care Products

Foams are probably most commonly seen in everyday life in personal hygiene products. However, their presence in products such as shampoos, shower gels and shaving foams is mostly due to consumer demands [2]. The foam's ability to cling to a surface until

(a)

(b)

(c)

Figure 1.1: Some examples of foams: (a) a good foamy head is an essential ingredient in a good pint of beer! (Photo courtesy of *www.PDPhoto.org* [4]). (b) An aqueous foam is seen when washing-up dishes. (c) An aluminium solid foam is strong and light, which makes it an ideal material for building structures. (Picture courtesy of Stefhun *en.wikipedia.org/wiki/Foam*) [5].

being washed away gives the perception that it is better for washing hair and skin. It is also the case that foam does not improve the shaving process as it clogs up the razor. However the soft foam lather can provide a more comfortable shave. Such a soft lather brings a more luxurious feel to these products, whence increasing their value to manufacturers.

The work presented in this thesis on the sedimentation of large particles through a foam is not directly applicable to improving personal care products. However, improving the prediction of foam response is of interest to manufacturing companies within this field. Thus, a simulation that correctly predicts foam response during sedimentation might be expected to work well in these applications too.

1.1.2 Food and Drink Products

Liquid foams are produced when whisking egg whites or whipping cream for baking cakes, making ice cream or other mousses. The proteins or fat globules of the ingredients provide good surfactants and their volume is greatly increased when foamed in this way, making the mixture less dense. Once a cake is baked, a solid foam is formed.

Foams often improve the texture of the food product, making for a lighter snack. Another way of thinking is that foaming food in this way bulks out a product so that the consumer appears to get more for their money with no change in weight. Food manufacturing companies are interested in the rheology of foam for improving their product and supplying what the consumer demands. Improving the prediction of foam response is also required for improving the efficiency of manufacturing processes involved in making the food products. For example, the efficiency of processes such as the flow of foam through extrusions can be improved through research into foam response.

Moreover, the work presented in this thesis on the sedimentation of relatively large particles through a liquid foam is of interest for food manufacturers using foams. Some products contain large solid objects such as nuts or raisins within a solid foam. It is desirable to have these solid particles spread out within the product instead of being concentrated at the bottom due to gravity. Thus, one needs to know what type of liquid

foam precursor is required to support these particles. The size and weight of particles such a foam can support needs to be known so that the product is of the best quality in a competitive market.

As well as food products, foams are also evident in many beverages. A layer of frothed up milk on top of a coffee provides decoration as well as insulation, thus keeping the drink hotter for longer. In this case, the foam improves the product and increases its value. Foams are also considered an essential ingredient in a good pint of beer (figure 1.1(a)). A foamy head improves the experience of drinking the beer and can also provide a brewing company with a standout feature in a competitive market.

1.1.3 Fire-Fighting

Fires in general require a supply of fuel, oxygen and heat to spread. Extinguishing a fire involves removing one of these constituents from the "fire triangle". Fire fighters have long used liquid foams to extinguish fires as they can attack all three factors at once [1].

Their use has become more prominent over the years due to the use of liquid hydrocarbons in everyday life [2]. In many cases, extinguishing a fire with water is not possible, and can often prove hazardous, because water is too dense, and therefore sinks below the surface of burning liquid hydrocarbons. This leads to the water boiling and exploding, often leading to catastrophic consequences. In this case, a foam provides all the necessary properties required to avoid such problems. It is much lighter than water, whence it flows over the surface of a burning liquid hydrocarbon to provide a cooling barrier to the fire. This barrier also keeps the supply of oxygen away from the fire.

1.1.4 Enhanced Oil-Recovery

Foams are very important materials for improving the efficiency of oil recovery, a process vitally important to the supply of the world's energy.

The standard technique of recovering oil from a porous rock is to pump water through the rock, thus physically forcing the oil out. However, the efficiency of this process on its own is poor, and up to half the oil is left in the porous rock [1]. The re-

covery of this residual oil requires the insertion of chemicals in the water that alter the interfacial tension of the flow, thus breaking up the oil droplets. To reduce the expense of this recovery process the chemicals are distributed through the porous rock by liquid foam. Its large surface area means that the distribution of the chemicals through the rock is improved and much less water is required.

In recent years, the sweep efficiency of recovering oil from reservoirs has been drastically improved through the use of liquid foams [6]. As well as improving the efficiency of oil recovery, foams are also used in other processes within the field. These include the drilling for oil, cleaning out of wells and fracturing impermeable formations in the earth [2].

Solid foams are used to seal formations or plug unproductive reservoir layers near a production well. This stops unwanted gas and water getting into the production well. In recent years, even more ambitious methods that use foam to improve the efficiency of oil recovery have been deployed. An example of this is the use of foam to control the flow patterns of the whole reservoir. This often involves filling large regions of an oil reservoir with foam, and is a process that can take months or even years to complete.

In this case, predicting the response of foam is of great importance in the field of oil-recovery. It is required that the flow of foam through a porous media is understood in detail. Thus, the foam's response to obstacles of different shapes as well as extrusions requires good predictions. The work presented in this thesis aims to improve the prediction of the flow of foam relative to solid objects.

1.1.5 Mineral Flotation and Separation Processes

Foam flotation processes are used worldwide for separating valuable metallic minerals from other non-metallic minerals from extracted ore [7]. In this case, it is the fact that foam is a two-phase fluid consisting of gas bubbles and a network of liquid content (Plateau borders) that makes them ideal. During these processes, minerals are separated by their different surface properties. A liquid foam is pumped through the extracted ore supply and the particles that are rich in metal minerals become suspended in the foam

while particles with a low concentration of metallic mineral are left behind. In this case, the hydrophobicity of particles determines whether they become attached to the bubbles as the foam flows through the mixture.

Over the years, the foam flotation process has developed to be the most important technique for mineral separation in the mining industry [7]. In this case, understanding the motion of small particles in a wet foam is of great importance [8, 9]. This work is reviewed in section 1.8.1.

1.1.6 Other Applications

Apart from the applications listed, foams are used for countless other purposes. They are used for many purposes in the textile industry. Their high surface area makes them ideal for transportation of dying or cleaning chemicals in textiles [2]. Their use in the industry leads to cost-cutting as efficiency of such processes is increased.

Solid foams are used for insulation of buildings due to their low density and the fact that they expand after aeration. They are also used for the same reasons in packaging of countless products for transport.

Solid metallic foams, such as aluminium foam (see figure 1.1(c)), have low density and high strength to weight ratio. Thus, they are beneficial for many purposes. For example, they are used in sandwich structures in which they are bounded between two metal plates. Sandwich structures are cheaper than solid plates of the same metal and also much stronger. Their lightness also makes them much easier to transport making them the material of choice in many building constructions.

In summary, foams have such a wide range of use that it is impossible to list all of them. In this section, a brief summary of the importance of foams in industry and the home has been presented.

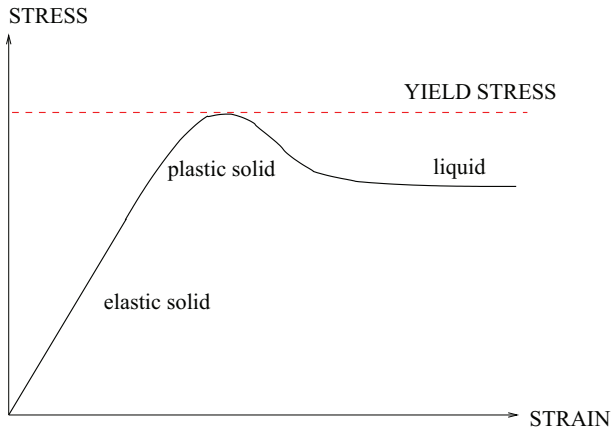

Figure 1.2: A typical stress-strain relation for an aqueous foam. It responds like an elastic solid at low stresses. As the stress is increased towards a critical "yield stress" bubbles rearrange in plastic events. Increasing the applied stress above this yields stress, results in the foam flowing like a viscous liquid. The figure is based on a similar plot by Weaire and Hutzler [1].

1.2 Foam as a Complex Fluid: A Continuum Approach

A liquid foam is a complex fluid which exhibits elasticity, plasticity and viscosity depending on the applied stress. For low applied stress, it behaves as an elastic solid. However, increasing the applied stress deforms the foam sufficiently so that bubbles rearrange. These rearrangements are plastic events in that they are not instantly reversible. Increasing the applied stress exerted on the foam above a critical "yield stress" results in the foam flowing like a viscous fluid. A liquid foam is shear thinning above this yield stress. A typical stress-strain relation for a liquid foam undergoing shear start-up is shown in figure 1.2.

The exact definition of the yield stress in a material has courted much controversy and debate over the years [10, 11]. In the work presented in this thesis, the term yield stress denotes a critical stress where the foam behaviour qualitatively changes from an elastic solid to a elasto-plastic fluid. At this critical stress, a foam yields in a series of irreversible topological changes. In general terms, these topological changes may be independent of each other or can take the form of avalanches [12].

When a large strain rate $\dot{\epsilon}$ is applied, a foam can be crudely modelled by the Bingham equation

$$S = S_y + \eta_p \dot{\epsilon} \,, \tag{1.1}$$

where S denotes the shear stress applied, S_y the foams yield stress and η_p its plastic viscosity. It is commonplace in rheology to look at the dependence of a materials effective viscosity (η_{eff}) as the strain rate is increased. This effective viscosity is simply the ratio of stress S over strain rate $\dot{\epsilon}$. In this case, the Bingham relation of equation (1.1) can be re-written as:

$$\eta_{\text{eff}} = \frac{S_y}{\dot{\epsilon}} + \eta_p \,. \tag{1.2}$$

In fact, a preferred model for foam flow is the Herschel-Bulkley relation. A slightly more complicated model than the Bingham model, it fits the shear stress with shear rate to a power law exponent n. The equation of this model is written as:

$$S = S_y + K\dot{\epsilon}^n \tag{1.3}$$

In this case, the fitting of any rheological data for the stress versus strain rate is done via three model parameters. These are the yield stress of the foam S_y, a consistency parameter K and a power-law exponent n. These value for these parameters when modelling foam is still debated within the foam community [13].

Here, as a motivation to our bubble scale simulations, we present a continuum approximation of a 2D foam's response using the Bingham model. We consider a constant velocity flow of a Bingham fluid in a 2D channel past fixed circular obstacles. The flow is simulated by a finite element method through the use of the computational fluid dynamics program Polyflow [14]. In this case, the software solves the Bingham constitutive equation by the finite element method where the channel is divided into nodes and elements by a 2D mesh.

The channel that the fluid flows through has width 20cm and length 50cm while the circular obstacles each have a radius of 2.5cm. They are positioned midway through the channel, adjacent to each other. Their centre points lie at (5cm,25cm) and (15cm,25cm)

respectively. The boundary conditions of the simulations are such that solid walls are positioned on each side of the channel so that no fluid flows laterally past each boundary. Similarly, a no flow condition is set on the boundaries of the circular obstacles. The bottom boundary of the channel is where the fluid enters the channel while the fluid exits along the top boundary of the channel.

The fluid parameters are then chosen so that the Bingham fluid resembles an aqueous foam. In this case, the zero shear-rate viscosity of the fluid is set to $10^3\eta_w$ (where η_w denotes the viscosity of water at room temperature), which corresponds to a value calculated for an aqueous foam by Buzza *et al.* [15]. The yield stress is set to $1.5Pa$, which corresponds to the value calculated in the three-dimensional pendulum experiments of Gardiner *et al.* [16] for the yield stress of an aqueous foam.

The foam flows through the channel at a constant rate of 10cm^3 per second. Polyflow solves the Navier-Stokes equations for a Bingham fluid by the finite element method over the mesh made up of small triangular elements. Thus, we can visualize the variation of the fluid's shear rate, effective viscosity, pressure as well as velocity magnitude in the channel as it flows past the circular obstacles (see figures 1.3 and 1.4).

Figure 1.3(a) demonstrates the shear rate of the fluid as it flows through the channel and past the obstacles. It can be seen that the shear rate is at its highest on the boundary of the obstacles where the fluid flows between them. This region of the fluid is yielded as shown by the low values for the effective viscosity here compared to the rest of the fluid (see figure 1.3(b)). The pressure variation throughout the channel due to the flow of the fluid is shown in figure 1.4(a). It can be seen that the pressure is higher between the entry side (bottom boundary) of the channel and the circular obstacles than between the obstacles and the channel exit (top boundary).

Figure 1.4(b) demonstrates how the magnitude of the velocity of the fluid varies throughout the channel. A perfectly symmetric flow field is seen with a maximum velocity occurring in the region directly in between the two circular obstacles.

The contour plots seen in figures 1.3 and 1.4 provide information on the deformation and flow field of a Bingham fluid. Simulations such as this provide good visualization at the continuum scale. However, a benefit of studying the rheology of foams is that

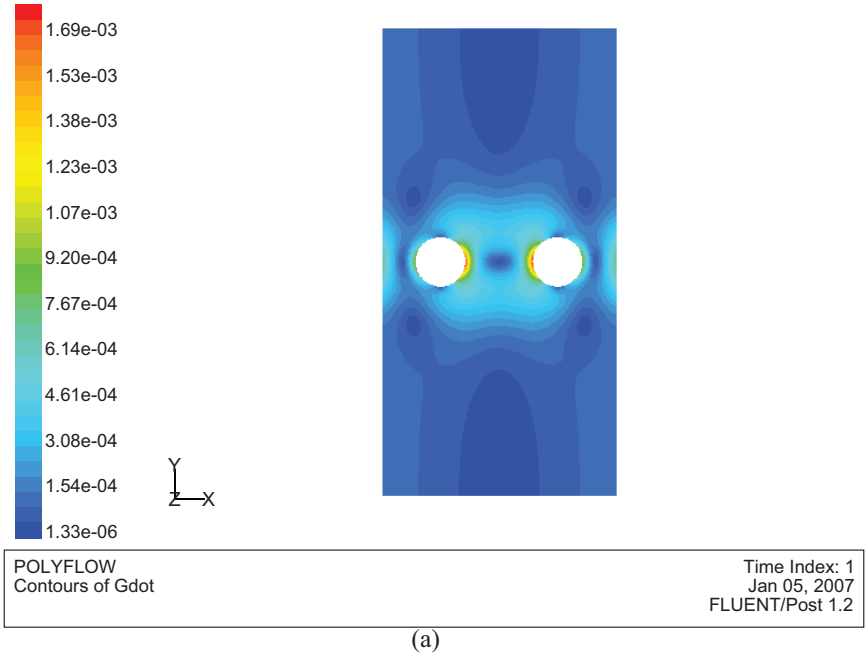

(a)

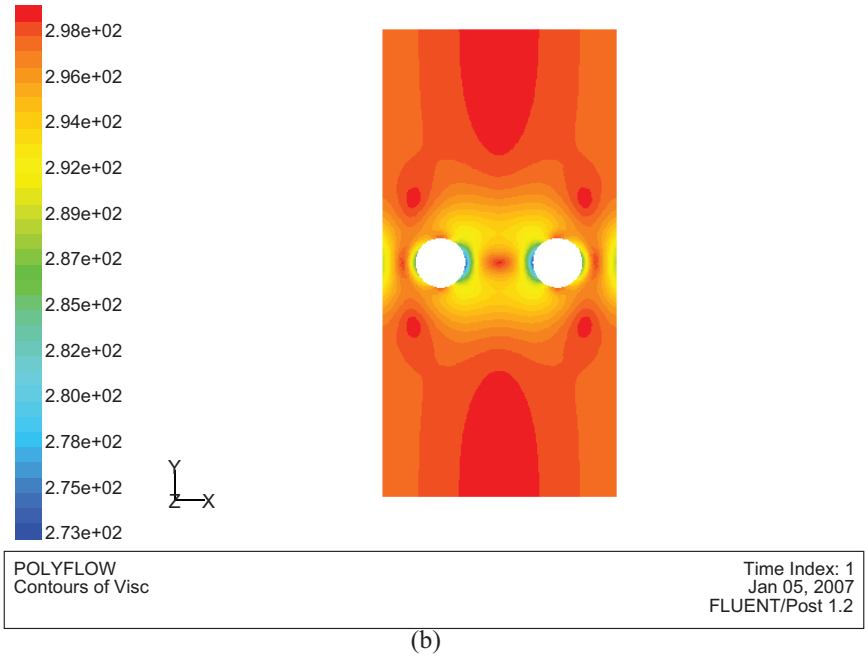

(b)

Figure 1.3: The flow of a Bingham fluid through a channel and past fixed circular obstacles is simulated using the Polyflow software. The channel has dimensions 20cm×50cm while the two fixed adjacent circular obstacles have radii 2.5cm. The fluid has a zero shear-rate viscosity $\eta_0 = 10^3\eta_w$ and a yield stress of $1.5Pa$. The contours demonstrate how the (a) shear rate $\dot{\epsilon}$ and (b) effective viscosity η_{eff} of the fluid varies throughout the channel.

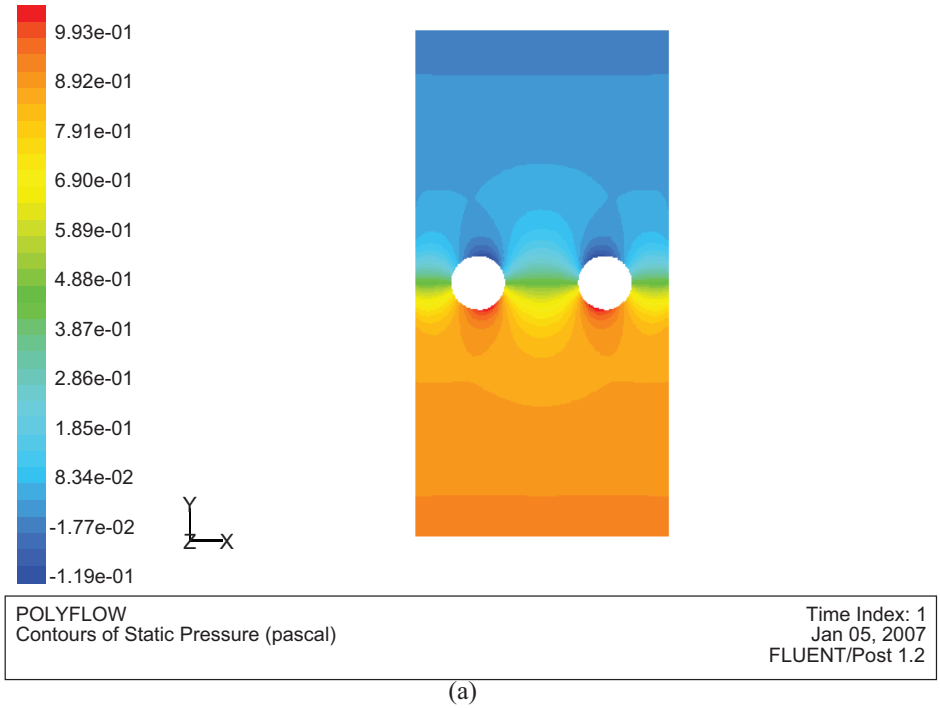

(a)

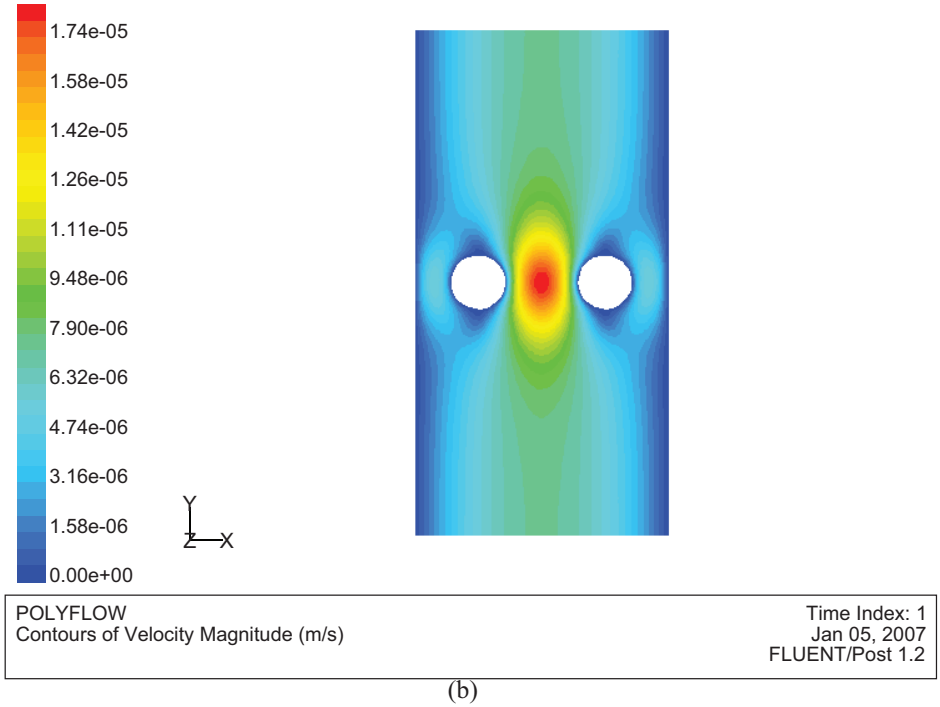

(b)

Figure 1.4: As before the flow of Bingham fluid past fixed circular obstacles is simulated using Polyflow (see figure 1.3 for channel and fluid parameters). The contours demonstrate how the (a) pressure and (b) magnitude of the velocity of the fluid varies throughout the channel.

one can visualize its flow at the bubble scale. Thus, the positions and shapes of bubbles are easily traced in experiments and simulations. The role of plasticity and elasticity of the foam can be investigated in greater detail at the bubble scale as one can see what is happening to the foam as it flows. The bubble scale of a foam provides an insight into its response that cannot be visualized in continuum simulations. This results in foam being used as a prototype to model other fluids that display similar behaviour. Due to these advantages, the work presented in this thesis is based on bubble scale simulations.

1.3 2D *versus* 3D

The study of foam rheology presented in this thesis is restricted to 2D. The visualization of foam response in 2D experiments and simulations is much easier than in 3D. The restriction also simplifies the theory and minimizes the computational expense of simulations. The simplification of the theory in some cases enables some phenomena to be isolated and studied more easily [13].

This work considers low-velocity sedimentation of objects in a dry foam in 2D. This is investigated using 2D quasi-static simulations. In this case, the 2D foam is in equilibrium between small increments in the strain. The equilibrium rules for a 2D foam are described in section 1.4 and the resulting dynamics of such a foam in seen in section 1.6. The quasi-static model is described in detail in section 2.1.1.

An equivalent experiment is quasi-2D since it consists of a monolayer of bubbles that is confined between two glass plates. The object used to probe the foam's response is in this case three-dimensional. It is a circular (or elliptic) cylinder with a height that is equal to the gap between the glass plates. Such an object would be released so that it descends through the foam under its own weight. In this case, care must be taken to minimize the effects on the motion of the object due to the 2D confinement of the experiment. An example of such an effect is the friction that exists between the object and the glass plates bounding the foam. Thus, cylinders with concave surfaces should be used to minimise the friction and ensure that the motion of the object is due to the response of the foam.

The results presented in this thesis can be generalized into the 3D case. However, the development of equivalent 3D simulations should be considered in the future.

1.4 Foam Structure

A foam can be defined simply as a two-phase system of gas bubbles separated by thin films of liquid [1]. These thin films join at Plateau borders (see figure 1.6) which contain most of the liquid in a foam. The local structure of the foam is well known as the liquid-gas interfaces follow specific mathematical equilibrium laws.

1.4.1 Laplace-Young Law

The shape of the bubbles and the curvature of the thin films are governed by bubble pressures (p) and surface tension (γ) respectively. The shape of each interface is governed by the Laplace-Young law (1.4), that relates the pressure difference sustained across the gas-liquid-gas interface Δp to the film tension (2γ) and the local curvature of the film surface κ. In two-dimensional context, we refer to the film tension as a line tension during the work.

$$\Delta p = 2\gamma\kappa \tag{1.4}$$

In two-dimensions, films have a single curvature and are therefore circular arcs. In this case, the curvature of each film is given by $\kappa = 1/r$, where r denotes the radius of the circular arc (as shown in figure 1.5).

1.4.2 Plateau's Law

In addition to the Laplace-Young law, Plateau proposed a further rule that is satisfied by a 2D foam in equilibrium. For dry foams, films always meet threefold at an angle of $2\pi/3$ to each other, forming Plateau borders at this point (for very dry foams, the Plateau borders reduce to vertices). This stable topology for three films with equal line tension 2γ is shown in figure 1.5.

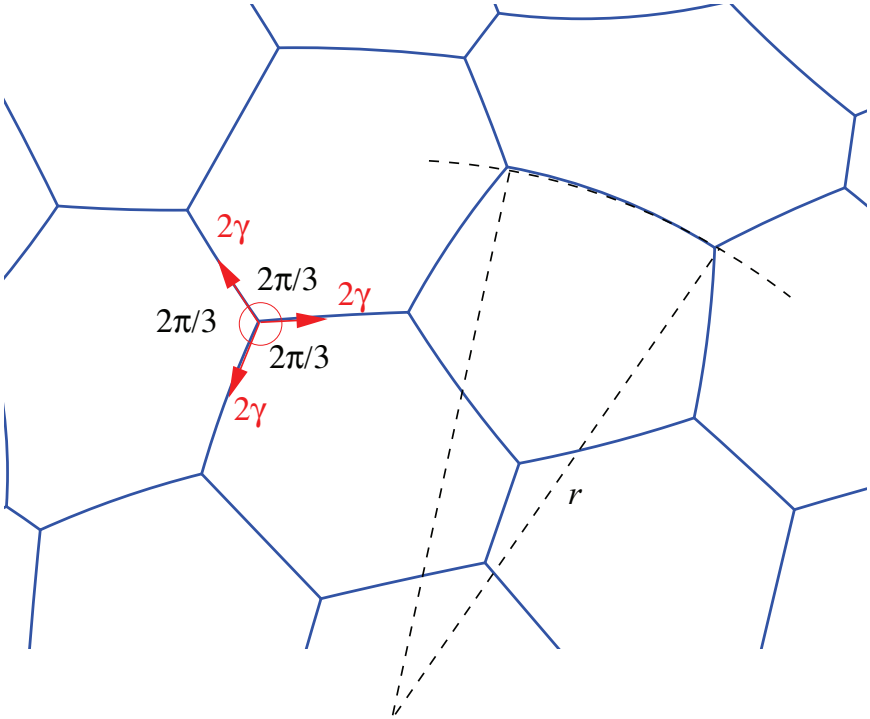

Figure 1.5: The structure of a 2D dry foam. Bubbles are separated by thin films which are circular arcs, each with a curvature $\kappa = 1/r$ (where r denotes the radius of the circular arc) that is dependent on the adjacent bubble pressure. Each film meets at a vertex (or Plateau border) at angles of $2\pi/3$ to each other.

The rules given by Laplace-Young and Plateau form the basis for the quasi-static simulations described in chapter 2.

1.4.3 Euler's Law

For a cellular material such as a foam, there is a strict relation between the number of faces F, edges E and vertices V (and cells in 3D) that such a structure must have. These follow Euler's equation, which for a 2D foam is given by

$$F - E + V = 1 \, . \tag{1.5}$$

In a dry 2D foam, Plateau's law states that each vertex is formed by three edges, in which case $E = (3/2)V$. Substituting back into equation (1.5) yields the relation $E/F = 3$. Therefore, within a foam structure with a large number of bubbles, it follows

that there are three times more edges than faces. Since each edge separates two bubbles, on average, each bubble has $n = 6$ sides [1].

1.4.4 The Statistics of Foam Structure

It is often required to classify two-dimensional foams using statistical descriptions. A 2D foam with this complex structure has a distribution of bubble areas and number of edges per cell, denoted by $p(A_b)$ and $p(n)$ respectively. Euler's law implies that in an infinite dry foam, each bubble has on average six edges (i.e. $\overline{n} = 6$). A useful measure of these distributions is given by their second moments. These are defined by

$$\mu_2(A) = \sum_{A_b} (A_b - \langle A_b \rangle)^2 \, p(A_b) \, , \tag{1.6}$$

$$\mu_2(n) = \sum_{n} (n - 6)^2 \, p(n) \, , \tag{1.7}$$

where $\langle A_b \rangle$ denotes the average bubble area of the whole foam. These statistical distributions are clarified when using different notation, in which case they are written as

$$\mu_2(A) = \left\langle \frac{(A_b - \langle A_b \rangle)^2}{\langle A_b \rangle^2} \right\rangle \, , \tag{1.8}$$

$$\mu_2(n) = \left\langle (n - 6)^2 \right\rangle \, . \tag{1.9}$$

The normalized parameter $\mu_2(A)$ is used to calculate the bubble area dispersity of the foam sample. In this case, for a monodisperse foam, i.e. a foam with bubbles of equal area, $\mu_2(A) = 0$. A polydisperse foam will have a positive non-zero value for $\mu_2(A)$. Similarly, the second moment of $p(n)$, the distribution of the number of sides of the cells, shows how much the foam deviates from the ordered case.

1.4.5 Foam Liquid Fraction

A foam's liquid fraction Φ_l is used for classification as it is an important parameter that affects the rheology of the foam. It quantifies the amount of liquid in the foam

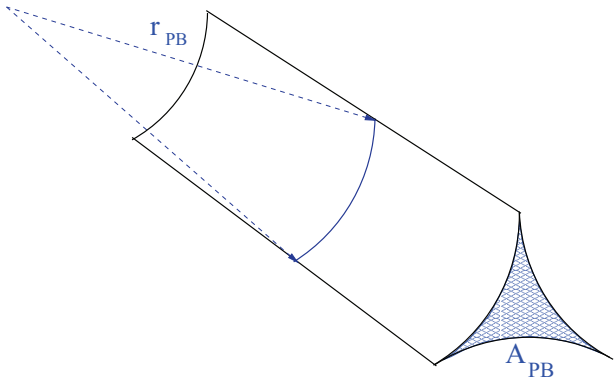

Figure 1.6: The liquid content of the foam resides mostly within Plateau borders. In a 2D foam, these are positioned where the films of the foam meet three-fold at angles of $2\pi/3$ to each other. In an ideal 2D foam, their cross-section resembles a concave triangle with curved edges which are circular arcs all with equal radius r_{PB}. The cross-sectional area of the Plateau border is denoted by A_{PB} and is given by (1.10).

relative to the amount of gas. For a 2D foam, a critical value for the liquid fraction is $\Phi_l = 16\%$, at which point, the foam resembles a random close packing of circular discs [17]. Increasing the liquid fraction above this value, the foam loses its rigidity and it behaves like a bubbly liquid.

We are interested in the rheology of foam in the dry limit, where $\Phi_l < 5\%$. In this case, most of the liquid is contained within the Plateau borders of the foam. Recall that in a 2D foam, a Plateau border forms where three edges meet at angles of $2\pi/3$ to each other (§1.4.2). The geometry of a Plateau border in an ideal foam is shown in figure 1.6.

It is shown here that the cross-section of a Plateau border is a concave triangle, where the radius of the curvature in an ideal foam is r_{PB} for all three boundaries. Its cross-sectional area is given by

$$A_{pb} = \left(\sqrt{3} - \frac{\pi}{2} \right) r_{PB}^2 \,, \tag{1.10}$$

as shown by Weaire and Hutzler [1]. For a 2D foam, the liquid fraction Φ_l is simply the ratio between the area occupied by the liquid (A_l) and the area of the foam sample (A),

i.e.

$$\Phi_l = \frac{A_l}{A} \,. \tag{1.11}$$

Consider a foam that has n bubbles. Thus, for a perfectly ordered monodisperse 2D foam, the area of the foam sample is simply $A = nA_b$, where A_b denotes the bubble area. Every bubble has 6 Plateau borders in this case, each of which are shared between three bubbles. In this case, the area occupied by the liquid is simply $A_l = 2nA_{PB}$. Thus, the liquid faction of the foam is written as

$$\Phi_l = \left(2\sqrt{3} - \pi\right) \frac{r_{PB}^2}{A_b} \,. \tag{1.12}$$

The dimensionless parameter Φ_l is chosen to classify and compare foams. In the simulations presented in this thesis, equation (1.12) is used to approximate the liquid fraction of the foam with A_b representing the average bubble area. In this case, the radius of the curvature to the Plateau border (r_{PB}) is related to a cut-off length (l_c) defined to trigger T1 events (see §1.5.2 and §2.2.1.2) in our simulations.

1.5 Foam Rheology

Our main goal is to improve predictions of the complex rheology of a 2D aqueous foam. Having described the structure of the foam, we next describe the basic flow properties of a 2D foam. It was stated when considering continuum models for foam rheology that a foam exhibits elasticity, plasticity and a viscous response to deformation. An elastic material is able to return to its original form when an applied stress under which it deforms is removed. On the other hand, the plasticity of the foam describes its ability to permanently deform for applied stresses greater than or equal to a critical (yield) stress. Its viscous response refers to its internal resistance to flow due to friction between fluid particles.

In this work, the viscous effects of the foam are deemed negligible as we work within a quasi-static regime (see §2.1.1). In this case, we model a dry 2D foam as an elasto-plastic material.

1.5.1 Elastic Response

A dry foam is elastic for small applied stresses. In this case, the films of the foam stretch and the bubbles become elongated or squeezed without rearranging. Thus, if the applied stress was removed, the foam would relax back into its original undeformed state; whence the foam behaves as an elastic solid.

1.5.2 Plastic Response - T1s

For larger applied stress however, the foam yields as a result of irreversible plastic topological changes denoted as T1 events. These topological changes denote a neighbour swapping of bubbles.

The applied stress forces bubbles to rearrange so that two neighbouring bubbles become next nearest bubbles and two next nearest bubbles become neighbours. Such T1 events occur in a dry 2D foam when it is strained so that two three-fold vertices approach each other. Plateau's law states that the stable topology for the equilibrium state of a 2D foam is such that all edges meet three-fold at angles of $2\pi/3$. Thus, when two three-fold vertices approach each other and move towards an energetically unstable topology (i.e. a fourfold vertex), the films rearrange to minimize the foam's total edge length. This leads to a neighbour swapping of bubbles and a local topology of two neighbouring three-fold vertices is retained. A typical T1 event is shown in figure 1.7.

T1 locations in a foam yield information about the general flow of the foam. A region of the foam where T1s are concentrated is said to be a fluidized or yielded region of the foam.

1.6 Foam Dynamics

The foam structure can be altered in many ways. For example, shearing a foam will elongate the bubbles, stretch the films and cause topological rearrangements. These processes contribute to the general flow of foam described in section 1.5. However, other physical processes affect the structure of the foam. These are explained in this

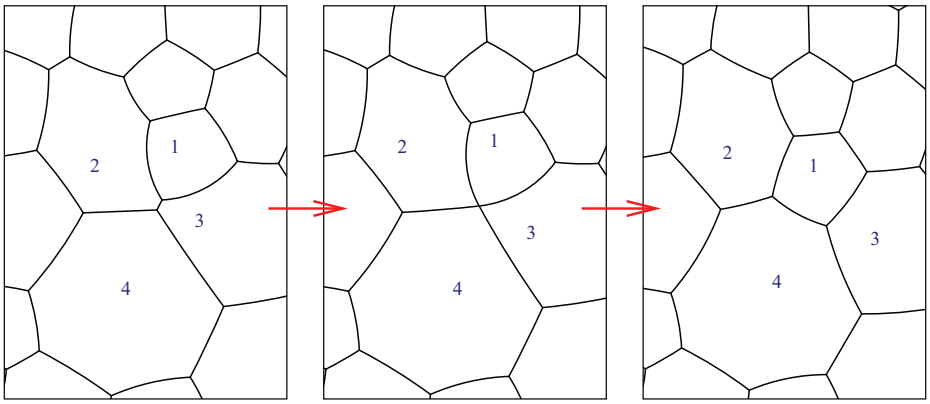

Figure 1.7: An example of a T1 event is shown. (a) The applied stress on the foam results in deformation in which two three-fold vertices approach each other. (b) An unstable topology of the foam films is approached (where they meet each other at a fourfold vertex). (c) The films rearrange to minimize the energy (total edge length) of the foam. The total edge length between two three-fold vertices is less than the equivalent single four-fold vertex. This topological change results in neighbour swapping between two pairs of bubbles. Bubbles 2 and 3 were initially neighbours but have become next-nearest neighbours after the T1 event. Similarly, bubbles 1 and 4 were previously next-nearest neighbours and became neighbours after the T1 event.

section, although will not be considered further in this thesis. We describe how these processes can be suppressed, so as to provide a means to test the predictions of this work.

1.6.1 Coarsening

The pressure difference (Δp) between neighbouring bubbles drives gas to diffuse from bubble to bubble through the thin films that separate them. In this case, some bubbles will shrink and disappear altogether while others initially grow in size. Thus a 2D foam coarsens when the number density of bubbles decreases (or the average bubble area increases) with time due to gas diffusion between cells.

In 2D, the rate at which gas diffuses from bubble to bubble is proportional to the length of the films and the pressure difference between neighbouring bubbles, *i.e.*

$$(\textit{area rate of gas transfer}) \propto (\textit{film length}) \times (\textit{pressure difference}) \ . \tag{1.13}$$

The above equation represents Fick's law [1]. Inserting a proportionality constant K (permeability constant) into the above relation, the area rate of gas transfer for a bubble i with neighbouring bubbles j is given by

$$\frac{dA_i}{dt} = -K \sum_j l_j \left(p_i - p_j\right). \tag{1.14}$$

where l_j denotes the contact length of bubble i with its neighbour j, while p_i and p_j denote the pressures of bubble i and j respectively. Inserting Laplace's law (1.4) into equation (1.14) and using the Gauss-Bonnet formula yields von Neumann's law (1.15), which gives the area rate of gas transfer for a bubble with n sides:

$$\frac{dA_n}{dt} = \frac{2\pi}{3}\gamma K(n-6). \tag{1.15}$$

A consequence of this law is that a 6-sided bubble's area will remain constant until a topological change occurs. The law as stated is confined to describing the coarsening process in 2D, however, it has been recently successfully extended to 3D by Macpherson and Srolovitz [18].

Since the effect of coarsening on the sedimentation of objects through a foam is not of interest in this work, the area of each bubble is kept constant throughout. In experiment, one would aim to slow down the coarsening process as it cannot be completely suppressed. This involves making the films less permeable to the gases by choosing a concentrated surfactant or using a mixture of non-permeable gases when making the foam.

1.6.2 Drainage

The distribution of liquid in the foam is often non-uniform. The process of foam drainage is dependent on the interplay of gravity, surface tension of the foam films and viscous forces [19, 20, 21]. In a typical scenario, gravity forces the vast majority of the liquid within the foam to drain downwards, while viscous forces oppose this. Surface tension provides a "capillary" effect so that at equilibrium, some liquid is kept

in the foam. The drainage is modelled in 2D by considering the cross-sectional area of a Plateau border at a time t and vertical position y. Verbist *et al.* [22] model the vertical drainage of fluid through a 2D foam using the foam drainage equation

$$\frac{\partial \alpha}{\partial \tau} + \frac{\partial}{\partial \xi}\left(\alpha^2 - \frac{\sqrt{\alpha}}{2}\frac{\partial \alpha}{\partial \xi}\right) = 0\,, \tag{1.16}$$

where α, ξ and τ are non-dimensional counterparts of the A_{PB}, y and t respectively. In this case, the distribution of fluid at equilibrium (i.e. when the flow rate is zero) satisfies the equation

$$\alpha_{eq}(\xi) = \frac{1}{\left(\alpha_1^{-1/2} + \xi_1 - \xi\right)^2}\,, \tag{1.17}$$

where α_1 denotes the value of α at a point ξ_1.

The work presented in this thesis aims to improve the prediction of dry foams' response by considering the sedimentation of objects through the foam. Since the foams are so dry, the drainage of liquid through the foam is not considered an important factor that affects the foam's rheology or the motion of the objects. In this case, since the liquid content in the foam is minimal, the Plateau borders are represented as vertices. In this case, the small amount of liquid in the foam is evenly distributed. For simulation of wetter foams in the quasi-static regime, one would aim to represent the areas of the Plateau borders throughout the foam so that (1.17) is satisfied.

An equivalent experiment would require the liquid content of the foam to be in equilibrium as the objects sediment through the foam. The foam could be left to drain for some time until equilibrium is reached. In this case, a region of the foam high up in the channel can be approximated to have a constant value for $\alpha_{eq}(\xi)$ and would therefore correspond well with simulations.

1.6.3 Collapse

When observing a stationary foam over a long period of time, it can be seen that films rupture and the foam collapses [1]. Many factors contribute towards this collapse. Rupturing can occur when the concentration of surfactant molecules on the surface of a

foam film becomes too low so that the surface tension force becomes too strong for the film. The drainage and evaporation of liquid from the foam also contribute to make the films thinner, causing them to burst when forces become too strong. The process can also be accelerated by dust or other unwanted materials that work as anti foaming agents; they cause rupture of the films by interfering with their surface chemistry. These are some examples of the many factors that can cause thin films in a foam to rupture. The stability of a foam depends on slowing down this rupturing process [23].

In experiments, foam collapse can be minimized by using highly concentrated surfactants, making the foam more stable. Any surfaces or objects in contact with the foam should be thoroughly cleaned so that no dirt acts as anti foaming agents. This should enable experiments to proceed over a certain time limit without any rupturing of the foam.

1.7 The Classical Stokes Experiment

In this thesis, a simulated variation to the classical Stokes experiment [24] is used to probe the rheology of a two-dimensional foam. The Stokes experiment dates back to 1851 when it was used to find the viscosity (η) of a fluid by measuring the drag force (F_y) exerted on a small spherical object descending through that fluid. Stokes' law yields a relation between the drag force exerted on the sphere and the viscosity of the fluid through which it descends:

$$F_y = -6\pi\eta R_s V_s \,, \tag{1.18}$$

where R_s denotes the radius of the sphere and V_s its terminal velocity in the fluid. This equation applies when the sphere descending through the fluid is small enough (i.e. the Reynolds number (Re) satisfies $Re < 0.5$) so that the resulting flow is slow.

The Stokes experiment is an important tool in the field of rheology and is the basis for the falling-ball viscometer which is widely used to probe the properties of a fluid. Such a viscometer consists of a cylindrical tube that is filled up with a fluid, and a

spherical ball is left to fall under its own weight. Its terminal velocity is recorded and the viscosity of the fluid calculated by Stokes' law (1.18). The work of Cygan and Caswell [25] and Sutterby [26] are prominent examples where the falling ball viscometer has been developed as an efficient tool to study the rheology of fluids.

Many variations of the classical Stokes experiments have been used over the years to probe the rheology of different fluids. A brief review of the experiments used and their findings are presented below for complex fluids in general (§1.9) as well as the specific case of foams (§1.10). Firstly, a clarification is given of how the work of Stokes differs from that other famous work involving the motion of particles through a fluid, namely the work of Albert Einstein. This work concentrates on the random nature of the motion of small particles in a fluid and its application in foam is reviewed in section 1.8.1.

1.8 Einstein's Particle Theory

The motion of particles in fluid has long been of interest to scientists. Brownian motion describes the random nature of motion for small solid particles suspended in fluids. This type of motion was explained by Albert Einstein's 1905 classical paper [27] to be the result of fluid particles colliding with the solid particles. The Brownian motion of a solid particle (visible through an ordinary microscope) suspended in a fluid was accurately predicted by his molecular-kinetic theory on the motion of fluid molecules. This indirectly led to confirmation of the existence of atoms and molecules.

In this thesis, the objects that descend through the fluid (a dry foam) are much larger and therefore impose larger deformation fields than considered in the work of Einstein. Their motion in this case is not Brownian.

1.8.1 Small solid particles in a foam

Before reviewing existing work where variations of the classical Stokes experiment has been used to probe foam rheology, it is important to consider another active research field: the motion of small solid particles in foams. These are particles that are much

smaller than the bubble size and can move within a Plateau border. The study of this motion is of interest to the mining industry in the separation of minerals through foam flotation. Cilliers and co-workers [8, 9] performed both simulations and experiments on the motion of solid particles within a foam during the flotation process.

Modelling the motion of small solid particles in foam flow requires knowledge of the liquid and gas motion. Coalescence and rupturing processes affect the motion of these solid particles in the foam. The efficiency of the foam flotation process is reduced by an unstable foam as particles that are attached to the bubbles become detached when a film of that bubble ruptures. These particles become mixed with previously unattached (and unwanted) particles that flow within the liquid in the Plateau borders.

They investigate the motion of solid particles in Plateau borders and vary the size of the particles as well as their concentration in the liquid. The motion of small particles in the liquid is Brownian as explained by Einstein [27]. Larger particles are less mobile and are more liable to get in contact with the walls of the Plateau borders. The Plateau border wall effects constrain the motion of such particles. This is confirmed in more recent experiments by Bennani *et al.* [28]. Increasing the concentration of solid particles within the Plateau borders confines the drainage of fluid through the Plateau borders. The work of Cilliers *et al.* shows that the motion of small solid particles in a foam is indistinguishable from that of liquid. Both are dispersed by a network of Plateau borders in the same diffusive manner.

The work presented in this thesis concentrates on the motion of larger particles in a foam. These are objects are much larger than a foam bubble and could never move within a Plateau border. They are used to probe the foam's rheology.

1.9 The Stokes Experiment for Fluids

Dropping a spherical particle into a fluid has become an important rheological probe. Since the pioneering work of Stokes, research has increasingly concentrated on complex (non-Newtonian) fluids. Researchers often compare their results with the Newtonian case since by doing so they are able to quantify the effect that properties such as

viscoelasticity, viscoplasticity and shear-thinning have.

Simulation methods have been developed, as well as imaging techniques in experiments. They enable visualization of the fluid's response as the object moves, applying a non-isotropic stress.

1.9.1 One Sphere

A benchmark paper looking at the creeping motion of a sphere in a viscoplastic material is that of Beris *et al.* [29]. Their numerical modelling showed that a sphere falls through the medium in a small envelope of yielded (or fluidized) material. The rest of the material is unyielded. The size and shape of the yielded region surrounding such a sphere was probed further in the numerical simulations of Beaulne and Mitsoulis [30] and Blackery and Mitsoulis [31]. They examined the creeping motion of a sphere through a viscoplastic material modeled by the Herschel-Bulkley and Bingham constitutive equations respectively. This is done by solving Papanastasiou modifications [32] to Herschel-Bulkley (1.3) and Bingham (1.1) equations over the appropriate boundary conditions by finite element method. The Papanastasiou modification ensures that the constitutive equations can be applied everywhere in the flow field, i.e. the yielded and unyielded regions. These simulations correspond well to the experimental results of Atapattu *et al.* [33], who visualized the yielded region surrounding the sphere by a laser speckle imaging method. There is also good agreement for the drag coefficient calculated.

The simulations of de Besses [34] showed that measuring the drag force on a sphere creeping through a viscoplastic fluid could yield information about whether an object will sediment or not. In other words, one could calculate the weight of a particular object necessary for it to be neutrally buoyant.

The experiments of Tabuteau *et al.* [35, 36] measure the drag force exerted on a sphere as it moves steadily through a clay suspension which is shear thinning and has a yield stress. They show that the stress and shear rate can be related to the Herschel-Bulkley model (1.3) without aging of the fluid. It is shown that a very dense sphere

reaches a terminal velocity in which case it is surrounded by a volume of fluidized material. A very light sphere is brought to a halt by the fluid so that they are neutrally buoyant. In this case, the material surrounding the sphere is unyielded and is therefore in the solid regime. There is however an intermediate stage where the sphere is neither brought to a halt nor reaches a terminal constant velocity. In this case, the sphere reaches its maximum velocity which then decreases throughout the experiment. This is suggested to be due to localized changes in the material close to the sphere. In this case the material surrounding the sphere is not totally fluidized.

They also use this experiment to probe the aging properties of the fluid. It is shown that as the fluid ages, the motion of the sphere and the forces it experiences change as the yield stress decreases. Good agreement for the drag coefficient and the yielding criterion of the fluid is reached between these experiments and the aforementioned simulations of Beris *et al.* [29] and Beaulne and Mitsoulis [30].

1.9.2 Wall Effects

The effects of a nearby wall on the descending motion of an object can yield further information on the response of the fluid. A sphere descending in a Newtonian fluid will migrate away from a nearby wall towards the centre of the fluid container. This has been shown to be the case in the experiments of Joseph *et al.* [37].

Tatum *et al.* [38] and Harrison *et al.* [39] investigate the flow field surrounding a sphere descending in a Newtonian fluid near to a wall by particle image velocimetry. They show that the flow field surrounding the sphere as it sediments near a wall is very different compared to when it sediments centrally in the container. The nearby wall interferes with the flow field surrounding the sphere, resulting in repulsion between the sphere and the wall. This repulsion between descending spheres and a nearby wall in a Newtonian fluid is also demonstrated in the numerical simulations of Liu *et al.* [40] and Singh and Joseph [41].

Tanner [42] was the first to present evidence of the opposite effects when a sphere falls near a wall in non-Newtonian (viscoelastic) *versus* Newtonian fluids. The sphere

in a falling ball viscometer was found to migrate away from the wall when falling in a Newtonian fluid while it migrated towards the wall in a viscoelastic fluid. The elasticity of the fluid was confirmed to cause a migration of a sphere towards a nearby wall in the experiments of Liu *et al.* [40] and the simulations of Becker *et al.* [43]. They also notice that the elasticity of the fluid changes the direction in which spheres rotate as they sediment near a wall. In this case, a sphere was shown to rotate as if rolling down the wall during its descent in a Newtonian fluid while rotation occurred in the opposite direction in a viscoelastic fluid.

The simulations of Feng *et al.* [44] found that there exists a critical separation between sphere and wall for attractive or repulsive migration as the sphere descends through a (Oldroyd-B) viscoelastic fluid in a cylindrical tube. When a sphere is initially separated by less than this critical separation to the wall, it is repulsed by the wall; conversely it is attracted to the wall if placed further away than this critical separation. This critical separation was also found in the simulations of Binous and Phillips [45] who model a viscoelastic fluid as a suspension of finite-extension non-linear dumbbells. They show that either side of the critical separation, the direction in which the sphere rotates reverses. At very small initial separations between wall and sphere, the sphere descends and rotates as if it is rolling down the wall as in a Newtonian fluid. The direction of rotation is reversed when the separation between sphere and wall is increased above the critical separation.

The simulations of Tatum *et al.* [46, 38] compared the descending motion of spheres near a wall in a Newtonian, Boger (constant viscosity, elastic fluid) and a shear-thinning viscoelastic fluid. They showed that the critical separation between wall and sphere is maximized in shear-thinning viscoelastic fluids.

A sphere sedimenting through a viscoplastic fluid only experiences wall effects if the wall is in contact with the fluidized volume of the material [47]. Migration towards or away from the wall is less evident in such fluids and the effects contribute mostly to changing the drag force exerted on the object.

In this thesis, the wall effects on an object sedimenting near to a wall in a dry 2D foam is investigated. The foam is modelled as an elasto-plastic fluid. Thus, it

is expected from the results reviewed from the literature that the foam's elasticity will cause a sedimenting object to migrate towards a nearby wall. This is expected to happen if the object is positioned further from the wall than a critical separation. The value for this critical separation and the role of the foam's elasticity and plasticity in any wall effects experienced are quantified in chapter 3.

1.9.3 Negative Wake

The wake above a falling object in a fluid can yield valuable information into a fluid's response. The material in the wake is highly deformed and is part of a yielded (or fluidized) region. It is the volume of fluid directly above a falling sphere in which the flow moves laterally to fill the area of low pressure. In Newtonian fluids, any flow directed vertically in the wake of a descending object is always directed downwards. However, this is often not the case for viscoelastic fluids, where the flow is often directed upwards. This unexpected phenomena was called a negative wake by Hassager [48] who observed it in a viscoelastic fluid.

The experiments of Arigo and McKinley [49] and Harlen [50] showed that a negative wake is most prominent in shear-thinning fluids of high elasticity. Although not seen in our continuum simulations (§1.2), one would expect to see some negative flow in the wake of a sedimenting object in a dry foam.

Some evidence of this was seen in the 2D experiments of Dollet and Graner [51]. Here they study the flow of a monolayer of bubbles bounded between a liquid and a glass plate past a circular obstacle. They observe by image analysis, a velocity overshoot in the negative direction to the flow of the foam in the wake of the obstacle. We aim to investigate the existence of such a negative wake for sedimenting objects in a dry foam in our 2D simulations. If present, we will probe the effect that the discrete nature of the foam has on the nature of a negative wake.

1.9.4 Multiple Objects

The sedimentation of, and interaction between, more than one similar object is another variation of the Stokes experiment. Chapters 4 and 5 examine the sedimentation of two circular discs sedimenting from being initially side by side or directly above each other in a dry foam. In this section, examples of existing work quantifying the interaction between multiple spherical objects moving in Newtonian, shear-thinning viscoelastic and viscoplastic fluids is reviewed. We are interested mainly in the effect that the elasticity and plasticity of fluids has on the interaction between the objects.

The experiments of Jayaweera *et al.* [52] provides an early example where the interaction between more than one spherical particle descending through a large container full of purely viscous Newtonian fluid was considered. They showed that small spheres (where $Re < 0.3$) initially side by side descended through such a fluid at a constant separation and their orientation relative to each other remains constant (see figure 1.8(a)). In this case, the interaction between such spheres is minimal. This result corresponds with the analytically result of Goldman *et al.* [53]. The numerical simulations of Feng *et al.* [54] show that two small spheres descending close together through a Newtonian fluid will rotate about one another until they are directly side-by-side (see figure 1.8(c)).

It was found by Michele *et al.* [55] that an element of elasticity within the fluid greatly increased the amount of interaction between similar spheres. They studied the interaction between two spheres settling through a viscoelastic fluid by experiment. They found that when two spheres settle from being initially side by side, they attract and rotate such that they come into contact and are positioned one above the other (see figure 1.8(b)).

These alignment and aggregation effects were demonstrated to be the result of elasticity in the experiments of Joseph *et al.* [37]. They compare the interaction between two spheres settling from being initially side-by-side in a Newtonian and in a viscoelastic fluid. For a Newtonian fluid, the spheres initially separate (when they are very close together) and then sediment side by side through the fluid in a stable orientation. However, two spheres settling at similar separations in a side-by-side configuration in

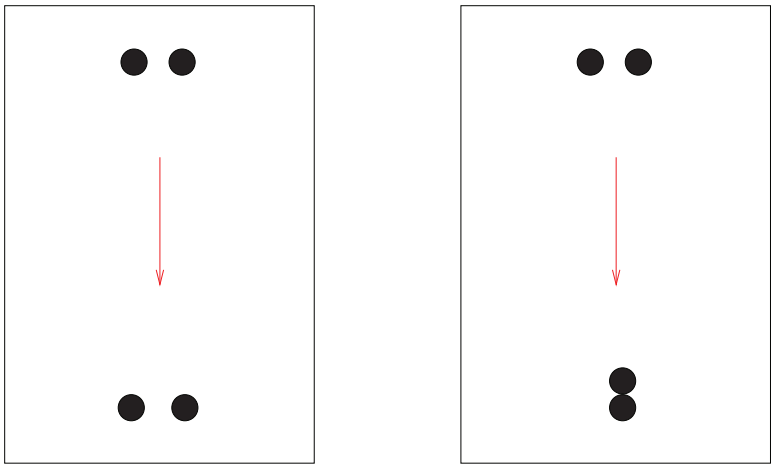

(a)

(b)

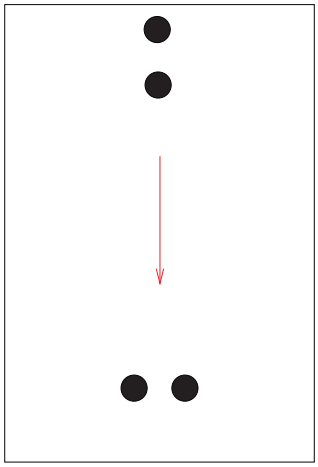

(c)

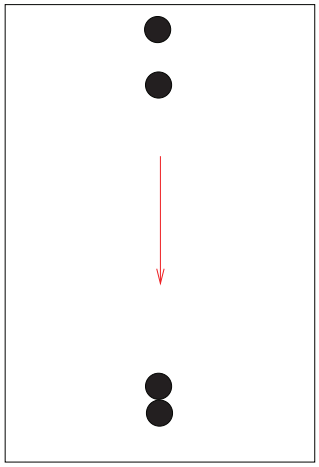

(d)

Figure 1.8: The change in orientation between two close spherical particles descending in a fluid. (a) Two spheres initially side-by-side in a Newtonian fluid remain in this configuration throughout their descent. (b) Two spheres initially side by side in a shear-thinning viscoelastic fluid rotate about one another so that their line of centres becomes parallel to gravity. They also move closer together so that they touch. (c) Two spheres initially oriented so that their line of centres is parallel to gravity in a Newtonian fluid rotate about one another until they are side-by-side in the fluid. Once in this relatively stable configuration, their separation remains constant. (d) Two spheres initially oriented so that they are one above the other in a shear-thinning viscoelastic fluid move closer together until they touch. Their line of centres remains parallel to gravity throughout.

a viscoelastic fluid initially attract then rotate about one another so that their line of centres becomes parallel to gravity. This interaction doesn't occur when the spheres are initially too far apart. The spheres must also be light enough so that their motion is slow through the fluid. This interaction between two spheres was also reported by the simulations of Feng *et al.* [44].

The stable configuration for two spheres sedimenting in a viscoelastic fluid is such that their line of centres is parallel to the direction of gravity. The experiments of Daugan *et al.* [56] and Verneuil *et al.* [57] study the interaction between two settling spheres initially in this configuration in a shear-thinning viscoelastic fluid. They find that the two spheres come together and form a doublet if they are within a critical separation. If they are initially too far apart, they remain at a constant separation in the same configuration.

The alignment of two spheres does not occur in all non-Newtonian fluids. For example, the experiments of Merkak *et al.* [58] show that the plasticity of a fluid can reduce the extent to which two spheres interact. Here, they quantify the interaction between two spheres moving at low controlled velocity in a viscoplastic fluid. They consider two configurations for the spheres; one has them side-by-side and in the other their line of centres is parallel to the flow. They show high plasticity limits the ranges of separation at which objects interact as they descend through the fluid. When two spheres settle so that their line of centres is parallel to the flow, the critical separation for interaction is smaller than found in viscoelastic fluids. Such spheres are considered to be interacting if the drag force exerted on the trailing sphere is smaller than that exerted on the leading sphere. The interaction between two spheres settling side by side is minimal in the viscoplastic fluids tested.

The flow field imposed in a viscoplastic fluid by two sedimenting spheres was simulated by Liu *et al.* [59]. They find that spheres interact at greater separations than would be predicted by looking at the flow field surrounding a single sphere sedimenting in the same fluid. The size and shape of the region of yielded fluid that a single sphere sediments within is greatly affected by the presence of a second sphere in the fluid. Evidence of this is also presented in the experiments of Gueslin *et al.* [60].

Two spheres sedimenting one above the other through a yield stress fluid that "ages" (Laponite suspension) are seen to move closer together independently of the flow field imposed. In some cases, a negative wake was seen in between the two spheres, but it did not contribute to the interaction between the objects.

In the case of two circular discs sedimenting in a 2D dry foam (modeled as an elasto-plastic fluid), one would expect them to move into a stable orientation where their line of centres is parallel to gravity. This is predicted to happen if the discs are placed within a critical separation of each other, whether they are initially side-by-side or one above the other. Discs positioned further away from each other than this critical separation will not interact. The critical separation is related to the plasticity of the foam, thus it is expected to decrease with increasing liquid fraction.

1.9.5 Long Objects

The study of the sedimentation of long objects such as cylindrical rods (in 3D) or elliptical objects (in 2D) through non-Newtonian fluids is closely related to the literature on the interaction between two spheres. Investigating the falling motion of long objects in yield stress fluids also dates back to the 1960s. During this time, three related letters by Boardman and Whitmore [61, 62] and Rae [63] discussed the settling of long rectangular objects in a yield stress fluid. Boardman and Whitmore state that the nature and size of the fluidized region surrounding the long object is highly dependent on the orientation of that object while Rae argued that it is dependent on the aspect ratio of the object.

Let us consider the stable orientation for long objects settling in fluids, firstly for the Newtonian case. Huang *et al.* [64] studied the descent of an elliptical object in a purely viscous fluid in 2D simulations. The ellipse was found to oscillate during its fall but its stable orientation was such that its major axis was perpendicular to gravity.

The theoretical work of Leal [65] and Brunn [66] showed that rod-like cylindrical particles turn parallel to gravity when falling through viscoelastic fluids, and that this occurs due to the elasticity of the fluid. This is equivalent to the rotation of two spherical

particles about one another in a viscoelastic fluid so that their line of centres becomes parallel to gravity (§1.9.4).

Joseph *et al.* [67] proposed that the tilt angle of a long body falling in a viscoelastic liquid is determined by the competition between viscous, viscoelastic and inertial effects. For small inertial effects, the viscoelasticity of the fluid dominates, turning the long body such that its major axis is parallel to gravity. The viscoelasticity of the fluid was shown in the 2D simulations of Wang *et al.* [68] to control the orientation of elliptical objects in pressure-driven flow so that their broadside is parallel to the net flow.

In chapter 6, we aim to investigate the role of elasticity and plasticity of a 2D foam in the sedimenting motion of an elliptical object. The stable orientation for such an elliptical object in a pressure-driven flow of a 2D foam was shown by Dollet *et al.* [69] to be so that its major axis is parallel to the direction of the flow. This work is reviewed in section 1.10. In this case, one would expect the stable orientation of an ellipse sedimenting in a 2D dry foam to be such that its major axis is parallel to gravity.

1.10 The Stokes Experiment and Foams

In the year 2000, Cox *et al.* [70] performed a 3D experiment in which a spherical bead was dropped through a foam. The liquid fraction (Φ_l) of the foam was varied and its effect on the terminal velocity of the sphere descending through the foam measured. It was found that the velocity of the falling ball increased linearly with the square of the liquid fraction.

For a dry foam, the motion of the object is initially slow, but it gains in velocity as the foam coarsens. The drag force exerted on the bead by the foam reduces as it coarsens due to the increase in bubble size; Cox *et al.* propose that the average bubble diameter of the foam (d_b) is inversely proportional to the yield stress, and use a Herschel-Bulkley relation to model the foam.

The experiments of Cantat and Pitois [71, 72] are a slight variation on this idea. Instead of constant force experiments (weight), they performed constant velocity ex-

periments. The foam flows around a fixed sphere or equivalently, the sphere is moved at a fixed slow velocity through a stationary foam. In their experiments, the foam is monodisperse (bubble area dispersity is less than 10%) with average bubble diameter (d_b) of roughly 2.5mm. The foam is allowed to drain fully so that the liquid fraction (Φ_l) lies between 1% and 2%. The radius of the sphere is 0.5cm. They measured the drag force exerted on the sphere by the foam. They also investigate the T1 locations during the relative motion of the sphere and the foam filled tube. Through image analysis, it was found that these plastic events occur mainly within the first couple of layers of bubbles surrounding the sphere (i.e. within two bubble diameters (d_b) of the sphere boundary). They show that further away from the sphere, the foam structure is not strongly modified as the sphere moves through the foam.

The experiments of de Bruyn [73, 74] are similar; they consisted of a fixed spherical bead immersed in a shaving foam filled tube that moved at constant velocity. The drag force exerted on the object by the foam is measured. Coarsening of the foam results in a decrease in the force exerted on the object; in inverse proportion to the mean bubble size. The work also records the transient build up of forces on the sphere as it moves from rest to its terminal constant velocity at the beginning of each experiment. Equivalently, the resulting relaxation of the foam and the forces it exerts on the sphere when the sphere is instantaneously stopped at the end of the experiment is also measured. The Herschel-Bulkley relation is again proposed to model the flow of foam.

These experiments provide the only existing work of purely three-dimensional variations to the Stokes experiment probing foam rheology. Instead, most experiments in the field are performed in two-dimensions. As already stated, it is more convenient to work with foam in 2D as we can easily trace bubbles in flow though image analysis.

The experiments of Dollet *et al.* [75, 76] consisted of an obstacle positioned in a monolayer of foam that is bounded below by a liquid sub-phase and above by a glass plate. The object is attached to an elastic fibre which is connected to a fixed base. In this case, the displacement of the object from its position when the foam is stationary is used to measure the drag force it experiences due to the constant flow of a monodisperse foam. They varied the obstacle size and shape as well as the size of the bubbles and

investigated its effect on the drag force exerted by the foam. The shapes considered for the obstacle were cylinders (with equal width to the monolayer of bubbles), squares as well as an airfoil.

They measure two contributions to the drag force exerted on the obstacle by the foam; an elastic and a fluid contribution. The elastic contribution is the drag force exerted by the foam at vanishing flow rate and is called the yield drag. This yield drag has two contributions; an elastic one due to the network of films and a pressure one due to bubbles in contact with the obstacle. It was demonstrated in the work that the pressure of bubbles in contact with a circular obstacle contributes 30% to the total yield drag. The fluid contribution to the drag increases with flow rate. It is the yield drag that is of interest for comparison of the work of this thesis.

They investigated the effect that bubble size has on the drag force exerted on a circular obstacle with diameter 30mm. They varied the bubble area of the monodisperse foam between 12mm^2 and 40mm^2. It was shown that the yield drag decreased for increasing bubble size. They also varied the size of the obstacle and showed that the drag force exerted on the obstacle increases with its size.

They showed that a square obstacle is stable in whatever orientation it is placed in the flowing foam. Conversely, the airfoil (which was not cambered) was shown to have two stable orientations; both of which had the major axis parallel to the flow. They demonstrate that the boundary conditions of the object do not significantly affect the drag force exerted on them. They considered cogwheels of similar dimensions to the circular objects used and showed that their rough boundary has insignificant effect on the flow of the foam and the drag force exerted.

Raufaste *et al.* [77] combine 2D experiments with equivalent simulations of a circular obstacle positioned in a constant low-velocity flow of foam. A similar experimental setup to that of Dollet *et al.* [75] is used while quasi-static simulations are performed using both the Surface Evolver [78] software as well as the Potts model (see §2.1.1 and 2.1.2 for details of these simulation techniques). They investigate the variation of the yield drag exerted on the obstacle for different obstacle size and foam liquid fraction (Φ_l). In this low-velocity limit, viscous dissipation of the foam is negligible. In

this case, the total yield drag (F_y) has two contributions; due to the pull of the foam films (network force F_y^n) and the pressure of the gas bubbles in contact with the obstacle (F_y^p). The yield drag describes the drag force exerted on an obstacle when there is relative motion between obstacle and foam. In this case, the total yield drag is given by

$$F_y = F_y^n + F_y^p \,. \tag{1.19}$$

Simulations enable a more detailed investigation of the separate contributions towards this total yield drag.

They show that the network contribution to the yield drag exerted on the circular obstacle increases affinely with its diameter (d_0). Dollet provided an argument in the paper by Raufaste *et al.* [77] that predicted a power-law relation between the network drag (F_y^n) exerted on a circular obstacle and the foam's liquid fraction (Φ_l). In this argument, he assumed that the change in the deformation of bubbles between being squeezed upstream of the object to being elongated downstream of the object to be smooth. The contact length (L) of a bubble with the object was computed as a function of the ortho-radial angle along the object's boundary. In this case, the maximum value for the contact length is directly at the front of the object and the minimum contact length is directly at the back of the object. The inverse of L denotes the density of the vertices along the boundary of the object. Assuming that each film exerts a pulling force 2γ on the object, the network contribution to the drag is given by

$$F_y^n = \gamma d_0 \int_{-\pi}^{\pi} \frac{\cos\theta}{L(\theta)} d\theta \tag{1.20}$$

This integral was solved by introducing dimensionless parameters and consequently a power-law relation (1.21) was predicted between the network drag and the liquid fraction of the foam.

Combining their simulation and experimental results, they show that the network yield drag varies with obstacle diameter d_0, average bubble area (A_b) and the foam's

liquid fraction with the relation

$$F_y^n = \frac{1.032}{\Phi_l^{1/4}} \frac{\gamma d_0}{\sqrt{A_b}} , \tag{1.21}$$

where 2γ represents the line tension of the foam films.

Asipauskas *et al.* [79], Dollet and Graner [51] and Marmottant *et al.* [80] investigate the deformation fields of a two-dimensional foam through the use of the texture tensor ($\overline{M}$) [81]. This is defined by

$$\overline{M} \equiv \left\langle \vec{l} \otimes \vec{l} \right\rangle , \tag{1.22}$$

where $\vec{l}$ denotes the vector connecting the centres of a pair of neighbouring bubbles. Using this texture tensor and image analysis techniques, they quantify the elasticity and plasticity field of the foam as it flows past a fixed circular obstacle. This work provides clear images of the how foam deforms and rearranges as it approaches such an obstacle and in its wake.

The texture tensor has also been used to analyse the shearing of a Langmuir foam (a foam monolayer on the surface of water) by Courty *et al.* [82]. A circular obstacle was placed within the foam monolayer and its motion tracked as the foam was sheared. This experiment uses the obstacle as a force sensor for a shear flow of foam. This is a different type of flow to what is considered in the other experiments reviewed here since it is a result of a force gradient. The force that drives the flow is not constant along the entry of the foam channel, as seen in the rest of the experiments discussed.

Investigation into foam response is also performed in simulations. The Surface Evolver software, used in this thesis and reviewed in section 2.1.1 was used by Cox *et al.* [83] to investigate the lift force exerted on a circular obstacle in a 2D channel as foam is forced to flow between it and a wall. It was found that the lift force exerted on the disc is directed such that it is repelled by the wall. The magnitude of this lift force due to the foam flow increased when decreasing its separation from the wall. The drag force was also measured and found to be independent of the obstacle's proximity to a wall.

Sun and Hutzler [84] used a hybrid lattice-gas model (see §2.1.3) to investigate the plasticity of the foam as a small circular disc is forced to move through the foam in a 2D channel. They find that the localization of T1s for a foam flowing in this manner is highly dependent on the liquid fraction of the foam. Plastic events occur in a smaller region around the obstacle in dry foam than for a wet foam. It is shown that most rearrangements occur mainly within the first five bubble layers surrounding the object for wet foams. However, for a dry foam, most plastic rearrangements occur within the first two bubble layers surrounding the object.

Other variations of the Stokes experiment include the investigation of flow of foam past different shaped obstacles to the sphere or circular disc.

The use of less symmetric shapes such as an ellipse enables further investigation of a foams' complex response. Dollet *et al.* [69] used the same experimental setup as in their previous work with an elliptical object placed within a monolayer of bubbles in a channel. Its centre was attached to a thin elastic fibre which was used to measure the drag, lift and torque exerted on the object by the constant velocity flow of a monodisperse dry foam. The major axis of the ellipse was 48mm long and its minor axis 30mm. The ellipse was free to rotate as a result of the forces exerted by the foam.

They investigated the rotating motion of the ellipse as it is initially oriented so that its major axis is at an angle of $\pi/10$, $4\pi/15$, $16\pi/45$ and $19\pi/45$ to the direction of the flow of foam. They found that the ellipse rotated so that its major axis becomes parallel to the direction of foam flow. This tendency is shown to be independent of the initial orientation of the ellipse in the foam. The only stable orientation for an ellipse in the foam is such that its major axis is parallel to the flow. They detected that the angular velocity of the ellipse increased when the angle between its major axis and the direction of the flow was between $\pi/12$ and $2\pi/9$.

They also showed that the drag force exerted on the ellipse when its major axis was perpendicular to the flow was similar to that exerted on a circular obstacle of diameter 48mm. Similarly, when the ellipse was oriented so that its major axis was parallel to the flow, the drag force it experienced corresponded to that exerted on a circular disc with diameter 30mm.

In this thesis, we are interested in a 2D dry foam's response to the sedimentation of an elliptical object (chapter 6). We aim to probe the response of the foam further by varying more control parameters such as the size of the ellipse as well as its eccentricity. We will also compare our results to that of Dollet *et al.* by varying the initial orientation of the ellipse in the foam. It is expected that the stable orientation for the ellipse will be such that its major axis is parallel to gravity.

Another asymmetric object that has been used to probe foam response is a cambered airfoil. Dollet *et al.* [85] used the same experimental setup as before, with a cambered airfoil attached to a fixed base by an elastic fibre. In this case, the drag, lift and torque exerted on the object by the foam are measured by tracing the motion of the airfoil from its stationary position. The liquid fraction of the foam Φ_l is roughly 10%. The zero torque orientation of the airfoil is considered, where the major axis is parallel to the flow. They discovered that a downward lift was exerted on the cambered airfoil in foam flow. This is the opposite to what occurs in equivalent situations in aerodynamics. It was shown that it is the elasticity of the foam that causes this "negative lift".

Another interesting experiment that can be considered a variation of the Stokes experiment in foam is that of Cantat and Delanney [86]. They track the motion of a large bubble in a plug flow of smaller bubbles in a two dimensional experiment. The velocity of the bubble is compared with the mean flow rate of the foam. In this case, viscous effects within the foam result in the large bubble moving at a quicker rate than the rest of the foam for particular velocities of the plug flow.

These variations of the classical Stokes experiment have generated vast information on foam rheology. It provides a basis for the work presented in this thesis. The aim of the work is to enhance the information on foam flow using new simulation methods. The variations of the Stokes experiment proposed in this work include the sedimentation of a single circular disc through a two-dimensional dry foam, an equivalent system with two circular discs and a third case where the discs are replaced by an elliptical object. These simulations aim to improve the prediction of a foam's response by investigating the role of the foam's elasticity and plasticity in detail.

Some of the results presented in this thesis have been published in two papers [87,

88]. These papers are provided in appendix A at the end of the thesis.

Chapter 2

Methodology

There have been many attempts to predict foam rheology by simulation. The models used currently are presented and reviewed in this chapter (see section 2.1). The work presented in this thesis is based on the quasi-static model, which is introduced in section 2.1.1. The reasons for choosing this model are discussed here.

This chapter includes a detailed description of the model that we use to simulate the interaction of a dry two-dimensional foam with circular and elliptical objects that pass through it. The methodology of the simulations is split into three parts. We firstly describe how the initial structure of the foam is created (section 2.2). Part 2 describes how the quasi-static model is incorporated into the Surface Evolver [78] to simulate the sedimentation of circular discs (see section 2.3). Part 3 is devoted to describing the adjustments that are required to this method for simulating the motion of an elliptical object (see section 2.4). These simulation techniques are applied in chapters 3, 4 and 5 for circular discs and in chapter 6 for the elliptical object.

A note on the computational time for the simulations is provided in section 2.5.

2.1 Review of Simulation Techniques

Many simulation techniques have been used to model foam response. Some of these are limited to two-dimensions and none are capable of encapsulating all of the foam's behaviour perfectly. It is therefore an ongoing primary aim of researchers in the foam

community to improve these simulation techniques for modelling the complex nature of foams. In this section, a review of the current simulation techniques is presented and subsequently the choice for the simulation work of this thesis is justified.

2.1.1 Quasistatic Model

The main assumption of the quasistatic model is that the relaxation of the foam (e.g. after a T1 event) is much faster than the shear rate and diffusion of the foam. Thus, the deformation of the foam is sufficiently slow so that viscous effects remain negligible.

Simulations using a quasi-static model consists of a foam structure that passes through a sequence of equilibrium configurations between small increments in the strain. Recall that the structure of a foam in equilibrium satisfies the Laplace-Young law (see 1.4.1). Thus, in 2D the foam films are represented simply by circular arcs as shown in figure 2.1. The pressure difference between two bubbles (Δp) balances with the curvature of the film between them (κ) by Laplace's law (1.4). The equilibration of the foam is driven by the minimization of its total edge length $\sum_i l_i$ (i denotes the foam's films) subject to the constraints

$$E = 2\gamma \sum_i l_i + \sum_k p_k \left(A_k - A_k^t\right) \ , \tag{2.1}$$

where 2γ denotes the line tension of the films, A_k denotes bubble k's area, A_k^t its area when undeformed (or a target area) and p_k its pressure. Similarly in 3D, the equilibration of the foam is driven by the minimization of its total surface area.

This type of model has long been used to model foam rheology and was developed into a prominent tool by the 2D-froth simulations of Kermode and Weaire [89]. Their code simulates the rheology of an idealised dry froth structure in 2D. An initial structure is produced by a Voronoi construction [90] where a unit square plane is divided into convex cells defined by vertices and edges (see §2.2.1 for details). The equilibration of the froth proceeds by iteration. Each iterative step consist of changing the coordinates of a vertex (x_k, y_k) of the structure and the pressures of three neighbouring cells (p_1, p_2, p_3).

All the vertices of the structure are tested in turn (up to 10 times) and T1 events are triggered. These are triggered when the distance between two neighbouring vertices becomes less than a predefined critical length. This process is repeated until a consistent foam structure is found.

The PLAT code of Bolton and Weaire [91] extends the quasi-static model to study the rheology of wet 2D foams. In this case, an initial structure is again produced by Voronoi construction and the vertices are replaced by Plateau borders. For a wet 2D foam, the balance between pressure forces and surface tension dictate that the edges of Plateau borders are circular arcs. The vertices of the structure are positioned where a cell edge meets a Plateau border. A list of the bubble pressures p_i is maintained by the code while the pressure of the Plateau borders p_b is constant throughout. As for the 2D-Froth model, the foam is equilibrated by an iteration process that involves adjusting the bubble pressures and vertex positions. Again, a T1 is triggered when two vertices become closer than a predefined critical distance. Such T1 events involve separation or coalescence of Plateau borders. A local equilibrium is again found when a consistent foam structure is found.

The Surface Evolver software of Brakke [78] provides a more powerful alternative for implementing the quasi-static model to study foam rheology. It provides more flexibility than the 2D-Froth or PLAT code as more constraints and different boundary conditions can be specified. Where the 2D-Froth and PLAT codes aimed to solve the equilibrium equations of a foam directly by changing the coordinates and curvature of the films until everything is consistent, the Surface Evolver minimizes the foam's total edge length by changing the coordinates (and therefore the curvature of the films) with respect to the area constraints of the bubbles. The software is also capable of simulating three-dimensional dry foams, as seen in the work of Reinelt and Kraynik [92, 93].

In 2D, an initial structure is again created using Voronoi construction. The films of the foam are then represented by circular arcs which join threefold at vertices. The software equilibrates the foam by minimization of (2.1). The foam's total edge length is minimized by moving the vertices subject to the area constraints of the bubbles. T1 events are triggered during the equilibration (see §1.5.2 for details) when an edge

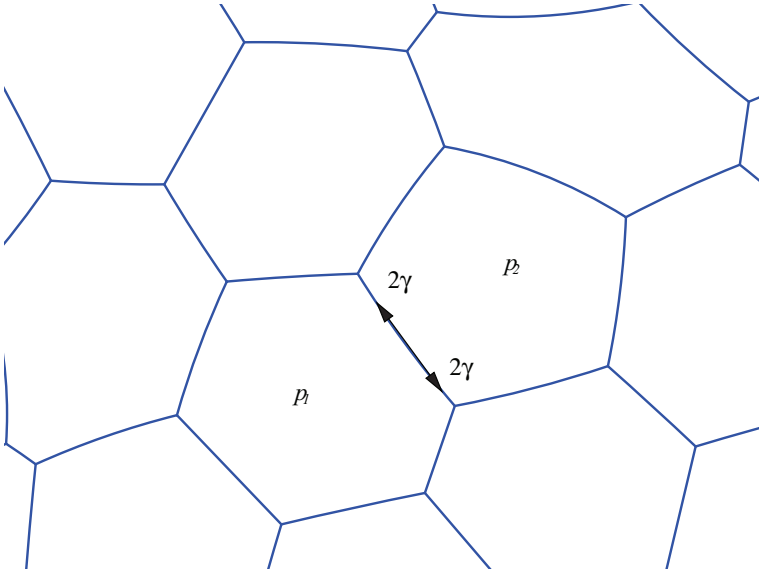

Figure 2.1: The foam structure is in equilibrium between small increments in the strain in quasi-static simulations. Thus, the force balance acting on a 2D foam film is such that Laplace's law (1.4) is satisfied. Thus, the pressure difference between two adjacent bubbles ($\Delta p = p_2 - p_1$) is equal to the local curvature of the film κ multiplied by the line tension 2γ.

shrinks below a predefined critical length l_c. A single iteration involves applying a small increment in strain before equilibration of the foam. Therefore, during a simulation iteration, many T1 events can occur and there is no way of distinguishing their order. This can prove to be a limitation of the method, but is not of interest in this work.

The implementation of the quasi-static model by the use of Surface Evolver has been extensively used in the foam community. The work of Raufaste *et al.* [77] and Cox *et al.* [83] provides prominent examples where the technique is used to probe a foam's response as it flows past a circular obstacle. It is the technique that has been chosen in this work to simulate the sedimentation of circular and elliptical objects through a dry 2D foam. Further details of its implementation can be seen in section 2.2.

2.1.2 The Large Q-Potts Model

The extended large-Q Potts model or the Monte Carlo method has proved very popular to model foam structure and rheology mainly due to its computationally quick nature

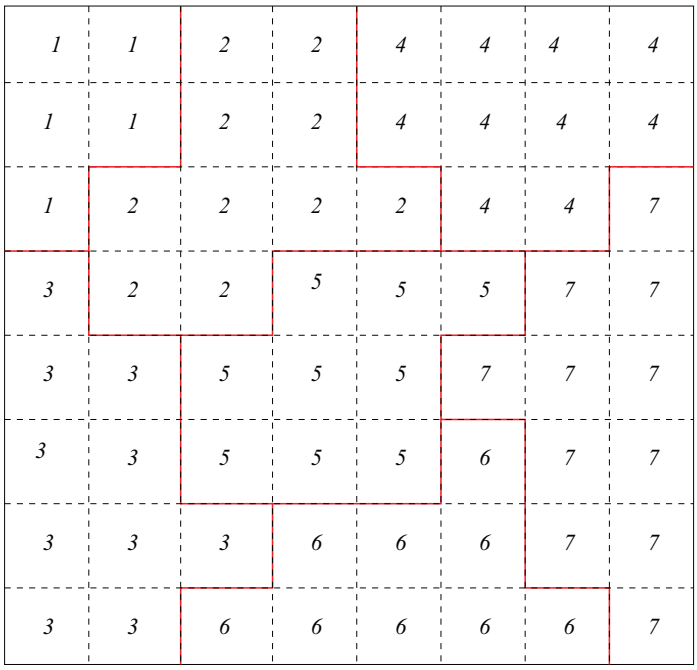

Figure 2.2: The large-Q Potts model represents a 2D foam by division of a square lattice into sites i (8×8 sites are shown) with index values σ_i ($\sigma_i = \{1, 2, 3, 4, 5, 6, 7\}$ in this example). Thus a bubble k is defined by the domain of like sites integer values; 7 bubbles are shown.

and therefore capability of providing good statistical data. It was initially developed to study foam rheology by Jiang *et al.* [12]. In this section, a brief description of the model is given and its advantages and disadvantages are discussed.

The large Q-Potts model is a stochastic method. It is therefore not structurally precise but produces good statistical data. It can be used to model the rheology of 2D or 3D dry foams. It is the two-dimensional case that is considered here.

For a typical 2D simulation the initial foam structure is represented by a square lattice. The lattice is divided up into $i = (x_i, y_i)$ sites with each site assigned an (integer) index σ_i chosen from $\{1, ..., Q\}$. In this case, bubble k is defined to be the domain of like index values $\sigma_i = k$. The boundary of these domains defines the foam films. The lattice is therefore filled by non-overlapping bubbles separated by films (as shown in figure 2.2).

The evolution process that finds the foam equilibrium is driven by the minimization

of the same energy as in the quasi-static model (2.1). This evolution equation aims to minimize two components; the total length of the interfaces between bubbles and the difference between the bubble area when they are deformed (A_k) and undeformed (A). The evolution equation that drives this minimization is given by

$$\mathcal{H} = \sum_{i,j} \mathcal{F}_{ij}\left(1 - \delta_{\sigma_i\sigma_j}\right) + \Gamma \sum_{k} (A_k - A)^2 \ . \tag{2.2}$$

The expression $\mathcal{F}_{ij}$ denotes the coupling strength between neighbouring indices σ_i and σ_j which, when summed over the whole lattice, simplifies to denote a constant line tension γ (Raufaste *et al.* [77]). δ denotes the Kronecker symbol which is given by

$$\delta_{\sigma_i\sigma_j} = \begin{cases} 0 & \text{for } \sigma_i \neq \sigma_j \\ 1 & \text{for } \sigma_i = \sigma_j \end{cases} \ . \tag{2.3}$$

In this case, the first term of (2.2) drives the minimization of the total edge length of the foam. The second term constrains the minimization of the total edge length to the area constraints of the bubbles. This term contains a compressibility constraint Γ, and can be chosen to be high enough such that the bubble area remains constant (within a few pixels) in simulations. The balance between the evolution of the minimization of both of these terms simulate a foam relaxing to mechanical equilibrium [12].

The Potts model uses a Metropolis algorithm to evolve the foam. At zero temperature, this involves randomly selecting a site i at a bubble boundary and changing its index to the value of its neighbouring site if and only if the energy of the foam is decreased. Many independent changes are tried successfully and a full Monte Carlo step has been performed when the number of tries equals the number of sites in the lattice.

The model has both advantages and disadvantages when compared to other models. One of its main advantages is its simplicity and greater simulation speed (than that of the Surface Evolver for example). Due to the speed of the simulation model, it is often used to study foams with a large amount of bubbles. It also means that the geometric parameters can be varied to a greater extent which results in a greater amount of data, whence better statistics. It is a model that can also incorporate many interactions such as

temperature effects and allows for direct measurements of events such as T1s. Although it cannot accurately represent a foam structure, it can provide a realistic representation of the dynamics of the system.

One of its main limitations is the fact that it does not incorporate a qualitative description of foam viscosity. The Monte Carlo algorithm also results in some uncertainties in the relative timing of events. In this case, the measured interval between frequent events such as T1s in a region of high foam deformation can be less accurate than sometimes desired.

2.1.3 Hybrid Lattice Gas Model

The Hybrid Lattice Gas is a computational fluid dynamics model based on collisions between fluid particles. It was adapted by Sun and Hutzler [94] to model liquid foams. The model works over a range of liquid fractions Φ_l, as fluid particles are introduced into a foam structure.

The model is based on a hexagonal lattice, as shown in figure 2.3. A bubble surface is represented by evenly spaced surface nodes (black dots in figure 2.3) that are not part of the hexagonal lattice. Intermediate bounding sites represented by red squares approximate this solid boundary within the lattice. These are mutually attracted to each other by a constant force mimicking the effect of surface tension.

The gas in the bubbles can move between the white circular nodes in figure 2.3. The liquid particles are free to move between the white square nodes. They can move in one of six directions or stay at rest. The arrows in figure 2.3 show particles that interact with the surface of the bubbles. A fluid particle that encounters a solid surface is reflected back in the same direction. Fluid particles that encounter another fluid particle collide and their velocities and direction are decided by the collision rules of the lattice-gas model.

The gas in the bubbles exerts pressure on the surface of the bubble. In this case, a pressure force is applied on the intermediate surface nodes that are directed perpendicular to the links between the intermediate nodes. A disjoining force due to nearby

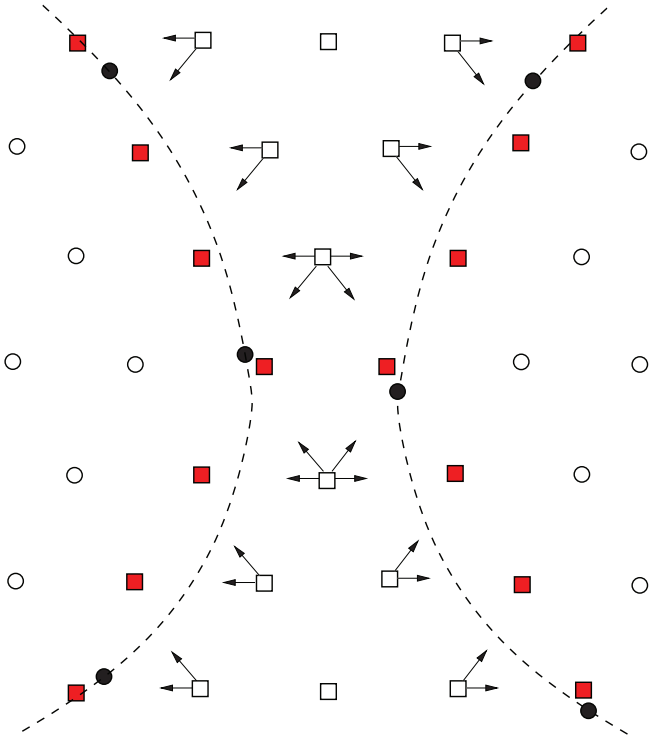

Figure 2.3: The foam structure is equilibrated within a hexagonal lattice. The bubble surfaces (dashed line) are represented by evenly distributed solid nodes (black dots) which are not part of the hexagonal lattice. Intermediate surface nodes are introduced within the lattice (filled red squares) which attract each other with a constant force (surface tension). Fluid particles are free to move in one of six directions (within the empty white squares) between the two surfaces. Arrows denote fluid particles interacting with the solid interface.

interfaces is represented by a mutually repulsive force between the two neighbouring surfaces.

An iteration consists of calculating the total force applied on the intermediate surface nodes and updating their positions and velocities accordingly. The liquid particles are then equilibrated according to the collision rules of the lattice gas model. This is repeated several thousand times such that an equilibrium configuration of a foam structure is computed.

This method of simulations is relatively new in foam rheology. It is confined at the moment to relatively small foam samples. Another limitation of the model is that the only contribution to viscous dissipation is due to the bulk viscosity of the fluid.

However, the model provides a means to interpolate between the dry and wet models described in this section. As for previous simulation models described, it is capable of simulating 3D foams.

2.1.4 The Vertex Model

The vertex model was developed for simulating foam rheology by Okuzono *et al.* [95, 96]. The model is computationally efficient as it reduces the degrees of freedom of complex cellular systems such as foams. Such a system is represented by a network of straight edges that meet threefold at vertices.

Here, a 2D foam is modelled with the Plateau borders denoted as vertices (with position r_i and velocity v_i) and the films denoted as segments (of length l_{ij}). The model simulates foam rheology through the motion of its vertices. The equation of motion of the vertex i is given by

$$\frac{\partial Q}{\partial v_i} + \frac{\partial H}{\partial r_i} = 0 \,, \tag{2.4}$$

where Q denotes a dissipation function and H denotes the total energy of the 2D foam. The foam evolves towards an equilibrium state by the motion of the vertices (2.4) supplemented by T1 topological changes. As in the previous models discussed, a T1 event is triggered by a predefined cut-off length. Thus, a T1 is performed if any two vertices become closer than a critical separation l_c, which is related to the foam's liquid fraction.

The Vertex Model is a simple, computationally effective method for simulating dry two-dimensional foams. It approximates the curvature driven motion of the films and viscous dissipation of the foam by moving its vertices. However it does not provide a realistic representation of the foam structure as the edges are constrained as straight edges. It is also not applicable for simulation of wet foams as the dynamics of Plateau borders cannot be represented by vertices in this case.

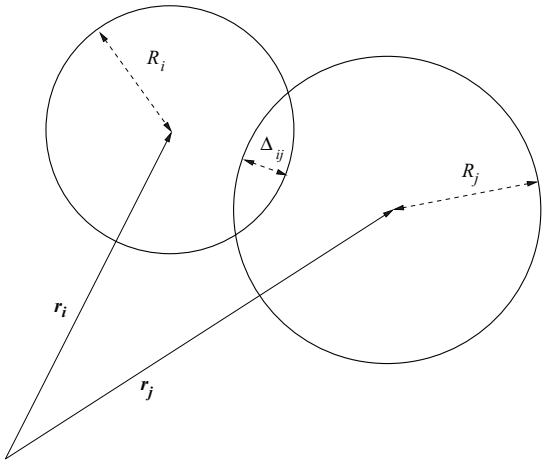

Figure 2.4: The bubble model treats bubbles as circular discs. Here, two neighbouring bubbles i and j are shown. Their centre positions are denoted by the position vectors $\mathbf{r}_i$ and $\mathbf{r}_j$ and their radii given by R_i and R_j respectively. The bubbles interact since they overlap ($\Delta_{ij} \neq 0$), in which case they experience a mutually repulsive force $\vec{F}^r_{ij}$. A drag force $\vec{F}^v_{ij}$ between bubbles surfaces is also included that represents viscous dissipation in the foam.

2.1.5 The Bubble Model

The Bubble Model [97], also referred to as the Soft Disk Model [98], is a simulation method that treats each bubble as a disk.

The model is based upon the idea that a bubble experiences two main forces when it is packed in a foam. The first force is a strictly repulsive force between a pair of neighbouring bubbles. This force exists if the neighbouring bubbles overlap (as shown in figure 2.4). This repulsive force between neighbouring bubbles i and j is denoted by ($\vec{F}^r_{ij}$) and given by

$$\vec{F}^r_{ij} = \gamma \langle R \rangle \left[\frac{1}{\left| \vec{r}_i - \vec{r}_j \right|} - \frac{1}{R_i + R_j} \right] \left(\vec{r}_i - \vec{r}_j \right) , \tag{2.5}$$

where $\langle R \rangle$ is the average bubble radius and γ denotes the surface tension of the foam. $\vec{r}_i$ and $\vec{r}_j$ denote the position vector of the centre point of each bubble while R_i and R_j denote their radii.

The second force between the neighbouring bubbles is a dissipative force ($\vec{F}^v_{ij}$) due to the relative motion between them. This can be considered to represent a simple form

of the viscous drag in a foam. It is proportional to the velocity difference between the neighbouring bubbles, thus given by

$$\vec{F}^{v}_{ij} = -b\left(\vec{v}_i - \vec{v}_j\right) . \tag{2.6}$$

In this case, b denotes a friction coefficient between the two neighbouring bubbles i and j that move with velocities $\vec{v}_i$ and $\vec{v}_j$.

The bubble model assigns to each bubble centre the equation of motion

$$\vec{v}_i = \left\langle \vec{v}_j \right\rangle + \frac{\gamma \langle R \rangle}{b} \sum_j \left[\frac{1}{\left|\vec{r}_i - \vec{r}_j\right|} - \frac{1}{R_i + R_j} \right] \left(\vec{r}_i - \vec{r}_j\right) . \tag{2.7}$$

The sum is performed over bubble i's neighbouring bubbles j which are close enough for interaction to occur. In this case, $\left\langle \vec{v}_j \right\rangle$ denotes the average velocity of bubble i's neighbouring bubbles.

One of the main advantages of the bubble model over other models is that it applies to foam of arbitrary disorder, liquid fraction, dimensionality and strain-rate. While the model has proved successful in studying the deformation and flow of foam at length scales greater than the average bubble size [99], it has its disadvantages over other models in that it cannot describe dry foams. It is a model that works best when describing wet foams with bubbles that resemble closely packed spheres or circles in 3D or 2D respectively and is unsuitable for the dry foams studied in this thesis. It is computationally fast but does not represent the foam by a realistic structure.

2.1.6 The Viscous Froth Model

The viscous froth model was developed by Kern *et al.* [100] to model foam rheology and coarsening. The main aim of the viscous froth model is to go beyond the quasistatic approximation for foam rheology (see §2.1.1). It is a model that includes the quasi-static regime used for the work presented in this thesis, but is not confined to this regime. In this case, it extends the Laplace-Young law (§1.4.1) to the case of external friction.

The model is based on the idea that the films of a two-dimensional foam confined

between solid planes move with a normal velocity v (relative to the bounding plates) and experience a resistive drag force to this motion. The drag is due to the flow of liquid in the Plateau border that lies at the point where the film is in contact with the external plane surface of such an experiment. The drag force has a coefficient λ that is dependent on the liquid fraction of the foam and the bulk viscosity. In this case the force balance on a segment of film is given by

$$\Delta P - 2\gamma\kappa = \lambda v^{\alpha} \tag{2.8}$$

where ΔP denotes the bubble pressure difference between adjacent bubbles and κ the local curvature of that film. Each film is assumed to have a constant film tension 2γ. This model reduces to the quasi-static model when the film velocity reduces to $v = 0$. The value for the power-law coefficient α is still debated, but it is shown in the experiments of Cantat *et al.* [101] that $\alpha = 1$ is a reasonable approximation. This approximation minimizes the computational expense of the model.

Experiments studying the rheology of two dimensional foams involve the competition between viscous, coarsening and shear time-scales. The viscous froth model limits viscous dissipation to one time-scale, when in reality much more are required, as shown in the work of Buzza *et al.* [15]. Any attempt to incorporate viscous effects into a model for simulating foam rheology while retaining the full details of the foam structure provides a positive development in improving the simulating techniques available. However, the viscous froth model is limited to normal dissipative forces; therefore other viscous contributions are neglected. For example, the effect of longitudinal flow of liquid in the Plateau borders is not incorporated in the model. The model is also confined to 2D as the viscous dissipation of the foam is represented as a friction between the foam films and the glass plates. Although these are limitations, the viscous froth model does provide an important step in the development of a model that incorporates all of the realistic components of foam dynamics.

The model can be easily incorporated into the Surface Evolver [102] but proves to be much more computationally expensive than the quasi-static model. Thus, for the

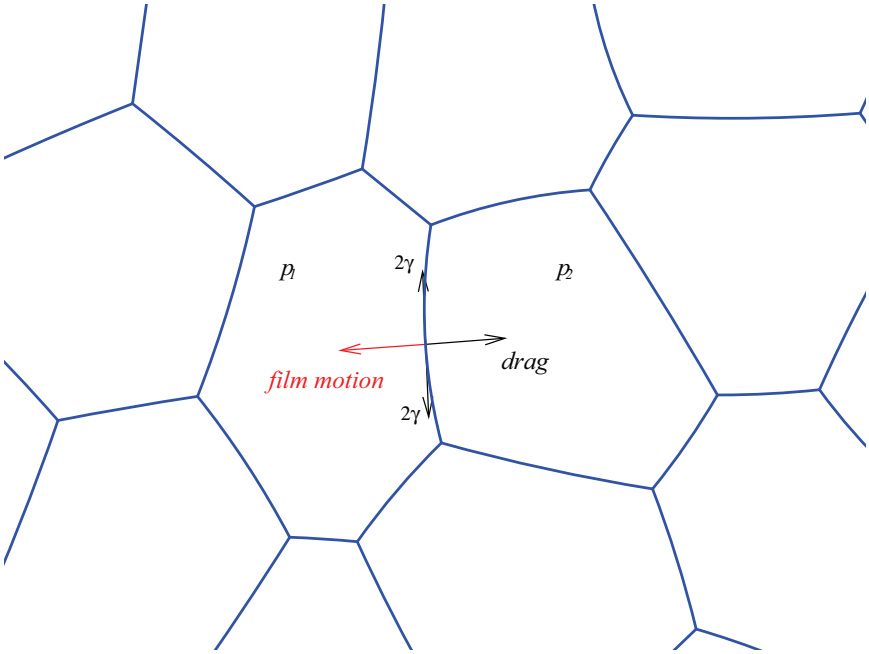

Figure 2.5: The viscous froth model for a 2D foam. Contributions to the force balance on a film that moves at a velocity v arise from film tension 2γ, bubble to bubble pressure difference ΔP and a viscous drag force λv (which in the quasistatic model is zero due to the velocity of the films being $v = 0$).

large foam structures used (see table 2.1) in this thesis, it was decided that the viscous froth model would be unsuitable.

None of the models presented provide a perfect simulation technique that encapsulates all of foam's rheological properties. It is aimed that in the future, a computational model will allow exact simulation of foam rheology. In this case, a realistic structure of the foam should be provided as well as all the viscous effects of flow within the Plateau borders. The hydrodynamic codes of Li *et al.* [103] and Higdon [104] are prominent examples of simulation codes that have been developed for similar cellular material. However, such codes are unsuitable for the work presented in this thesis as they are confined to very small samples of cellular structures. The insertion of solid objects would further enhance the computational expense.

2.2 Surface Evolver Method for the Sedimentation of Objects

Our aim is to investigate the response of a dry two-dimensional foam to the sedimentation of objects such as circular discs or ellipses by simulation. The objects used are too heavy to be supported by the foam but are light enough so that their descending motion is slow. The deformation of the foam due to the objects is much slower than the relaxation time associated with T1 rearrangements of the foam. In this case, it is clear that the quasi-static model described in section 2.1.1 is appropriate since the viscous effects of the foam can be neglected. The Surface Evolver [78] applies this model to a 2D foam with minimum computational expense and provides a realistic representation of the foam's structure throughout.

2.2.1 Initial Structure

Firstly, a two-dimensional foam structure is required. In this case, the unit square with periodic boundary conditions in all four directions is divided into convex polygons by the process of random Voronoi construction [90]. This involves the generation of a random set of points S in the plane. Each point is associated with a cell that contains the region that is closer to that point than any other. Thus, the plane is divided into cells. The number of cells that this initial structure has is chosen depending on the number of bubbles that is required for the final foam structure. An example of such an initial structure with 2000 cells is shown in figure 2.6(a). The cells of the structure will represent bubbles in the simulations and the edges will denote films. To proceed towards a more suitable foam channel, cells are deleted sequentially from the top and bottom of the structure. This is done until the number of bubbles required for the simulation is reached. In this case, we have a rectangular structure that is longer in the horizontal direction than the vertical direction. The x and y axis are reversed in this case so that the structure is longer in the y-direction. Figure 2.6(b) shows a structure that has been reduced to contain 1000 cells and rotated so that its vertical length is greater than its

horizontal width.

The structure is then imported to the Surface Evolver [78] and the peripheral films on either side of the channel are constrained to straight walls (see figure 2.6(c)). A periodic boundary condition is retained at the top and bottom of the channel. The edges of the cells are then represented as circular arcs which meet threefold at vertices (figure 2.6(d)).

2.2.1.1 Area Constraints of Bubbles

Before moving on to describe the process where the foam is equilibrated according to equation 2.1, the method that the Surface Evolver uses to calculate the area of cells requires understanding.

Let's consider a bubble that it bounded by n edges denoted by e_i ($i \in \{1, 2, 3, ..., n\}$). Each edge e_i have two vertices which are denoted (x_i, y_i) and (x_{i+1}, y_{i+1}). It is required that the orientation of the edges are defined to be positive or negative. This proceeds from choosing the vertex (x_1, y_1) to be the vertex of the bubble that has the smallest y-coordinate. The boundary of the bubble formed by the edges e_i is then followed as a path in the clockwise direction from this vertex. Thus the path around the bubble from (x_1, y_1) and back follows the edges in the order $e_1, e_2, e_3, ..., e_n$ (in which case, e_n has the vertices (x_n, y_n) and (x_1, y_1)) as shown in figure 2.7(a). Thus, the vector direction of each edge e_i is from (x_i, y_i) to (x_{i+1}, y_{i+1}) (while e_n is directed from (x_n, y_n) to (x_1, y_1)). In this case, an edge e_i has a positive orientation if $y_{i+1} > y_i$ and a negative orientation if $y_i > y_{i+1}$. The area under each edge is defined to be the area bounded by by $x = 0$, $y = y_i$, $y = y_{i+1}$ and the edge e_i and is denoted by A_i (see figures 2.7(b) and 2.7(c)). Thus, the bubble area A_b is computed by summing the areas A_i multiplied by the sign of the orientation of the edge e_i; i.e. $A_b = \sum_{i=1}^{n} sgn(e_i)A_i$.

The 2D structure initially consists of N bubbles (indexed by the integer values k) with area A_k. The initial step of the simulation is to set the target area A_k^t of the bubbles. The target area for each bubble is dependent on the bubble area dispersity of the foam required for the simulation. In the case of a polydisperse foam, the target areas of the bubbles are equal to the initial area of the cells produced by the Voronoi construction.

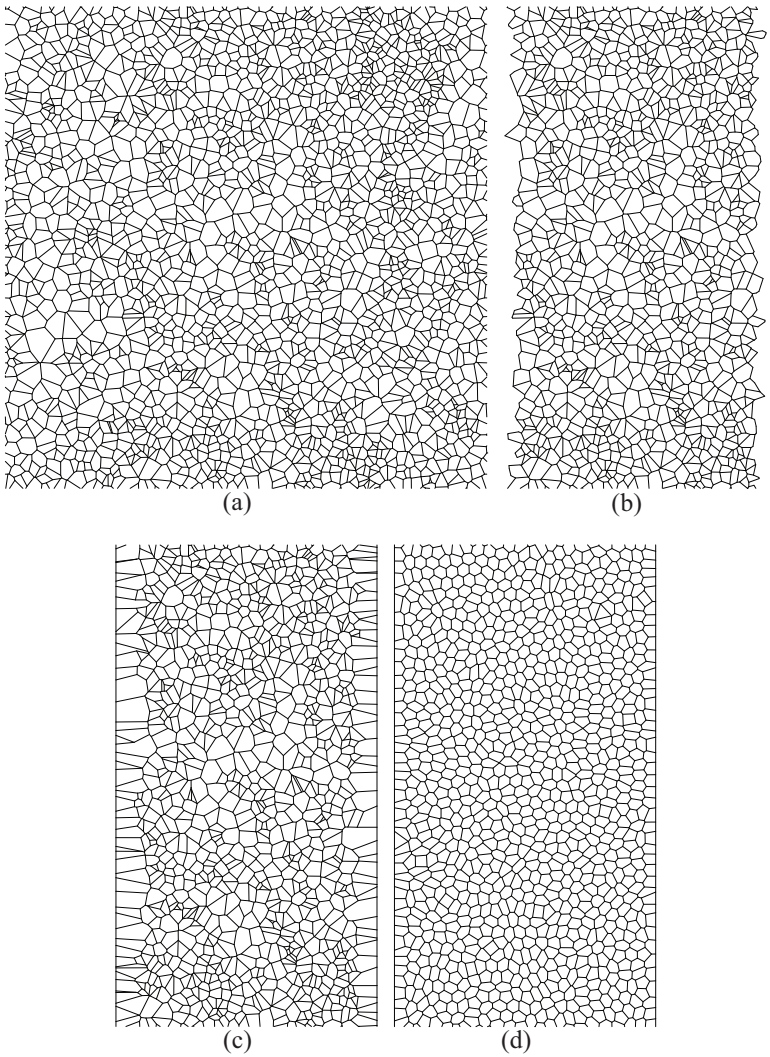

Figure 2.6: A step by step description of the creation of a foam structure. (a) A fully periodic unit square is divided into 2000 convex polygon cells (which represent bubbles in simulations) through Voronoi construction. (b) Bubbles are sequentially deleted from either side of the plane until the desired number of cells is left (1000 cells in this case). (c) The edges of the bubbles either side of the channel are constrained to straight vertical walls and periodic boundary conditions are retained at the top and bottom. (d) The bubble areas are changed in small steps so that they equal a pre-determined target value A_k^t. Here a monodisperse foam is shown, in which case, all bubbles have the same target area of WL/N, where W denotes the channel width, L its length and N the number of bubbles. A realistic foam structure is found as the Surface Evolver equilibrates the structure by equation 2.1.

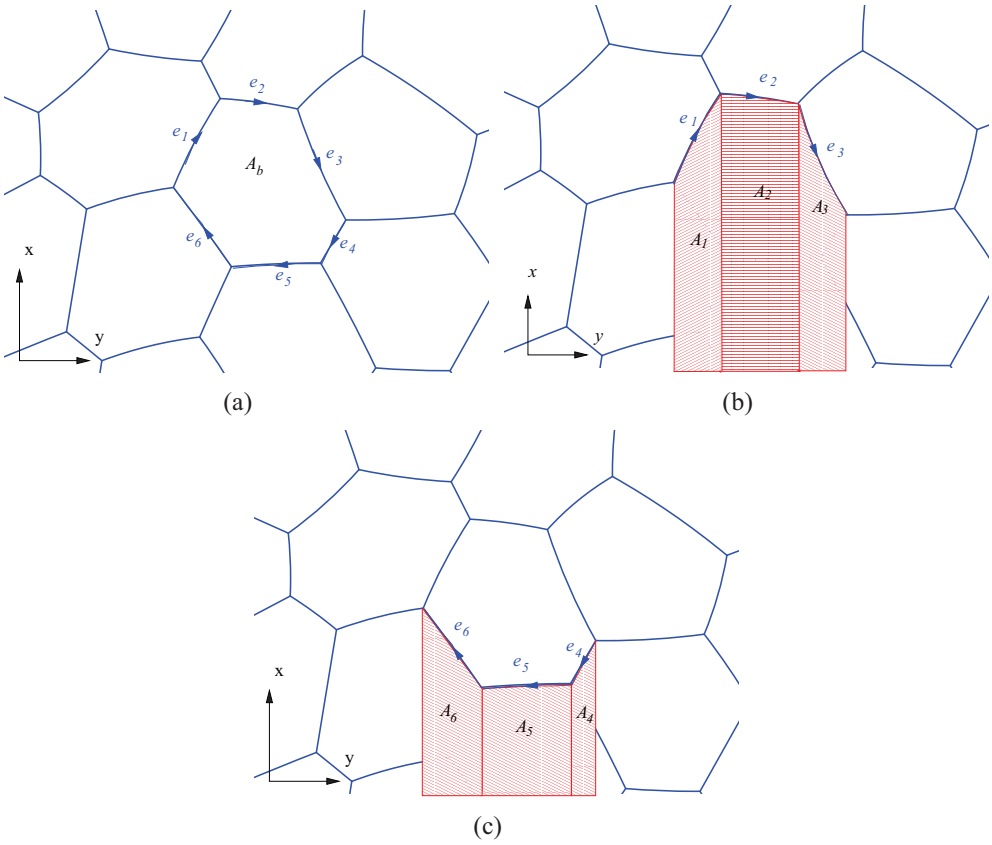

Figure 2.7: The method that Surface Evolver uses to set the bubble area constraints is shown. Recall that the x and y axes have been reversed earlier and that the positive y-direction denotes the direction of gravity. (a) The orientation of the edges e_i of the bubble must be defined. This is done by choosing the vertex with the smallest y-coordinate, i.e. the vertex furthest to the left. The edges are then oriented in the direction formed by a path that follows the edges around the bubble in a clockwise direction from the initial vertex. In the picture shown here, the first there edges (e_1, e_2, e_3) are directed to the right, in which case they have positive orientation. Similarly, the edges (e_4, e_5, e_6) are directed to the left, whence they have negative orientation. The bubble area is calculated by summing the areas under each edge multiplied by the sign of their orientation. Thus the area of the bubble shown here is simply the area shown in (c) subtracted from the area shown in (b). Thus, for a bubble with n edges, its area is given by $A_b = \sum_{i=1}^{n} sgn(e_i)A_i$.

However, the majority of the simulations presented in this work required a monodisperse foam. In this case the target area for each bubble in the initial structure is set to be equal. Therefore, the target area for each bubble is $A_k^t = WL/N$ where W and L denote the channel width and length respectively. The area of each bubble is changed in small steps until it equals this target value. During these small steps, the vertices of the foam are moved so that the total edge length of the foam is minimized relative to the new bubble area constraints. Once the bubble areas are all equal to their target area, the foam is again equilibrated by equation 2.1. An example of a monodisperse foam produced by this process is shown in figure 2.6(d).

2.2.1.2 T1 Events

Finding a realistic 2D foam structure proceeds from minimization of the total film length in relation to the bubble areas set in section 2.2.1.1. The length minimization requires that T1 events (§1.5.2) are triggered when a film shrinks so small that an unstable fourfold vertex is approached. In this case, a critical length l_c is chosen and a $T1$ is triggered when an edge length shrinks below this value. This critical length l_c sets the foam's liquid fraction Φ_l. It is the length between two vertices when two plateau borders touch each other. Thus, it is related to the radius of curvature of the Plateau borders (r_{PB}), defined in section 1.4.5. This relation was calculated geometrically by Cox [13] and is given by

$$\frac{r_{PB}}{\sqrt{3}} = \frac{l_c}{2} \,. \tag{2.9}$$

Thus, it follows from (1.12) that the foam's liquid fraction can be written in terms of the critical length (l_c)

$$\Phi_l = \frac{3}{2}\left(\sqrt{3} - \frac{\pi}{2}\right)\frac{l_c^2}{A_b} \approx 0.242\frac{l_c^2}{A_b} \,. \tag{2.10}$$

When an edge shrinks below this length it is deleted and a new edge is inserted in a direction that is perpendicular to the previous direction of the deleted edge. This results in a neighbour swapping of bubbles and constitutes a drop in the foam's total edge

Label	number of bubbles (N)	width (W)	length (L)	bubble area (A_b)
A	1500	0.432	1	2.88×10^{-4}
B	727	0.792	1	1.09×10^{-3}
C	746	0.805	1	1.08×10^{-3}
D	2200	0.397	1	1.80×10^{-4}
E	750	0.680	1	9.07×10^{-4}
F	600	0.471	1	7.85×10^{-4}

Table 2.1: The foam structures used for simulations throughout the thesis. The table describes the dimensions of the two-dimensional foams used. A letter is assigned to each foam which will be used for reference throughout the work. Here, A_b denotes the bubble area for the monodisperse case, or equivalently, the average bubble area in a polydisperse case.

length. A local equilibrium of the foam is found when all the edges are longer than the critical length and meet three-fold at angles of $2\pi/3$, i.e. when no other T1s are required.

2.2.1.3 Structures Used

The results presented in chapters 3, 4, 5 and 6 involve simulations that use different 2D foam structures. The requirements of the simulations presented throughout this thesis vary. Some for example, require a longer foam channel and a large number of bubbles. In other cases, shorter channels and fewer bubbles are adequate and therefore the computational expense may be minimized. Some of these foam structures are pictured in figure 2.8. Each foam structure used is given a label A, B, C, D, E and F and is described in table 2.1. The table gives the number of bubbles each foam has as well as the width (W) and length (L) of the channel. Also given is the average bubble area A_b of the foam.

2.3 Circular Discs

Having set the bubble area constraints, we insert a solid object within the foam. The description below applies to a circular disc (studied in chapters 3, 4 and 5).

2.3.1 Initial Placement

The initial position of the disc's centre coordinates (x_0, y_0) is chosen such that it is well within the foam channel. The bubble that contains this point within the channel is found and its edges are constrained so that it forms a circular disc. In this case, the disc's area (A_d) is initially equal to the average bubble area A_b. It is however of interest to consider the sedimentation of objects that are larger than the bubbles in the channel. In this case, the target area of the circular disc is set to an integer multiple of the average bubble area. Thus, the disc is allowed to grow slowly while as a consequence, all the other bubbles in the channel decrease slightly in area. This must be the case as the whole system (disc and foam) has a fixed area. As the disc grows towards its target area, the foam is equilibrated as before. Having grown to its full size, the circular constraint of the disc is fixed for the rest of the simulation. The disc is then moved so that its centre coordinates lie at the pre-determined point in the foam channel.

Having fixed the circular constraint of the disc, the vertices of edges that join either wall are fixed so that a no-slip boundary condition is imposed. This ensures that the resulting flow of the foam as the disc moves in the foam will not resemble a plug flow. Since the vertices at the walls are fixed, the straight edges do not contribute to the simulations and may be deleted to reduce the computational time of simulations. As a consequence of the minimization of the foam's energy, the films that meet the circular disc do so at an angle of $\pi/2$. An example of the final structure of the foam with a circular disc correctly positioned is shown in figure 2.8(a).

The setup for the simulations involving two circular discs follows the same process as described here. Examples of initial foam structures with the two discs placed side by side and one above the other are shown in figure 2.8(b) and 2.8(c) respectively.

2.3.2 Disc Motion

The circular disc is assigned a dimensionless value for its weight (mg) that will ensure it descends through the foam. After the equilibrium structure of the foam is found, the forces exerted on the discs by the foam are calculated. These forces are due to a

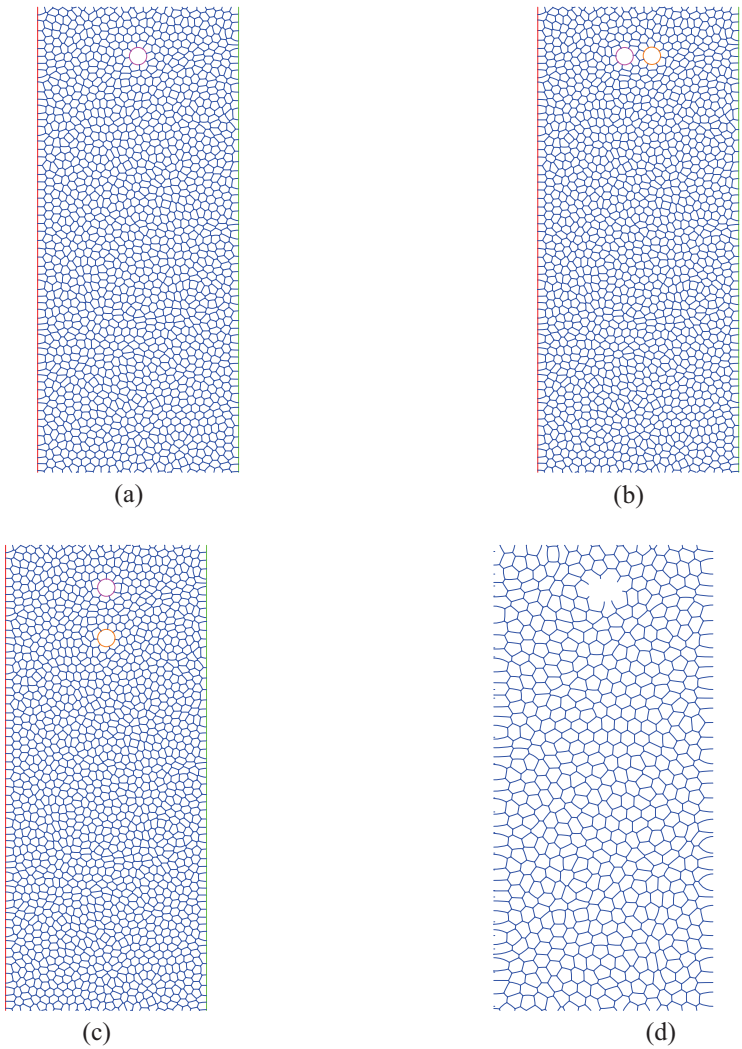

Figure 2.8: The initial setup for the four types of simulations considered in this work is demonstrated. Each represent the starting point of simulations where the response of the two-dimensional foam is probed by the sedimentation of (a) one circular disc, (b) two circular discs placed side by side (configuration 1), (c) two circular discs placed one above the other (configuration 2) and (d) an elliptical object. Note that the elliptical object is represented by a void in the foam as its boundary cannot be represented by circular arcs.

pull of the foam films (network force $\vec{F}^n$) and the push of gas bubbles (pressure force $\vec{F}^p$) in contact with the disc. These forces are shown in figure 2.9. Each foam film i contributes a force equal to the line tension 2γ which is set to $2\gamma = 1$ for all the simulations presented. A film that is in contact with the circular disc at a point (x_i, y_i) makes an angle θ_i to the positive y-direction, with θ_i defined by

$$\tan\theta_i = \frac{x_i - x_0}{y_i - y_0} \,. \tag{2.11}$$

The total contribution of the network force exerted on the disc is the sum over all films i in contact with the disc:

$$\vec{F}^n = 2\gamma \sum_i (\sin\theta_i, \cos\theta_i) \,. \tag{2.12}$$

A bubble k with contact length l_k pushes the disc due to its pressure p_k. In this case, the midpoint of l_k is found and the angle that the inward normal vector to the disc at this point makes with the positive y-direction is denoted by θ_k, defined as

$$\tan\theta_k = \frac{x_k - x_0}{y_k - y_0} \,. \tag{2.13}$$

Each bubble in contact with the disc therefore contributes an inward pressure force of $(p_k l_k \sin\theta_k, p_k l_k \cos\theta_k)$ on the disc. In this case, the total pressure force exerted on the disc is

$$\vec{F}^p = \sum_k p_k l_k (\sin\theta_k, \cos\theta_k) \,. \tag{2.14}$$

The network and pressure contributions to the force exerted on a disc that has position $\vec{x}$ at a time t within the foam channel resist the gravity driven motion. In physical situations, this motion is also opposed by a viscous force from the foam films as well as the friction between the disc and the plane face that bounds the 2D experiment. The friction coefficient between the moving disc and both the foam's films and the bounding surface of the experiment is denoted by λ. In this case, the force balance on the disc

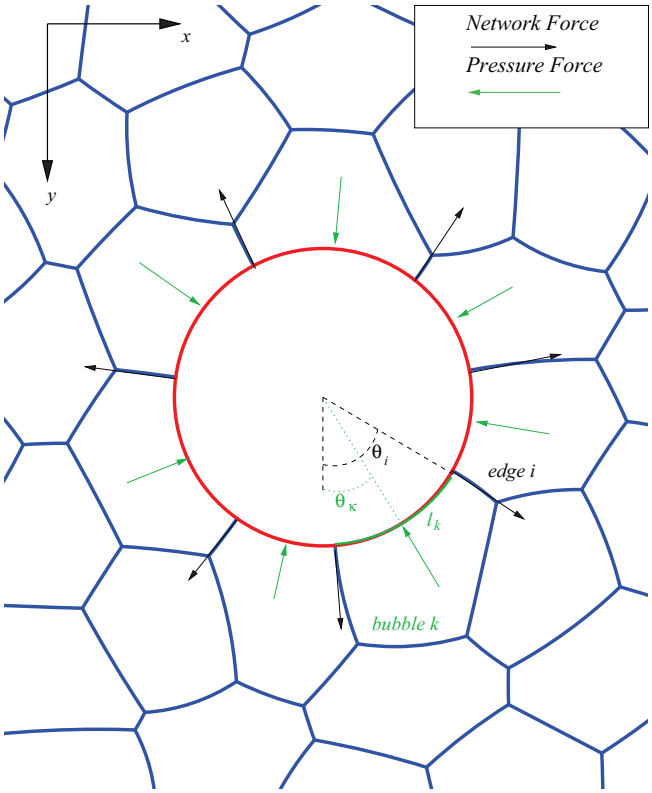

Figure 2.9: The network ($\vec{F}^n$) and pressure ($\vec{F}^p$) forces exerted on a circular disc due to the pull of the foam films and push of the bubble pressures.

must satisfy Newton's second law of motion:

$$m\frac{d\vec{x}^2(t)}{dt^2} = mg\tilde{y} - \lambda\frac{d\vec{x}(t)}{dt} - \vec{F}^p - \vec{F}^n \,, \tag{2.15}$$

where $\tilde{y}$ denotes an unit vector in the positive $y-$direction.

We assume over damped dynamics for the motion of the object through the foam. In this case, the time-scale of the motion is set by either the drag on the bounding plates of a 2D experiment or by the frictional drag of the soap films. This drag is assumed to be proportional to the translational velocity of the disc. Test simulations that include acceleration of the discs suggest that assuming steady motion is a good approximation [105]. The motion of the disc through the foam is assumed to be so slow that viscous effects don't change the structure of the foam. In this case, the motion of the object through the foam is described by

$$\frac{1}{\epsilon}\frac{dx(t)}{dt} = mg\tilde{y} + \vec{F}^{p} + \vec{F}^{n} \,, \tag{2.16}$$

where ϵ sets the effective time scale of the simulation. To avoid numerical problems, ϵ is chosen to be much smaller than the critical length l_c. It is assigned a small value throughout that ensures that the assumptions of the quasi-static model are satisfied.

A simulation iteration proceeds from a foam structure that is at equilibrium. The disc is moved in the direction of the resultant force applied by the foam and its own weight. Thus, for each iteration ($\Delta t = 1$), the coordinates (x_0, y_0) of the centre of the disc are moved a small amount Δx in the horizontal direction and Δy in the vertical direction:

$$\begin{aligned} \Delta x &= \epsilon\left(F_x^n + F_x^p\right) \,, \\ \Delta y &= \epsilon\left(F_y^n + F_y^p + mg\right) \end{aligned} \tag{2.17}$$

where subscripts x and y refer to the x and y components of the network and pressure forces.

Once the disc has been moved to its new position, the equilibrium structure of the foam is again found iteratively by minimization of (2.1). This process is repeated and the circular disc descends through the foam channel if its weight is sufficiently large. The simulations are stopped when the disc reaches the bottom of the foam channel.

2.4 Elliptical Object

The method used to simulate the sedimentation of an ellipse through a 2D foam differs slightly from the method described for discs because the boundary of an ellipse cannot be represented by circular arcs, as used previously.

The creation of the foam proceeds as before; its total edge length is minimized relative to the bubble area constraints as before. For the ellipse simulations the foams used are monodisperse.

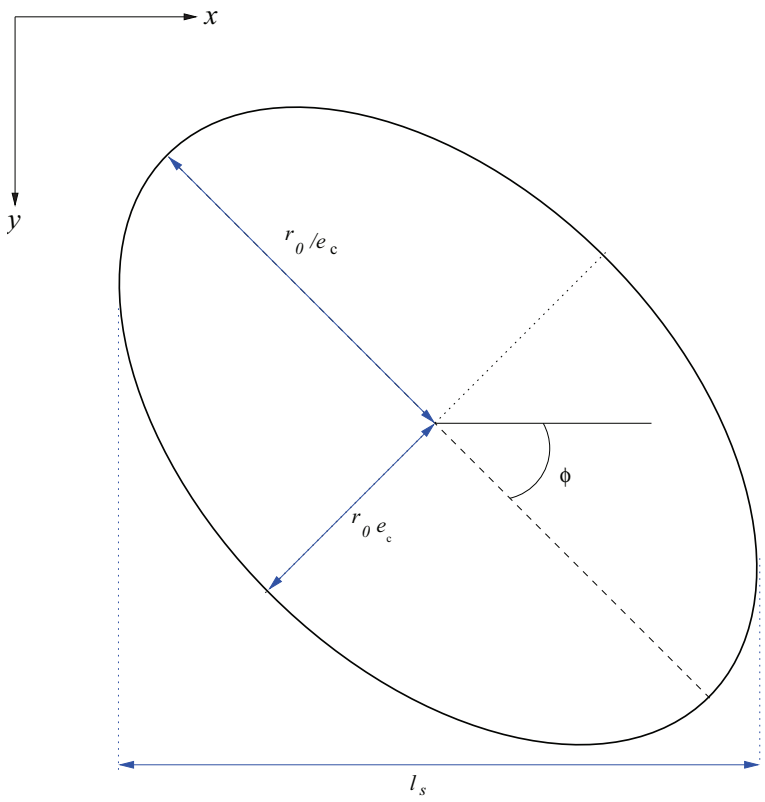

Figure 2.10: The shape parameters of an ellipse: area A_e, average radius r_0 and eccentricity e_c. The angle at which the ellipse's major axis is inclined under the horizontal line is denoted by ϕ. l_s denotes the spanwise width of the ellipse.

The ellipse cannot be represented by the films of the structure (as they are circular arcs), therefore it must be represented by a solid void within the foam. An example of this is demonstrated in figure 2.8(d). Consider an ellipse with centre coordinates (x_0, y_0) and eccentricity e_c. Its area is denoted by A_e and its average radius is r_0; in which case $r_0 = \sqrt{A_e/\pi}$. The equation that defines its boundary is

$$\frac{1}{e_c^2}\left((y-y_0)\cos\phi - (x-x_0)\sin\phi\right)^2 + e_c^2\left((y-y_0)\sin\phi + (x-x_0)\cos\phi\right)^2 = r_0^2\,, \quad (2.18)$$

where ϕ denotes the angle that the ellipse's major axis makes with the horizontal x-axis. Such an ellipse is shown in figure 2.10.

Since circular arcs cannot be used to define the ellipse, the vertices of the edges that meet the ellipse are constrained by equation 2.18 and the edges connecting them are

removed. Since, the bubbles in contact with the ellipse are missing an edge, their areas must be constrained by imagining that the missing edge is the ellipse boundary. The method for constraining the areas of these bubbles is described in two parts; firstly for the simplest case when an ellipse is oriented so that $\phi = 0$ (§2.4.1) and then the more difficult case where $\phi \neq 0$ (§2.4.2).

2.4.1 Area Constraint at Ellipse Boundary when $\phi = 0$

Let us first consider the simplest orientation of the ellipse and choose $\phi = 0$. In this case, the major axis of the ellipse is parallel to the horizontal x-axis (if $e_c < 1$).

An "area content" integral is defined piecewise, dependent on the position of a vertex (x_i, y_i) on the ellipse boundary. The method used for calculating the area of the bubble on the ellipse boundary follows from the method described in section 2.2.1.1 and in figure 2.7. It was shown that the bubble area is calculated by summing the areas under each edge of the bubble (and above the line $x = 0$) multiplied by the sign of the edge's orientation. The same method is required to keep the area of the bubbles in contact with the ellipse boundary fixed. These bubbles have a deleted edge at the boundary of the ellipse. In this section, the method of finding the area under the missing edge of any bubble in contact with the ellipse is described.

Figures 2.11 and 2.12 provide examples of the area required to calculate for the missing edge of a bubble positioned on the right and left side of the ellipse boundary. Consider a bubble k in contact with the ellipse boundary. The vertices of the bubble touching the boundary are denoted by (x_i, y_i) and (x_{i+1}, y_{i+1}), where $y_{i+1} > y_i$. Thus, it is required to calculate the area beneath the ellipse boundary between the two vertices and bounded by $x = 0$. This is done by separately calculating the area bounded by the axis $x = 0$ and the elliptical boundary between $y = y_0 - r_0 e_c$ and each vertex y-coordinate. The computation of these two areas is simplified by including a rectangular area from the origin in the calculation (see figures 2.11(a) and 2.11(b)). Let these two areas be denoted by $C_1(x_i, y_i)$ and $C_1(x_{i+1}, y_{i+1})$ respectively. Thus, the area required is given by $C_1(x_{i+1}, y_{i+1}) - C_1(x_i, y_i)$ (see figure 2.11(c)).

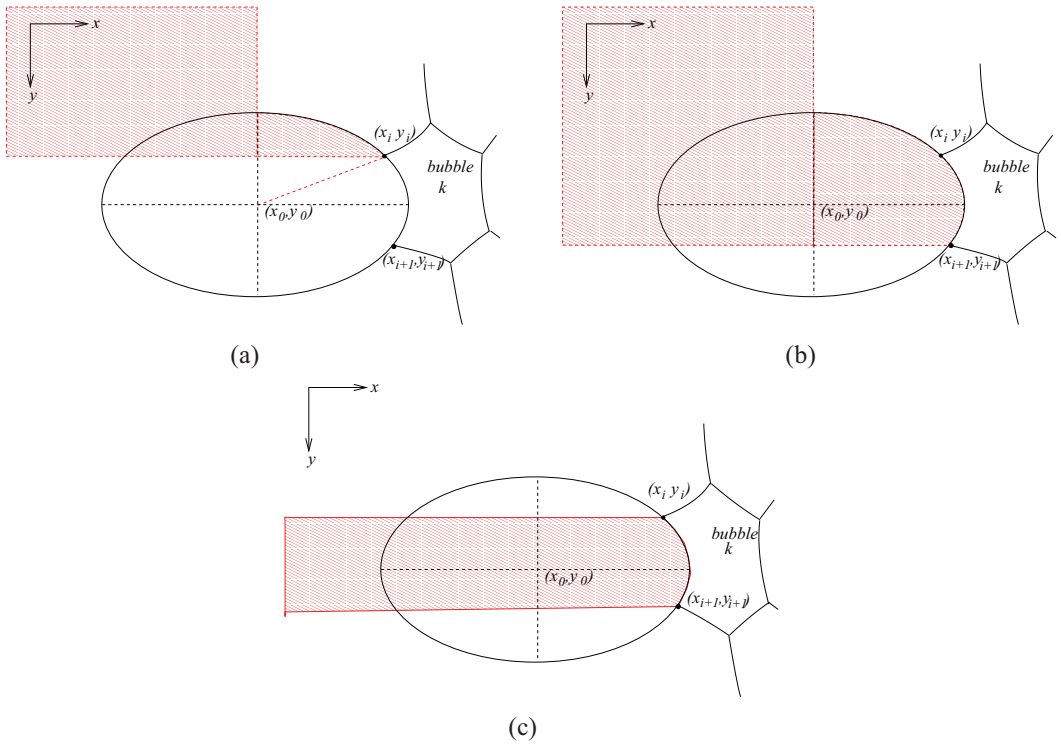

Figure 2.11: The method used to fix the area of a bubble that is in contact with the ellipse. Recall that the x and y axes have been reversed earlier and that the positive y-direction denotes the direction of gravity. The bubble has vertices (x_i, y_i) and (x_{i+1}, y_{i+1}) on the ellipse boundary. Thus, it is required to calculate the area under the "missing edge" of the bubble. This area is bounded by the ellipse boundary between the two vertices and the lines $x = 0$, $y = y_i$ and $y = y_{i+1}$. The calculation of this area is completed by considering two areas: (a) The area bounded below by $x = 0$ and bounded above by $x = x_0$ between $y = 0$ and $y = y_0 - r_0 e_c$ and the ellipse boundary between $y = y_0 - r_0 e_c$ and $y = y_i$. (b) The area bounded below by $x = 0$ and bounded above by $x = x_0$ between $y = 0$ and $y = y_0 - r_0 e_c$ and the ellipse boundary between $y = y_0 - r_0 e_c$ and $y = y_{i+1}$. If we denote the area calculated in part (a) by $C_1(x_i, y_i)$ and in part (b) by $C_1(x_{i+1}, y_{i+1})$ then the required area under the missing edge of the bubble is given by $C_1(x_{i+1}, y_{i+1}) - C_1(x_i, y_i)$.

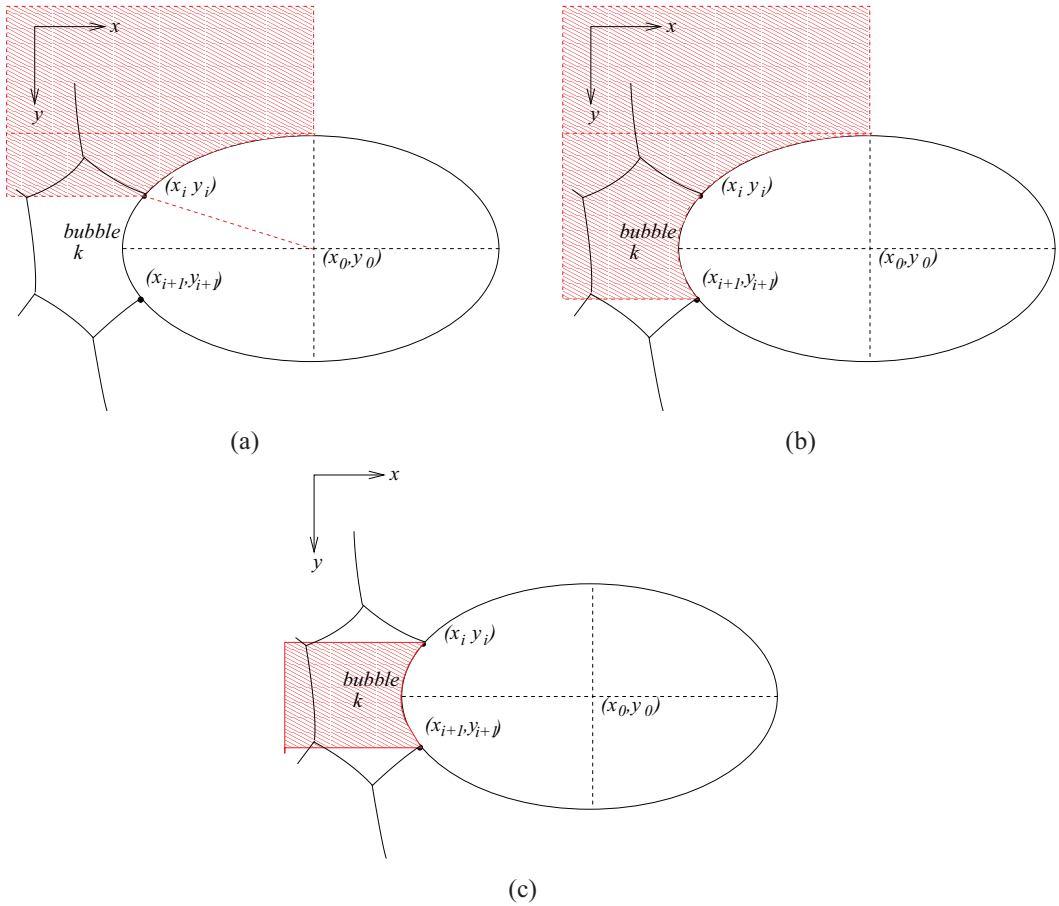

Figure 2.12: The method for calculating the area under the missing edge of a bubble in contact with the ellipse is illustrated for a bubble position on the left hand side of the ellipse boundary. The x and y axes have been reversed earlier, the positive y-direction denotes the direction of gravity. (a) The area $C_1(x_i, y_i)$ is shown for a vertex positioned so that $x_i < x_0$ and $y_i < y_0$. (b) The area $C_1(x_{i+1}, y_{i+1})$ is shown for a vertex positioned so that $x_{i+1} < x_0$ and $y_{i+1} > y_0$. (c) The area required to constrain the bubble's area is given by $C_1(x_{i+1}, y_{i+1}) - C_1(x_i, y_i)$.

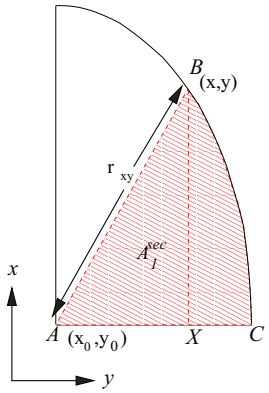

Figure 2.13: The points $A(x_0, y_0)$, $B(x, y)$, $C(x_0, y_0 + e_c r_0)$, and $X(x_0, y)$ form an ellipse sector. The area of this sector is calculated by integration. The area is denoted by A_1^{sec} when $y \geq y_0$ and A_2^{sec} when $y < y_0$. These are calculated by (2.20) and (2.21) respectively.

Calculating the area $C_1(x, y)$ for vertex positions $(x, y) = (x_i, y_i), (x_{i+1}, y_{i+1})$ proceeds from summation and subtraction of areas to pieces that are easily calculated. These pieces include a rectangle, triangle as well as an ellipse sector.

The area of a sector to the ellipse from its nearest minor axis to the vertex (x_i, y_i) (as shown in figure 2.13) is calculated by integration. Let the area of the sector ABC shown in this figure (where $y_i \geq y_0$) be denoted by A_1^{sec}. In this case, the area A_1^{sec} is given by

$$\begin{aligned} A_1^{sec} &= A_{ABX} + A_{XBC} \\ &= \frac{1}{2} r_{xy}^2 \cos\theta \sin\theta + \frac{1}{e_c} \int_{r_{xy}\cos\theta}^{e_c r_0} \left(r_0^2 - \frac{y^2}{e_c^2} \right)^{1/2} dy \,. \end{aligned} \tag{2.19}$$

where X denotes the point (x_0, y_i). The integration in (2.19) is made by substitution of $y = e_c r_0 \cos\psi$, in which case $dy = -e_c r_0 \sin\psi d\psi$. It is simplified by the fact that the angle θ satisfies $\cos\theta = \frac{y_i - y_0}{r_{xy}}$ where $r_{xy} = \left((x_i - x_0)^2 + (y_i - y_0)^2 \right)^{1/2}$. In this case, the calculation of the area A_1^{sec} continues from (2.19) as follows:

$$\begin{aligned} A_1^{sec} &= \frac{1}{4} r_{xy}^2 \sin 2\theta + \frac{1}{e_c} \int_{\cos^{-1}\left(\frac{y_i - y_0}{e_c r_0}\right)}^{0} \left(r_0^2 - r_0^2 \cos^2\psi \right)^{1/2} (-e_c r_0 \sin\psi)\, d\psi \\ &= \frac{1}{4} r_{xy}^2 \sin 2\theta + \int_0^{\cos^{-1}\left(\frac{y_i - y_0}{e_c r_0}\right)} r_0^2 \sin^2\psi d\psi \end{aligned}$$

$$
\begin{aligned}
&= \frac{1}{4}r_{xy}^2 \sin 2\theta + \frac{r_0^2}{2}\int_0^{\cos^{-1}\left(\frac{y_i-y_0}{e_c r_0}\right)} (1-\cos 2\psi)\, d\psi \\
&= \frac{1}{4}r_{xy}^2 \sin 2\theta + \frac{r_0^2}{2}\left[\psi - \frac{\sin 2\psi}{2}\right]_0^{\cos^{-1}\left(\frac{y_i-y_0}{e_c r_0}\right)} \\
&= \frac{1}{4}r_{xy}^2 \sin 2\theta + \frac{r_0^2}{2}\left(\cos^{-1}\left(\frac{y_i-y_0}{e_c r_0}\right) - \frac{1}{2}\sin 2\left(\cos^{-1}\left(\frac{y_i-y_0}{e_c r_0}\right)\right)\right) . \quad (2.20)
\end{aligned}
$$

Equivalently, the area of a sector to the ellipse when $y_i < y_0$ is denoted by A_2^{sec}. This is given by

$$
A_2^{sec} = \frac{1}{4}r_{xy}^2 \sin 2\theta + \frac{r_0^2}{2}\left(\cos^{-1}\left(\frac{y_0-y_i}{e_c r_0}\right) - \frac{1}{2}\sin 2\left(\cos^{-1}\left(\frac{y_0-y_i}{e_c r_0}\right)\right)\right) . \quad (2.21)
$$

The calculation of the area $C_1(x_i, y_i)$ proceeds from summation and subtraction of known pieces. This summation is dependent on the location of the vertex on the ellipse boundary. Equation 2.22 defines $C_1(x_i, y_i)$ for all possible positions (x_i, y_i) can take on the ellipse boundary when it is oriented such that $\phi = 0$.

$$
C_1(x_i, y_i) = \begin{cases}
x_0 y_i + A_2^{sec} + \frac{1}{2}(x_i - x_0)(y_0 - y_i) & \text{if } x_i \geq x_0 \quad \text{and } y_i \leq y_0, \\
x_0 y_i + \frac{1}{2}\pi r_0^2 - A_1^{sec} + \frac{1}{2}(x_i - x_0)(y_i - y_0) & \text{if } x_i \geq x_0 \quad \text{and } y_i > y_0, \\
x_0 y_i - A_2^{sec} + \frac{1}{2}(x_0 - x_i)(y_0 - y_i) & \text{if } x_i < x_0 \quad \text{and } y_i \leq y_0, \\
x_0 y_i - \frac{1}{2}\pi r_0^2 + A_1^{sec} - \frac{1}{2}(x_0 - x_i)(y_i - y_0) & \text{if } x_i < x_0 \quad \text{and } y_i > y_0 .
\end{cases} \quad (2.22)
$$

The above expression for $C_1(x_i, y_i)$ is relatively simple due to the fact that the major and minor axes of the ellipse are parallel to the horizontal x-axis and vertical y-axis respectively. Matters are complicated further when the angle of orientation of the ellipse is changed so that it has the range $0 < \phi < \frac{\pi}{2}$. The method for calculating $C_1(x_i, y_i)$ in this case is described in section 2.4.2. However, it is firstly required to mention a singular point of the content integral, and the calculation of a bubble area that is in contact with this point.

2.4.1.1 Singular Point in Content Integral

A singular point exists on the ellipse boundary for the method described to calculate the area of bubbles in contact with the ellipse. When an ellipse is oriented so that $\phi = 0$, this singular point lies at $(x_0, y_0 + r_0 e_c)$. Consider a bubble that is in contact with the ellipse over the singular point. It has one vertex above the singular point at (x_i, y_i) and another vertex below at (x_{i+1}, y_{i+1}). Without the singularity, the area bounded by the missing edge of the bubble and the lines $x = 0$, $y = y_i$ and $y = y_{i+1}$ could be calculated by subtraction of $C_1(x_i, y_i)$ from $C_1(x_{i+1}, y_{i+1})$. However, this calculation will not give the desired area in this case. This is demonstrated in figure 2.14. It is required to include the area of the ellipse (which equals πr_0^2) in the calculation. Thus, the area bounded by the ellipse boundary between y_i and y_{i+1} and the lines $x = 0$, $y = y_i$ and $y = y_{i+1}$ for the bubble that lies on the singularity is given by $C_1(x_{i+1}, y_{i+1}) - C_1(x_i, y_i) + \pi r_0^2$ (as shown in figure 2.14).

It is also important that a foam film doesn't get stuck at this singular point as the ellipse descends through the foam. In this case, any foam film that approaches the singular point is moved randomly by a small distance so that no pinning occurs.

2.4.2 Area Constraint at Ellipse Boundary when $\phi \neq 0$

The calculation of the content integral $C_1(x_i, y_i)$ is complicated when the ellipse's major and minor axes are non-parallel to the x and y axes. The method used for calculation of the area constraints of bubbles in contact with the ellipse is the same in principle as before. However, the fact that the ellipse's major axis is at a non-zero acute angle ϕ to the horizontal x-axis makes the piecewise calculation of $C_1(x_i, y_i)$ slightly more difficult. Firstly, we must find the ranges over the ellipse boundary for the position of a vertex (x_i, y_i) where the piecewise calculation of $C_1(x_i, y_i)$ will differ. In this case, the ellipse is split into ten segments as shown in figure 2.15.

The first two limits for the calculation of $C_1(x_i, y_i)$ that we find are the points on the ellipse boundary where the tangent to the ellipse is parallel to the horizontal x-axis. These points are denoted by (a, b) and (c, d) (see figure 2.15) and are found by

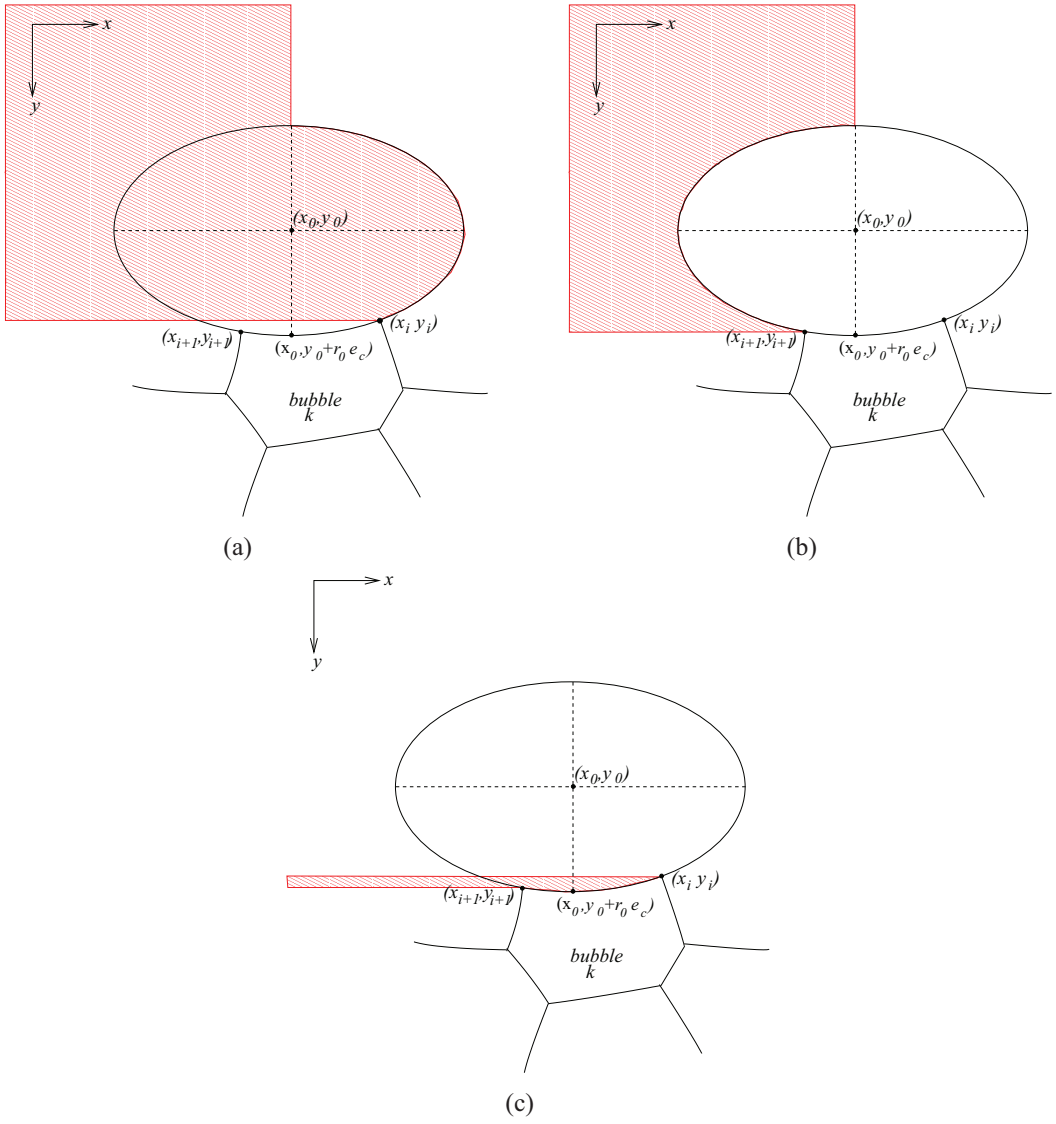

Figure 2.14: A singular point of the content integral exists at $(x_0, y_0 + r_0 e_c)$ on the ellipse boundary. Thus, consider a bubble with vertices (x_i, y_i) and (x_{i+1}, y_{y+1}) either side of the singular point on the ellipse boundary. As before, the area given by (a) $C_1(x_i, y_i)$ and (b) $C_1(x_{i+1}, y_{i+1})$ are calculated. However, the area under the missing edge of the bubble (i.e. the boundary of the ellipse between the two vertices), bounded by $x = 0$, $y = y_i$ and $y = y_{i+1}$ is not given by $C_1(x_{i+1}, y_{i+1}) - C_1(x_i, y_i)$. (c) The required area is simply given by $C_1(x_{i+1}, y_{i+1}) - C_1(x_i, y_i) + \pi r_0^2$.

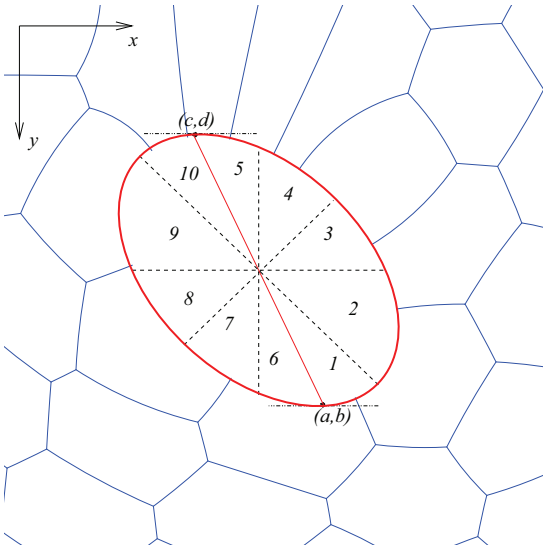

Figure 2.15: The calculation of $C_1(x_i, y_i)$ is dependent on the position of a vertex on the ellipse boundary. The method used to calculate $C_1(x_i, y_i)$ when the ellipse is oriented so that $0 < \phi < \pi/2$ requires that the ellipse is divided into ten segments. This will allow a straightforward piecewise calculation of C_1. The piecewise calculation of $C_1(x_i, y_i)$ differs for the ten segments shown (see (2.37) for details).

differentiation of the ellipse equation with respect to the variable y.

We expand (2.18) and rearrange to give

$$(y-y_0)^2\left(\frac{\cos^2\phi}{e_c^2}+e_c^2\sin^2\phi\right)+(x-x_0)^2\left(e_c^2\cos^2\phi+\frac{1}{e_c^2}\sin^2\phi\right)$$
$$+2\,(y-y_0)\,(x-x_0)\left(e_c^2-\frac{1}{e_c^2}\right)\cos\phi\sin\phi=r_0^2$$

and then differentiate with respect to y

$$2\,(y-y_0)\left(\frac{\cos^2\phi}{e_c^2}+e_c^2\sin^2\phi\right)+2\,(x-x_0)\left(e_c^2-\frac{1}{e_c^2}\right)\cos\phi\sin\phi+$$
$$2\,(y-y_0)\,\frac{dx}{dy}\left(e_c^2-\frac{1}{e_c^2}\right)\cos\phi\sin\phi+2\,(x-x_0)\,\frac{dx}{dy}\left(e_c^2\cos^2\phi+\frac{1}{e_c^2}\sin^2\phi\right)=0\,.$$

Then

$$\frac{dx}{dy}=\frac{\left(1-e_c^4\right)\cos\phi\sin\phi\,(x-x_0)-\left(\cos^2\phi+e_c^4\sin^2\phi\right)(y-y_0)}{\left(e_c^4-1\right)\cos\phi\sin\phi\,(y-y_0)+\left(e_c^4\cos^2\phi+\sin^2\phi\right)(x-x_0)}\,. \tag{2.23}$$

The tangent to the ellipse boundary is parallel to the horizontal x-axis at both points (a, b) and (c, d), i.e. when $\frac{dy}{dx} = 0$. This gives

$$(y - y_0) = (x - x_0)\,\frac{e_c^4 \cos^2\phi + \sin^2\phi}{(1 - e_c^4)\cos\phi\sin\phi}\,. \tag{2.24}$$

For simplification of future calculations, the gradient of (2.24) is denoted by κ_1, i.e.

$$\kappa_1 = \frac{e_c^4 \cos^2\phi + \sin^2\phi}{(1 - e_c^4)\cos\phi\sin\phi}\,. \tag{2.25}$$

Thus, the coordinates of the points (a, b) and (c, d) are found by substitution of (2.24) into the equation of the ellipse (2.18). This yields that the x coordinates of the two points satisfy

$$(x - x_0)^2 \left(\frac{1}{e_c^2}(\kappa_1\cos\phi - \sin\phi)^2 + e_c^2(\kappa_1\sin\phi + \cos\phi)^2\right) = r_0^2\,. \tag{2.26}$$

Again for simplification of future calculations, δ^2 is chosen so that it represents the expression dependent on the ϕ in (2.26), i.e.

$$\delta^2 = \left(\frac{1}{e_c^2}(\kappa_1\cos\phi - \sin\phi)^2 + e_c^2(\kappa_1\sin\phi + \cos\phi)^2\right)\,. \tag{2.27}$$

Thus, $(a, b) = (x_0 + r_0/\delta, y_0 + r_0\kappa_1/\delta)$ and $(c, d) = (x_0 - r_0/\delta, y_0 - r_0\kappa_1/\delta)$.

As in the section 2.4.1, the calculation of the area of a bubble that is in contact with the ellipse involves computing a content integral C_1 for its two vertices (x_i, y_i) and (x_{i+1}, y_{i+1}) on the boundary of the object. The boundary of the ellipse is split into ten segments, as shown in figure 2.15. Five of the boundary segments lie above the line joining points (c, d) and (a, b) while the other five lie below. The piecewise summation in the calculation of $C_1(x_i, y_i)$ differs when a vertex (x_i, y_i) is positioned in each of these ten segments of the boundary.

Figure 2.16 provides an example of the area required to calculate a bubble's area when it is in contact with the ellipse. The area of C_1 is split into pieces that are straightforward to calculate. Here, we describe the pieces required for the calculation of the

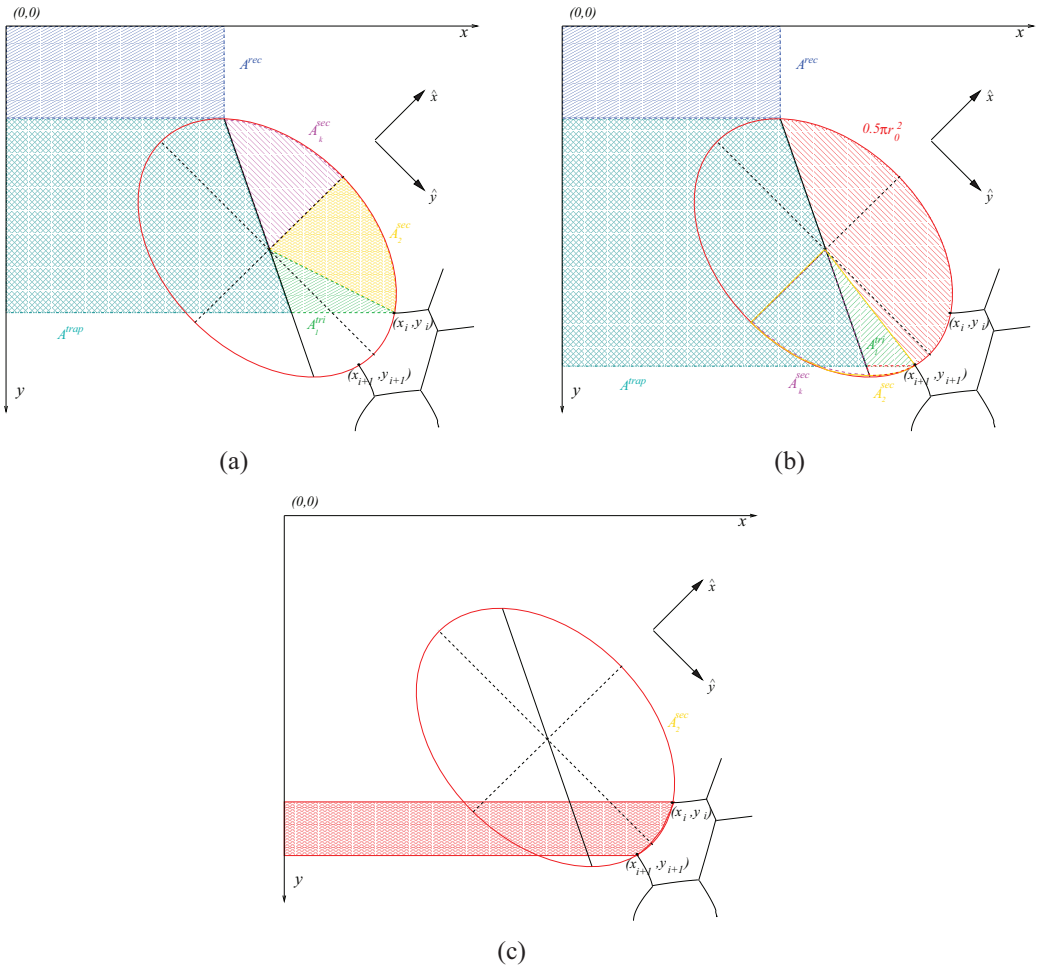

Figure 2.16: The method used to fix the area of a bubble that is in contact with the ellipse (oriented so that $\phi \neq 0$). Here, the bubble has vertices (x_i, y_i) positioned on the boundary of segment 2 (see figure 2.15) and (x_{i+1}, y_{i+1}) on the boundary of segment 1. (a) The calculation of $C_1(x_i, y_i)$ involves the summation of the rectangular area A^{rec}, the trapezium A^{trap}, the ellipse sectors $\hat{A}_2^{sec}$, $\hat{A}_\kappa^{sec}$ and the triangle A^{tri} (see text of §2.4.2 for details). (b) Similarly, the calculation of $C_1(x_{i+1}, y_{i+1})$ involves the summation of A^{rec}, A^{trap}, $\hat{A}_\kappa^{sec}$, A_1^{tri}, the area of half of the ellipse $(\frac{1}{2}\pi r_0^2)$ and the subtraction of $\hat{A}_1^{sec}$. (c) The area under the missing edge of the bubble (bounded below by $x = 0$) is given by $C_1(x_{i+1}, y_{i+1}) - C_1(x_i, y_i)$ as before.

content integral $C_1(x_i, y_i)$ when (x_i, y_i) is positioned anywhere on the ellipse boundary.

It can be seen from the example provided in figure 2.16 that the pieces required to calculate C_1 are a rectangle, trapezium, triangle and an ellipse sector. The rectangle has edges parallel to the x and y axes and corners at the origin $(0, 0)$ and at (c, d), its area is

denoted by A^{rec} and is given by

$$A^{rec} = \left(x_0 - \frac{r_0}{\delta}\right)\left(y_0 - \frac{r_0\kappa_1}{\delta}\right) . \tag{2.28}$$

The area of the trapezium under the line that joins (c, d) with (a, b) and bounded by $y = d, y = y_i$ and $x = 0$ is denoted by A^{trap} and easily calculated as

$$A^{trap} = \frac{1}{2}\left[\left(x_0 - \frac{r_0}{\delta}\right) + \left(\frac{(y_i - y_0)}{\kappa_1} + x_0\right)\right]\left(y - \left(y_0 - \frac{r_0\kappa_1}{\delta}\right)\right) . \tag{2.29}$$

Since the ellipse's major and minor axis are at an angle $0 < \phi < \frac{\pi}{2}$ to the horizontal and vertical axes, the calculation of the area of a sector (as shown in figure 2.13) of the ellipse is not as straightforward. A rotation of the coordinate system (x, y) axes by an angle of ϕ in the clockwise direction solves this problem. Let this rotated coordinate system be denoted by $(\hat{x}, \hat{y})$. Thus, the general point on the ellipse boundary (x, y) is expressed in terms of the new variables $(\hat{x}, \hat{y})$ by the relation

$$\begin{aligned} \hat{x} &= y\sin\phi + x\cos\phi , \\ \hat{y} &= y\cos\phi - x\sin\phi . \end{aligned} \tag{2.30}$$

The equation of the ellipse (2.18) can be re-written relative to this new coordinate system as

$$\frac{1}{e_c^2}(\hat{y} - \hat{y_0})^2 + e_c^2(\hat{x} - \hat{x_0})^2 = r_0^2 . \tag{2.31}$$

The area of a sector of the ellipse is calculated using the same method described for (2.20) and (2.21). In this case, $\hat{A_1}^{sec}$ and $\hat{A_2}^{sec}$ denote the ellipse sector area for points on its boundary in the ranges $\hat{y}_i \geq \hat{y}_0$ and $\hat{y}_i < \hat{y}_0$ respectively. The area of the ellipse sector when it has been rotated by an angle ϕ is given by

$$\hat{A}_1^{sec} = \frac{1}{4}r_{\hat{x}\hat{y}}^2 \sin 2\hat{\theta}_1 + \frac{r_0^2}{2}\left(\cos^{-1}\left(\frac{\hat{y}_i - \hat{y}_0}{e_c r_0}\right) - \frac{1}{2}\sin 2\left(\cos^{-1}\left(\frac{\hat{y}_i - \hat{y}_0}{e_c r_0}\right)\right)\right) \tag{2.32}$$

when $\hat{y}_i \geq y_0$ (where $\cos\theta_1 = \frac{\hat{y}_i - \hat{y}_0}{r_{\hat{x}\hat{y}}}$ and $r_{\hat{x}\hat{y}} = \sqrt{(\hat{x}_i - \hat{x}_0)^2 + (\hat{y}_i - \hat{y}_0)^2}$). Similarly, when

$\hat{y}_i < \hat{y}_0$ the area of the sector is given by

$$\hat{A}_2^{sec} = \frac{1}{4} r_{\hat{x}\hat{y}}^2 \sin 2\hat{\theta}_2 + \frac{r_0^2}{2}\left(\cos^{-1}\left(\frac{\hat{y}_0 - \hat{y}_i}{e_c r_0}\right) - \frac{1}{2}\sin 2\left(\cos^{-1}\left(\frac{\hat{y}_0 - \hat{y}_i}{e_c r_0}\right)\right)\right), \tag{2.33}$$

where $\hat{\theta}_2 = \cos^{-1}\left(\frac{\hat{y}_0 - \hat{y}_i}{r_{\hat{x}\hat{y}}}\right)$.

Since the line that joins the points (a, b) with (c, d) is at an angle to the new rotated axes, it is required to calculate the area of the ellipse sector between the $\hat{y}$ axis and the point $(\hat{a}, \hat{b})$. This area is denoted by $\hat{A}_\kappa^{sec}$ and given by

$$\hat{A}_\kappa^{sec} = \frac{1}{4}\hat{r}_{ab}^2 \sin 2\theta_\kappa + \frac{r_0^2}{2}\left(\cos^{-1}\left(\frac{\hat{b} - \hat{y}_0}{e_c r_0}\right) - \frac{1}{2}\sin 2\left(\cos^{-1}\left(\frac{\hat{b} - \hat{y}_0}{e_c r_0}\right)\right)\right), \tag{2.34}$$

$$\text{where } \theta_\kappa = \tan^{-1}\left(\frac{\hat{a} - \hat{x}_0}{\hat{b} - \hat{y}_0}\right) \text{ and } \hat{r}_{ab} = \left((\hat{a} - \hat{x}_0)^2 + \left(\hat{b} - \hat{y}_0\right)\right)^{1/2} .$$

Similarly, the area of the ellipse sector from the point $(\hat{c}, \hat{d})$ to the $\hat{y}$-axis is also equal to $\hat{A}_\kappa^{sec}$.

It is also required to take great care in defining the triangular areas A^{tri} that enable the calculation of the content integral in all segments of the ellipse. These triangular areas involve the subtraction or addition of the area of the triangle A_κ^{tri} (see figure 2.17) which has its corners at (x_0, y_0), (x_0, y_i) and $(\frac{1}{\kappa_1}(x_i - x_0) + y_0, y_i)$. The area of this triangle is given by

$$A_\kappa^{tri} = \frac{1}{2\kappa_1}(y_i - y_0)^2 . \tag{2.35}$$

There are six triangular areas required for defining the content integral $C_1(x_i, y_i)$ for all positions on the ellipse boundary when it is oriented in this manner; they are given by

$$\begin{aligned}
A_1^{tri} &= \frac{1}{2}(y_i - y_0)(x_i - x_0) - A_\kappa^{tri} , \\
A_2^{tri} &= \frac{1}{2}(y_0 - y_i)(x_i - x_0) + A_\kappa^{tri} , \\
A_3^{tri} &= -\frac{1}{2}(y_0 - y_i)(x_0 - x_i) + A_\kappa^{tri} , \\
A_4^{tri} &= -\frac{1}{2}(y_i - y_0)(x_i - x_0) + A_\kappa^{tri} , \\
A_5^{tri} &= \frac{1}{2}(y_i - y_0)(x_0 - x_i) + A_\kappa^{tri} ,
\end{aligned}$$

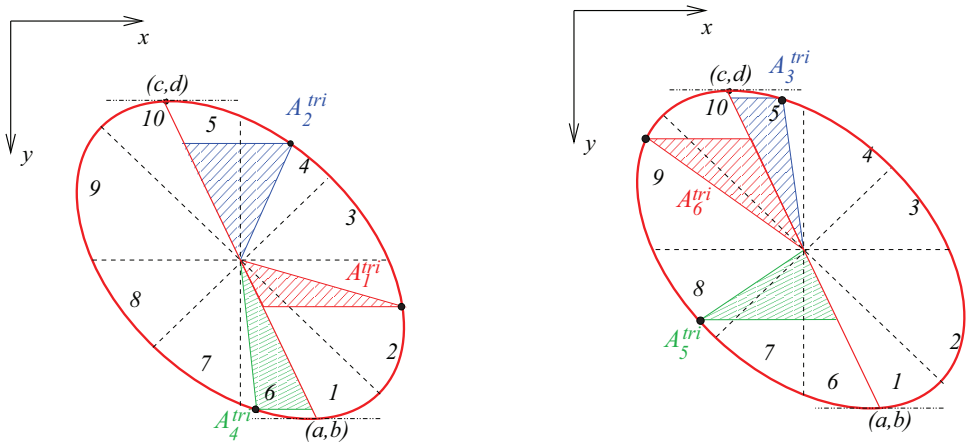

(a) (b)

Figure 2.17: The piecewise definition of C_1 for a vertex (x_i, y_i) on the ellipse boundary includes a triangle. The calculation of the area of the triangle differs when the vertex is positioned in each segment of the ellipse boundary. There are six triangular areas required for the full definition of the content integral C_1. They are (a) A_1^{tri}, A_2^{tri} A_4^{tri} and (b) A_3^{tri}, A_4^{tri}, A_5^{tri}. These areas are calculated by (2.36).

$$A_6^{tri} = \frac{1}{2}(y_0 - y_i)(x_0 - x_i) - A_\kappa^{tri}. \tag{2.36}$$

These are shown in figure 2.17.

Having defined all the pieces of areas required, the content integral is expressed as

$$C_1(x_i, y_i) = \begin{cases} A^{rec} + A^{trap} + \frac{1}{2}\pi r_0^2 - \hat{A}_1^{sec} + \hat{A}_\kappa^{sec} + A_1^{tri} & \text{if}\,(x_i, y_i) \in (\text{segment } 1)\,, \\ A^{rec} + A^{trap} + \hat{A}_2^{sec} + \hat{A}_\kappa^{sec} + A_1^{tri} & \text{if}\,(x_i, y_i) \in (\text{segment } 2)\,, \\ A^{rec} + A^{trap} + \hat{A}_2^{sec} + \hat{A}_\kappa^{sec} - A_2^{tri} & \text{if}\,(x_i, y_i) \in (\text{segment } 3)\,, \\ A^{rec} + A^{trap} - \hat{A}_2^{sec} + \hat{A}_\kappa^{sec} - A_2^{tri} & \text{if}\,(x_i, y_i) \in (\text{segment } 4)\,, \\ A^{rec} + A^{trap} - \hat{A}_2^{sec} + \hat{A}_\kappa^{sec} - A_3^{tri} & \text{if}\,(x_i, y_i) \in (\text{segment } 5)\,, \\ A^{rec} + A^{trap} - \frac{1}{2}\pi r_0^2 - \hat{A}_1^{sec} + \hat{A}_\kappa^{sec} - A_4^{tri} & \text{if}\,(x_i, y_i) \in (\text{segment } 6)\,, \\ A^{rec} + A^{trap} - \frac{1}{2}\pi r_0^2 - \hat{A}_1^{sec} + \hat{A}_\kappa^{sec} - A_5^{tri} & \text{if}\,(x_i, y_i) \in (\text{segment } 7)\,, \\ A^{rec} + A^{trap} - \frac{1}{2}\pi r_0^2 + \hat{A}_1^{sec} + \hat{A}_\kappa^{sec} - A_5^{tri} & \text{if}\,(x_i, y_i) \in (\text{segment } 8)\,, \\ A^{rec} + A^{trap} - \frac{1}{2}\pi r_0^2 + \hat{A}_1^{sec} + \hat{A}_\kappa^{sec} - A_6^{tri} & \text{if}\,(x_i, y_i) \in (\text{segment } 9)\,, \\ A^{rec} + A^{trap} - \hat{A}_2^{sec} + \hat{A}_\kappa^{sec} + A_6^{tri} & \text{if}\,(x_i, y_i) \in (\text{segment } 10) \end{cases} \tag{2.37}$$

where $\in$ means "on the boundary of". The area under a missing edge with vertices (x_i, y_i) and (x_{i+1}, y_{i+1}) (and above the line $x = 0$) of a bubble in contact with the ellipse is calculated by the subtraction $C_1(x_{i+1}, y_{i+1}) - C_1(x_i, y_i)$ (as shown in the example provided in figure 2.16).

As previously discussed, this definition of a content integral contains a singular point (as discussed in §2.4.1.1). When the ellipse is oriented in this manner, the singular point occurs at (a, b). The same method as in the previous case (where $\phi = 0$) is used to overcome the problem of calculating the bubble area when it is in contact with the ellipse over this singular point (see §2.4.1.1).

Combining the above, the area of the bubbles in contact with the ellipse can be constrained in the same way as the rest of the bubbles in the channel. Bubbles are free to slip along the surface and films meet the ellipse at an angle of $\pi/2$ as for the circular disc. However, in contrast to the circular disc, the push of the bubbles and pull of the films occur at a non-zero angle to the centre point of the object. In this case, a non-zero torque is exerted on the ellipse by the foam. The calculation of these forces and the subsequent evolution equation for the motion of the ellipse is described in detail in section 2.4.3.

2.4.3 Ellipse Motion

As in the case of a circular disc sedimenting through a 2D foam, the ellipse is moved a small amount during a simulation iteration as a result of the forces exerted on it by the foam. The network ($\vec{F}^n$) and pressure forces ($\vec{F}^p$) are calculated in a similar method as used for the circular disc, although the shape of the ellipse enforces slight adjustments to this calculation.

The foam films meet the ellipse boundary at an angle of $\pi/2$. The direction of the force on the ellipse can be found by looking at the derivative of the ellipse equation with respect to y (see equation (2.23)). The pull of the film at a vertex (x_i, y_i) is directed

at an angle α_i to the positive y direction. This angle is defined by

$$\tan\alpha_i = \frac{\left(1-e_c^4\right)\cos\phi\sin\phi\,(y_i-y_0) - \left(e_c^4\cos^2\phi+\sin^2\phi\right)(x_i-x_0)}{(1-e_c^4)\cos\phi\sin\phi\,(x_i-x_0) - \left(\cos^2\phi+e_c^4\sin^2\phi\right)(y_i-y_0)}\,. \tag{2.38}$$

In this case, the network force exerted on the ellipse contributes towards its downwards and rotating motion. The drag and lift components of the network force exerted on the ellipse are calculated simply as

$$\vec{F^n} = 2\gamma\sum(\sin\alpha_i, \cos\alpha_i) \tag{2.39}$$

where 2γ denotes the line tension of the foam films that is chosen to be equal to 1. The geometry of this calculation is shown in figure 2.18(a).

Since the pull of the films is not in line with the ellipse's centre point, the network force also rotates the ellipse by applying a non-zero torque. This torque is dependent on the difference between the angles α_i and θ_i. Recall that θ_i denotes the angle that the line joining the vertex (x_i, y_i) with (x_0, y_0) makes with the vertical y-axis (2.11). In this case, the network torque exerted on the ellipse is given by

$$\tau^n = 2\gamma\sum r_i\sin(\alpha_i-\theta_i)\,, \tag{2.40}$$

where $r_i = \sqrt{(x_i-x_0)^2+(y_i-y_0)^2}$. Note that a positive torque is in the clockwise direction.

As for the network force, the pressure force exerted by the bubbles in contact with the ellipse contributes towards its linear and rotational motion. In this case, a bubble k with pressure p_k in contact with the ellipse over a length l_k will exert a force in the inward normal direction of the centrepoint of l_k. The length l_k is approximated as the linear distance between the two vertices of the bubble that are on the ellipse boundary. These vertices are denoted by (x_i, y_i) and (x_{i+1}, y_{i+1}) respectively. The position where the inward normal is placed is the midpoint between (x_i, y_i) and (x_{i+1}, y_{i+1}), denoted by (x_k, y_k). In this case, the resultant pressure force exerted on the ellipse is a sum over all

the bubbles k in contact with the object:

$$\vec{F}^p = \sum_k p_k l_k \left(\sin\beta_k, \cos\beta_k\right) \tag{2.41}$$

where

$$\tan\beta_k = -\frac{x_i - x_{i+1}}{y_i - y_{i+1}}. \tag{2.42}$$

As the pressure exerted by each bubble k is not in line with the centre point of the ellipse, a non-zero pressure torque is exerted. As in the network force case, the amount of torque exerted depends on the difference between the angles β_k and θ_k. Thus, the torque exerted on the ellipse due to the pressure of the contacting bubbles is

$$\tau^p = \sum p_k l_k r_k \sin\left(\theta_k - \beta_k\right), \tag{2.43}$$

where $r_k = \sqrt{(x_k - x_0)^2 + (y_k - y_0)^2}$.

Figure 2.18 clarifies the method described here for calculating the forces exerted on the ellipse by the foam. Some approximation has been made for the calculation of the pressure force exerted on the ellipse. The contact length l_k of the bubble with the ellipse is approximated as a straight line between the vertices (x_i, y_i) and (x_{i+1}, y_{i+1}) with its midpoint at (x_k, y_k). Figure 2.18(b) suggests that this approximation is fairly accurate in describing the direction and magnitude of the pressure force exerted on the ellipse, and becomes more accurate as the eccentricity $e_c \to 1$ and for larger objects.

The ellipse is moved a small distance $(\Delta x, \Delta y)$ in the direction of the resultant force during a single iteration. Its linear motion for every iteration $(\Delta t = 1)$ is determined by the same expression as used for the sedimentation of a circular disc through the foam (2.16).

The ellipse is also allowed to rotate during sedimentation. As for the linear motion of an object through the foam, the rotational motion is governed by a force balance that must satisfy Newton's 2nd law of motion:

$$I\frac{d^2\phi}{dt^2} = \lambda_2\frac{d\phi}{dt} - \tau^n - \tau^p, \tag{2.44}$$

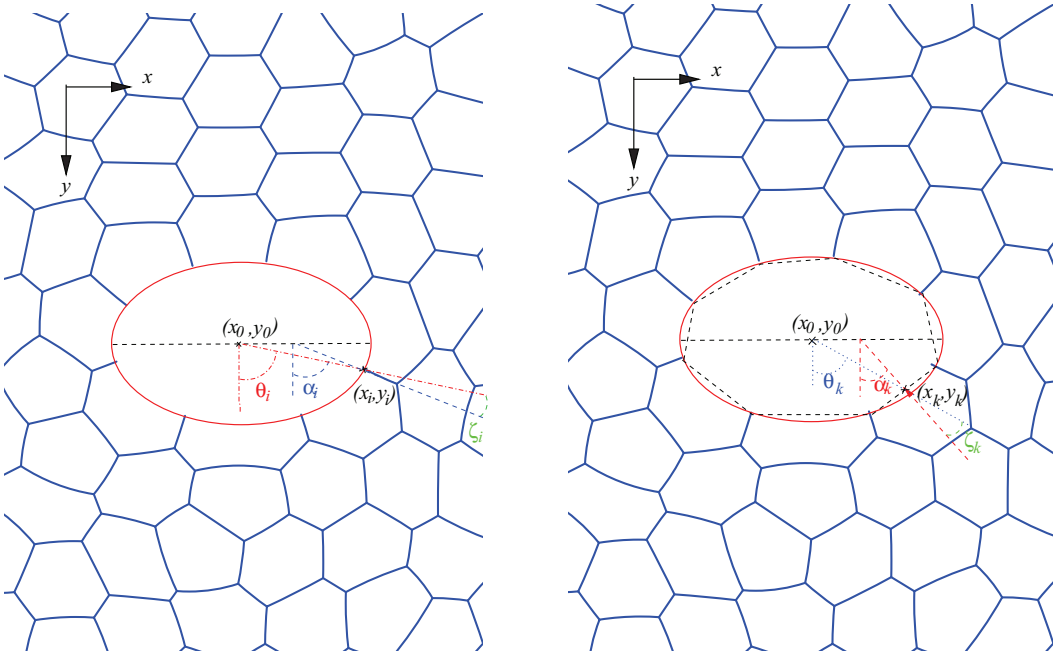

(a) (b)

Figure 2.18: The geometric calculation of the (a) network force F^n and (b) pressure force F^p exerted on the ellipse by the foam. The angles shown in each figure are described in greater detail in the text of section 2.4.3.

where I denotes the moment of inertia of the object and λ_2 the frictional coefficient of the ellipse with the films of the foam and the surface of the plate bounding the foam in a 2D experiment. Again, we assume over damped dynamics for this motion. In this case, the rotational motion of the object is steady and its angular velocity is proportional to the torque applied by the foam's films and the bubble pressures. The motion of the ellipse is so slow that visous effect don't have an effect on the structure of the foam, whence any contribution towards the torque from viscous effects is neglected. Thus, the rotational motion of the ellipse is governed by

$$\frac{1}{\epsilon_2}\frac{d\phi}{dt} = \tau^n + \tau^p \,. \tag{2.45}$$

Combining this rotational force balance with the linear force balance (2.16), the ellipse is moved a small amount linearly and rotated relative to the network and pressure force exerted by the foam. Thus, a simulation iteration ($\Delta t = 1$) consists of moving the

ellipse centre point (x_0, y_0) by an amount $(\Delta x, \Delta y)$ and changing the angle ϕ at which it is oriented by an amount $\Delta\phi$:

$$\begin{aligned} \Delta x &= \epsilon_1(F_x^n + F_x^p) \\ \Delta y &= \epsilon_1(F_y^n + F_y^p + mg) \\ \Delta\phi &= \epsilon_2(\tau^n + \tau^n)\ . \end{aligned} \tag{2.46}$$

The constant ϵ_1 sets the effective time-scale of the downward motion of the object as before. The constant ϵ_2 sets the effective time-scale for the rotational motion of the ellipse and is chosen so that $\epsilon_2 = 500\epsilon_1$. Choosing a much larger constant to set the effective time-scale of the rotational motion is required as a result of the small magnitude of torque exerted on the ellipse during sedimentation. Ideally, the simulation would be run using only one effective time-scale to govern the ellipse motion. However, any significant rotation of the ellipse would require the use of enormously long foam channels (more than a 100 times longer than used in this work) which are not feasible for this type of simulation. In this case, our simulations do not give the true time dependence of the sedimentation of an elliptical object in a foam. The ellipse is overly responsive to the torque applied on it during its sedimentation through the foam. However, the simulations still provide qualitative evidence on the response of a 2D foam to the sedimentation of long objects such as an ellipse that experiences non-zero torque during sedimentation.

2.5 Computational Time

Since the foam structures described in table 2.1 have a different number of bubbles, the typical computational time for a single simulation differs greatly. The computational time is also greater when simulating the sedimentation of an ellipse compared to discs as more computational tasks are involved. Typical values for the duration of the simulations are summarized in table 2.2.

Label	One disc (chapter 3)	Two discs (chapters 4 and 5)	Ellipse (chapter 6)
A	40 – 48 hours	40 – 48 hours	-
B	20 – 25 hours	20 – 25 hours	-
C	-	20 – 25 hours	–
D	-	up to 100 hours	–
E	-	–	35 – 45 hours
F	-	–	35 – 45 hours

Table 2.2: The computational time of the simulations for all the foam structures when they are run using a single 2.66GHz processor. An empty box means that the structures were not used in the relevant chapter.

Chapter 3

One Disc Sedimenting in a 2D Foam

3.1 Introduction

The non-isotropic flow of a two-dimensional dry foam, induced by the sedimentation of a single circular disc is investigated. This is done using numerical simulation methods described in chapter 2. How far a disc descends through the foam is dependent on whether it is heavy enough to overcome the forces exerted by the network of films and bubble pressures. In this case, the maximum disc weight a foam can support is quantified in section 3.2. This allows for choosing an appropriate weight that will result in a steady descent of similar objects through the foam; a requirement for the rest of the work presented in the thesis.

This chapter concentrates mainly on the sedimentation of the disc from a central position within the foam channel. A reference simulation of this case is presented in section 3.3. The disc motion is tracked and the forces exerted by the foam discussed in detail.

It is also important to quantify any wall effects that might occur when an object sediments closer to either channel wall. In this case, the sedimentation of a disc placed at different initial positions along the top of the foam channel is considered in section 3.4. The range of initial positions where wall effects can be neglected will be beneficial when considering the sedimentation and interaction between two circular discs placed

side by side in chapter 4.

Probing the foam response by looking at the sedimentation of such objects requires a study of the flow fields (§3.5). The bubble displacements (§3.5.1) and T1 positions (§3.5.2) as the disc sediments through the foam shows that it does so within a fluidized region of the foam. This is the region where the applied stress on the foam due to the disc is at its greatest; whence it is where most T1s occur. The flow of foam during the sedimentation of the disc results in variations in bubble pressures. In this case the pressure field of the bubbles is of interest and investigated in section 3.5.3.

The effect that varying the bubble area dispersity of the foam has on its response is discussed in section 3.6.

A disc that sediments from a central position is expected to be subjected to minimal lift. In this case, the drag force exerted on such a disc is of greater interest. Previous work by Raufaste *et al.* [77] derived that the network drag force (F_y^n) exerted on a fixed circular obstacle in foam flow depends on obstacle diameter d_0 and liquid fraction of the foam Φ_l. They model this relation by the equation:

$$F_y^n = \frac{1.032}{\Phi_l^{1/4}} \frac{\gamma d_0}{\sqrt{A}} \tag{3.1}$$

The relation of the drag force exerted on the disc with disc area and foam liquid fraction is described in sections 3.7.1 and 3.7.2 respectively. The results on the network drag F_y^n are compared with the relation of Raufaste *et al.* (equation 3.1). The relation of the pressure component to the drag force (F_y^p) with these control parameters is also discussed.

Further to this, section 3.8 comments on whether a negative wake exists when a disc sediments in a dry foam. This chapter provides the basis for the work on the interaction between two circular discs (chapters 4 and 5) and the sedimentation of an elliptical object (chapter 6) in a 2D dry foam.

3.2 Maximum Disc Weight that a Foam Supports

The sedimentation of a circular disc through a dry foam is gravity driven. In this case, the motion of the disc is highly dependent on its own weight. It is important in many fields such as the food production industry to know what dimensions an object must have for it to be neutrally buoyant within a stable foam. For example, the insertion of solid objects such as nuts or raisins in a chocolate foam that is liquid in the production stage, requires that they are suspended in the foam and do not all sink to the bottom of the mixture. Here, it is required that the maximum weight of an object that such a foam will support is known and also modelled with varying control parameters such as object size and foam wetness.

A dry liquid foam is limited in strength and the weight of solid objects it can support is limited. In experiments, if the suspended object is too heavy, the foam breaks when it is released. It is considerably more interesting to look at objects that are light enough so that their motion is slow (and affected by the foam) and foam breakage is avoided. It is also required for the work presented in this thesis for the sedimenting object to descend at a steady rate. In this case, the object is required to be of a weight that cannot be supported by the foam.

In this case, the maximum disc weight that a foam can support is found using a trial and error method. The disc is assigned a dimensionless value for its weight that could be dependent on factors such as bubble area and the surface tension of the foam. The value for ϵ is kept constant throughout this section (and the rest of the chapter) so that the amount the disc moves during an iteration is purely dependent on the value assigned for its weight and the resistance of the foam. The trial and error process begins when a very light disc (i.e. with a small dimensionless value for mg) is left to sediment from a central position in foam A (see table 2.1 for foam details). If it becomes stationary in the foam, the simulation is stopped. The next simulation is run with a slightly greater weight (mg is increased by 0.5) and the same process is repeated until a disc descends fully through the foam channel. The final disc to have been brought to a halt by the foam represents the maximum weight that the foam can support, denoted by $(mg)_{max}$.

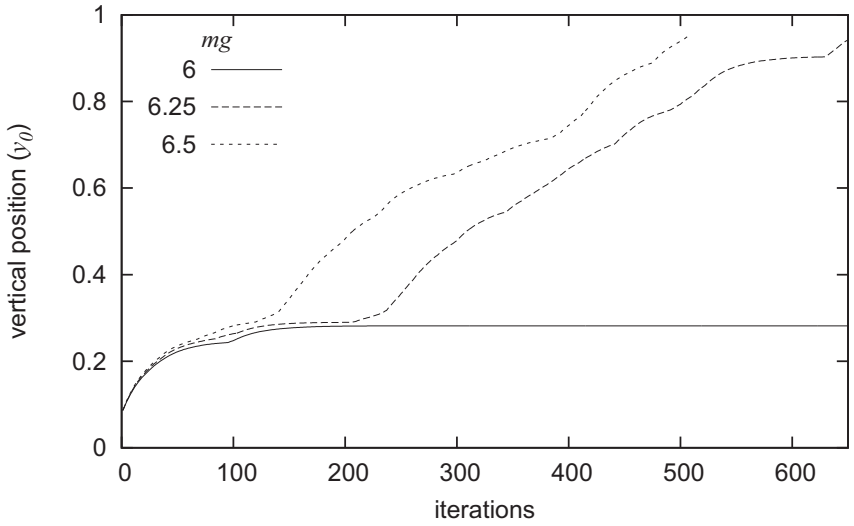

Figure 3.1: The maximum weight of a disc with area $8A_b$ that a foam can support is found by trial and error. Here, a disc weight of 6 is not sufficient for the disc to penetrate the foam while a weight of 6.25 sees the disc descend fully through the channel. In this case, the maximum weight the foam can support ($(mg)_{max}$) lies between these two values.

An example of the trial and error method is shown in figure 3.1 for a disc of area $8A_b$ sedimenting through a monodisperse foam of liquid fraction $\Phi_l = 0.004$. Initially, a disc of weight $mg = 6$ was tracked as it sedimented in the foam. It became apparent after a short while that it was not heavy enough to descend completely through the foam channel and came to a stop. The simulation is then repeated with a slightly heavier disc ($mg = 6.5$). This disc is seen to initially sediment at a similar rate to the previous lighter disc and its motion threatens to come to a halt at the same stage of the simulation. However, the disc is heavy enough to trigger some rearrangements in the foam and the disc motion restarts. This disc moves through the foam at an unsteady rate and is therefore of a weight that is very close to the maximum weight the foam can support. The accuracy of the calculation is improved by choosing a disc of weight $mg = 6.25$ to sediment through the foam channel. Again, this disc is slightly too heavy to be supported by the foam and sediments at a similar unsteady pace as the previous disc. It is therefore gathered for this case that the dimensionless value for the maximum weight the foam can support ($(mg)_{max}$) lies between 6 and 6.25.

This process is repeated for different disc sizes (§3.2.1) and foam liquid fractions

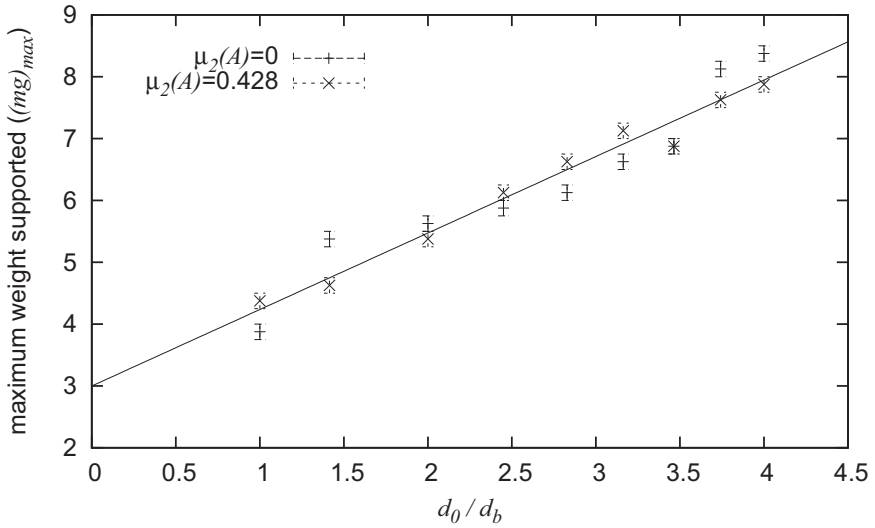

Figure 3.2: The maximum disc weight that a monodisperse ($\mu_2(A) = 0$) or a polydisperse foam with $\mu_2(A) = 0.428$ can support for different disc sizes follows a affine relationship. Here, the liquid fraction is constant at $\Phi_l = 4 \times 10^{-3}$. The error bars represent the values found in the trial and error method for the maximum disc weight that a foam can support and also the minimum disc weight it cannot support.

(§3.2.2). The results presented ensure that a suitable disc weight is chosen in subsequent simulations for its descending motion in the foam to be steady.

3.2.1 Variation of Disc Area

In this section, the trial and error method for finding the maximum disc weight a foam can support is repeated for discs of sizes ranging from $1A_b$ to $16A_b$. Foam A is used with liquid fraction that is kept constant at $\Phi_l = 4 \times 10^{-3}$. Both a monodisperse ($\mu_2(A) = 0$) and a polydisperse foam with $\mu_2(A) = 0.428$ are tested.

The work of Raufaste *et al.* [77] found an affine dependence between drag force and obstacle diameter in their constant velocity experiments of a foam flowing past a circular obstacle. A similar relationship between the maximum weight for neutral buoyancy and disc size is expected. This is logical as both the drag force and this critical weight are closely related. The maximum weight that the foam can support is also the maximum value reachable by the drag exerted on the disc.

It is shown in figure 3.2 that the maximum weight ($(mg)_{max}$) a foam can support

relates to the disc diameter (d_0) with the affine relation:

$$(mg)_{max} = 1.24\frac{d_0}{d_b} + 3.00\ . \tag{3.2}$$

The fitted line in this figure represents the critical weight for a disc to be neutrally buoyant or not. If a particular discs' weight lies well above this relation then it will sediment to the bottom of the foam channel at a steady rate. A disc weight that is greater but close to the critical value results in unsteady motion. If the weight of a disc is below the critical value, it can be considered to be neutrally buoyant. In subsequent chapters regarding the sedimentation of two circular discs and ellipses, the weight of the object is chosen so that its resulting motion is steady.

3.2.2 Variation of Liquid Fraction

It was also shown by the work of Raufaste *et al.* [77] that the drag force exerted on a circular object in a 2D pressure driven flow of foam is dependent on the liquid fraction of the foam. Equation 3.1 shows that the network drag force (F_y^n) depends on the foams liquid fraction with a power law relation of $\Phi_l^{-1/4}$. It follows that the liquid fraction is also a deciding factor in whether a suspended disc is neutrally buoyant or not. In this section, the liquid fraction of the foam is varied by changing the critical cut-off length l_c (see equation 2.10). The maximum weight a foam can support is expected to decrease with increasing foam wetness in a similar relation to that between drag force and liquid fraction.

Figure (3.3(a)) describes the motion of a light disc (of weight $mg = 5.5$) through foam A with different liquid fractions. The disc is neutrally buoyant for very dry foams (where $\Phi_l = 2\times10^{-3}$ or 4×10^{-3}) but is not supported for wetter foams ($\Phi_l > 6\times10^{-3}$). The amount the disc moves vertically during a simulation iteration increases with foam wetness.

The maximum weight that a foam can support is shown to decrease with the foam's liquid fraction Φ_l in figure 3.3(b). The data is best fitted by a power-law relation, given

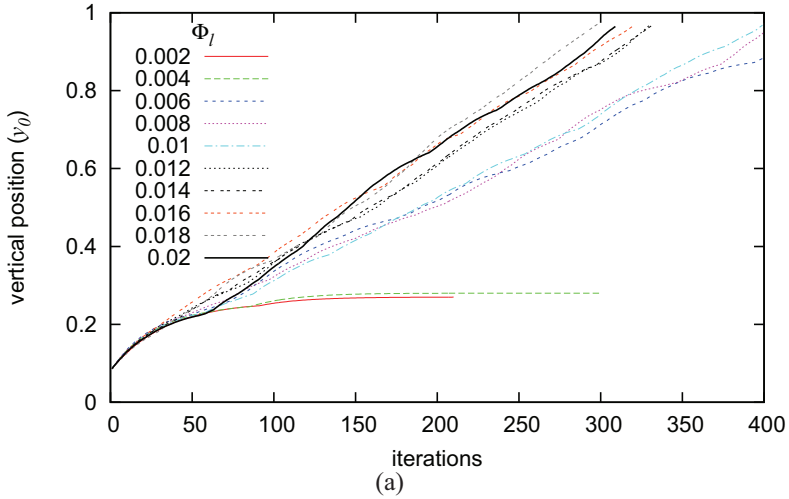

(a)

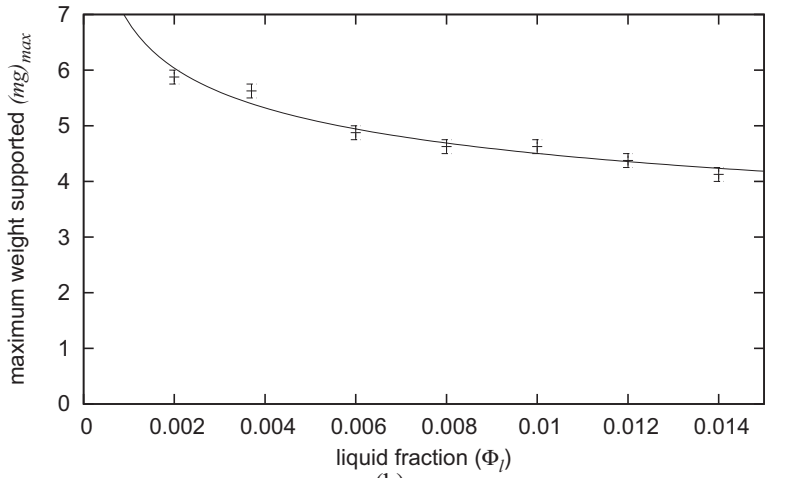

(b)

Figure 3.3: (a) The sedimentation of a light disc ($mg = 5.5$) of area $A_d = 4A_b$ in foam A (monodisperse) for different liquid fractions Φ_l is tested. Here, the vertical positioning (i.e. the value for y_0) of the disc as it sediments is shown for foam liquid fractions varying between 2×10^{-3} and 2×10^{-2} is demonstrated. The disc is shown to be neutrally buoyant for the very dry foams but cannot be supported by the wetter foams. (b) The maximum disc weight ($(mg)_{max}$) that the foam can support versus the liquid fraction Φ_l is fitted to a power law relation given in equation 3.3.

by:

$$(mg)_{max} = 1.95\Phi_l^{-0.182} \tag{3.3}$$

Note that this relation was determined using dry foams and will probably be different for very wet foams as their rheology is very different [106].

To conclude, the most important parameters when predicting whether a particle will be neutrally buoyant in a foam or not is the object to bubble size ratio, object weight and the liquid fraction of the foam. In essence, there exists a critical weight for objects suspended in the foam to be considered neutrally buoyant and this value is dependent on the liquid fraction of the foam as well as the ratio between object and bubble size.

3.3 A Reference Simulation

The sedimentation of a circular disc of area $4A_b$ and weight $mg = 10$ placed equidistant from both walls in foam A is chosen to be the reference simulation for this chapter (see figure 3.4(a)). The liquid fraction (Φ_l) of the foam is set to 4×10^{-3} and the bubble areas are equal (monodisperse). It is known from the previous section (3.2) that this disc will descend steadily throughout the foam channel and lateral motion is expected to be minimal. This reference simulation is required for a detailed explanation of the sedimentation process.

The centre coordinates (x_0, y_0) of the disc is tracked during sedimentation. Figure 3.4(b) shows that the motion is nearly vertical with only small lateral deviations from the centre line of the foam channel. These lateral deviations in motion are a result of the disordered nature of the foam; the local structure of the foam is different in different places along the foam channel.

Inspection of the forces exerted on the disc by the foam during sedimentation yields information about a foam's response to the gravity driven motion of the disc. The drag force exerted on the disc (figure 3.5(a)) opposes its downward motion and fluctuates during sedimentation. The initial phase of the simulation proceeds as a transient build up of the drag force. Here, the first 30 simulation iterations belong to this phase; after

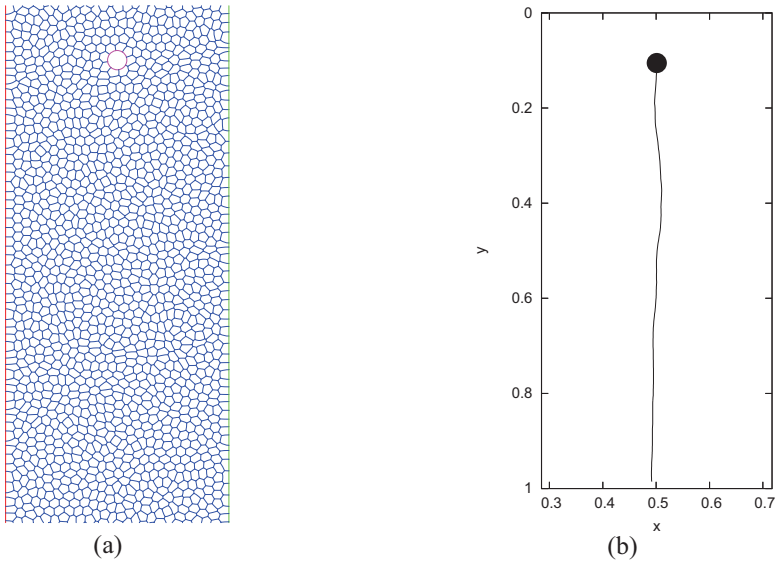

(a) (b)

Figure 3.4: Reference simulation: A disc of area $A_d = 4A_b$ and weight $mg = 10$ is left to sediment in foam A (see table 2.1) with equal bubble area (monodisperse) and liquid fraction $\Phi_l = 4 \times 10^{-3}$. (a) The initial position of the disc is central at the top of the foam channel ($(x_0, y_0) \equiv (0.5W, 0.1L)$ where W and L denote the width and length of the foam channel respectively). (b) Tracking the disc centre coordinates (x_0, y_0) as it sediments through the foam channel.

which the drag force fluctuates around a mean value denoted by the dashed line.

The fluctuations in the drag force about this mean value are a direct consequence of the flow of foam as the disc sediments. It is beneficial to consider the film tension (network) and bubble pressure contributions to the total drag force as separate components (figure 3.5(b)) as it ensures a more detailed investigation of the foam's response. It is possible to compare the influence both components have on the motion of the disc. In this case, the pressure contribution towards the drag is moderate in magnitude and variance compared to the network contribution.

The network contribution to the drag force fluctuates when T1s occur in the wake of the disc (see figure 3.6). The wake denotes the region of the foam behind the disc as it descends where the bubbles are elongated. It can be seen from figure 3.6 that the wake stretches back a couple of bubble layers from the disc.

As the disc descends in the foam, films slip along its boundary and bunch up at the top of the disc. As they bunch up here, the bubbles in the wake become more elongated

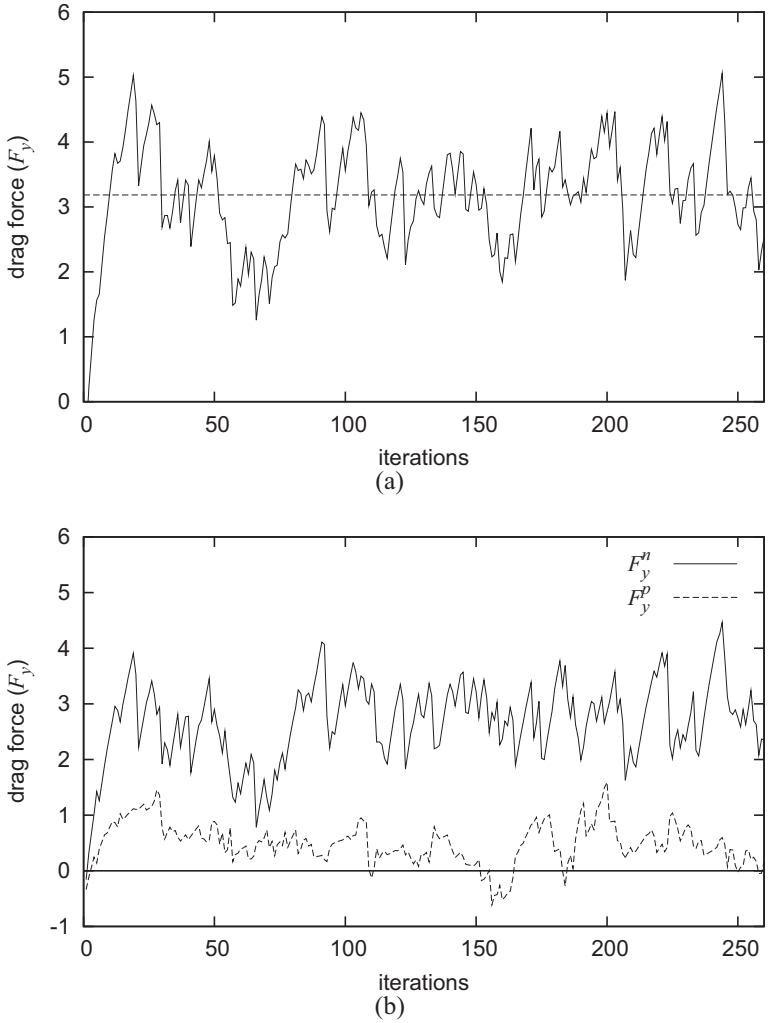

Figure 3.5: (a) The total drag force (F_y) and (b) network (F_y^n) and pressure (F_y^p) components to the drag force vary as the disc sediments through the foam. There is an initial transient build up of forces, after which the force fluctuates around a mean value.

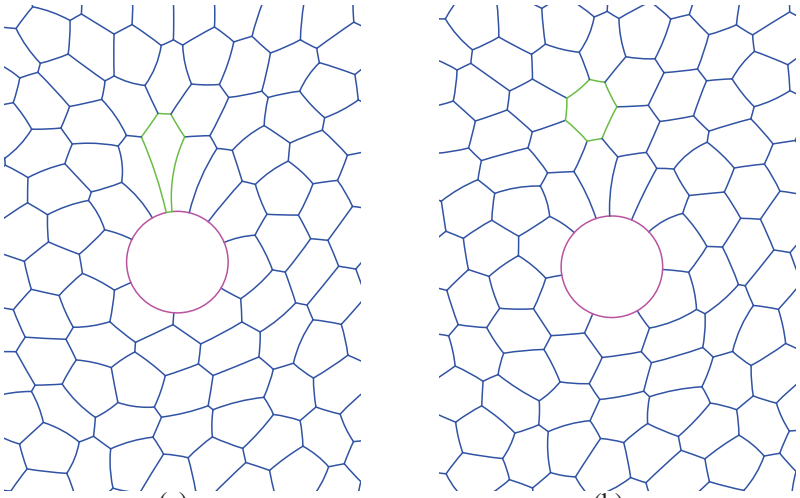

Figure 3.6: Fluctuations in the network contribution to the drag force (F_y^n) occurs due to bubbles detaching completely from the circular disc after T1s. The two pictures demonstrate the foam structure before and after a T1 rearrangement in the disc's wake. This rearrangement results in the films becoming less bunched up in this region, whence the network drag force decreases.

and detach from the disc when T1s are triggered. As a consequence of these bubble detachments, the network component of the total drag force suddenly decreases. The bubbles that replace the detached bubble in the wake of the disc are less elongated as a result of the rearrangements. However, they become more elongated as the disc continues its descent and the network force fluctuation is repeated in cycles about an average value.

The fluctuations in the pressure contribution to the drag force are smaller than those seen for the network contribution (see figure 3.5(b)). The pressure component of the force exerted on a disc is dependent on the bubble contact length with the disc and also the bubble pressure. In this case, the distributions of pressures of bubbles in contact with the disc are relatively consistent. Elongated bubbles in the disc's wake have a low pressure while bubbles in front of the disc are squeezed; whence have high pressures. The fluctuations in the pressure contribution to the drag force are a result of bubble rearrangements in these regions. This is demonstrated pictorially in figure 3.7.

Due to the motion of the disc being gravity driven and the distance of the disc from both walls being equal; it is to be expected by symmetry that the lift force (the force

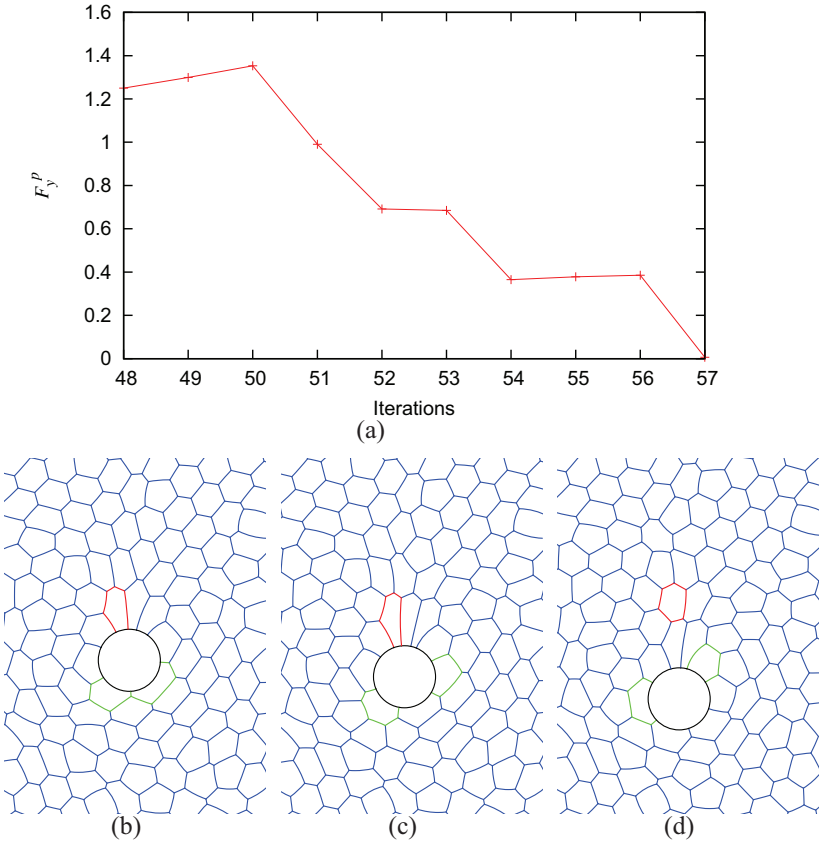

Figure 3.7: The pressure contribution to the drag force (F_y^p) fluctuates as the disc descends through the foam. Graph (a) demonstrates the fluctuations in F_y^p between simulation iterations 48 and 57 of the reference simulation. The foam structure at different stages of the interval is shown with a few bubble edges coloured for reference: (b) 50^{th} simulation iteration, (c) 53^{rd} simulation iteration and (d) the 57^{th} simulation iteration. The pressure contribution to the total drag is at its highest in the first picture where two bubbles (coloured green) below the disc are squeezed and have a large contact length with the disc. The pressure decreases as they are forced to separate, making way for bubbles that are less squeezed. The pressure contribution the drag is at its lowest in the third pictures where bubble rearrangements have resulted in a slightly more relaxed bubble shape distribution around the disc. The rearrangements continue and F_y^p continues to fluctuate about a mean value.

in the horizontal direction) exerted on the disc during sedimentation is negligible. It was previously noted that the disc drifted slightly laterally when it was tracked as it sediments (see figure 3.4(b)). Investigation of the lift force during sedimentation shows that the average lift (after a transient build up) is very close to zero (figure 3.8(a)). The fact that it is not exactly zero is due to the discrete and disordered nature of the foam.

The lift force exerted on the sedimenting disc is similar in nature to the drag force in the manner it fluctuates about the average value (see figure 3.8(b)). The fluctuations in the network and pressure contributions to the lift force is down to bubble rearrangements and changes to the distribution of films and bubbles along the boundary of the disc. It can be seen in figure 3.8(b) that the network lift (F_x^n) is in the opposite direction to the pressure lift (F_x^p). However they are very small forces that are centred about zero; whence the lift force on a disc sedimenting from a central position in the channel can be neglected.

3.4 Wall Effects on the Sedimentation Process

The sedimentation of the disc at an off-centre position in the channel is investigated. In this case it is expected that the lateral (lift) force exerted on the disc will be non-zero due to the symmetry of the foam flow being broken. Thus, the walls are expected to affect the flow of the foam and in turn, the motion of the disc. Previous 2D simulation work of a fixed disc placed near a wall in a constant velocity flow of foam discovered a repulsion between the disc and the wall [83]. However, the literature states that particles sedimenting in a viscoelastic fluid [45] at close proximity to a wall experience an attractive force. In this case the constant force and constant flow experiments do not yield similar results. The aim here is to answer the question of how wall effects affect the sedimentation of a disc in an elasto-plastic foam. Thus, the effect of wall proximity of the disc on its motion is studied.

The simulations are set up as for the reference case (§3.3) as a monodisperse form of foam A is used with a liquid fraction of $\Phi_l = 4 \times 10^{-3}$. However, the initial position of the disc at the top of the channel is varied between $0.1W$ and $0.9W$ (where W denotes

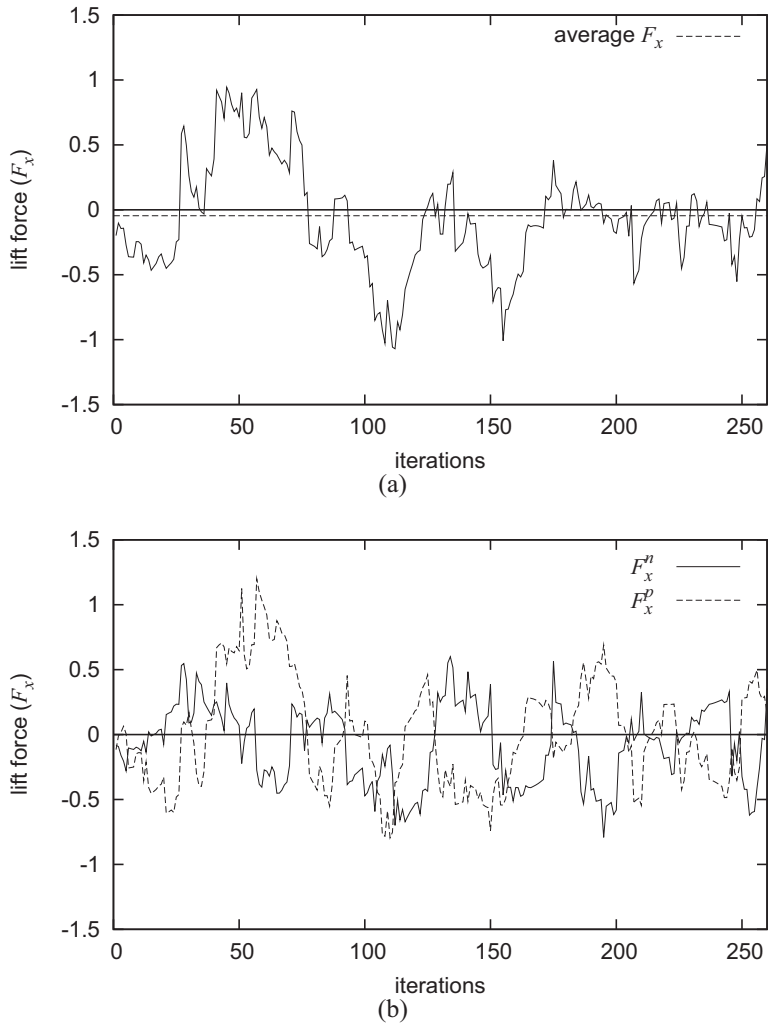

Figure 3.8: (a) Total lift force (F_x) and (b) network and pressure components (F_x^n and F_x^p respectively) of the lift force exerted on the disc (reference simulation) as it sediments through the foam. It can be seen that the lift force fluctuates (due to bubble rearrangements) about an average value close to zero. This is to be expected due to the flow of foam being symmetric as the disc sediments in a central position. This average value is not exactly zero due to the discrete nature and disorder of the foam structure. The network and pressure contributions also fluctuate about the value zero; in which case, the lift force is neglected when a disc sediments from a central position.

the channel width). In all, the disc is left to sediment from five different positions ($0.1W$, $0.3W$, $0.5W$, $0.7W$ and $0.9W$) along the top of the channel (see figure 3.9). The lift and drag forces are measured and the disc motion tracked as for the reference simulation. The effect of disc size on the influence of the wall effects is also studied, whence the process is repeated for discs of sizes $2A_b$ to $10A_b$ (the disc weight is fixed at $mg = 10$).

The motion of the disc with area $4A_b$ from these five positions is shown in figure 3.9. It is noticeable that in three cases the lateral motion of the disc is minimal. These three positions consist of the disc being placed at the centre of the foam channel and very close to either wall. In between these positions, lateral motion of the disc towards the closest wall is seen. Thus, the tendency appears to be that discs are attracted towards the closest wall unless they are already within a critical distance of the wall; in which case the attraction is minimal.

Investigation of the drag and lift force variations with wall proximity on different sized discs yields more detailed information of the wall effects during the sedimentation. It can be seen in figure 3.10(a) that the drag force exerted on a small disc of size $2A_b$ decreases slightly if the disc sediments close to either wall. In this case the disc sediments at a slightly quicker rate when placed near the wall. The corresponding relation for a larger disc does not report a drop in the average drag when placed near the wall (figure 3.10(b)). In this case the drag force exerted on the disc is independent of separation between the disc and the wall. Close inspection of the relation between drag force and initial placement of the disc for various disc sizes suggests independence between the two variables (figure 3.11(b)) for discs of size $6A_b$ and above. It is only for the smaller discs ($A_d = 2A_b, 4A_b$) that weak evidence of a decrease in drag force exerted on a disc when it is close to a vertical wall is seen.

In general, the lift force exerted on a sedimenting disc is directed towards the nearest wall; a tendency which is reflected by figure 3.11(a). It is seen that the lift force is highly dependent on the initial placement of the disc and that this dependence is highly non-linear. If the disc is placed initially at the centre point of the top end of the channel, the average lift is negligible and the motion is along the channel centreline. However, positioning the disc closer to either wall leads to an attractive force existing between

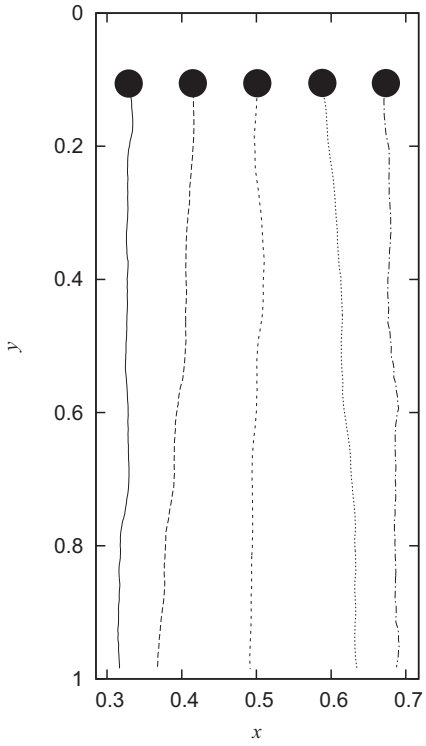

Figure 3.9: Tracking the disc motion from various initial positions (the centre co-ordinates (x_0, y_0) of the disc initially lies at $(0.1W, 0.1L)$, $(0.3W, 0.1L)$, $(0.5W, 0.1L)$, $(0.7W, 0.1L)$ and $(0.9W, 0.1L)$) for each simulation. It can be seen that lateral motion of the disc is at its greatest when the disc sediments from the positions $(0.3W, 0.1L)$ and $(0.7W, 0.1L)$. This lateral motion is such that the disc is attracted by the nearest wall. The lateral motion is minimal for the other three initial placements of the disc.

the wall and the disc. This is only true if the disc is still a certain distance from the wall. Placing the disc too close results in minimal lift exerted on the disc. Thus there exists a critical disc to wall separation that decides whether there is an attraction towards the wall or not. This critical disc to wall separation is dependent on the fluidized region surrounding the disc, a factor that will be investigated in greater detail in the section 3.5.

It is proposed that the critical separation between disc and wall equals the width of the fluidized region around the disc. This applies for discs of all sizes, and it is expected that the critical wall to disc separation increases with disc size as the fluidized region around the disc increases in size.

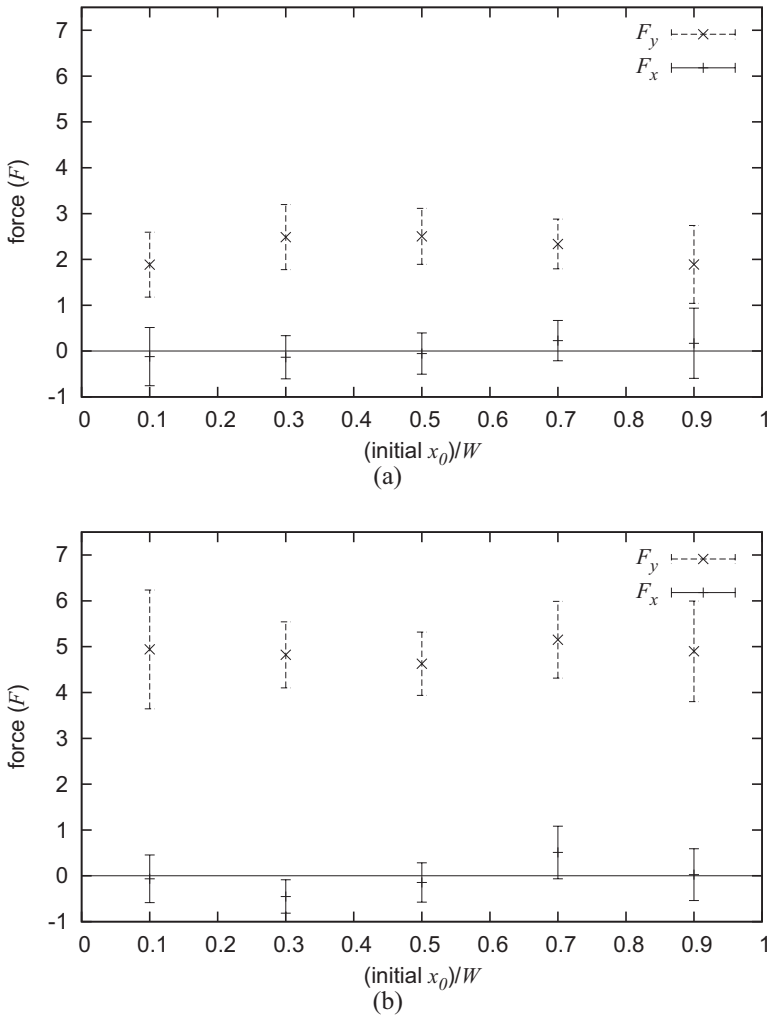

Figure 3.10: The average values for the total drag and lift forces (with standard deviation error bars) for discs sedimenting from the five initial positions (shown in figure 3.9) for: (a) disc of size $A_d = 2A_b$ and (b) a disc of size $A_d = 10A_b$. In the case of the small disc (a), a drag reduction is seen when a disc sediments close to the wall while the lift force appears to be minimal for all initial positions. In contrast, the drag exerted on a large disc (b) is independent of the initial placement of the disc. However it can be seen that the lift force exerted on the same disc is directed towards the nearest wall when its centre point is placed at $(0.3W, 0.1W)$ and $(0.7W, 0.1W)$. When the disc is placed either side of these positions, the lift force it experiences is minimal.

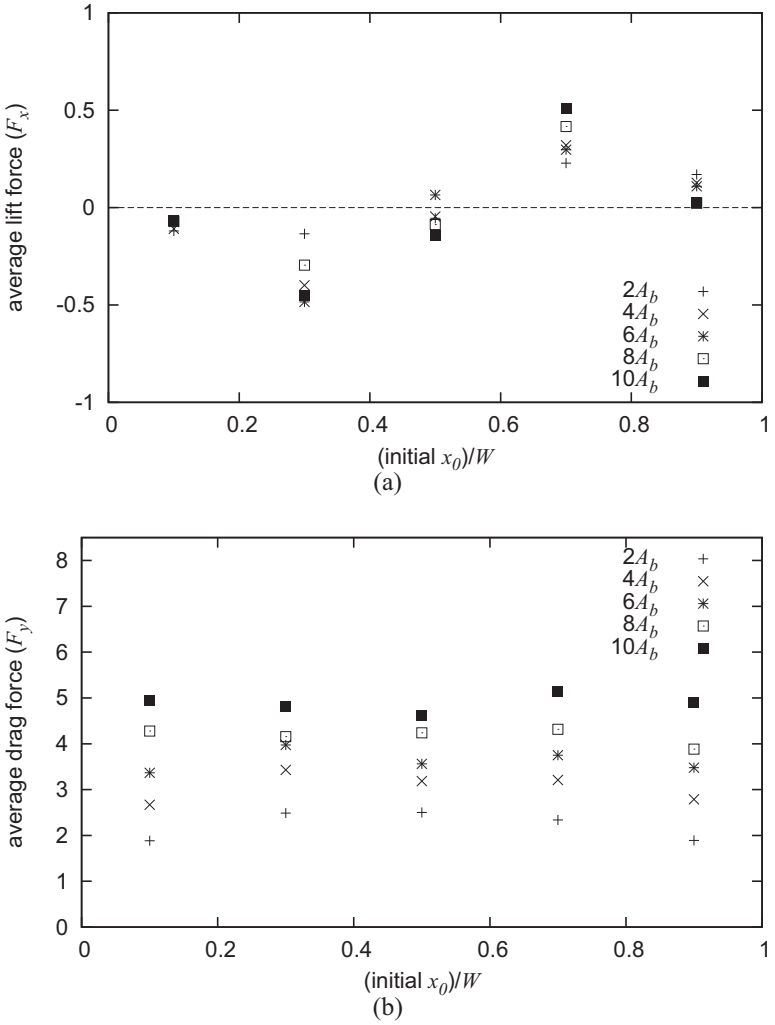

Figure 3.11: (a) Average values for the total lift force exerted on discs as their initial position is varied along the top of the channel for discs of size $2A_b$ to $10A_b$. (b) Average values for the total drag force on the same discs. It can be seen that there exists a non-linear dependence of lift force on initial position while the drag is independent of disc separation from the nearest wall. The result seen in figure 3.10 is shown to be true for all disc sizes used in the simulations.

3.5 Foam Fields

As well as investigating the foams' rheology by looking at the motion of sedimenting objects and the forces they experience, it is useful to characterize the flow of the foam during this process. Previous work on deformation fields of foam flow past a fixed circular disc [51] incorporated a tensorial view of the structure of the foam; this method is reviewed in an introductory section (1.10). Here, simple fields such as bubble displacement, T1 positions and bubble pressure during the sedimentation of the disc are studied. The investigation of such fields provides a clearer description of foam's response to the motion of the disc.

3.5.1 Bubble Displacement Field

The displacement field of the foam is computed through the tracking of bubble centre points (x_c, y_c) over a set number of simulation steps. The centre point coordinates of each bubble are calculated by averaging the coordinates of its vertices. In this section, the bubble centre coordinates are recorded every 30 simulation iterations and the displacement of the bubbles centres during this interval is represented by arrows. It was previously stated that the lift force exerted on a disc by a foam when it sediments from a central position in the channel is negligible. In this case the displacement field of the bubbles is expected to be symmetric during the sedimentation process. This is shown to be the case in figure 3.12.

During the downward motion of the circular disc, the bubbles in its way are forced to move. In this case, the bubbles directly below the disc move in the same direction as the disc. Bubbles beneath but slightly to the side of the disc, move away from the disc laterally. Bubbles on each side of the disc move very little and are sometimes stagnated. Stagnation points at each side of a circular object is a common phenomenon in viscoelastic [47] and viscoplastic [107] material and witnessed here for foams. Above these stagnation points are bubbles moving into the wake of the object. The flow seen here is asymmetric and deviations from this symmetry are a result of T1 topological changes and the discrete nature of foam.

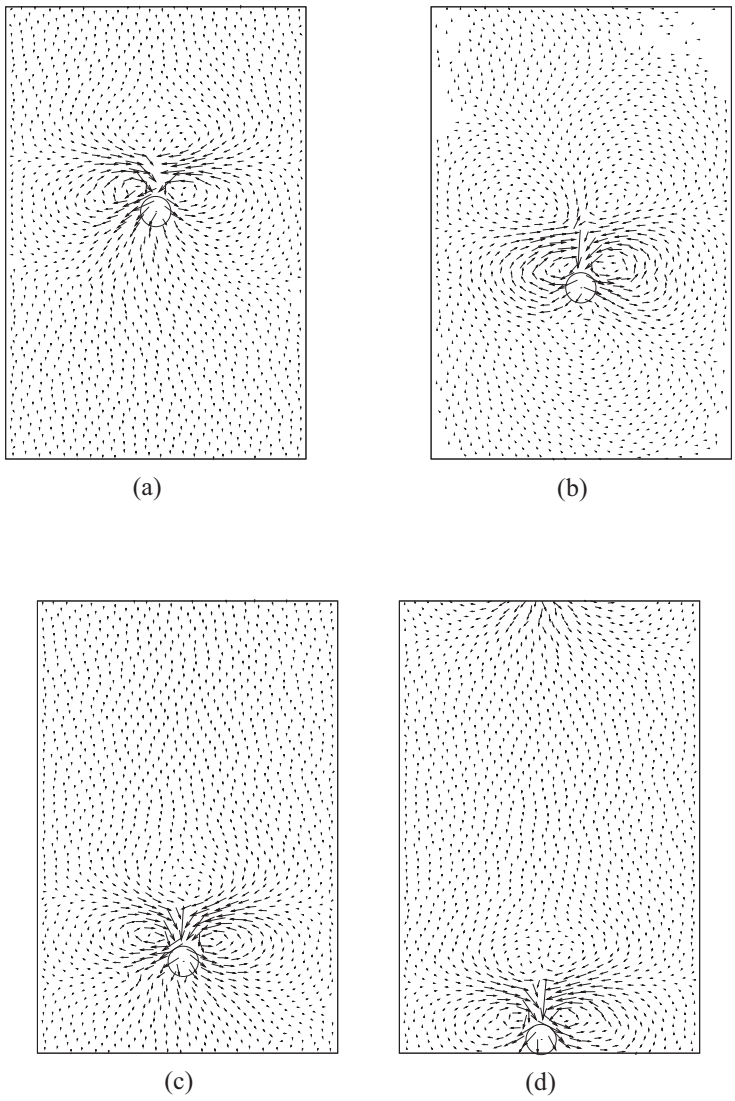

Figure 3.12: The bubble displacement field within foam A (monodiperse) when a disc of area $4A_b$ and weight $mg = 10$ sediments along the centre of the channel. Bubble centre point coordinates are recorded every 30 simulation iterations and their displacements during that time denoted by arrows. Each picture denotes the bubble displacement field during (a) 90 – 120 simulation iterations, (b) 150 – 180 iterations, (c) 210 – 240 iterations and (d) 270 – 300 iterations.

The study of foams' displacement field can enable better understanding of how a wall might influence the sedimentation process of a nearby disc. It is seen in figure (3.13) that when a disc sediments from $(0.7W, 0.1L)$, the wall breaks the symmetry of the flow. In this case the stagnation point between the disc and the wall is suppressed. This results in the push that would have been exerted on the disc by the circular flow about the stagnation point being slightly reduced. This results in the resultant lift force exerted on the disc being directed in the direction of the wall. As a result the disc moves closer to the wall as it sediments.

However, when the disc is initially very close to the wall (centre point is $(0.1W, 0.1L)$ or $(0.9W, 0.1L)$), i.e. separated by one or two bubble layers from the wall the attraction is minimal. This is a result of the no-slip boundary condition imposed at the walls in the simulations. The vertices of the edges that connect the foam to either wall are fixed, whence the bubbles positions are consequently fixed. In this case, the bubbles cannot rearrange such that the disc is pushed towards the wall any further. In this case, the disc descends along the edge of these more stationary layers of bubbles with minimal lateral motion.

3.5.2 T1 Positions

Another property of the foam that affects its flow is its plasticity. Thus, it is of interest to look at where the plastic events or T1s occur as the disc sediments. In this case, the position of a T1 is denoted by (x_i, y_i). This point is recorded wherever an edge shrinks below the critical length l_c (and the position where a new edge is inserted in a perpendicular direction by the simulation code). In this case, the distance of a T1 from the disc boundary is denoted as $T1^d$, and is given by

$$T1^d = \sqrt{\left((x_i - x_0)^2 + (y_i - y_0)^2\right)} - r_0 \,, \tag{3.4}$$

where r_0 is the disc radius and (x_0, y_0) its centre point coordinates. It will also be of benefit to consider the horizontal distances of T1s from a disc edge. This is denoted by

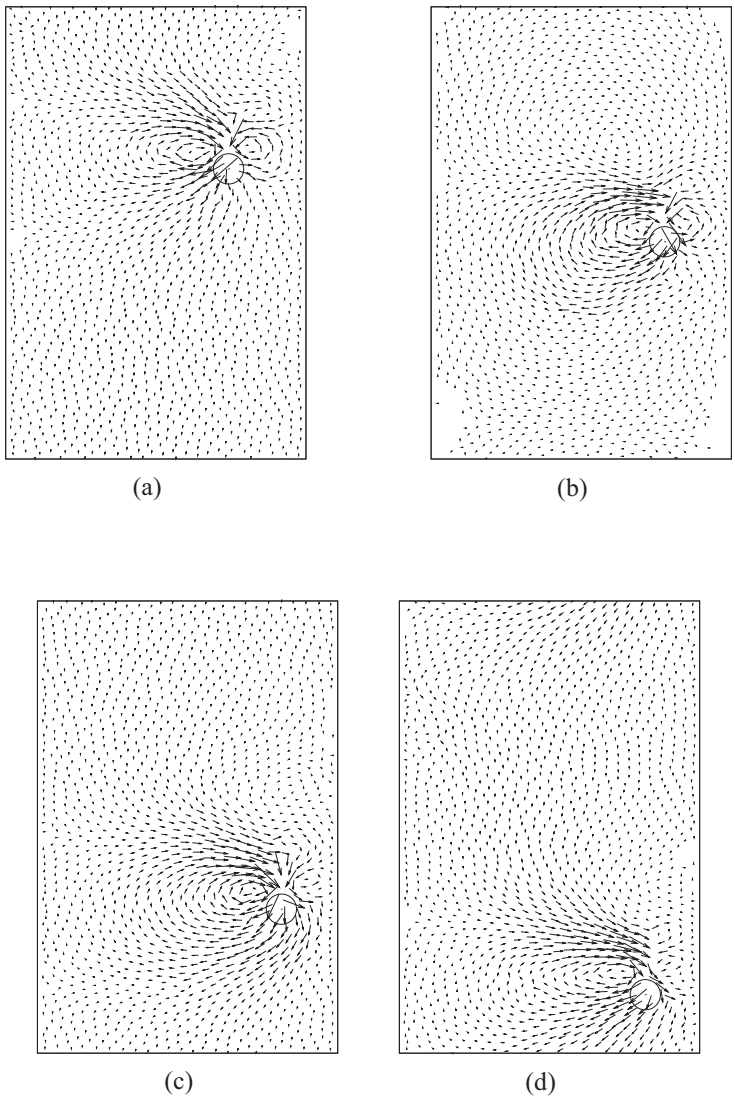

Figure 3.13: Displacement field within foam A (monodisperse) when a disc of size $4A_b$ and weight $mg = 10$ sediments nearer to a wall (initial position is $(0.7W, 0.1L)$). The bubble centre point coordinates are recorded every 30 simulation iterations and their displacement during this interval is denoted by an arrow. Each picture denotes the displacement field of the foam during (a) $60 - 90$ simulation iterations, (b) $120 - 150$ iterations, (c) $180 - 210$ iterations and (d) $240 - 270$ iterations.

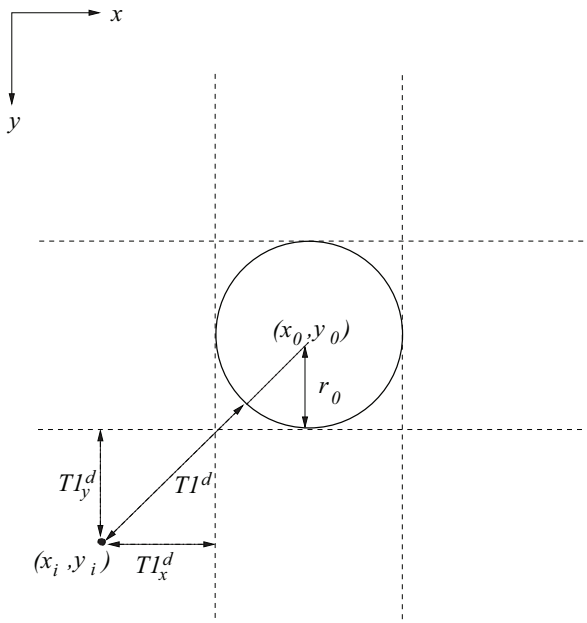

Figure 3.14: For a T1 event occurring at (x_i, y_i) in the channel, the values for $T1_x^d$, $T1_y^d$ and $T1^d$ yield information about the position of the event relative to the boundary of the sedimenting disc.

$T1_x^d$ and approximated by

$$T1_x^d = |x_i - x_0| - r_0 \; . \tag{3.5}$$

Similarly, the vertical distance separating a T1 and a disc edge is approximated by

$$T1_y^d = |y_i - y_0| - r_0 \; . \tag{3.6}$$

These values (see figure 3.14) ensure that a detailed description of the distribution of the distance between T1 events and the disc boundary is given.

It is expected that most T1s occur in a region close to the disc that is fluidized. It is within this region that the disc applies the greater stress on the foam and as a result it is also the region where the deformation rate of the foam is at its maximum. In this case, one would expect most T1s to take place directly in front or behind the disc as it falls through the foam. Figure 3.15 shows that during the sedimentation of the disc in the reference simulation, the vast majority of T1s have occurred within $5d_b$ of the boundary

of the disc. Closer inspection of the fluidized region shows that most T1s occur in the first two layers of bubbles surrounding the disc (see figure 3.15(b)).

The T1s positions when a disc sediments in an off-centre position are presented in figures (3.16). Here it is again demonstrated that most T1s occur close to the disc. Moreover the fluidized region surrounding the disc is mostly concentrated in front and in the wake of the disc. These are the regions where the deformation rates of the foam are at its greatest due to the applied stress of the disc. The amount of T1s occurring either side of the disc as it sediments is minimal. It is therefore proposed that the plasticity of the foam only minimally contributes to any wall effects. In this case the wall effects are a result of the mostly elastic deformation of bubbles either side of the disc being non-symmetric due to the presence of the nearby wall.

The dimensions of the fluidized region surrounding the descending object will be of importance in chapters 4 and 5 where the interaction between two discs is considered. It is of interest to look at how the size of the circular disc affects the distribution of T1s in the foam. In this case, the positions of T1 events are recorded during the sedimentation of discs of sizes $2A_b$, $6A_b$, $8A_b$, and $10A_b$ through the channel. The disc is initially placed so that its centre coordinates equal $(0.5W, 0.1L)$. The weight of the disc is kept fixed at $mg = 10$, so that steady descent through the channel is ensured. Foam A is used with the liquid fraction kept constant at $\Phi_l = 4 \times 10^{-3}$.

Figure 3.17 demonstrates how the T1s are distributed in terms of distance from the disc edge ($T1^d$) during the sedimentation of each disc. As seen in figure 3.15, most T1s events occur within the first two or three layers of bubbles surrounding the disc. It is shown in this figure that increasing the size of the disc results in more frequent T1 events. This increase in the number of T1s with disc size shows that the fluidized region surrounding a disc increases in area. This is to be expected as bigger objects apply a greater stress on the foam and results in more deformation and rearrangements.

It is possible to look at how the fluidized region surrounding a disc increases in width and height with disc size. In this case, one would like to look at particular regions of the fluidized region and how they vary with disc size. The regions of interest are directly either side of the disc and directly above (the wake) and below the disc. The

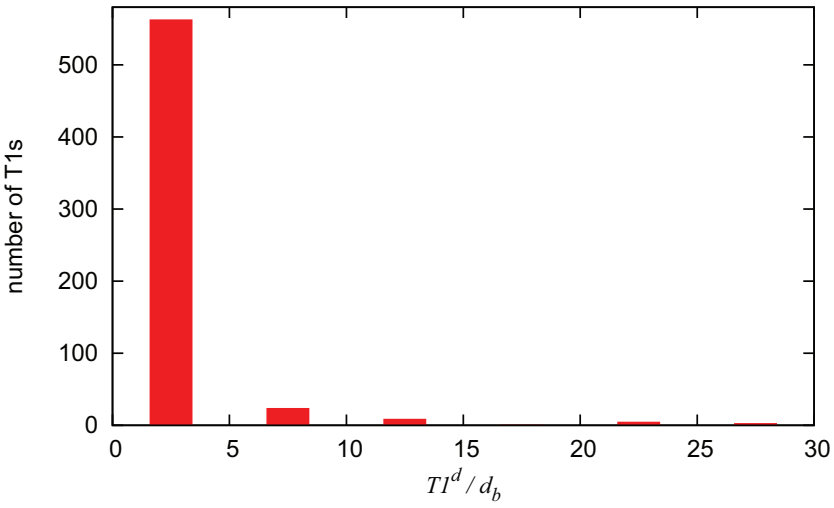

(a)

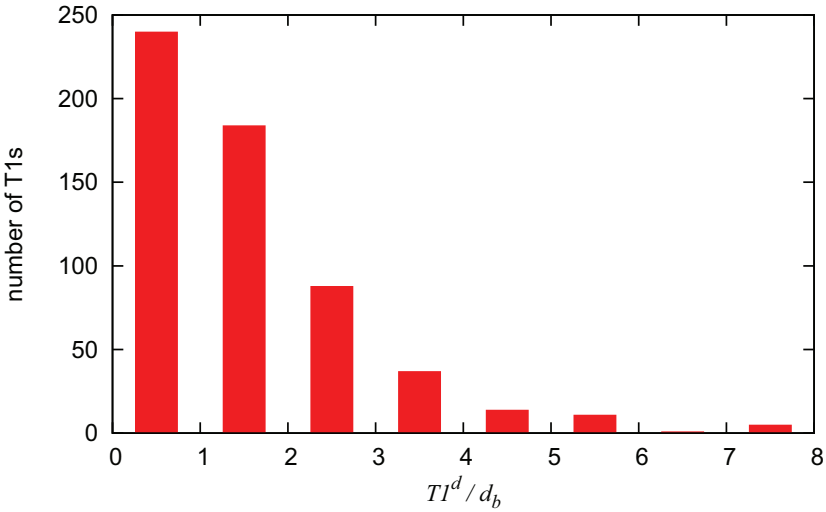

(b)

Figure 3.15: Histograms showing how the T1s are distributed in terms of their separation from the disc boundary ($T1^d$) as the disc sediments in the reference simulation (see §3.3 for details). (a) Describes how the T1s are distributed within intervals of $5d_b$. In this case, it can be seen that most T1s occur within the first five layers of bubbles surrounding the disc. (b) Describes in greater detail the distribution of T1s within the first eight bubble layers surrounding the disc. It is shown here that the T1s occur mainly in the first two bubble layers surrounding the disc as it descends.

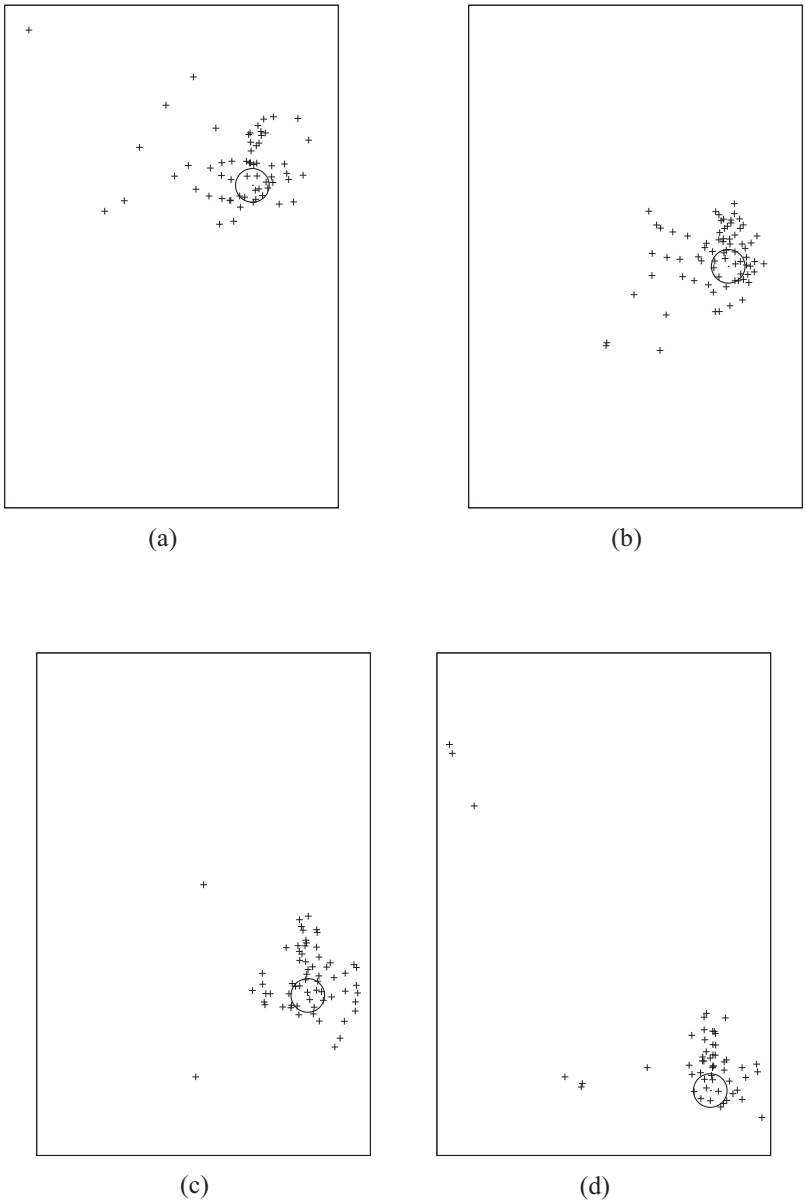

Figure 3.16: The positions of T1s within a foam channel is recorded when a disc sediments from an initial position of $(0.7W, 0.1L)$ at the top of the channel. This is done for intervals of 30 simulation iterations and each plot represent the T1 positions for (a) 60 – 90 simulation iterations, (b) 120 – 150 iterations, (c) 180 – 210 iterations and (d) 240 – 270 iterations.

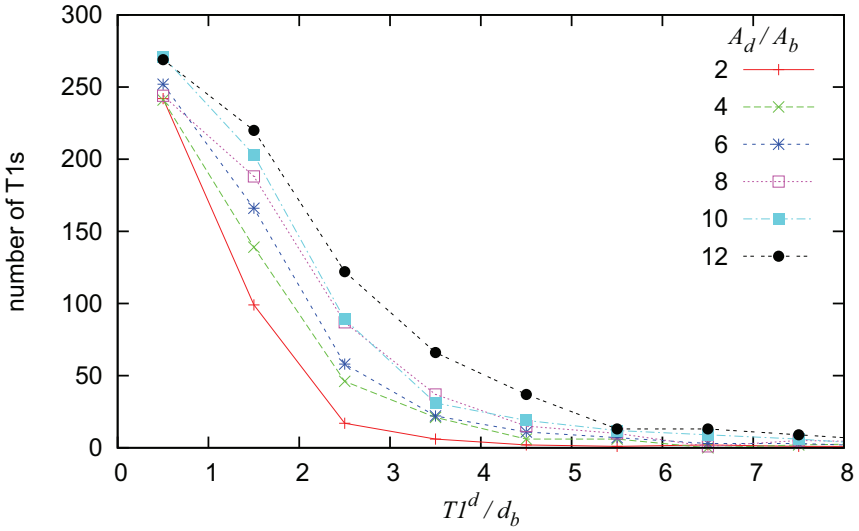

Figure 3.17: The distance of T1 events that occur at (x_i, y_i) from the boundary of the disc is given by $T1^d$ (3.4) and is shown here in terms of the average bubble diameter d_b. The distribution for $T1^d$ when discs of sizes $A_d \in \{2A_b, 4A_b, 6A_b, 8A_b, 10A_b\}$ and weight $mg = 10$ are allowed to sediment separately from a central position in foam A (monodiperse) with liquid fraction $\Phi_l = 4 \times 10^{-3}$. It can be seen that most T1s occur within the first couple of layers of bubbles surrounding the disc. It is also clear that the fluidized region surrounding the disc (where most T1s occur) increases in size with disc area.

distributions of T1s in these regions can be described by looking separately at strictly positive values of $T1_x^d$ and $T1_y^d$ (see equations 3.5 and 3.6 respectively).

The distribution for the horizontal distance of T1s from a disc's boundary (for $T1_x^d > 0$) is shown in figure 3.18(a). This range for $T1_x^d$ means that the T1s that occur directly below or above the disc as it sediments are omitted. It can be seen that the vast majority of the T1 events occur within two to three bubble layers of the disc in this lateral direction. The fluidized region expands its horizontal reach as the disc size is increased.

Similarly, the vertical distance of T1s from the disc edge in the region where $T1_y^d > 0$ is shown in figure 3.18(b). The range denoted for $T1_y^d$ means that the T1s positioned directly to either side of the disc as it sediments are omitted. In this case, the remaining part of the fluidized region surrounding the disc is considered. This includes the wake and the region in front of the disc as it sediments. It can be clearly seen that more T1s occur within this region than for figure 3.18(a). Also interesting is that more T1 events

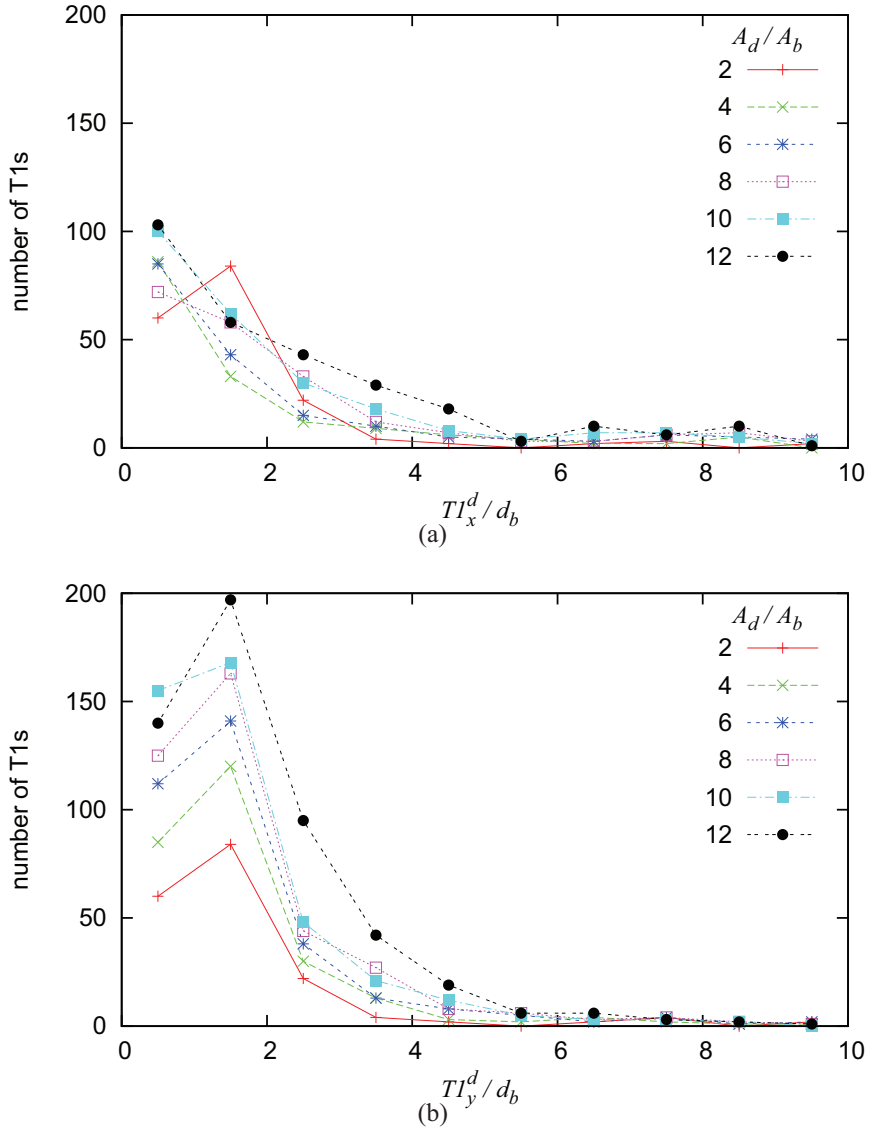

Figure 3.18: The distribution of the distance between T1 events and disc edge in the (a) horizontal direction ($T1_x^d > 0$) and the (b) vertical direction ($T1_y^d > 0$). It can be seen that more T1s occur in the vertical regions of the fluidized region of the foam (i.e. wake and in front of the disc) than horizontally either side of the disc. The horizontal and vertical range of the fluidized region of the foam increases with disc size. A more detailed explanation of the figure is given in the text (see the section 3.5.2).

occur in the range $1-2d_b$ rather than $0-1d_b$. However, this is merely a result of how the distance between the disc edge and the T1 is calculated in terms of the average bubble diameter of the relaxed foam (d_b). The region of the foam considered here contains bubbles that are very elongated in the wake of the disc. They elongate to roughly twice the average bubble diameter d_b. In this case, even though most T1 events occur in the region $1-2d_b$, more occur within the first layer of bubbles surrounding the disc than in the second. It is noticeable that the vertical reach of the fluidized region surrounding the disc increases with disc size.

3.5.3 Bubble Pressure

Another important field to investigate is that of bubble pressure. Bubbles located in front of the disc as it sediments have high pressure (compared to bubbles far from the disc) as they are squeezed by the disc. Meanwhile bubbles in the wake of the sedimenting disc are stretched, therefore have a low pressure.

This general description for the pressure field close to the disc is demonstrated by figure (3.19). These figures provide a picture of the pressure field as the disc sediments but should not be compared with each other. The bubbles are coloured by comparable pressure to a reference bubble chosen to be far away from the disc and the high deformation area. In this case a T1 near the reference bubble would change the colour scheme dramatically; thus one should consider each figure separately when looking at the pressure distributions.

When the disc sediments from a central position the low pressure region of the wake is seen to extend on average 5 to 6 bubble diameters from the disc. This is how far the disc influences the foam. It is seen that the region of high pressure in front of the disc only extends one or two bubbles from the disc boundary. Moving downwards from these bubbles of high pressure, the pressure distribution varies from bubble to bubble and resembles the region of the foam that is far away from the disc.

The pressure field when a disc sediments near a wall is expected to show similar patterns. This is shown to be the case in figures (3.20) and (3.21). The region of low

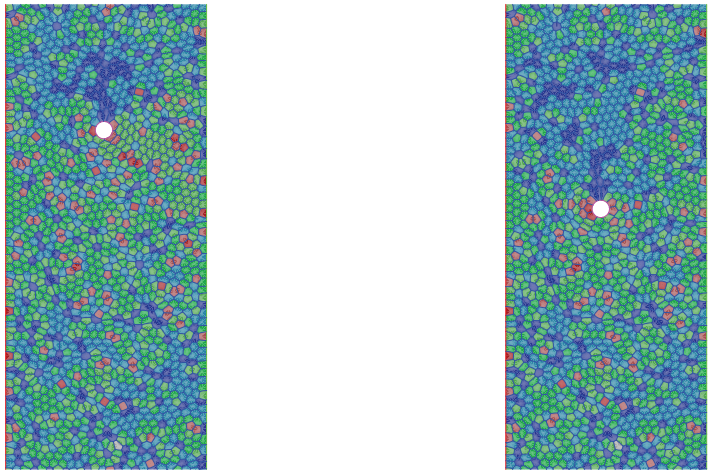

(a) (b)

(c) (d)

Figure 3.19: The bubbles are colour coded depending on their pressure (which is related to the curvature of their edges) comparable to a reference bubble chosen to be in a region far from the disc. Here the pressure increases with the order dark blue, light blue, green, light green, light red to red. Each figure represent an example of such pressure fields during the reference simulation (see §3.3 for details); these examples are (a) the 50^{th} simulation iteration, (b) 100^{th} iteration, (c) 150^{th} iteration and (d) 200^{th} iteration.

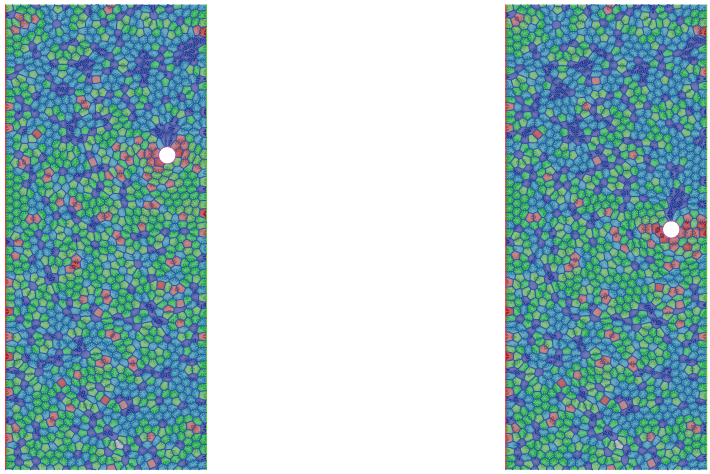

(a) (b)

Figure 3.20: The pressure field of foam A (monodisperse) with liquid fraction $\Phi_l = 4 \times 10^{-3}$ when a disc of area $A_d = 4A_b$ and weight $mg = 10$ is initially placed close to the wall at $(0.8W, 0.1L)$. As for the disc sedimenting from a central position, the order of relative pressure compared to the reference bubble follows from blue, light blue, green, light green, light red to red. The examples given are for (a) the 50^{th} simulation iteration and (b) the 100^{th} iteration.

pressure in the wake extends 5 to 6 bubble diameters as before and the bubbles with high pressure are situated in front of the sedimenting disc. Here it is shown that new information about the wall effects cannot be deduced from studying the pressure field of the foam.

It is therefore the case that the pressure field is most interesting in the wake (that stretches $5d_b$ to $6d_b$ from the disc) and just below the disc (that stretches $1d_b$ to $2d_b$ from the disc). Combining the analysis of the fields of bubble displacement, T1 position and bubble pressure yields that these are the two regions that exhibit most deformation as the disc sediments.

3.6 Variation of the Bubble Area Dispersity

The bubble area dispersity of a foam is a parameter that affects the local topology and structure of the foam. In this section, the aim is to check whether the bubble area dispersity changes the rheological response of the foam to a sedimenting circular disc.

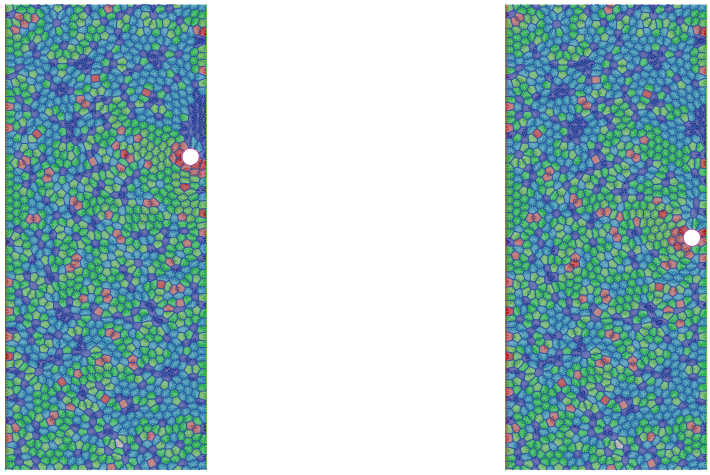

(a) (b)

Figure 3.21: The pressure field of foam A (monodisperse, with liquid fraction $\Phi_l = 4 \times 10^{-3}$) when a disc of size $A_d = 4A_b$ and weight $mg = 10$ is initially placed very close to the wall at $(0.9W, 0.1L)$. Again, the order of relative pressure compared to the reference bubble follows from blue, light blue, green, light green, light red to red. The examples given are for (a) the 50^{th} simulation iteration and (b) the 100^{th} iteration.

It was found in the oscillatory experiments of Saint-Jalmes and Durian [106] that for a moderate range of bubble area dispersity, the elastic response of a foam is not greatly affected. It was found in this work that the liquid fraction of the foam was a much more important parameter that affected the foam's response. In the case of simple shear experiments, the polydipersity of the foam can determine the nature of the flow as it controls the nature of T1 localization [87].

In this section, consideration is given to the sedimentation of a circular disc in a completely monodisperse and also a polydiperse foam. Such a disc is expected to fluidize a small region of the foam near the disc but the vast majority of the foam will be unaffected by its slow descent. The differences in the rheology due to dispersity is investigated by comparing the motion of the same disc in the two different foams (figure 3.22).

Recall that the bubble area dispersity of the foam is measured in 2D simulations by a parameter $\mu_2(A)$ which is given by

$$\mu_2(A) = \left\langle \frac{(A_b - \langle A_b \rangle)^2}{\langle A_b \rangle^2} \right\rangle , \tag{3.7}$$

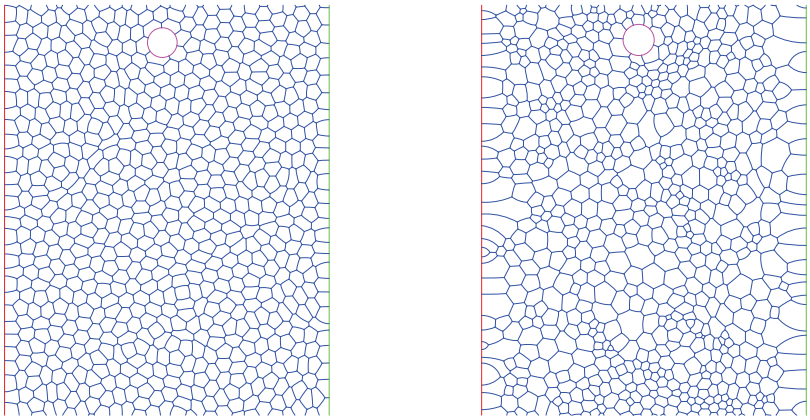

(a) (b)

Figure 3.22: The dispersity of the foam is varied so that comparison can be made between the response of (a) a monodisperse foam ($\mu_2(A) = 0$) and (b) a polydisperse foam with $\mu_2(A) = 0.428$ to the same sedimenting disc.

where A_b denotes each bubble area and $\langle A_b \rangle$ the average bubble area throughout the foam. For a monodisperse foam $\langle A_b \rangle = A_b$. In this section the two foams used were a monodisperse foam ($\mu_2(A_b) = 0$) and a polydiperse foam where $\mu_2(A_b) = 0.428$.

To minimize the computational time of the simulation, foam B is used (see table 2.1 for details) as it contains less bubbles than foam A. The foam has a liquid fraction of $\Phi_l = 4 \times 10^{-3}$ for both the monodisperse and polydisperse case. A disc with area $A_d = 4\langle A_b \rangle$ and weight $mg = 10$ is left to descend through the foam from the same initial position of $(0.5W, 0.1L)$ in each foam. The effect that the bubble area dispersity has on a foam's response is investigated by comparing the motion of the disc in both foams as well as the forces they experience.

It was previously noted that the lift force exerted on a disc sedimenting along the centreline of the channel was negligible; bubble area dispersity does not change this fact. The variation of the drag force exerted on the disc during sedimentation in both foams is shown in figure 3.23. Here, it is clear that the drag force exerted by the two foams on the disc is similar in magnitude but differs slightly in nature. It fluctuates about its mean value to a greater extent in the polydisperse case than in the monodisperse foam.

It was shown by Dollet *et al.* [75] that the drag force exerted on an obstacle by a constant velocity flow of foam increased with decreasing bubble size. It follows that the drag force fluctuates more dramatically when the distribution of the bubble areas is more scattered. This information can be extracted by looking at the pressure and network components to the drag force exerted by both foams (figure 3.24).

It is clear that the polydispersity of the foam does not have a great affect on the bubble pressure contribution to the drag exerted on the disc (see figure 3.24(b)). It was shown that the fluctuations in the drag force exerted on a disc was mainly due to the network contribution (see §3.3). The pressure contribution to the drag force is less dependent on bubble size. This pressure contribution fluctuates similarly about a mean value for both foams tested. In this case, the regions of low pressure in the wake and high pressure in front of the disc is similar whether these regions contain bubbles of equal area or not.

The greater fluctuations for the drag force in a polydisperse foam is a result of the network component fluctuating more dramatically than in the monodisperse foam. This can be justified on the basis that there are regions within the polydiperse foam where bubbles are smaller, and therefore foam films are highly concentrated. This leads to a high network drag force exerted on the disc. Conversely, minimal network drag is exerted in local regions of the same foam where the bubbles are larger. It follows that having a foam with a large variance of bubble size will exert a greater fluctuating network force on a sedimenting disc.

Having detected minimal differences between the drag force exerted on the disc by two foams with different bubble area dispersity, it was shown that the polydispersity of the foam has only a minimal effect on the motion of the disc (figure 3.25). As a result, the polydispersity of a foam can be considered to be a parameter that does not greatly affect the qualitative response of the foam to the sedimentation of a circular disc. More evidence of the this is shown in section 3.7.

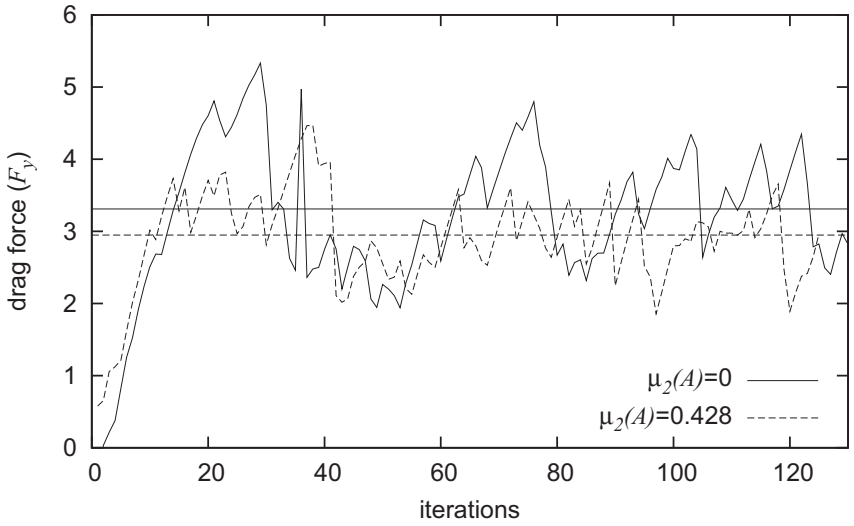

Figure 3.23: The total drag force (F_y) on a disc of area $A_d = 4A_b$ and weight $mg = 10$, sedimenting in monodiperse ($\mu_2(A_b) = 0$) and polydisperse ($\mu_2(A_b) = 0.428$) versions of foam *B*. The liquid fraction is fixed at $\Phi_l = 4 \times 10^{-3}$. The drag force is found to be similar in magnitude (shown by the horizontal lines) when the disc sediments in each foam but the fluctuations are greater for the polydisperse foam. The slightly lower value for the drag force exerted on the disc in a polydiperse foam than in the monodisperse foam is a result of a high concentration of large bubbles along the centreline of the channel (see figure 3.22(b)).

3.7 Forces Exerted on the Disc during Sedimentation

Having shown that the bubble area dispersity of the foam does not dramatically change the response of the foam to a sedimenting disc; the variation of parameters that are known to affect the forces exerted on such an object are now investigated. The work of Raufaste *et al.* [77] showed that the drag force exerted on a fixed circular object in a constant velocity two-dimensional flow of foam depends mainly on two factors; the ratio of obstacle to bubble size and the foam's liquid fraction. The effect that varying these parameters has on the drag force exerted on the sedimenting circular disc is quantified in sections 3.7.1 and 3.7.2 respectively.

3.7.1 Drag Force Dependence on Disc Size

It is to be expected that larger objects will experience greater drag than smaller objects. This is logically the case in any situation, and sedimentation in foam is no different. It

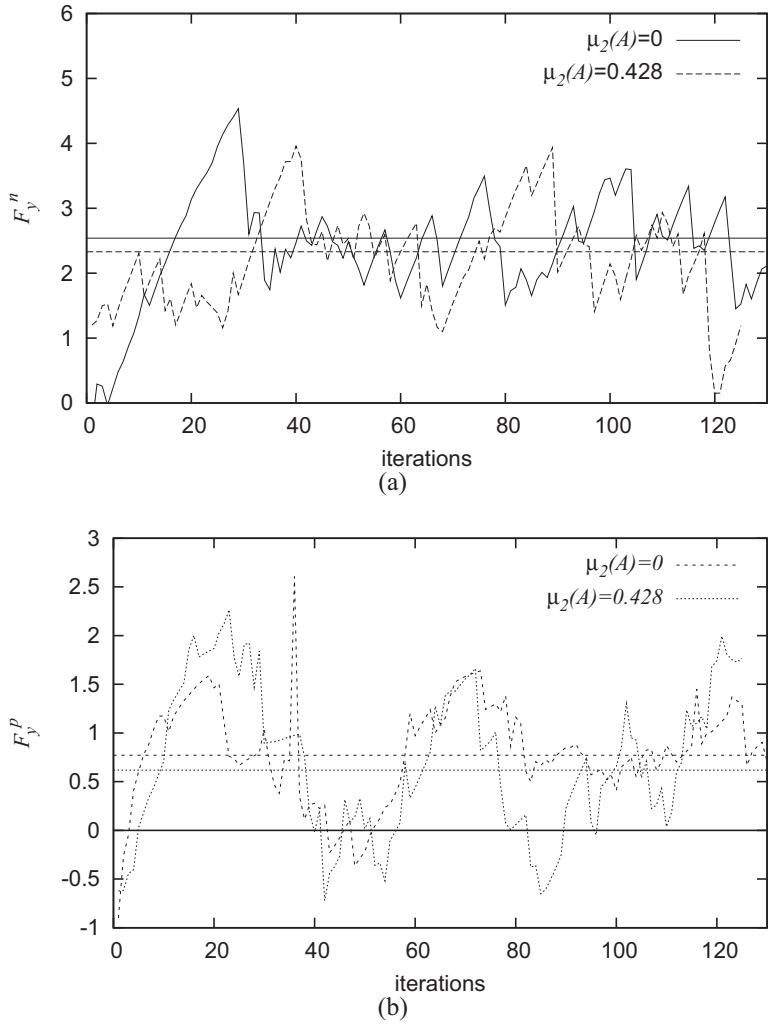

Figure 3.24: The (a) network (F_y^n) and (b) pressure (F_y^p) contributions of the total drag force exerted on a disc of size $4A_b$ and weight $mg = 10$, sedimenting along the centre line of the channel, in monodiperse ($\mu_2(A) = 0$) and polydiperse ($\mu_2(A) = 0.428$) versions of foam B. The liquid fraction is set to $\Phi_l = 4 \times 10^{-3}$. The network contribution fluctuates more dramatically when the disc sediments in the polydisperse foam than in the monodisperse foam. This is due to the greater variations in concentration of foam films in the polydisperse foam. The pressure contribution to the drag force exerted on the disc is very similar in both foams.

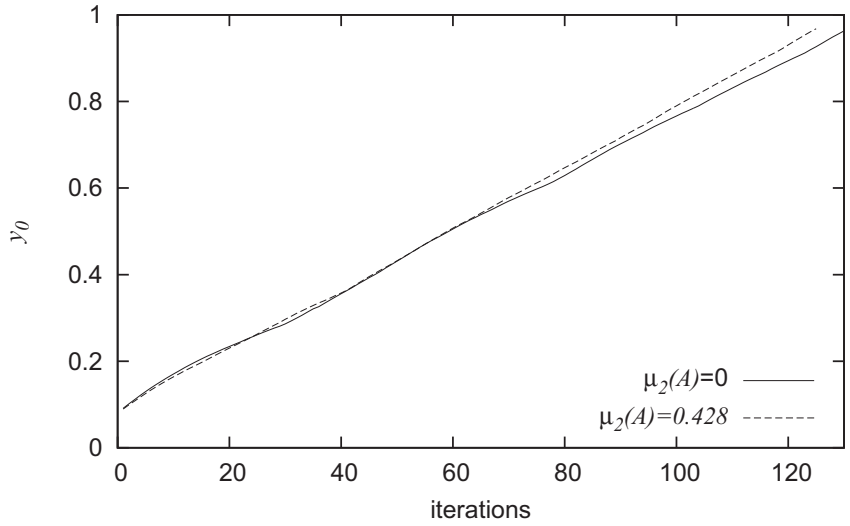

Figure 3.25: The vertical position of the disc centre point (y_0) as it sediments from a central position at the top of foam channel in monodiperse ($\mu_2(A) = 0$) and polydiperse ($\mu_2(A) = 0.428$) versions of foam B. As before, the disc size is $4A_b$ and its weight is $mg = 10$. The liquid fraction of the foam is $\Phi_l = 4 \times 10^{-3}$. It can be seen that the bubble area dispersity of the foam does not have a great effect on the amount of simulation iterations it takes for the disc to descend through the channel.

was found in a previous section (3.5.2) that a larger disc increases the amount of deformation in the foam as it sediments. Recall that the work of Raufaste *et al.* [77] showed that the network contribution to the drag force increased affinely with disc diameter d_0 (see equation 3.1). In this section, the relation between the network and pressure contributions to the drag force exerted on the sedimenting disc with the ratio between disc and bubble sizes is studied.

It has already been noted that the network contribution to the drag force exerted on the disc is related to the bubble size (§3.6). Increasing the disc size is equivalent to decreasing the size of the bubbles. Here, the sedimentation of discs sizes in the range between $1A_b$ and $18A_b$ in foam B is studied. Since we are only interest in the effect that the obstacle's geometry has on the response of the foam, and not of the effect of the object's weight, the dimensionless value for the weight of the disc is kept constant at $mg = 10$ throughout. Also kept fixed in this section is the liquid fraction of the foam, its value being $\Phi_l = 4 \times 10^{-3}$. As in section 3.6, monodisperse and polydisperse versions of foam B are used; with $\mu_2(A) = 0$ and $\mu_2(A) = 0.428$ respectively.

The mean values for the separate network (F_y^n) and pressure (F_y^p) contributions to the drag force as well as the total drag force (F_y) after the transient build up are calculated. The relation between these forces and the ratio between disc and bubble sizes are presented in figures 3.26 and 3.27 respectively.

It is seen in figures 3.26(a) and 3.26(b) that the network drag force (F_y^n) on the disc increases affinely with disc diameter for both the monodisperse and polydisperse foams. The slope for the relation in a monodisperse foam is 0.75 while it is 0.60 for the polydisperse foam. This linearity confirms that the relation between disc size and drag force can be described by equation 3.1.

The same figures also demonstrate that the pressure contribution (F_y^p) to the total drag force exerted on a sedimenting disc increases affinely with the ratio of disc size and bubble size. Again, the slopes of the relations are similar to the each other for a monodisperse and a polydisperse foam; 0.46 and 0.34 respectively. In this case, one could fit either set of data to an affine relation with equal slopes without greatly increasing the error of the fit. It can be seen that the slope for the relation between the network contribution to the drag and the disc size is greater than that of the pressure contribution. Moreover, the slopes of the relations of both contributions to the drag with the ratio of disc to bubble size are also slightly greater for the monodisperse foam than the polydisperse foam. However, considering the standard deviation error bars seen in these figures, the qualitative difference in the slopes is minimal.

The total drag force (F_y) is shown to increase affinely with the ratio of disc diameter (d_0) over bubble diameter (d_b) in figure 3.27. That similar linear relations apply to foams with different bubble area dispersity reiterates the fact that the dispersity of the foam is an insignificant parameter when predicting the drag force exerted on the disc.

3.7.2 Drag force Dependence on Liquid Fraction

A foam's liquid fraction Φ_l influences its rheology. It is known that wet foams behave differently to dry foams as topological changes occur at a greater rate and the bubbles generally become more rounded [1]. It was shown in section 3.2.2 that the maximum

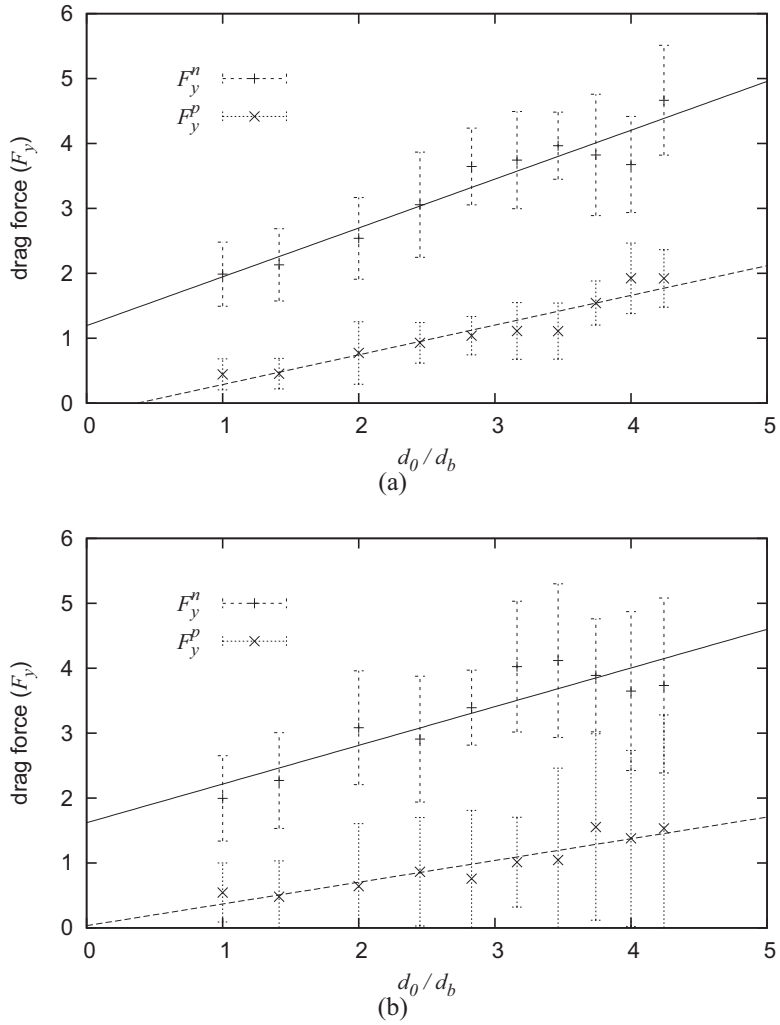

Figure 3.26: The relation between the network and pressure contributions to the drag force (F_y^n and F_y^p) and disc diameter (relative to the average bubble diameter d_b) for a (a) monodisperse foam ($\mu_2(A) = 0$) and (b) a polydisperse foam ($\mu_2(A) = 0.428$). For the monodisperse foam, the network and pressure components of the drag force exerted on the disc increase affinely with the ratio of disc to bubble size with the relations $F_y^n = 0.75\frac{d_0}{d_b} + 1.19$ and $F_y^p = 0.46\frac{d_0}{d_b} - 0.17$ respectively. Similarly for the polydisperse foam the relations are written as $F_y^n = 0.60\frac{d_0}{d_b} + 1.62$ and $F_y^p = 0.34\frac{d_0}{d_b} + 0.03$. Notice that the affine relations are similar for both the monodisperse and the polydisperse foam.

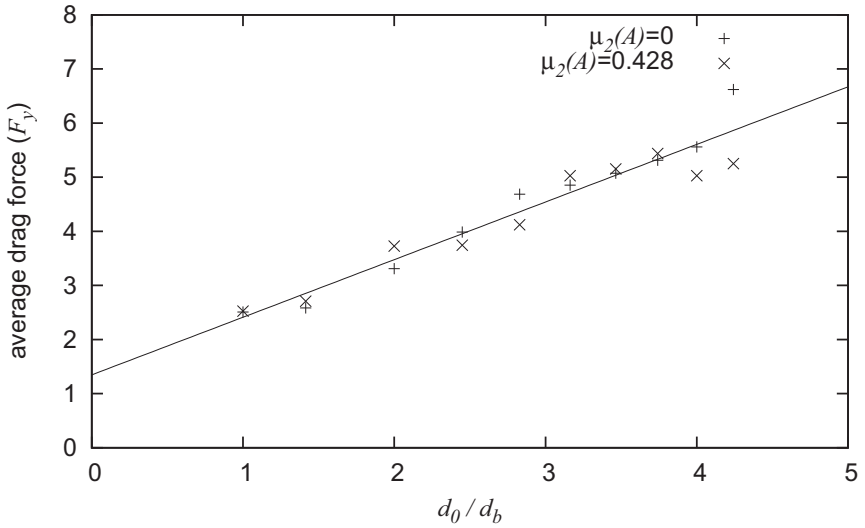

Figure 3.27: The relation between the average of the total drag force F_y exerted on a disc (descending in monodisperse and polydisperse version of foam B) and the ratio of disc size to bubble size (d_0/d_b) is found to be affine. The equation of the fitted line is given by $F_y = 1.06\frac{d_0}{d_b} + 1.35$. The line is a relatively good fit for both the monodisperse and polydisperse foams used.

disc weight a foam could support decreased with increasing liquid fraction with a power law relation of $\Phi_l^{-0.182}$. It was predicted by Raufaste *et al.* [77] that the network drag force (F_y^n) exerted on a fixed circular obstacle in a constant velocity flow of foam decreases when increasing the liquid fraction with a relation of $\Phi_l^{-1/4}$ (3.1). The relation between the liquid fraction of the foam and the network and pressure contributions to the total drag force exerted on a sedimenting disc is investigated in this section.

A disc of size $4A_b$ and weight $mg = 10$ is left to sediment from a central position at the top of the channel $(0.5W, 0.1L)$ in foam B (monodisperse). The foam in each simulation has a different liquid fraction; Φ_l is varied between 2×10^{-3} and 2×10^{-2}.

Firstly, the effect that varying the liquid fraction has on the motion of the disc is investigated. It is shown in figure (3.28) that the rate of downward motion of the disc increases with the foam's liquid fraction. This is to be expected as the wetter the foam, the plastic T1 events occur more frequent; whence the fluidized region surrounding the disc becomes larger. Conversely, plastic events (T1s) are less common in a very dry foam; thus the fluid region surrounding the disc is smaller. In this case the elasticity of

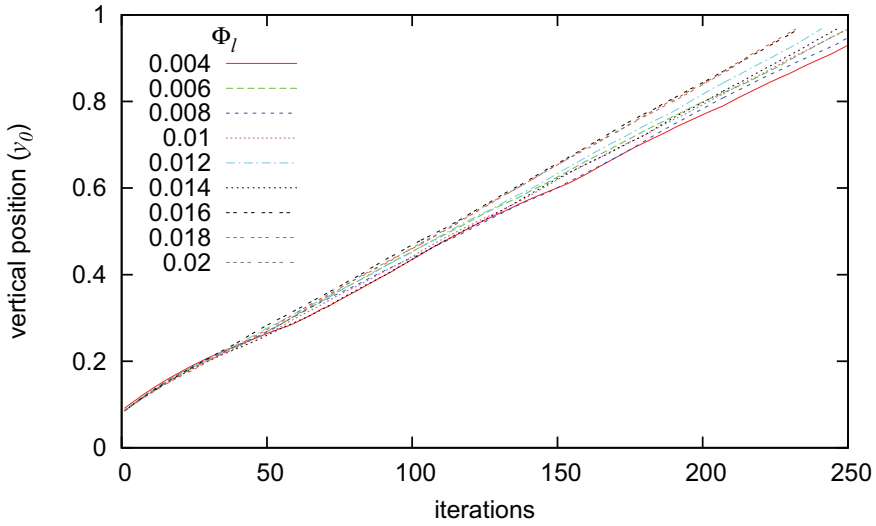

Figure 3.28: The vertical position of a disc's (of size $4A_b$ and weight 10) centre point (y_0) as it sediments in monodisperse versions of foam B for liquid fractions varying between $\Phi_l = 4 \times 10^{-3}$ and 2×10^{-2}. It is seen that increasing the liquid fraction of the foam within the range considered here slightly increases the rate of descent of the disc through the foam. The sedimenting motion of the disc is steady in all cases.

the foam is more dominant. For the liquid fractions investigated here, the motion of the disc is steady (see figure 3.28).

Since the motion of a sedimenting disc is quicker in a wetter foam it follows that the drag force exerted by the foam decreases with liquid fraction. This is shown to be the case in figure 3.29(a). Fitting the data to a power-law yields the following relationship between total drag force (F_y) and liquid fraction Φ_l of the foam:

$$F_y = 0.915\Phi_l^{-0.247} \, . \tag{3.8}$$

For comparison with the work of Raufaste *et al.* [77] and a more detailed investigation of the foam's response, the relations of network and pressure contributions to the drag force with liquid fraction are considered separately in figure 3.29(b). It can be seen here that it is the network contribution to the drag force that decreases with a non-linear relation to the foam's liquid fraction. The data for the network drag versus the foam's

liquid fraction is best fitted to a power-law curve that is given by

$$F_y^n = 0.390\Phi_l^{-0.363} \, . \tag{3.9}$$

This is shown to be in good agreement with the relation derived by Raufaste *et al.* for the network drag force exerted on a fixed obstacle in a constant (slow) velocity flow of foam. The same figure shows that the pressure contribution to the drag does not vary much with liquid fraction. The data relates the pressure contribution to the drag to the foam's liquid fraction by the equation

$$F_y^p = 10.84\Phi_l + 0.626 \, . \tag{3.10}$$

The slight linear increase in the pressure contribution to the drag as the liquid fraction of the foam is increased is minimal when compared to the decrease experienced in the network contribution. For the ranges of the liquid fractions considered in these simulations, the elongation of bubbles in the wake of the disc and the squeezing of bubbles in front of the disc remains relatively unaffected by a change in the T1 criterion for the foam. In this case, the pressure contribution towards the total drag force is not greatly affected by variations in Φ_l.

It has therefore been shown that changing the liquid fraction of the foam yields similar results for the case of a sedimenting disc as it did for a constant velocity flow experiment past a fixed circular obstacle [77]. The network drag (F_y^n) decreases with a similar power-law coefficient in both cases. Due to the similarities between both experiments, this relation is to be expected.

3.8 Does a "Negative Wake" Exist in a Dry Foam?

The negative wake is a flow phenomenon of complex fluids such as foams [48]. It describes the flow of fluid in an opposite direction to the bulk flow in the wake of the obstacle. In the case of a sedimenting object, such a flow would be in the upwards

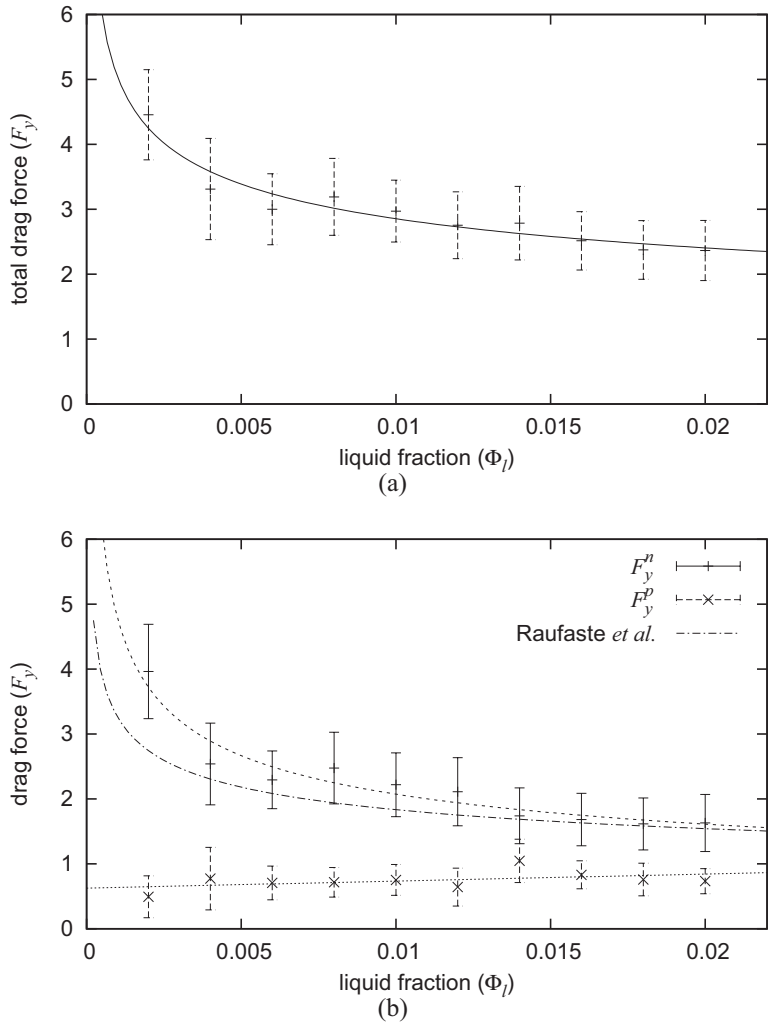

Figure 3.29: (a) The relation between the total drag force exerted on a disc (of area $4Ab$, weight $mg = 10$ sedimenting in monodisperse foam B) and the foam's liquid fraction Φ_l. The total drag force is seen to decrease with increasing liquid fraction with the power-law relation $\Phi_l^{-0.247}$. (b) The separate relations of the network and pressure contributions to the drag force with the foam's liquid fraction Φ_l. The relation between the network drag force and the liquid fraction of the foam yields similar power-law relation to (3.1), derived by Raufaste *et al.* [77] for a fixed disc in foam flow. The pressure contribution to the drag force increases slightly with the liquid fraction of the foam.

direction in the wake. It is a property of shear thinning fluids and is shown to occur in foams in the two dimensional experiments of Dollet and Graner [51].

The results provided on the displacement field in a foam as a disc sediments shows some evidence for the negative wake (see figures 3.12 and 3.13). It can be seen in these figures that some of the arrows in the disc's wake denoting the bubble displacements are directed in the upward direction. Here, the reasons for the existence of the negative wake in our simulations are discussed.

The deformation of the foam in the wake of the disc was discussed in detail in section 3.3 and more specifically in figure 3.6. Here, it was shown that T1 events happen at the back of the disc resulting in bubble detachments from the disc itself. The question is whether this detachment of bubbles results in a local region of foam flowing upwards? It is believed that if many T1s occur consecutively here then some negative flow is probable. In this case the size of the disc relative to the bubbles is a factor that will affect this negative flow. A bigger disc results in more T1s at the back of (or above) the sedimenting disc. Thus the accumulation of plastic rearrangements in the wake of large discs results in a negative wake. However, the negative wake is not seen at all instances during sedimentation. It is often seen that after a few T1s happen in the wake, the foam is stable for a short period where rearrangements are minimal and the bubbles elongate elastically. During this period no T1 events occur in the region and the foam flows in the same direction as the disc. The elongation of the bubbles reaches a stage where T1 events are triggered again in this region and the elongated bubbles detach from the disc. This, yet again results in a small negative flow in the wake. This description for the foam flow in the wake of the disc follows a cycle; in which case the negative wake appears and disappears repetitively during the sedimentation of a circular disc.

The existence and nature of such a negative wake is dependent on many factors such as the disc size and the liquid fraction of the foam as well as the polydispersity of the foam. It has already been discussed that the greater the disc size is, then the more consistent the negative wake of the foam becomes. It is expected that the wetter the foam is, the smaller the negative flow is in magnitude. It is expected that a negative

wake will vanish for a wetter foam than studied in this work as it has been shown to be controlled by the foam's elasticity. Increasing the dispersity of the foam should have minimal effect on whether the negative wake exists. However, a negative wake will be more inconsistent with increasing polydispersity as is it predicted to be related to the local distributions of bubble sizes.

3.9 Concluding Remarks

The sedimentation of a circular disc through an elasto-plastic dry two dimensional foam yields information on the response of the foam. Let us briefly summarize the results obtained in this chapter.

The maximum disc weight that a foam can support was found to increase affinely with disc diameter. It decreases with the liquid fraction of the foam with a power-law relation. For the rest of the work presented in this thesis, the disc weight chosen is much greater, ensuring that the objects descend through the foam at a steady rate. The forces exerted by the foam on a sedimenting disc were studied in detail. Fluctuations in the network and pressure contributions to the drag and lift force were shown to be the result of variations in the local structure of the foam surrounding the disc.

The lift force was shown to be negligible when the disc sedimented centrally in the channel. However, this was not the case when the disc was in close proximity to a vertical wall. In this case, an attractive force exists between a sedimenting disc and a wall if and only if the disc is within a critical separation of the wall. It was found that the disc migrates towards the wall when positioned further than two bubble diameters from that wall. This corresponds to the results of Feng *et al.* [44] and Binous and Phillips [45] who studied the wall effects for a sphere descending in a viscoelastic fluid.

The bulk of the work presented in this thesis investigates the sedimentation of objects from a central position in the channel. This scenario is considered for discs of different sizes and foams with different liquid fractions. The relation of the network and pressure contributions to the drag force exerted on a disc with these control parameters were studied in detail.

It was shown that the network contribution to the drag was typically three to four times greater than the pressure contribution. This corresponds well with the results obtained by the experiments of Dollet *et al.* [75, 76]. Both the network and pressure contributions to the drag force were shown to increase affinely with the disc diameter. The network contribution decreases with the liquid fraction of the foam with a power-law relation that corresponds well with the results of Raufaste *et al.* [77].

The work presented in this chapter provides the basis for further study of the effect of foam rheology on the sedimentation and interaction of more than one circular disc (chapters 4 and 5) as well as an elliptical object (chapter 6).

Chapter 4

Two Discs Sedimenting and Interacting in a 2D Foam: Configuration 1

4.1 Introduction

The investigation of foam response to the sedimentation of a circular disc (chapter 3) is expanded by the introduction of a second disc in the foam. In this chapter, the sedimentation and interaction between two circular discs initially placed side by side in the foam channel is studied. This orientation of the discs is denoted by configuration 1 throughout the work. This is another variation of the Stokes experiment, discussed in section 1.9 and has been scarcely used within the foam community. Here, we aim to improve the prediction of foam response by studying the interaction between two discs. The concepts discussed in chapter 3 form the basis to the arguments presented in this chapter. Similarly, another initial orientation where the two discs are initially placed one above the other in the foam is discussed in chapter 5. This orientation is denoted by configuration 2 throughout.

Similar experiments have been performed on other fluid materials in the past. It has been shown that in a viscoelastic fluid, light spherical particles in this configuration rotate about one another into a stable orientation where they are positioned one above the other (in configuration 2) as they sediment [56, 60, 44, 37]. Particle interaction of

this kind is seen to a lesser extent in viscoplastic fluids [58, 59]. The existing work on sedimentation and interaction of spheres in these fluids is discussed in greater detail in section 1.9.4. In this chapter, disc-to-disc interaction in an 2D dry foam (modelled as an elasto-plastic fluid) is used to quantify the role of elasticity and plasticity in the foam's response.

During the sedimentation process, the motion of each disc is tracked as their centre point coordinates (x_1, y_1) and (x_2, y_2) are recorded at every iteration. The interaction between the discs is quantified by how their separation (d_1) and angle of orientation (θ) varies during the sedimentation process (see figure 4.1). The separation d_1 between the discs is given by

$$d_1 = \sqrt{(x_1 - x_2)^2 + (y_1 - y_2)^2} - 2r_0 \,, \tag{4.1}$$

where r_0 denotes the radius of both discs. The orientation of the two discs relative to each other is measured by the angle θ which is given by

$$\theta = \tan^{-1}\left(\frac{y_2 - y_1}{x_2 - x_1}\right) . \tag{4.2}$$

As in the one disc case, the drag (F_y) and lift (F_x) force exerted on the discs during sedimentation are measured. Recall that the drag force is the force directed vertically and is resistive to the downward motion of the discs while the "lift" denotes a lateral force. Control parameters such as the initial separation between the discs (d_1^{init}) and disc area (A_d) are varied with the aim of qualitatively describing how the foams rheology is influencing the interaction and general motion of the two discs.

4.2 Reference Simulation for Configuration 1

The test simulation in this case is similar to that used for the one disc case. Foam A is used with the liquid fraction set to $\Phi_l = 3.7 \times 10^{-3}$ and the discs are of size $A_d = 4A_b$. Each disc weighs $mg = 10$. This weight was previously shown (§3.2) to be adequate to ensure steady motion of the discs through the foam. The discs are initially placed adjacent to each other (and equidistant to the vertical centreline of the

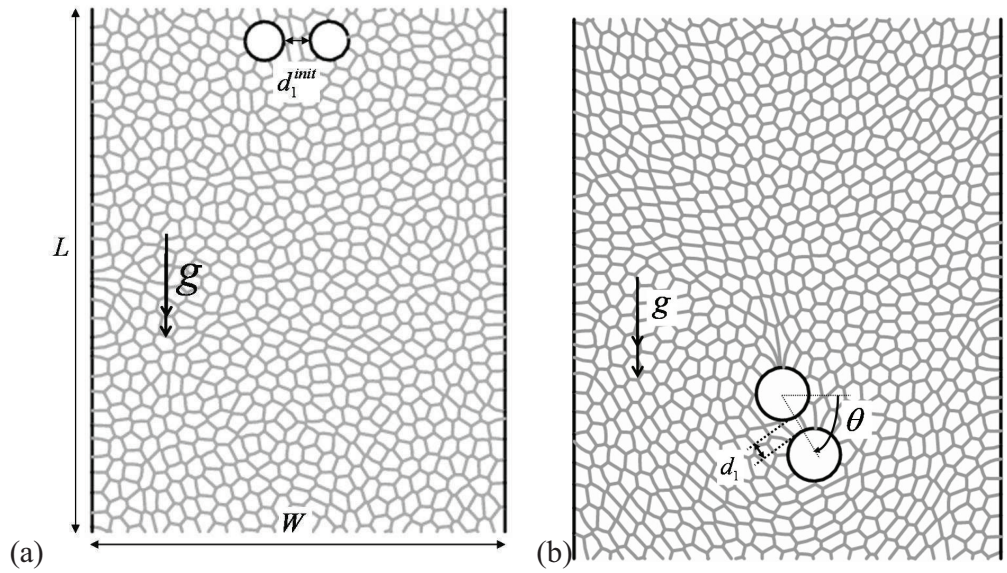

Figure 4.1: The setup of the simulations presented in this chapter is such that (a) two discs are initially positioned side-by-side separated by d_1^{init} in a 2D foam. Disc 1 denotes the disc initially on the left hand side, while disc 2 denotes the disc on the right hand side. Their centre point coordinates are denoted by (x_1, y_1) and (x_2, y_2) respectively. (b) The angle θ defines the orientation of the two discs relative to each other (see (4.2) for definition). In this case θ is initially zero for configuration 1.

channel) at the top of the channel with a separation of roughly $1d_b$ (where d_b denotes the average bubble diameter). This initial configuration is shown in figure 4.2. Since their placement is symmetric about the centre line of the channel, the distance of either disc from the nearest wall is equal (the discs centre points lie at $(0.49W - r_0, 0.1L)$ and $(0.51W + r_0, 0.1L)$). The wall to disc distance is also sufficient so that the wall effects on the motion of the discs is negligible. This was shown to be the case in section 3.4 and is discussed in section 4.6 in this chapter.

The motion of each disc is tracked from this starting position until either disc has reached the bottom of the foam channel. Figure 4.3(a) demonstrates that the variation in the separation of the discs (d_1) during this descent is fairly constant. They stay within a distance of $1d_b$ to $2d_b$ apart. In contrast, the angle θ between the discs changes dramatically during the sedimentation process (figure 4.3(b)). It is shown that the angle θ decreases towards a plateau value at $\theta = -\frac{\pi}{2}$. In this case, the two discs have rotated about one another such that disc 1 (initially on the left hand side) is directly below disc

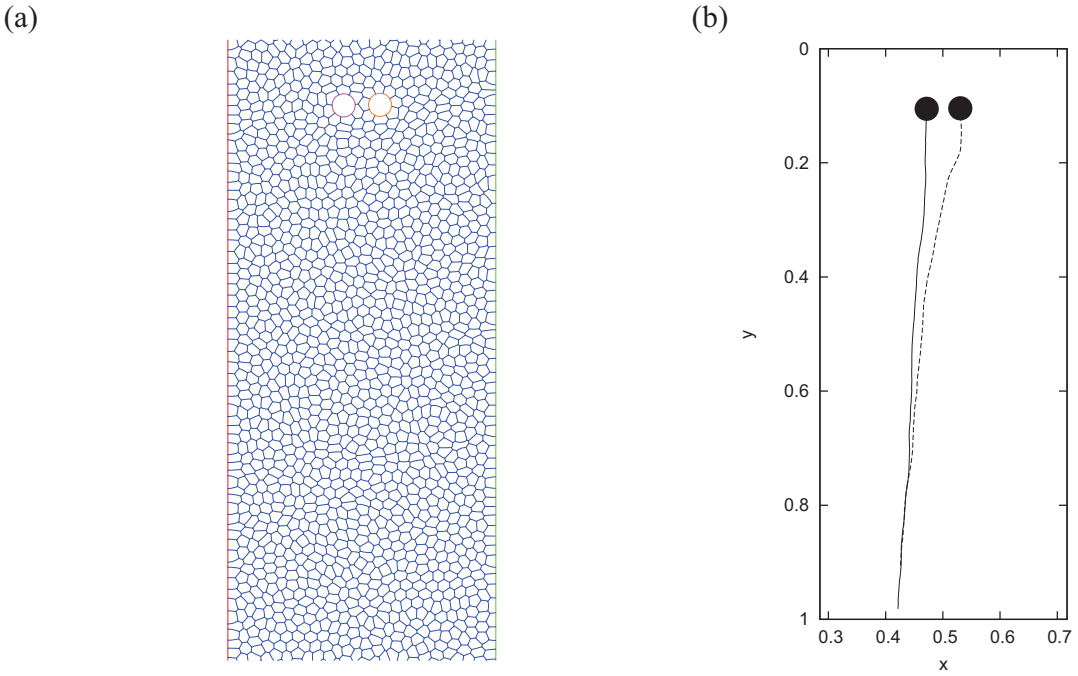

Figure 4.2: The reference simulation for configuration 1. (a) Initial position of the discs side by side at the top of the foam channel is such that the centre coordinates of disc 1 and disc 2 are at $(0.49W - r_0, 0.1L)$ and $(0.51W + r_0, 0.1L)$. They are separated by $1d_b$ and their line of centres is parallel to the horizontal x-axis. (b) The discs' centre coordinates (x_1, y_1) and (x_2, y_2) are tracked as they sediment and the interaction is quantified by the variation in separation d_1 and angle θ.

2 (initially on the right hand side). In this case, the line of centres of the discs becomes parallel to the direction of gravity during sedimentation. This is the orientation denoted by configuration 2.

The drag and lift forces exerted on both discs by the foam during the sedimentation process is demonstrated in figure 4.4. These forces were investigated in detail for a single disc sedimenting through the foam (chapter 3). Here, patterns and correlations between the forces exerted on each disc, yields information on the amount of interaction that occurs during sedimentation.

The drag force is seen to overshoot for one of the discs early on in the simulation (figure 4.4(a)) which results in slower downward motion of the disc, whence it is left trailing. In response to the drag overshoot, an increase in the lift force is seen for the same disc (figure 4.4(b)). This is directed towards the other disc, thus the trailing disc moves into the wake of the leading disc. In this case, the discs begin to rotate about

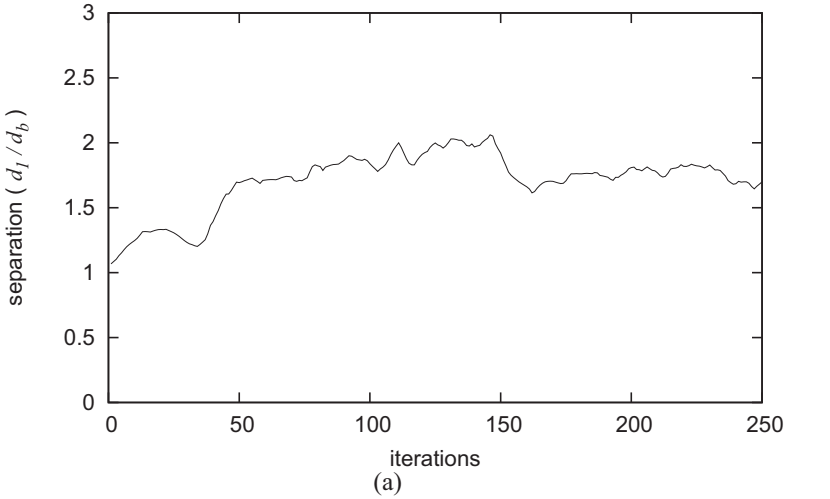

(a)

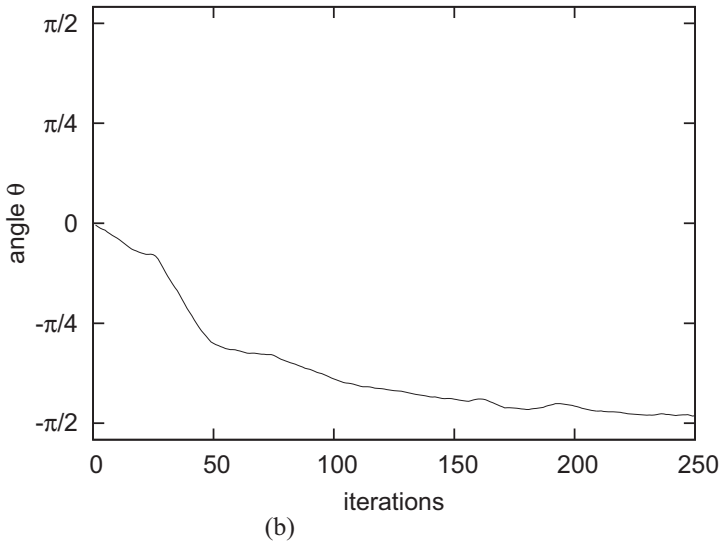

(b)

Figure 4.3: The interaction between the discs is investigated by measuring (a) the separation (d_1) and (b) the angle θ as they descend through the foam. In this case, the discs stay close together with d_1 only varying between $1d_b$ and $2d_b$ throughout the sedimentation. They rotate about one another until the angle between their line of centres and the horizontal x-axis reaches $\theta = -\frac{\pi}{2}$. That is, they prefer to sediment one above the other in the foam. Thus, the initial configuration of the discs was unstable and it is proposed that configuration 2 is a stable orientation for the two discs.

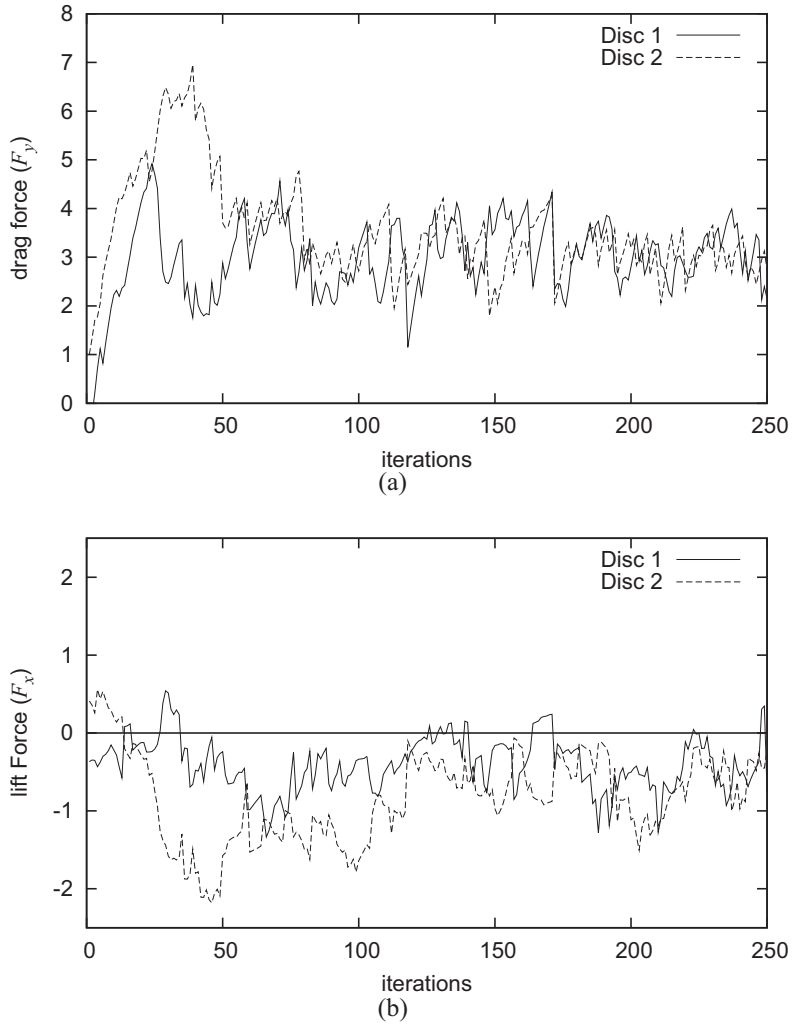

Figure 4.4: (a) The drag F_y and (b) lift F_x force exerted on the two discs as they sediment and interact in the reference simulation. An overshoot in the drag force on one disc occurs between the 25*th* and 50*th* iteration which initiates the rotation of the two discs about one another. In response, a negative lift force is exerted on the same disc between the 25*th* and 100*th* iteration. In this case, disc 2 trails disc 1 and moves laterally into the wake of disc 1.

one another to a more elastically favourable configuration where the deformation of the foam is reduced. After full rotation into configuration 2 has occurred, the drag and lift forces on both discs become very similar and thus the motion of the discs becomes stable.

Placing the discs side by side in configuration 1 is seen to be an unstable orientation; they will rotate about one another into configuration 2. This pattern for the motion of

the two discs in the elasto-plastic foam studied here is analogous to what is seen in the literature for viscoelastic fluids. This is discussed in detail in section 1.9.4. In this case, the effect of plasticity on the nature of the sedimentation remains unclear and is investigated further in this chapter.

4.3 Variation of Initial Separation

The initial separation between the discs is expected to have a dominant effect on the interaction during sedimentation. The interaction between discs is expected to be strong if they are close together and weak if far apart. It is investigated whether the discrete nature of the foam results in a sharp decrease in the interaction between the discs as the separation is increased. In other words, does the foam screen the motion of one disc from the other for large disc separations?

Similar foams to those used in these simulations were seen to screen small perturbations (such as enforced T1s) for distances of a few bubble diameters [108]. It is proposed that a critical separation d_1^c between the discs exists. Thus, if discs are closer together than this critical separation sedimentation proceeds as for the reference simulation (§4.2). However, if the discs are further apart than this critical separation, the interaction between them is minimal and in some cases negligible. In this case, each disc sediments independently of the other and their motion is similar to what was seen for one disc sedimenting in the foam (chapter 3).

In this section, the simulation process described in section 4.2 is repeated for various initial separation between the discs. The discs are placed such that their initial positions are both equidistant from the centre line of the foam channel and their initial separation d_1^{init} ranges between $0.5d_b$ and $5.25d_b$.

The variation in disc separation (d_1) and angle of orientation of the discs relative to each other (θ) during sedimentation from all initial separations d_1^{init} is shown in figure 4.5. The variation in the discs' separation is highly dependent on their initial separation (figure 4.5(a)). For discs that are initially close ($0 < d_1^{init} < 4d_b$), there is a tendency for them to move together so that they are separated by $1d_b$ to $2d_b$. (There is one case

here where the discs have moved so close together during sedimentation that they're touching each other, but they then separate and follow the same pattern.)

Discs that are initially further apart than $4d_b$ don't move closer in the same manner. In some cases, these discs move away from each other.

The variations in the discs' separation is highly related to the variations of θ during sedimentation. Figure 4.5(b) demonstrates that the two discs rotate about one another in a clockwise (so that disc 2 is directly below disc 1) or anticlockwise direction (disc 1 lies directly below disc 2) until θ reaches a plateau value at $|\theta| = \frac{\pi}{2}$ i.e. their line of centres is parallel to the direction of gravity. Once the discs are directly one above the other, they stay in this configuration. This is seen to be the case for discs that were initially close together ($0 < d_1^{init} < 4d_b$). Rotation of the system is less apparent for discs that are initially far apart ($d_1^{init} > 4d_b$). In this case, the aforementioned critical separation d_1^c between the discs is roughly $4A_b$.

The existence of a critical separation d_1^c can be visualized clearly when we consider the settling angle of orientation (θ_a) between the discs as they reach bottom of the channel (figure 4.6). Here, the strong relationship between the initial separation of the discs and the settling angle is shown for discs of area $4A_b$ and weight 10 sedimenting in foams A, B, and C with a liquid fraction of $\Phi_l = 3.7 \times 10^{-3}$. In this case, the critical separation was found to be within $d_1^c = (4 \pm 1)d_b$ in the three cases. In this figure, the settling angle θ_a is modelled by

$$\theta_a = \frac{\pi}{4}\left(1 + \tanh\left(\beta\frac{(d_1^c - d_1^{init})}{d_b}\right)\right), \tag{4.3}$$

where $d_1^c = 4d_b$ and the slope is $\beta = N/1000$ which measures the extent to which the plateau has been reached. In this case, the foams B and C although showing the relationship between the settling angle and initial separation, are of insufficient channel length for full rotation of the two discs about one another. It is the data for the longer channel of foam A that best demonstrates how the discrete nature of the foam dramatically effects the interaction between the discs at a critical separation.

The variation in the drag and lift force exerted on each disc as they sediment also

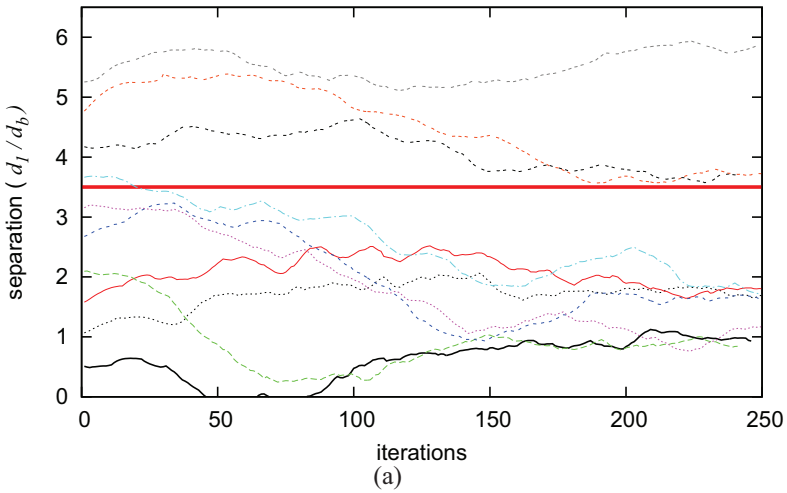

(a)

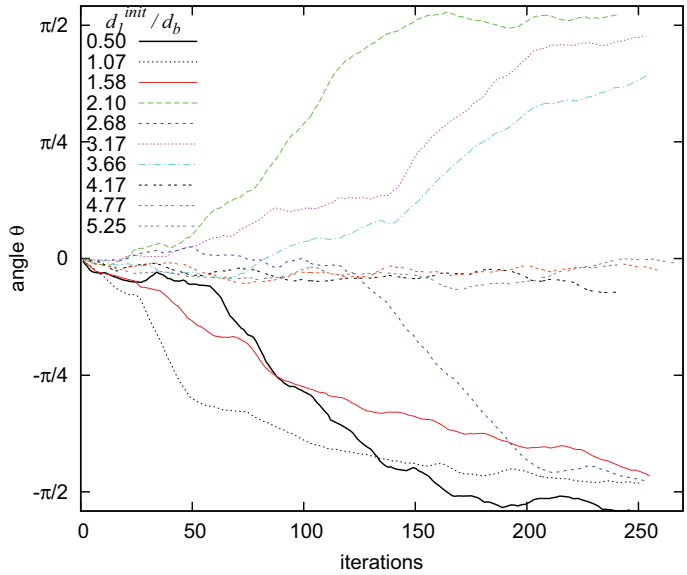

(b)

Figure 4.5: (a) Variation in the separation between the discs of size $4A_b$ and weight 10 as they sediment from configuration 1 at different initial separations (in foam A with $\Phi_l = 4 \times 10^{-3}$). (b) The variation in the angle at which the two discs are oriented relative to each other (θ) as they sediment from the different initial separations (d_1^{init}). The discs move in a different way with respect to each other depending on whether the initial separation is above or below the critical separation $d_1^c = 4d_b$ denoted by the red horizontal line. Discs closer together than this separation rotate about each other into configuration 2 and become terminally separated by 1 or 2 bubbles. Discs that are initially further apart than d_1^c do not rotate about each other and stay far apart. Variations in the separation between the two discs in this case are down to local differences in the order and structure of the foam.

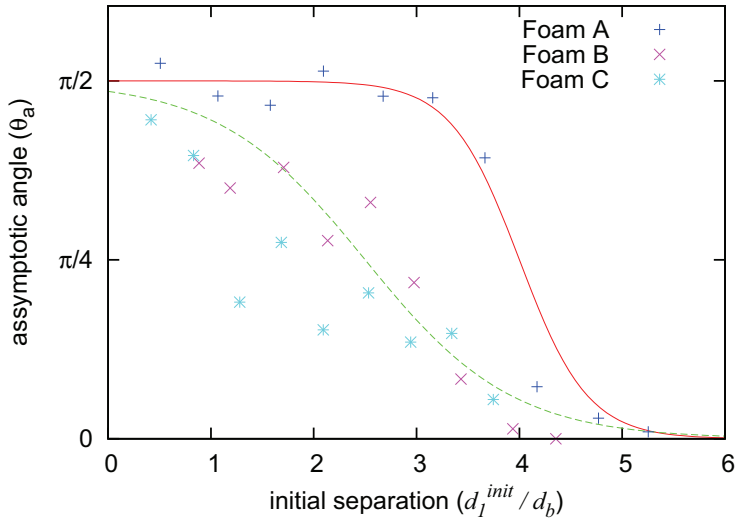

Figure 4.6: The asymptotic angle θ_a is the value that θ takes when one of the discs has reached the bottom of the foam channel (at which point, the simulation is terminated). This settling angle is plotted versus the initial separation d_1^{init} between the discs. The discrete nature of the foam means that a critical separation d_1^c for the discs exists that governs the interaction between them. This critical separation is shown here by fitting the relationship between θ_a and d_1^{init} to a tanh model (4.3). The red line is for foam A where $N = 1500$ while the green dashed line fits the data for both foam B and C. It can be seen that foam B and C are too short for full convergence of the relation between θ_a and d_1^{init}.

indicates how much interaction occurs during sedimentation. In section 4.2, overshoots in the drag and lift force exerted on two interacting discs was seen (figure 4.4). It is shown in figure 4.7 that these overshoots are absent when investigating the sedimentation of two discs placed so far apart ($d_1^{init} = 4.2d_b$) that they don't interact. In this case the forces exerted are similar in nature and magnitude, demonstrating that the motion of each disc is independent of the other. This is expected to be the case whenever the initial separation is greater than the the critical separation d_1^c.

It is proposed that the critical separation between the discs (d_1^c) is dependent on many parameters. Variation of these parameters will affect the response of the foam in the region surrounding the disc. In this case, control parameters such as disc area, foam liquid fraction, bubble area dispersity and disc weight are considered in this chapter. However, before moving on and varying these control parameters, the reasons for the presence of a critical separation need to be explained. This is done by investigating the

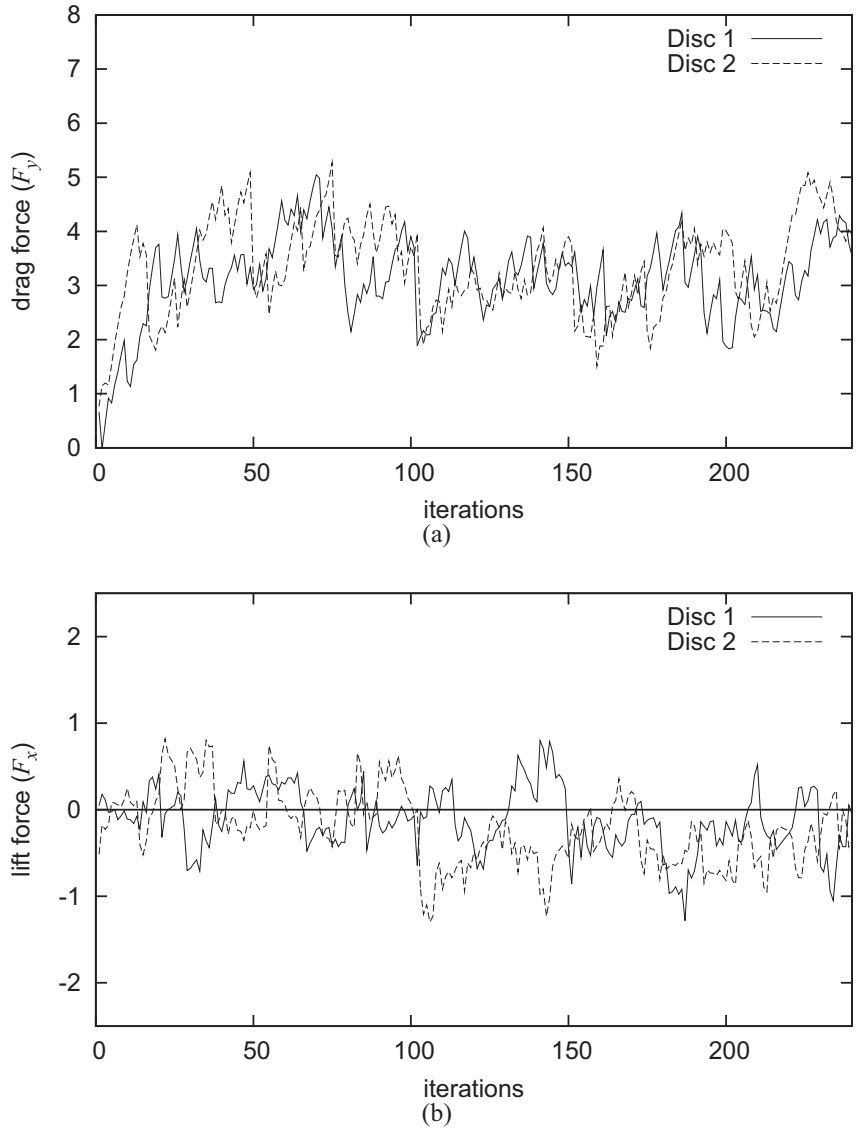

Figure 4.7: (a) The drag force exerted on both discs as they sediment in configuration 1 relatively far apart ($d_1^{init} = 4.2d_b$) in foam A. (b) Variation in the lift force exerted on the same discs as they sediment. The forces exerted on disc 1 are similar to the forces exerted on disc 2 throughout the simulation. The forces exerted on either disc do not respond to each other during sedimentation and are relatively uncorrelated in this respect. This indicates that the discs do not interact.

flow fields of the foam as the two discs sediment.

4.4 Foam Fields

Investigation of fields such as bubble displacement, T1 positions and bubble pressure was introduced for the one disc case in section 3.5. Here, the fluidized region of foam around a disc was defined to be the region where most T1s occur and therefore bubble movement is at its greatest. When considering a disc of size $4A_b$ and liquid fraction of $\Phi_l = 3.7 \times 10^{-3}$, the fluid region was most apparent in the first two layers of bubbles surrounding the disc. In this section, these foam fields are investigated during the sedimentation of two nearby (interacting) discs.

4.4.1 Bubble Displacement

During the sedimentation of two discs it is expected that the flow field of bubbles surrounding each disc influences the interaction between them. If two discs are close together then the fluidized regions surrounding each disc intercept the other. In this case, the two discs are in effect sedimenting within one fluidized region. This results in the discs interacting and rotating about one another into configuration 2.

When the discs are close and interacting, bubbles forced to move by one disc may be influenced by the other disc as well. As in the one disc case (§3.5.1), the bubble centre positions (taken to be the average of the coordinates of the bubble's vertices) are tracked for intervals of 20 iterations. Their displacements during the 20 iterations are represented by arrows.

The displacement field for the foam when two discs sediment from being in configuration 1, initially placed $d_1^{init} = 1.0d_b$ apart is presented in figure 4.8. This is the displacement field for the test simulation described in section 4.2. In this case, the features seen for one disc in section 3.5.1 such as the stagnated bubbles either side of the discs and some evidence of a negative wake above the discs are again evident. The displacement field presented here is similar to that seen for the one disc (figure 3.12)

in that the motion of the bubbles is largely concentrated near the objects. The bubbles displacement displays that bubbles move in response to both discs as they are so close together.

The bubble displacement field when two discs sediment in configuration 1 with an initial separation of $d_1^{init} = 5.25d_b$ is presented in figure 4.9. This separation is above the critical separation (d_1^c) required for interaction between the discs (shown in §4.3). The imposed bubble displacement field yields information and possible reasons for minimal interaction. In this case, the discs stay far apart and the angle θ stays close to zero throughout the descent of the discs through the foam. It can be clearly seen that the bubble displacement field surrounding each disc doesn't intercept the other. In this case the foam screens the flow field imposed by one disc from the flow field imposed by the second disc. Each disc therefore sediments separately in the channel, within separate fluidized region.

It is therefore proposed that the critical separation d_1^c required for interaction of two discs placed side by side is dependent on the reach of the fluidized region surrounding a disc. Thus the critical separation increases with the size of this fluidized region.

4.4.2 Position of T1s

It is known that the plasticity of the fluid is not required to allow the rotation of the orientation between the two discs as they sediment. Here, we investigate the role that a foam's plasticity has on the interaction between two circular discs sedimenting in configuration 1.

As in the one disc case, (§3.5.2) the fluid region where most plastic events happen is close to the discs boundary. Indeed, most T1 events occur directly below a disc, where bubbles are squeezed and forced to move out of the disc's path, or in the wake, where bubbles detach after becoming elongated. It was shown that for the disc and foam parameters considered here, most T1s occur within the first two layers of bubbles surrounding each disc (figure 3.15(b)).

The discs are expected to interact if separated such that the fluid regions around

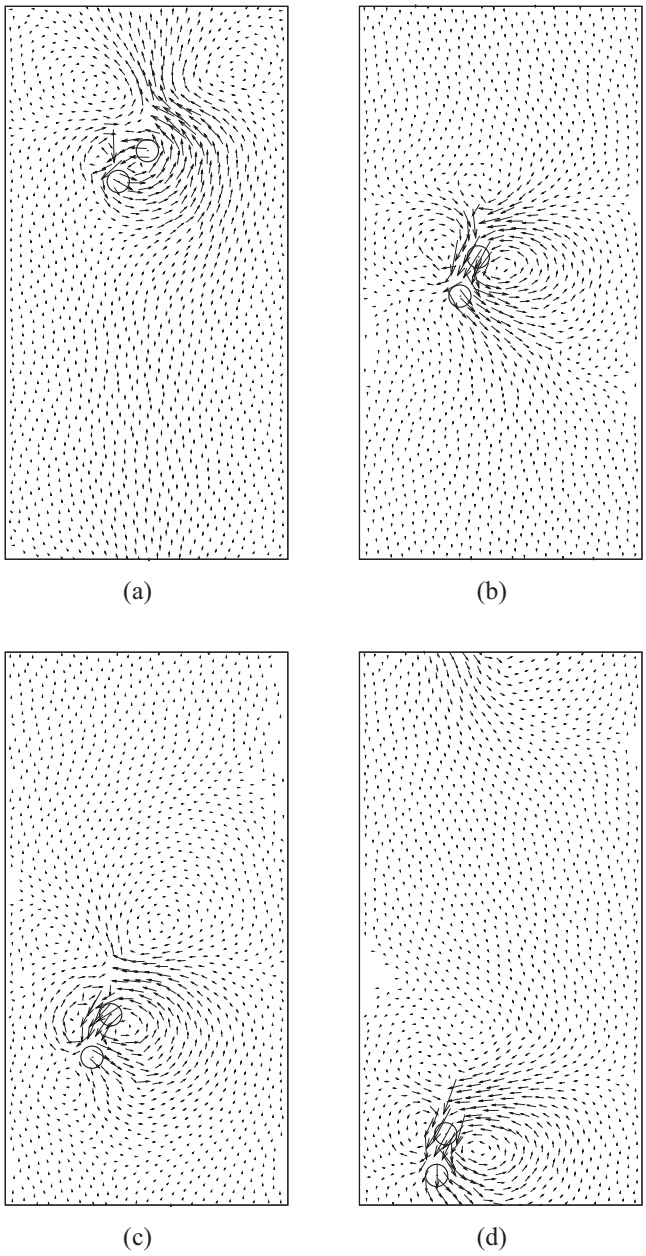

Figure 4.8: The bubble displacement field for foam A (with $\Phi_l = 3.7 \times 10^{-3}$) when two discs sediment in configuration 1 at an initial separation of $1d_b$. The discs interact and rotate about one another into configuration 2. Bubble centre points are recorded every 20 iterations and their displacement during this period denoted by arrows. The displacement fields for (a) $40 - 60$ iterations, (b) $100 - 120$ iterations, (c) $160 - 180$ iterations and (d) $220 - 240$ iterations are shown. It can be seen from all four figures that some bubbles that are very near to the two discs are displaced in response to the motion of both discs. In this case the two discs are so close together that they both apply some stress to the same region of the foam. In this case, the fluidized region surrounding each disc intersects the other and the discs interact.

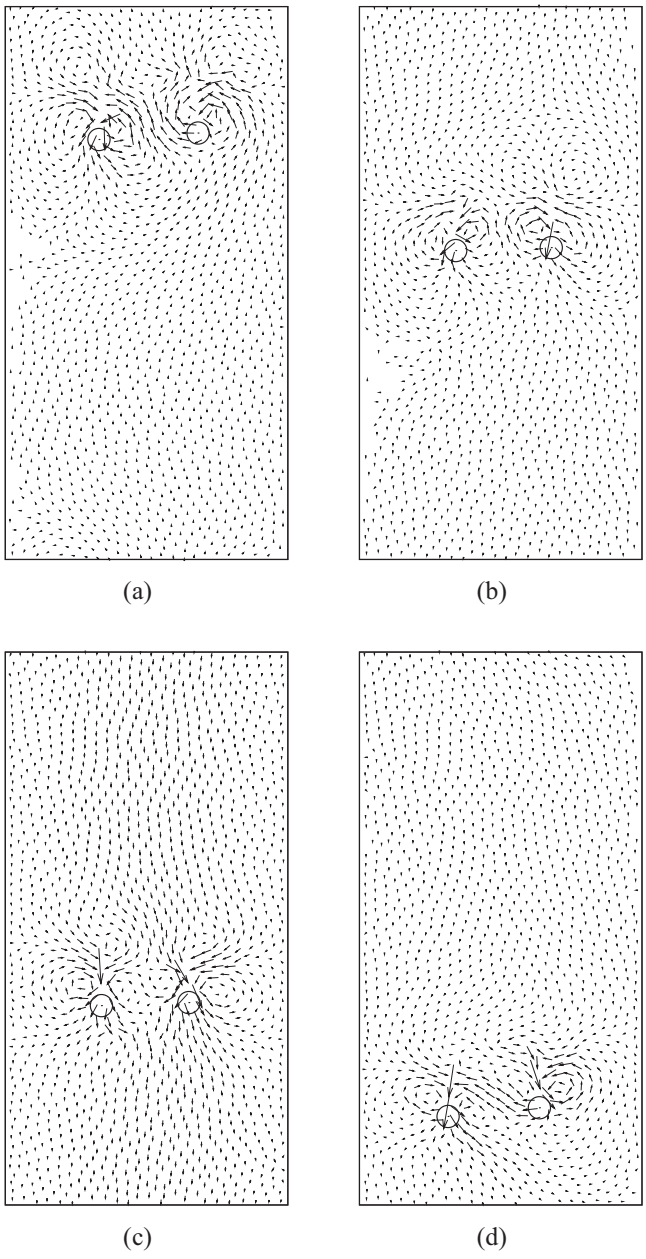

Figure 4.9: The bubble displacement field in foam A (with $\Phi_l = 3.7 \times 10^{-3}$) when two discs sediment in configuration 1 initially separated by $5.25d_b$. Bubble centre points are recorded every 20 iterations and their displacement during this period denoted by arrows. The displacement of bubbles during (a) 20 – 40 iterations, (b) 80 – 100 iterations, (c) 140 – 160 iterations and (d) 160 – 180 iterations. Since $d_1^{init} > d_1^c$, the discs do not rotate about one another to configuration 2. In fact the two discs sediment independently, imposing their own fluidized regions within the foam.

each disc intercept one another. In this case, discs of area $4A_b$ would be expected to interact if their separation was $4d_b$ or less. This corresponds to an initial $2d_b$ range of interaction for each disc. If two discs sediment such that their fluidized regions do not intercept then they will not rotate about one another into configuration 2.

The T1 positions for the sedimentation of two interacting discs and two non-interacting discs are presented in figures 4.10 and 4.11 respectively. It can be seen that for the two discs that are close together, one large fluidized region exists around the two disc system. This is the region where nearly all the T1s occur during sedimentation. Since the discs move in the same fluidized region the rotation of the system into the stable configuration occurs. However, when the discs are far apart, the fluidized regions surrounding the discs are completely separate and each disc sediments without influencing the motion of the other.

4.4.3 Bubble Pressure

Bubble pressure contributes directly to the forces exerted on each disc during sedimentation through the foam. Thus, the bubble pressure field yields further information about how the foam responds to the disc motion. It is possible to decipher more knowledge about a foam's rheology when considering its pressure field when two discs sediment side by side, interacting and rotating about one another.

Figure 4.12 demonstrates the pressure field within foam A for the reference simulation (see §4.2) for the 30^{th}, 100^{th}, 170^{th} and 240^{th} iteration. Bubbles are coloured relative to the difference between their pressure and the pressure of a reference bubble chosen to be far away from the discs. In this case, a blue coloured bubble has low pressure and red represents high pressure (see figure for greater detail). Here, as expected from the one disc case, there exist regions of high pressure under the discs and regions of low pressure in each wake. Here, the two discs are interacting and the pressure field of the foam yields visual evidence of this interaction. There exists a region of high pressure directly in between the discs at all stages of the simulation. Thus, the discs rarely come so close to each other that they're touching during sedimentation.

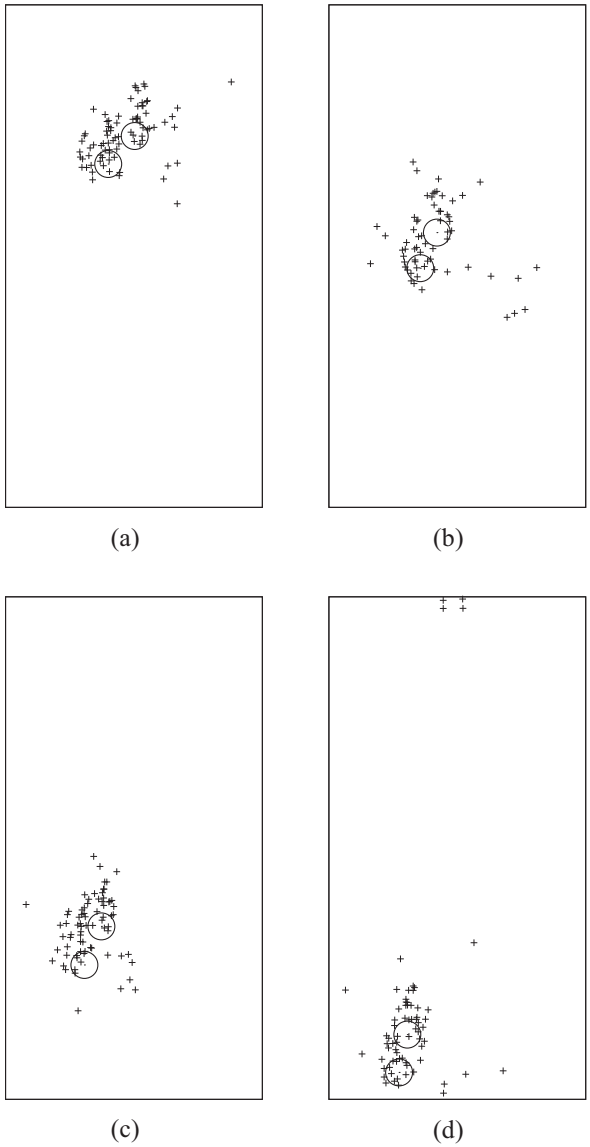

Figure 4.10: The positions of T1 events in the channel as the discs sediment through foam A in configuration 1, initially separated by $1d_b$ are recorded. Each plot shows T1 positions over intervals of 20 iterations at different stages of the simulation: (a) 40 – 60 iterations, (b) 100 – 120 iterations, (c) 160 – 180 iterations and (d) 220 – 240 iterations. The discs interact as they are so close together that one fluidized region surrounds both.

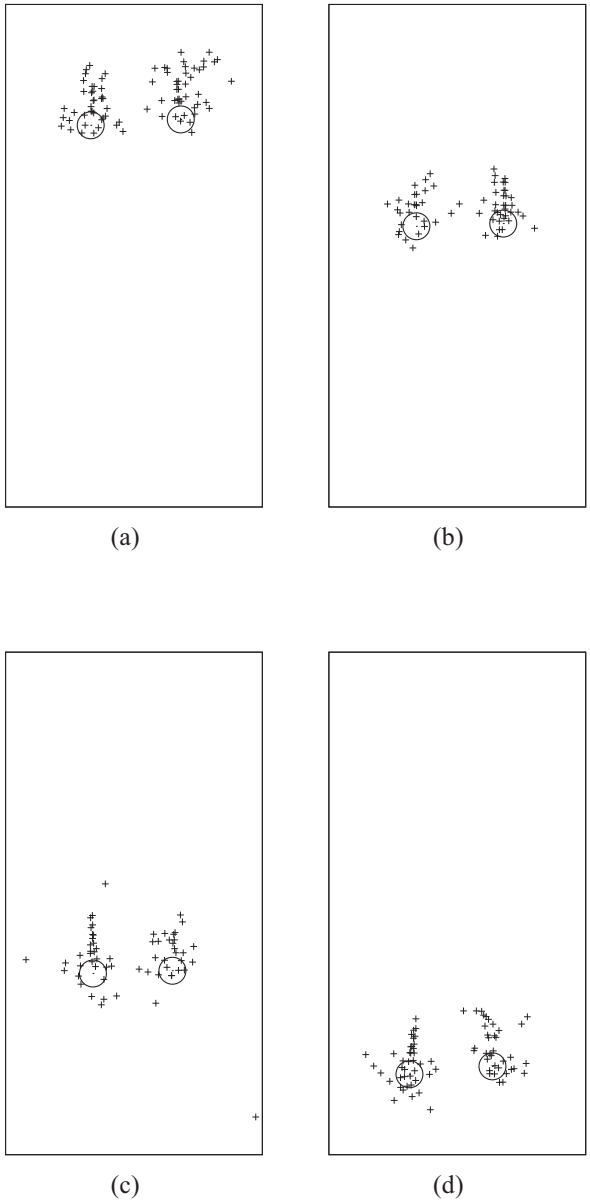

Figure 4.11: The positions of T1 events in foam A when two discs sediment in configuration 1, initially separated by $d_1^{init} = 5.25d_b$ are recorded over intervals of 20 iterations. Each plot shows the T1 positions for (a) 20 – 40 iterations, (b) 80 – 100 iterations, (c) 140 – 160 iterations and (d) 200 – 220 iterations. The discs are initially placed further apart than the critical separation d_1^c, whence the fluidized regions surrounding each disc are separate and interaction is minimal. In this case, the discs sediment independently and θ stays close to zero.

During the initial stages of rotation of the discs about one another, one region of low pressure is seen in the wake of the disc that is left trailing. A region of high pressure exists in front of each disc at this stage. In this case, the pressure contribution to the drag force exerted on this disc is greater, contributing to its slower descent.

The rotation of the discs about one another into configuration 2 is encouraged by the pressure force exerted on each disc. The pressure field either side of the system differs greatly. Here, the two discs rotate about one another in an anticlockwise direction. The foam region to the right of the two discs is of high pressure while the region to the left is of lower pressure. Due to these pressure differences, the trailing disc (that is on the right hand side) is pushed to the left into the wake of the other disc. This continues until the discs are directly above one another in configuration 2.

The pressure field for the same foam but when the discs are too far apart to interact is presented in figure 4.13. Here, the pressure fields surrounding each disc is similar to what was demonstrated when the sedimentation of a single disc through the foam was considered (see §3.5.3). In this case the foam is screening the presence of another disc within the foam. In this case, each disc sediment independently within their own imposed fluidized region.

4.5 Variation of the Bubble Area Dispersity

The bubble area dispersity of the foam was found to be a relatively unimportant control parameter when considering the sedimentation of one circular disc through the foam (§3.6). It's importance is checked for the sedimentation of two discs through the foam. Thus, the simulation process described in section (4.3) for a monodisperse foam is repeated for a polydisperse version of foam A where $\mu_2(A) = 0.428$ (see equation (1.8)). Here the initial separation between the discs of area $4A_b$ (where A_b denotes the average bubble area) and weight $mg = 10$ is varied between $0.5d_b$ and $6.25d_b$ (where d_b denotes the average bubble diameter of the undeformed foam).

The effect polydispersity has on the interaction between the discs for different initial separations d_1^{init} is investigated through comparison of results with the monodisperse

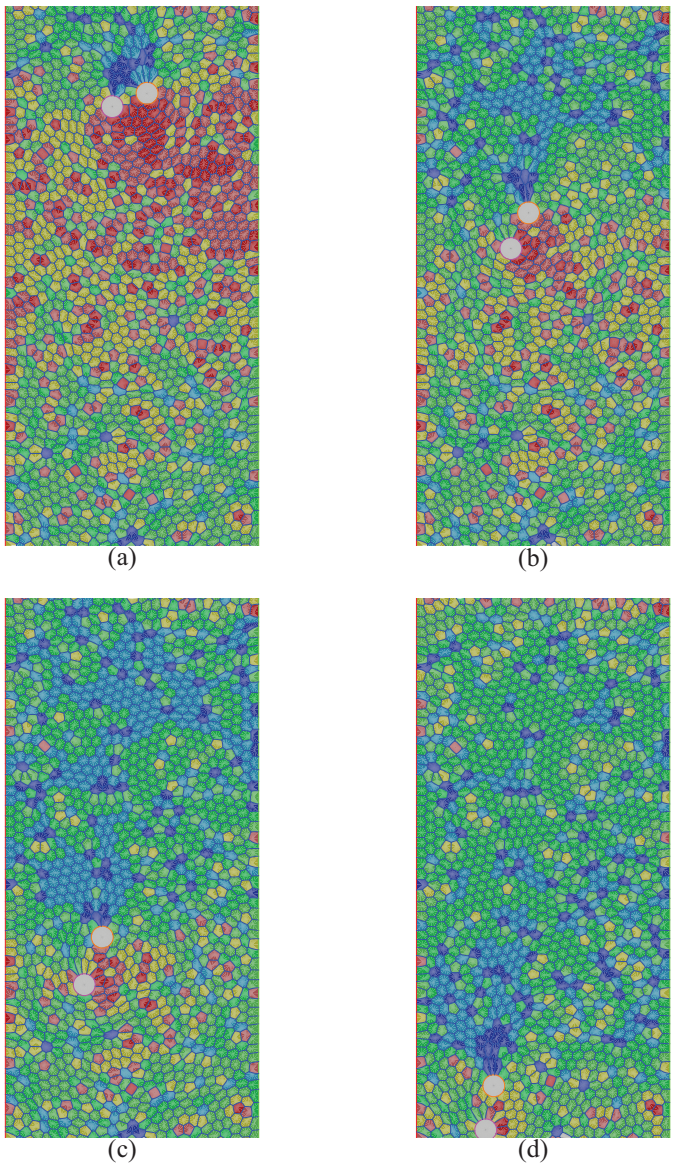

Figure 4.12: The bubble pressure fields as two discs sediment in configuration 1, initially separated by $1d_b$. The bubbles are colour coded depending on the difference between their pressure and a reference bubble chosen to be far away from the discs. Here the pressure increases with the order dark blue, light blue, green, light green, light red to red. Each figure represents the pressure field for the (a) 30^{th} iteration, (b) 100^{th} iteration, (c) 170^{th} iteration and (d) 240^{th} iteration.

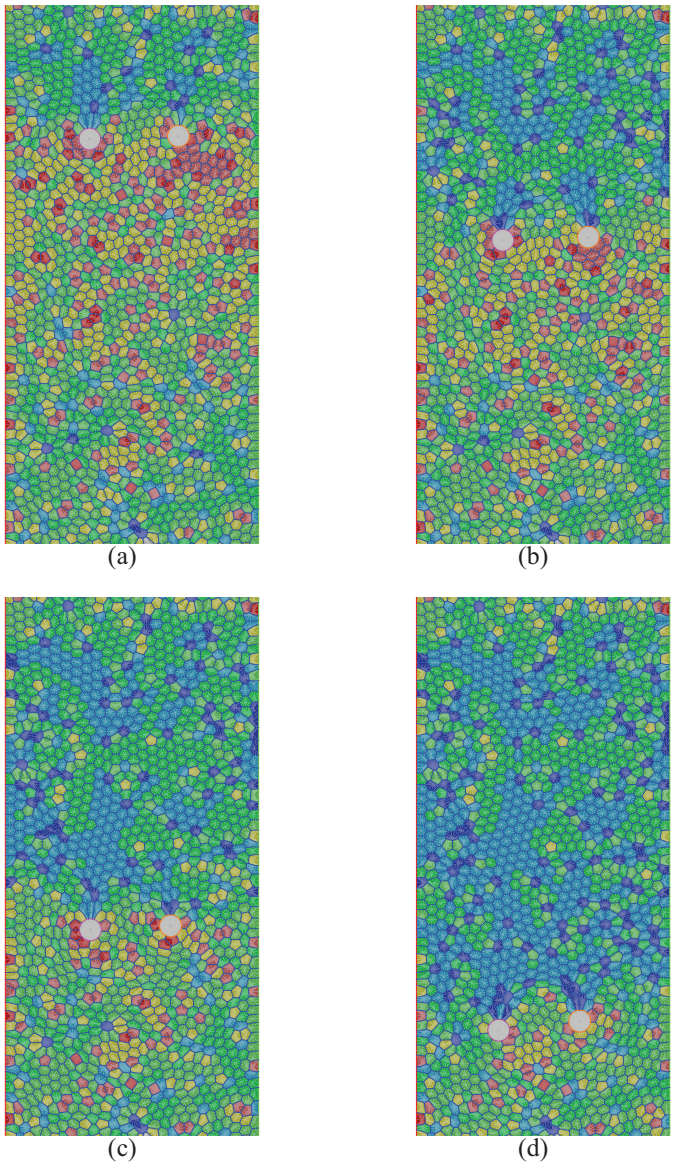

Figure 4.13: The bubble pressure field when two discs sediment through foam A (with $\Phi_l = 3.7 \times 10^{-3}$) in configuration 1 with an initial separation of $d_1^{init} = 5.25 d_b$. This has been shown to be too far for interaction. Again, the bubbles are colour coded depending on the difference between their pressure and the pressure of a reference bubble (chosen to be in a region far from either disc). Here the colour-coding is such that the pressure increases from dark blue to light blue to green to light green to light red to red. Each figure shows the pressure fields for the (a) 50^{th} iteration, (b) 100^{th} iteration, (c) 150^{th} iteration and (d) 200^{th} iteration.

foam. The angle of orientation (θ) between the discs as they sediment from various initial separations is investigated.

It can be seen in figure 4.14(a) that the two discs rotate in the same manner in the polydisperse foam as they did in the monodisperse case (§4.3). An equivalent critical separation d_1^c of roughly $4d_b$ is found for the polydisperse foam (figure 4.14(b)). In this case, the discs rotate about one another into configuration 2 if initially placed closer than this value. Interaction is minimal if they are separated by a distance of more than d_1^c.

It can be seen in 4.14(b) that the increase in the polydispersity of the foam slightly decreases the slope of the graph that relates the asymptotic angle θ_a with initial separation between the discs d_1^{init}. In this case, the rotation of the discs has not fully converged to plateau values of $|\theta| = \frac{\pi}{2}$ (or remained so that $\theta = 0$) as they reach the bottom of the channel. Thus, for full convergence for the settling angle between the discs, one would require longer channels for polydisperse foams. Overall, the sedimentation process on the whole is similar to that seen in monodisperse foams. In this case, other parameters such as disc size are shown to have a greater effect and are of a more immediate interest.

4.6 Wall Effects

So far in this chapter we have assumed that wall effects are negligible. We have considered the sedimentation of two discs within a central region of the channel, i.e. the region between $0.3W$ and $0.7W$. The wall effects have been shown to be negligible within this region when one disc sediments through the foam (see §3.4). However, when a disc is positioned somewhere not in this region, it is expected that its proximity to a wall affects its motion. In the case of one circular disc, it was shown that wall effects occurred due to the fact that the symmetry of the flow of foam close to the disc is suppressed by the wall (see §3.5.1). It is reported in that section that wall effects on a disc can greatly affect its motion. Thus, it is checked whether wall effects are important when considering the interaction between two discs in configuration 1. It is hoped that any wall effects can be neglected and that the interaction between the discs is not a result of

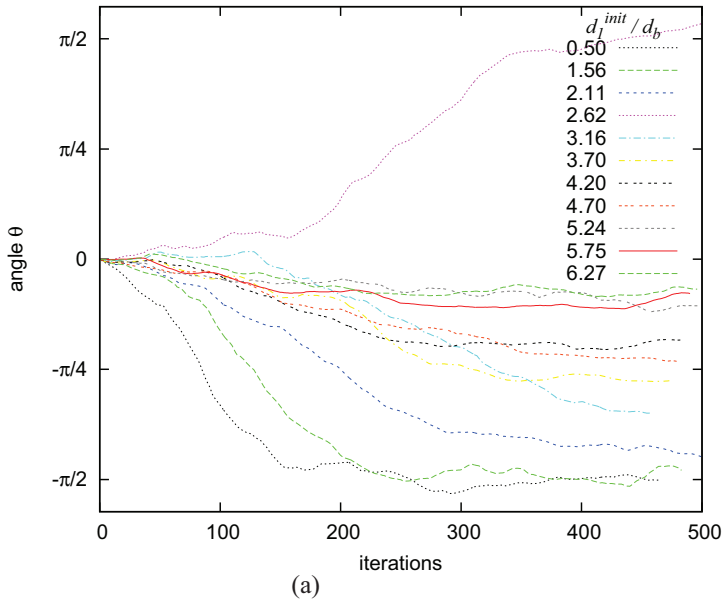

(a)

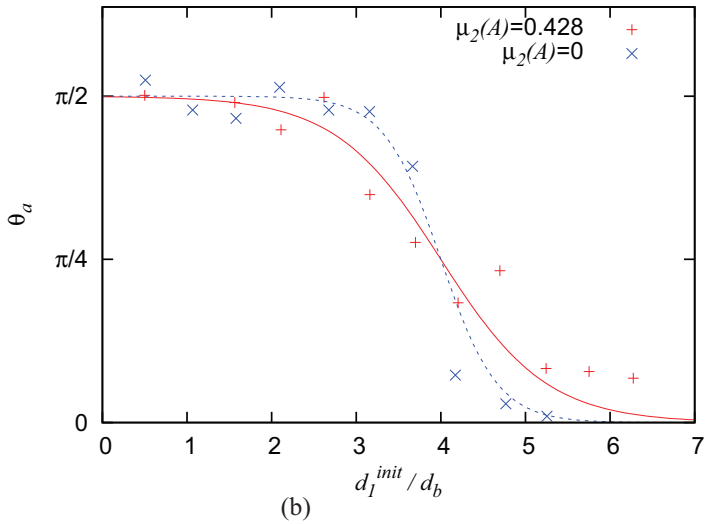

(b)

Figure 4.14: (a) The variation in the angle (θ) at which the two discs are oriented as they sediment from various initial positions from configuration 1 in a polydisperse foam A where $\mu_2(A) = 0.428$. (b) The variation in the settling angle θ_a (the value of θ when either disc reach the bottom of the channel) with initial separation d_1^{init} compared for a monodisperse ($\mu_2(A) = 0$) and polydisperse ($\mu_2(A) = 0.428$) foam. The dependence of θ_a on d_1^{init} is fully converged and clearly demonstrates that a critical separation d_1^c exits in the monodisperse case. The slope of the equivalent relation for the polydisperse foam is smaller and the results haven't converged to such a sharp change in θ_a at the critical separation d_1^c. However, the critical separation is of the same value for both cases and the nature of the interaction between the discs is very similar.

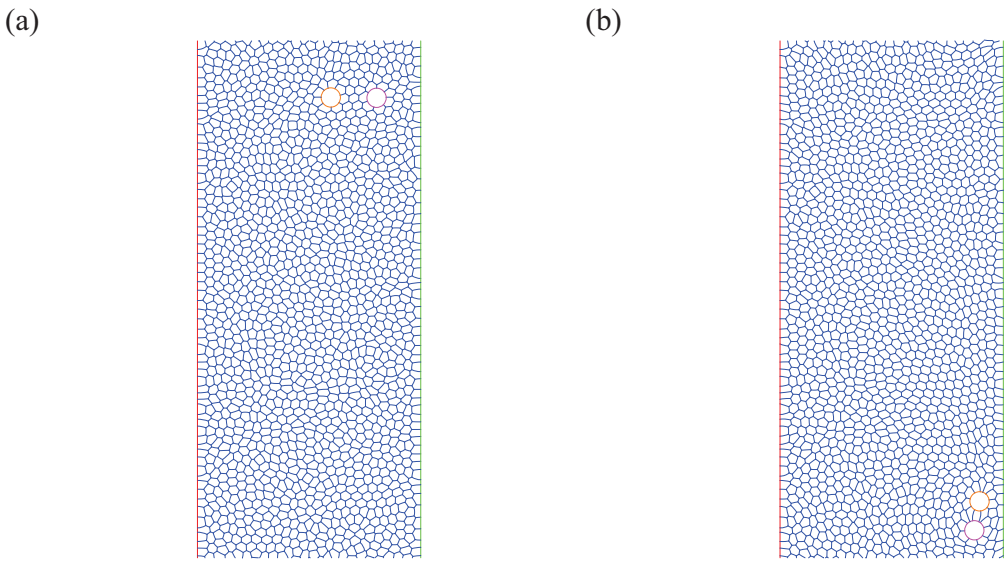

Figure 4.15: (a) Initial position of the discs placed in configuration 1 in $P2$. In this case, discs 1 and 2 have their centre point coordinates at $(0.6W, 0.1L)$ and $(0.8W, 0.1L)$ respectively. (b) The positions of the same discs as they reach the bottom of the channel. The discs have rotated about one another into configuration 2 even under the influence of the nearby wall. Here, the disc that was initially closest to the right hand wall leads the other discs as they reach the bottom of the foam channel. This is shown not to be the rule for similar simulations.

the boundaries.

In this case the discs are initially placed side by side at the top of the channel in an off-centre position. The initial separation between the discs is kept constant at $d_1^{init} = 2.5d_b$. Four different initial positions are chosen for the two discs. The initial placement $P1$ is such that one disc is placed such that its centre coordinates (x_1, y_1) lie at $(0.2W, 0.1L)$ while the other disc is positioned at $(0.4W, 0.1L)$. Similarly, position $P2$ is such that disc 1 is placed at $(0.6W, 0.1L)$ and disc 2 at $(0.8W, 0.1L)$. Thus, $P1$ and $P2$ are equivalent positions on the left and right hand side of the foam channel. Similar equivalent positions are taken by $P3$ and $P4$ where discs are placed at $(0.25W, 0.1L)$, $(0.45W, 0.1L)$ and $(0.55W, 0.1L)$, $(0.75W, 0.1L)$ respectively.

The initial positions of the discs placed in $P2$ and the resulting settling orientation of the discs is shown in figure 4.15. It can be seen here that the nearby wall has not changed the essential feature of interaction between the discs since they have rotated about each other in the same manner as seen for previous central initial placements.

The variation in the angle of orientation (θ) of the two discs and the separation d_1 as they sediment from all four positions is shown in figure 4.16. Here, it is seen that the discs rotate about one another into configuration 2 from all four initial positions. It is also clear that the direction of rotation is independent of whether the discs are closer to the left or right wall. For example when the discs are placed in position $P1$, the leading disc at the bottom of the channel is disc 2, i.e. the disc that was initially furthest from the left hand wall. Similarly for discs initially placed in position $P2$, the leading disc at the bottom of the channel is disc 2, i.e. the disc that was closest to the right hand wall. In this case, the nearby wall does not decide which disc will trail the other during the change of orientation into configuration 2, thus it is the local structure of the foam that determines the motion.

The variation in the separation d_1 is similar in nature to what was seen for two discs sedimenting in the same configuration within a central region of the channel (see figure 4.5(a)). In this case the discs are expected to interact such that they rotate about one another and move together so that they're separated by one to two bubbles. This is the case in three out of the four simulations. In the fourth case ($P4$), the discs have moved away from each other so that they're separated by 5 to $6d_b$ at one stage during the simulation. However, it can be seen towards the end of the plot in figure 4.16(b) that this separation is decreasing. It can be seen in figure 4.16(a) that by this time, the angle of orientation between the discs is reaching $\theta = -\frac{\pi}{2}$, whence they are approaching configuration 2. In this case the wall has contributed to delay the interaction between the discs as they sediment. The direction to which the orientation between the discs rotates is independent of the whether the discs sediment closer to the left or right hand wall. In other words, the leading disc at the bottom of the channel can either be the disc that was initially closest to a wall or not.

It is therefore the case that wall effects have a minimal influence on the interaction between two discs sedimenting in configuration 1. The two discs continue to rotate about one another even when placed close to either wall. The proximity of the discs to a wall does not determine the direction to which they rotate about one another. The only effect on disc interaction seen due to the walls was a delay in the two discs reaching

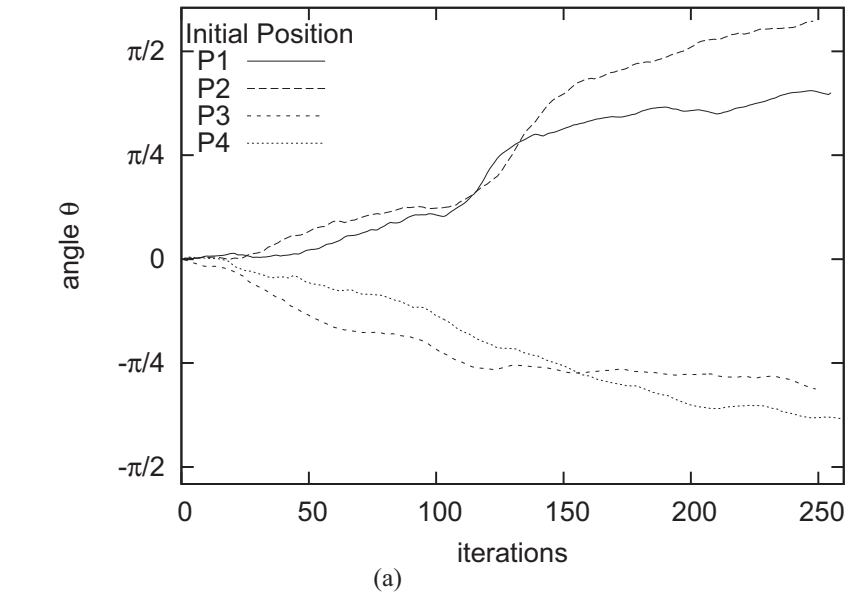

(a)

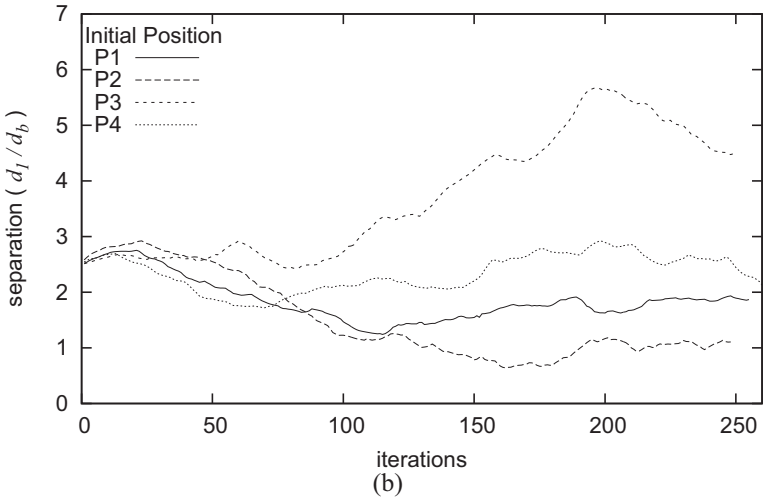

(b)

Figure 4.16: (a) The angle θ and (b) separation d_1 between the discs as they sediment side by side from four off-centre initial positions $P1$, $P2$, $P3$ and $P4$ (see text - §4.6 for details). The discs rotate about one another regardless of the proximity of one disc to a wall. Their variation in separation is also similar to what was seen for discs sedimenting in configuration 1 centrally in the channel.

their stable orientation (in one case). However, the interaction between the two discs is not suppressed by the nearby wall. Moreover, the results presented in this chapter are not due to the nearby boundaries.

4.7 Variation of Disc Area

The size of the discs is expected to be an important parameter that will influence the critical separation d_1^c that decides whether two discs in this configuration interact or not. In this case, the simulations of section 4.3 (where the initial separation between the discs is varied) is repeated for discs with area 2, 6, 8 and 10 times the bubble area. Foam A is used for the discs of sizes $2Ab$ and $6Ab$. However, it became clear that a longer channel was required to demonstrate the interaction between the larger discs ($8A_b$ and $10A_b$), and in this case foam D is used for these discs. A consistent liquid fraction of $\phi_l = 3.7 \times 10^{-3}$ is chosen for both foams.

It is shown in figure 4.17 that the interaction between the two discs is of the same nature for the range of disc sizes considered here. The size of the fluidized region surrounding a disc was shown to increase with disc size (see §3.5.2). Bigger discs apply greater stress to a larger region of the foam than smaller discs. Therefore, one would expect T1s to occur more frequently in regions further away than the first two layers of bubbles surrounding the disc. Bigger discs are also expected to impose greater bubble motion within this fluidized region and should have more effect on far field bubble pressure. In this case, it is to be expected that the critical separation between the discs increases with disc size.

Figure 4.17 demonstrates the variation in the settling angle (θ_a) between the discs with initial separation (d_1^{init}), for the disc sizes used. This asymptotic angle is fitted by a tanh function (4.3) of the initial separation for all disc sizes. It can be seen that a critical separation that determines whether the discs interact exists in all cases. The variation of the critical separation with disc area is presented in figure 4.18. It is seen that this critical separation increases affinely with the disc size.

The interaction process between the two discs is the same for discs sizes ranging

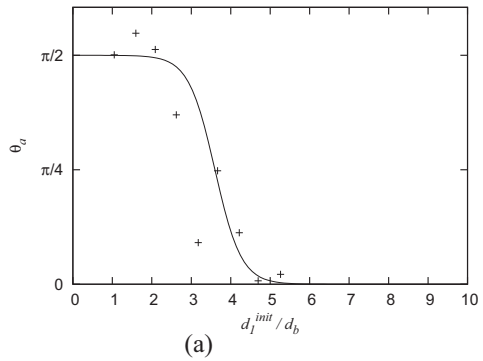

(a)

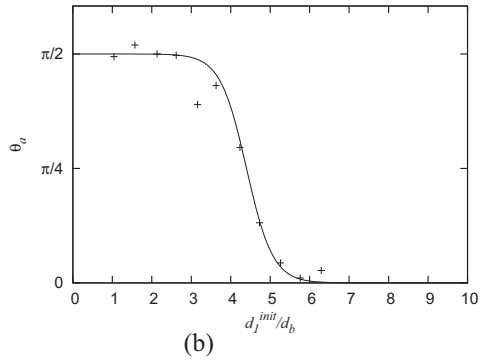

(b)

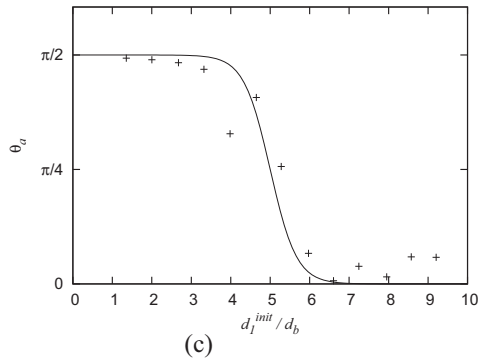

(c)

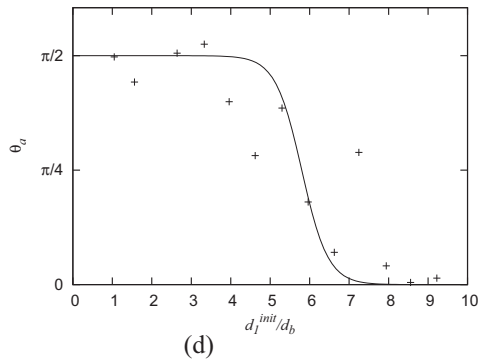

(d)

Figure 4.17: The variation of the settling angle θ_a with initial separation d_1^{init} for discs of size (a) $2A_b$, (b) $6A_b$, (c) $8A_b$ and (d) $10A_b$. A critical separation d_1^c exists for all disc sizes considered. Its value increases with the size of the discs.

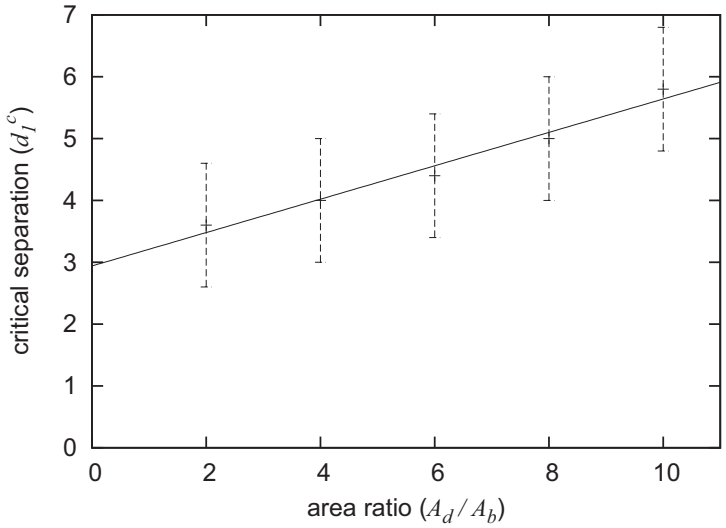

Figure 4.18: The critical separation d_1^c (with $\pm 1 d_b$ error bars) increases affinely with disc area. It is therefore proposed that the width of the fluidized region surrounding a disc increases in the same manner.

from $2Ab$ to $10Ab$. They all rotate about one another so that they move from being placed side by side in an unstable configuration towards the more stable configuration where their line of centres is parallel to their direction of motion. The critical separation d_1^c that decides whether the discs interact or not is shown to increase affinely with disc area. In this case, it is proposed that the horizontal reach of the fluidized region of foam surrounding the disc increases affinely with disc area.

4.8 Discussion

4.8.1 Effect of Disc Weight on Interaction

The fluidized region surrounding a disc is a result of applied stress exerted by the geometry of the object (see §3.5). Thus, it is dependent on the size of the disc. Variation of the disc's weight is considered in this work to be less interesting. It is to be expected that the size of the fluidized area surrounding the disc is independent of the disc's weight.

The rotation of the discs about one another is dependent on the disc weight. In this case, decreasing the weight results in the discs rotating about one another earlier within

the channel. It has been proved that for spheres placed side by side in a viscoplastic fluid, the maximum weight possible for the particles to be considered neutrally buoyant is unaffected by the presence of a second object [58]. This was seen in similar simulations to the ones presented in this chapter in which the discs' weight is decreased so that they can be supported by the foam. The maximum values for disc weight a foam can support correspond to the values found in section 3.2 for one disc. Increasing the disc weight above $mg = 10$ will result in longer channels being required to see the full rotation of the discs about one another.

4.8.2 Variation of Liquid Fraction

Increasing the liquid fraction of the foam would have a great effect on the nature of interaction between two discs in this configuration. It would in effect make the fluidized region of the foam surrounding the disc less prominent in its influence on the interaction process. In this case, the elasticity of the foam decreases as plastic events dominate its rheology [106]. In many ways, increasing the liquid fraction of the foam make the foam less discrete in nature as the topological changes (T1s) become more evenly spread from the disc circumference than in the dry limit.

In this case the critical separation d_1^c between the discs would decrease when increasing the liquid fraction of the foam. The sharp transition between strong interaction and weak interaction between the discs also becomes smoother. Increasing the liquid fraction is expected to weaken the interaction between the discs. Increasing the liquid fraction of the foam makes plastic events more likely, so that the "elastic band" between the discs may be "broken" by T1 events. So one would expect that the rotation of the two discs about one another takes longer in a wet foam and only occurs if the discs are very close together.

Another simulation method would be required for the consideration of wetter foams. The Plateau borders must be incorporated within the foam, as in the PLAT code of Bolton and Weaire [91] (see §2.1.1). Simulations of the type would be computationally expensive compared to the ones considered here but should be considered for future

work.

4.9 Concluding Remarks

The interaction between two discs sedimenting from an initial side by side orientation has been discussed. In the dry foam limit, there exists a critical separation between discs that determines whether they interact or not. Interacting discs rotate about one another towards a more stable configuration in which they are one above the other in the foam. The strength of interaction is dependent on the initial separation between the discs and the size of the discs. It was found that for discs of area $4A_b$, the interaction only occurred if the initial separation between them is less than 3 to 4 bubble diameters. When the initial separation was greater than 4 bubble diameters the discrete nature of the foam meant that the disc did not interact. The critical separation is found to increase affinely with disc size.

The rotation of two discs about one another to a stable configuration where their line of centres is parallel to gravity is driven by the network and pressure forces exerted on them by the foam. Thus, the motion of each disc is driven by its own weight but is also dependent on the local structure of the foam that surrounds it. In addition, the foam structure changes as it responds to the discs' descent while minimizing its perimeter, altering the forces imposed on the discs.

The rotation of the discs about each other commences as the initial downward rate of descent of each disc is not exactly equal due to differences in the local structure of the foam. If the discs are close enough, the deformation of the foam due to one disc will influence the deformation of the foam around the other disc, and *vice versa*. This reorientation of the films leads to the response shown: as one disc moves ahead, the forces due to the foam act to pull the trailing disc into its wake. As the rotational motion proceeds, the films between the discs become stretched; the discs then rotate further since this configuration reduces the deformation of the foam.

The motion of the discs through the foam is stable when their line of centres is parallel to the direction of gravity (i.e. in configuration 2). This configuration for the

discs is studied in more detail in the following chapter.

Chapter 5

Two Discs Sedimenting and Interacting in a 2D Foam: Configuration 2

5.1 Introduction

The sedimentation and interaction between two circular discs initially placed directly one above the other in a 2D dry foam is studied (figure 5.1(a)). In this case, the line of centres of the discs is initially parallel to gravity. This orientation of the two discs is denoted as configuration 2 throughout this work.

It is expected due to observations made in chapter 4 that this orientation between the discs remains constant throughout their fall through the foam. Configuration 2 is known to be stable for spheres falling in viscoelastic fluids in general [109, 110, 44, 111, 57]. It was shown in this case that two spheres in configuration 2 remained oriented in this way but move closer together during their fall until they are in contact. Meanwhile in a purely elastic fluid with constant viscosity (Boger fluid) a constant non-zero final separation, independent of the initial separation between the spheres was discovered [112]. It is expected that for discs initially placed in this configuration in a dry foam, the trailing disc (disc 1) descends at a greater rate than the leading disc (disc 2). The trailing disc therefore moves into the wake of the leading disc during their descent through the fluid. Thus, they remain in configuration 2 but move closer together until

separated by 1 or 2 bubbles (as seen in chapter 4)

This chapter presents how the interaction between the two discs differs for an inviscid, elasto-plastic dry foam. The interaction between such discs provides a benchmark experiment which has scarcely been used in the foam community. It enables further study of the discrete nature of foam and its consequence on disc-to-disc interaction.

A typical simulation (using the method described in section 2.2) of two discs sedimenting in configuration 2 is presented in section 5.2. The effect the discrete nature of the foam has on the interaction between the discs in configuration 2 is investigated by varying the initial separation between the two discs (§5.3). Again the response of the foam to the sedimentation and interaction of the discs is visualized by considering the fields of displacement, T1 positions and bubble pressures (§5.4.1, §5.4.2 and §5.4.3 respectively). The effect that increasing the disc area A_d has on the interaction is described in section 5.5.

5.2 Reference Simulation for Configuration 2

A reference simulation of the sedimentation and interaction between discs as they fall through the foam in configuration 2 is studied. In this case, the discs have area $A_d = 4A_b$ and weight $mg = 10$. Foam A is used with its liquid fraction set to $\Phi_l = 3.7 \times 10^{-3}$. The discs are placed in the channel such that their centre coordinates (x_1, y_1) and (x_2, y_2) lie at $(0.5W, 0.1L - r_0)$ and $(0.5W, 0.17L + r_0)$ respectively. Recall that $r_0 = d_0/2$ denotes the discs' radius. In this case, disc 1 is initially positioned directly above disc 2 in the foam and they are separated by $d_2^{init} = 3.66d_b$. The discs centre coordinates are tracked as before (figure 5.1(b)) and the drag (F_y) and lift (F_x) force exerted on each is calculated.

The angle between the line of centres of the discs and the horizontal line is given by

$$\theta = tan^{-1}\left(\frac{y_2 - y_1}{x_2 - x_1}\right), \tag{5.1}$$

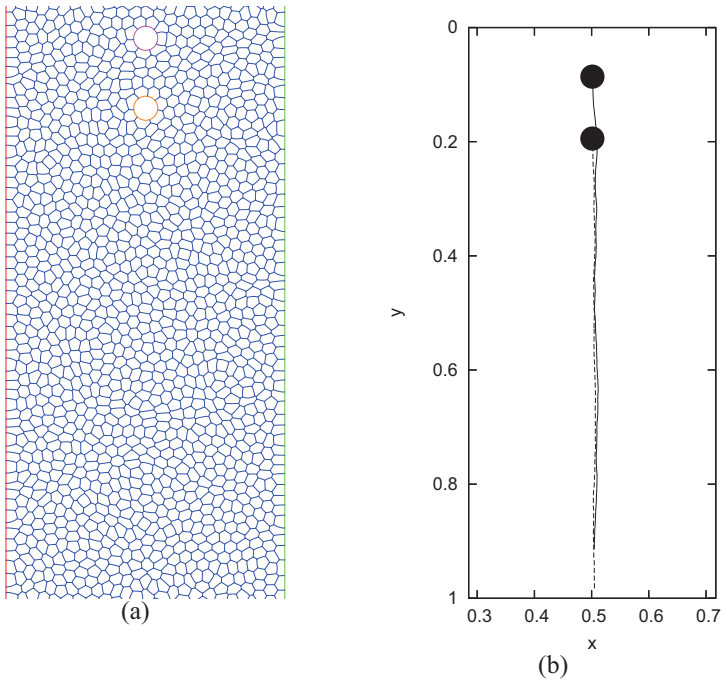

(a) (b)

Figure 5.1: (a) The initial position of two discs of area $4A_b$ and weight $mg = 10$ in configuration 2 (in foam A), initially separated by $d_2^{init} = 3.66d_b$. The angle θ between their line of centres and the horizontal line is calculated as before, i.e. $\tan\theta = (y_2 - y_1)/(x_2 - x_1)$ where (x_1, y_1) and (x_2, y_2) denote the centre coordinates of disc 1 (trailing disc) and disc 2 (leading disc) respectively. In this case θ is initially equal to $\pi/2$. (b) Tracking the discs' centre coordinates as they fall through the foam from the initial position described in (a). They descend along the centre line of the channel in a stable configuration. In other words, the angle of orientation (θ) of the discs is close to $\frac{\pi}{2}$ throughout.

and the separation d_2 by

$$d_2 = \sqrt{(x_2 - x_1)^2 + (y_2 - y_1)^2} - 2r_0 \, . \tag{5.2}$$

For configuration 2, the initial value for θ is $\frac{\pi}{2}$. As for two discs in configuration 1, the interaction between them is quantified by considering the variation in the separation d_2 and angle θ as they descend through the foam. The variation of both for the reference simulation is shown in figure 5.2. The configuration is confirmed to be a stable orientation of the two discs as the value for the angle θ stays close to $\frac{\pi}{2}$ throughout their descent through the foam. The separation of the discs decreases during sedimentation, until they are only separated by one or two bubbles. After becoming so close, the discs motion is stable as the separation d_2 and angle θ remains constant for the rest of the sedimentation process.

The forces exerted on the two discs are measured as before. Here, the lift force exerted on each disc is negligible since they are positioned centrally in the channel. In this case, lateral motion of either disc is minimal. It is of interest to consider how the drag force exerted on each disc differs during sedimentation. Let the drag force exerted on disc 1 be denoted by $F_{y,1}$ and that exerted on disc 2 by $F_{y,2}$. We consider how their average values (taken after the transient stage), denoted by $\overline{F}_{y,1}$ and $\overline{F}_{y,2}$ differ. Figure 5.3(a) demonstrates that the drag force exerted on the leading disc is greater than that exerted on the trailing disc (i.e. $\overline{F}_{y,2} > \overline{F}_{y,1}$). In this case, the trailing disc is moving a greater distance per iteration than the leading disc. Thus, the separation between them (d_2) decreases until the drag force exerted on both discs becomes similar.

It is proposed that discs descending in configuration 2 are interacting if their separation changes monotonically. In this case, their separation changes until they are terminally separated by one or two bubbles. The work presented in this chapter investigates how this interaction varies with initial separation d_2^{init} (§5.3) and disc size A_d (§5.5). The aim is to discover whether the discrete nature of foam results in ranges for these parameters where discs interact and where they don't. The response of the dry foam is probed further by looking at both interaction between the two discs and the

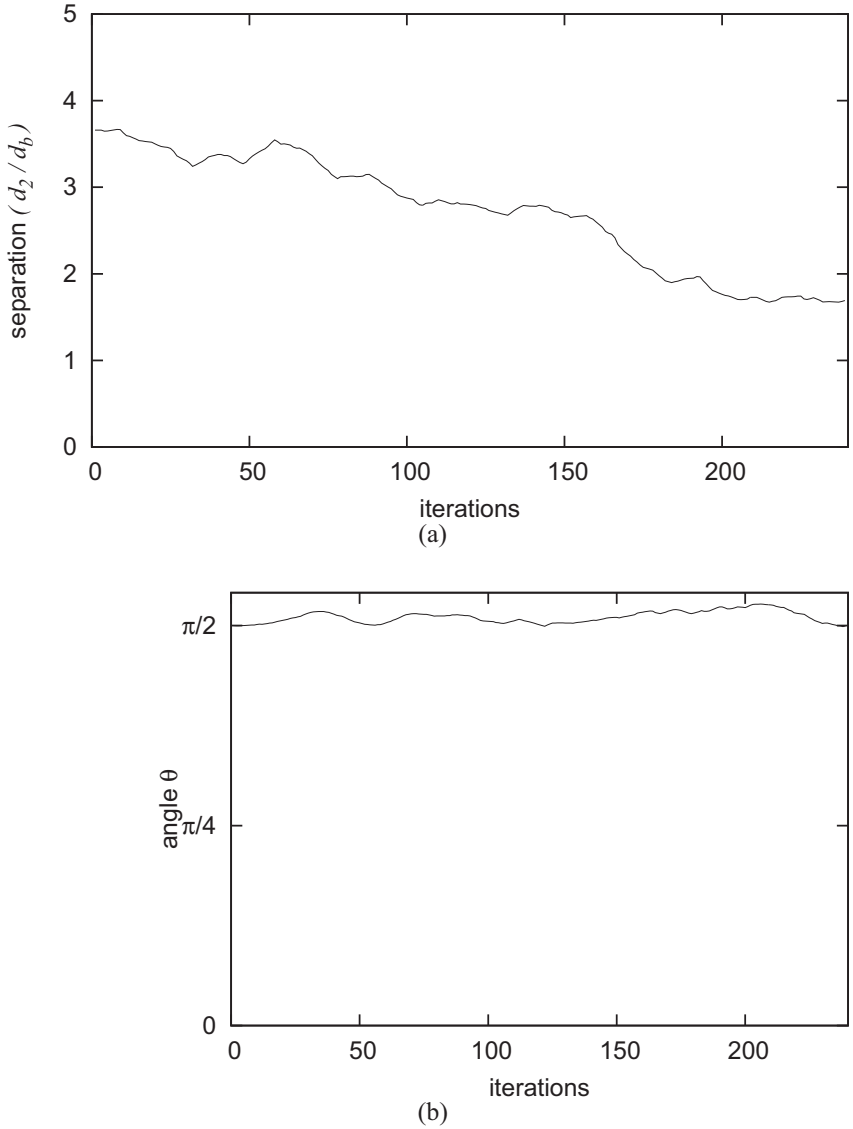

Figure 5.2: (a) The variation in the separation (d_2) between two discs (of area $4A_b$ and weight 10) as they sediment in configuration 2 from being initially separated by $d_2^{init} = 3.66d_b$. The discs move closer together during sedimentation until they are separated by roughly $2d_b$. (b) The angle (θ) at which the discs are oriented remains close to $\pi/2$ which confirms that configuration 2 is a stable orientation for the two discs.

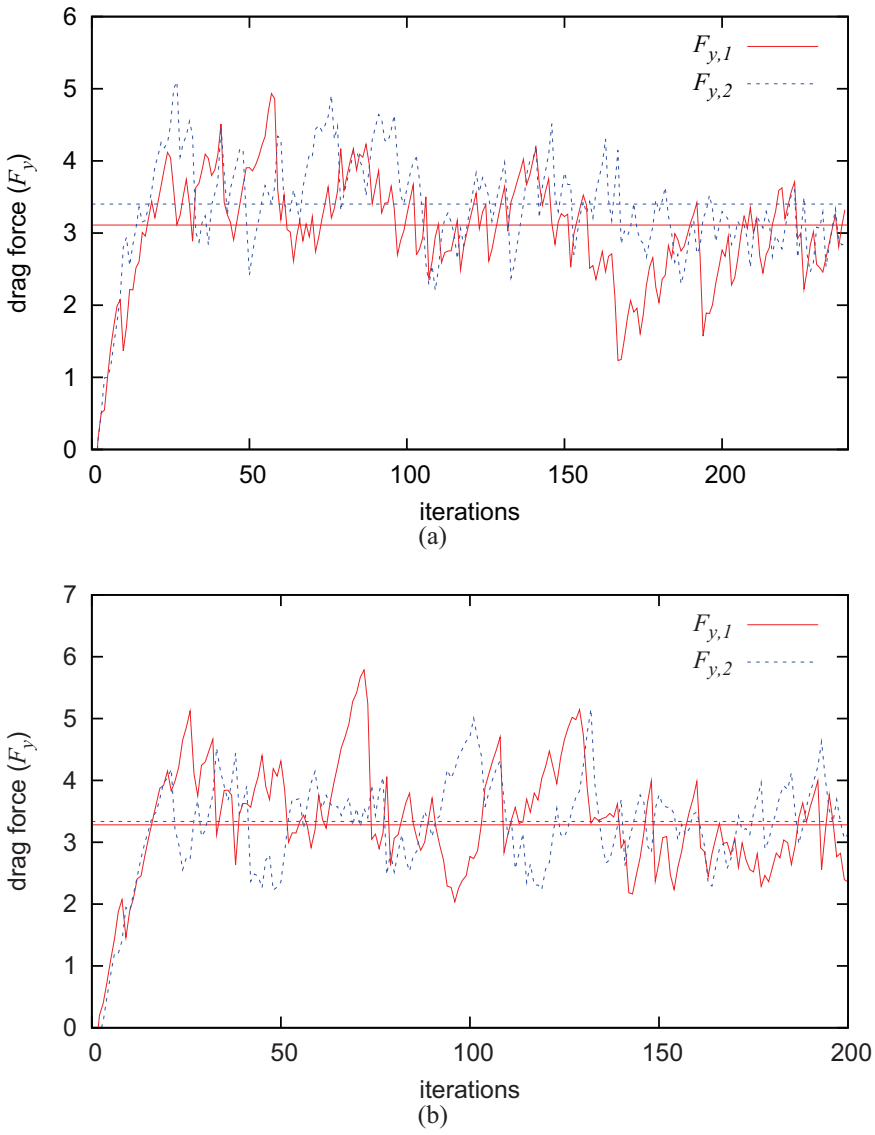

Figure 5.3: The variation in the drag force exerted on disc 1 ($F_{y,1}$) and disc 2 ($F_{y,2}$) as they sediment in configuration 2 with initial separations of (a) $3.66d_b$ and (b) $6.28d_b$. The average drag exerted on each disc, denoted by $\overline{F}_{y,1}$ and $\overline{F}_{y,2}$ respectively, are fitted to each plot. In case (a), $\overline{F}_{y,2} > \overline{F}_{y,1}$, thus, the discs move closer together as they fall through the foam. For (b) $\overline{F}_{y,1} \approx \overline{F}_{y,2}$, thus the discs stay far apart and do not interact.

foam fields imposed (§5.4).

5.3 Variation of Initial Separation

The initial separation d_2^{init} between the discs is expected to have a dominant effect on disc-to-disc interaction during their descend through the foam. As for discs in configuration 1, the interaction between them is expected to be strong if they are close together and weak if far apart. It is investigated whether the discrete nature of the foam screens [108] the interaction between the discs. It is proposed that a critical separation d_2^c between the discs exists. Thus, if discs are closer together than this critical separation; interaction proceeds as for the reference simulation (§5.2). However, if the discs are further apart than this critical separation, the interaction between them is minimal and in some cases negligible. In other words, if the discs are initially separated by less than d_2^c they move closer together until a terminal separation of one to two bubbles is reached. When the discs are initially separated by more than d_2^c their separation remains constant or they move further apart. In this case, the terminal separation of one to two bubbles is not reached.

The simulation described in section 5.2 is repeated for various initial separations d_2^{init} between the discs. The interaction between them is described and explained by looking at the discs' relative motion and the forces exerted on them by the foam. Figure 5.4 demonstrates how the separation between the discs vary when they are left to sediment from these different initial separations which range between $0.5d_b$ and $9d_b$.

The interaction between the discs is apparent in the way their separation varies during sedimentation. The variations (seen in figure 5.4) can be summarised as follows:

- Discs initially close together, i.e. with initial separations d_2^{init} in the range $1d_b$ to $2d_b$ descend with a constant separation throughout the sedimentation process. In this case, the motion of the discs is said to be stable as the discs are already separated by the terminal separation seen for interacting discs.

- Discs initially separated by $2d_b$ to $5d_b$ move closer together during their descent

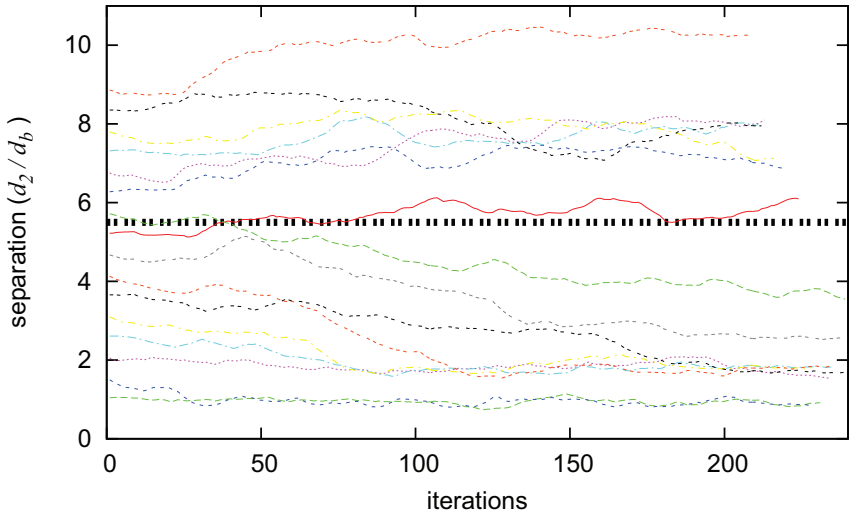

Figure 5.4: The variation in separation between the discs as they sediment in configuration 2 (in foam A with $\Phi_l = 3.7{\times}10^{-3}$) from various initial separations (varying between $1d_b$ and $9d_b$). As before, the discs are of area $4A_b$ and weight 10. It can be seen that for discs initially separated by up to $2d_b$, they descend in the foam at a constant separation. If the discs are initially separated by 2 to $6d_b$, then they move closer together until they eventually reach a terminal separation of 1 to $2d_b$, after which their relative motion is stable. If the initial separation is greater than $6d_b$ then the variation in separation is less and they stay far apart. The critical separation d_2^c is denoted by the dashed horizontal line and its value is close to $6d_b$ in this case.

until they are terminally separated by one or two bubbles. At this point their motion becomes stable (i.e. their separation stays constant).

- Discs initially separated by more than 5 to $6d_b$ stay far apart and their separation doesn't change monotonically. In this case, interaction between these discs is minimal and the terminal separation of one to two bubbles is never reached.

Thus, for discs of size $A_d = 4A_b$ and weight $mg = 10$ sedimenting in a dry foam where the liquid fraction is $\Phi_l = 3.7 \times 10^{-3}$, the critical separation d_2^c for disc-to-disc interaction is proposed to take a value of $6 \pm 1d_b$.

The ranges of disc separation d_2 where the discs are interacting or not is clarified by examining the differences in the drag force exerted on each disc (figure 5.5). The

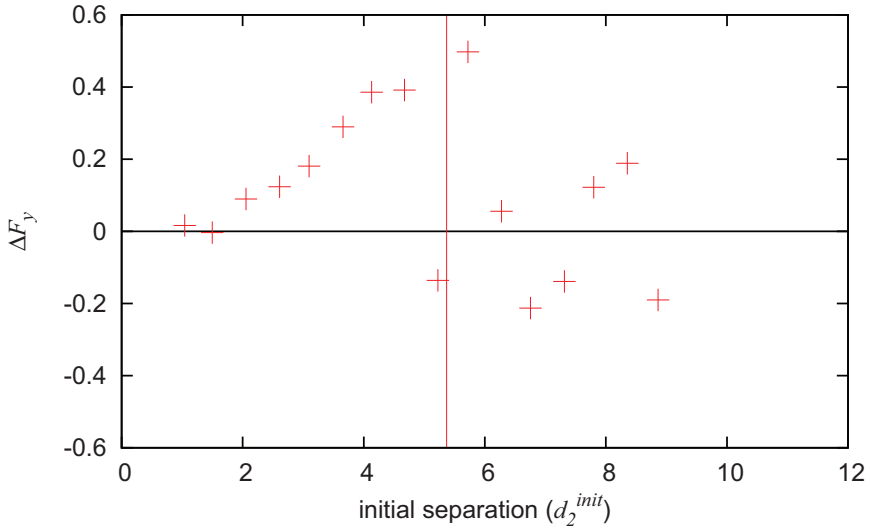

Figure 5.5: The difference between the drag force exerted on each disc ($\Delta F_y = \overline{F}_{y,2} - \overline{F}_{y,1}$) as they sediment in configuration 2 at different initial separations. ΔF_y is positive for initial separations ranging from $2d_b$ to $5d_b$. In this case, the drag force exerted on the leading disc is greater than that exerted on the trailing disc, whence the discs move closer together during sedimentation. Discs that are initially closer together than $2d_b$ stay close together as the drag force exerted on either disc is similar. When the discs are initially far apart ($d_2^{init} > 6d_b$) they stay far apart or move away from each other as the drag force differences become scattered about zero. In this case, the interaction between the discs is minimal. The critical separation d_2^c in this case is roughly 5 to $6d_b$.

difference in the drag force is denoted by ΔF_y and is given by

$$\Delta F_y = \overline{F}_{y,2} - \overline{F}_{y,1} \ . \tag{5.3}$$

In this case, the discs are interacting when the drag on the trailing disc is reduced due to the presence of the leading disc. It is to be expected that discs interact in this configuration when they are moving together into a stable separation. The existence of a critical separation is clarified by figure 5.5. The sharp drop for ΔF_y for initial separations d_2^{init} close to $5d_b$ and $6d_b$ yields that the critical separation is close to these values. Below these values, ΔF_y is clearly positive (i.e. $\overline{F}_{y,2} > \overline{F}_{y,1}$) while it appears scattered and closer to zero when the separation lies above this critical separation.

As in configuration 1, the amount of interaction that occurs between the two discs depends on the how far the fluidized region surrounding each disc reaches in the di-

rection of the other. This fluidized region was described for one disc to consist mainly of the first few layers of bubbles surrounding the disc. This is where most T1 events occur and where the bubbles move the most. However, the bubbles in the wake of each disc are elongated, whence the fluidized region is not uniform around each disc. In this case, the fluidized region extends slightly further than $2d_b$ in the wake of both discs. For configuration 2, the critical separation d_2^c for disc interaction is dependent on how far the wake of the leading disc extends towards the fluidized region in front of the trailing disc. If the upper disc is initially within this distance to the lower disc then it is able to move closer into its wake until the constant separation of one to two bubble diameters is reached. If the upper disc is initially above the yielded region in the lower discs' wake then the interaction is less apparent and the discs separation remains constant.

The existence of this critical separation is explained further in the section describing the foam fields (5.4). It is expected that this critical separation will increase with disc area, a factor which is investigated in section 5.5.

5.4 Foam Fields

It was shown in section 5.3 that the discrete nature of a foam results in the existence of a critical separation d_2^c where the discs interact if closer together than this value but don't if further apart. The response of the foam during the sedimentation of two interacting discs and two non-interacting discs is investigated here by visualizing the fields of bubble displacement, T1 positions and bubble pressure. It is hoped that these fields will demonstrate how the rheology of the foam governs the interaction or non-interaction between discs. All three fields are studied for two interacting discs (initially placed $3.66d_b$ apart) and two non-interacting discs (placed $8.35d_b$ apart). The discs have area $4A_b$, weight 10 and foam A is used with liquid fraction $\Phi_l = 3.7 \times 10^{-3}$.

5.4.1 Bubble Displacement

As in configuration 1, the discs interact if the flow field of bubbles surrounding each disc influences the other. If two discs are close together then the fluidized region surrounding each disc intercepts the other. In this case, discs that are very close together are in effect sedimenting within one large fluidized region. Thus, when the discs are close together it is possible to consider them to behave as one long object during sedimentation (see chapter 6). They reach a terminal separation of one or two bubbles (which remains fairly constant) and sediment with their line of centres parallel to gravity.

The bubble centre point coordinates lie at the average of the bubble's vertices. In this section, the centre-point coordinates of each bubble are recorded every 20 iterations and their displacement for this period represented by arrows.

The displacement field for two discs initially placed $d_2^{init} = 3.66d_b$ apart is shown in figure 5.6. This is the displacement field of the foam for the reference simulation described in section 5.2. Here, the motion of the bubbles is largely concentrated near the two disc system. The imposed flow of the bubbles implies that the discs are moving as a system and interacting with each other. In this case, bubbles forced to move due to one disc are influenced by the other disc as well.

Similarly, the bubble displacement field when two discs sediment in configuration 2, initially separated by $d_2^{init} = 8.35d_b$ is shown in figure 5.7. This separation is greater than the critical separation d_2^c required for interaction between the discs. The displacement field of the foam demonstrates why the two discs are not interacting. It can be seen that the bubble displacement field surrounding each disc doesn't intercept the other. In this case the foam hides the flow field imposed by one disc from the flow field imposed by the second disc. Each disc therefore sediments separately in the channel, each with its own fluidized region.

5.4.2 T1 Position

The fluidized region (defined in §3.5.2) is the region surrounding each disc where the applied stress on the foam is at its highest. Thus, it is where most T1 events occur in the

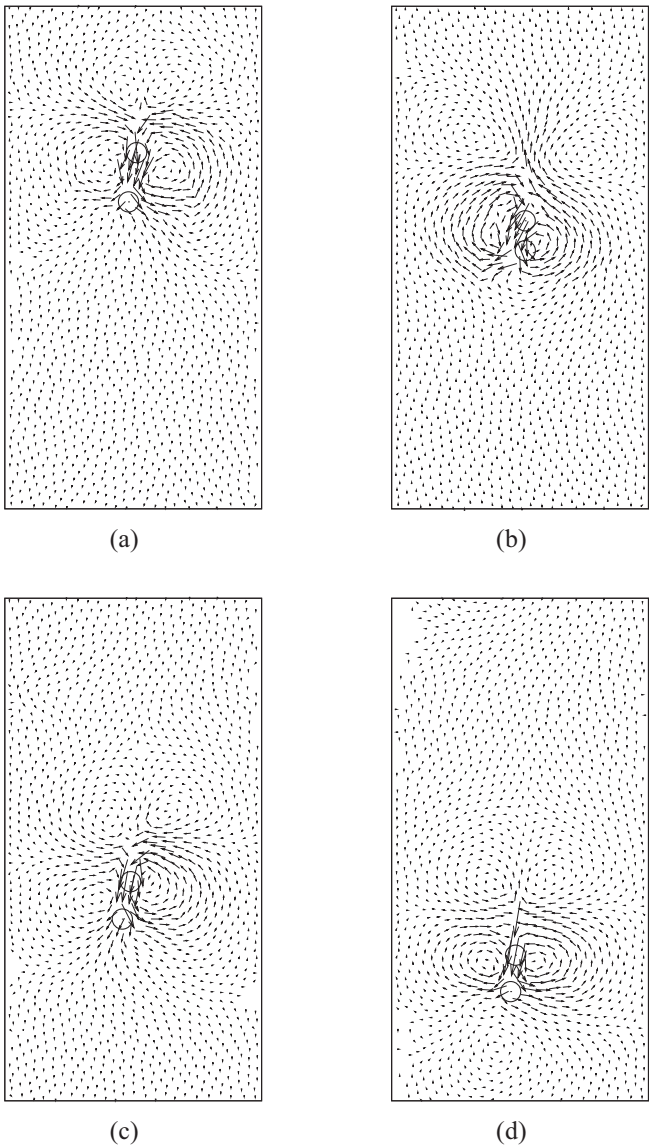

Figure 5.6: The displacement field of foam A (with $\Phi_l = 3.7 \times 10^{-3}$) when two discs (of area $4A_b$ and weight 10) sediment in configuration 2, initially separated by $3.66d_b$. Bubble centre points are recorded every 20 iterations and their displacement during this period denoted by an arrow. Each figure shows the bubble displacement field for (a) $40 - 60$ iterations, (b) $80 - 100$ iterations, (c) $120 - 140$ iterations and (d) $160 - 180$ iterations. Here, the discs interact by moving closer together until they are terminally separated by $1d_b$ to $2d_b$. The interaction proceeds as the flow field imposed by one disc intercepts the flow field imposed by the other. In this case the resulting flow field after which the discs reach their terminal separation of one to two bubbles resembles one large flow field imposed by the two discs.

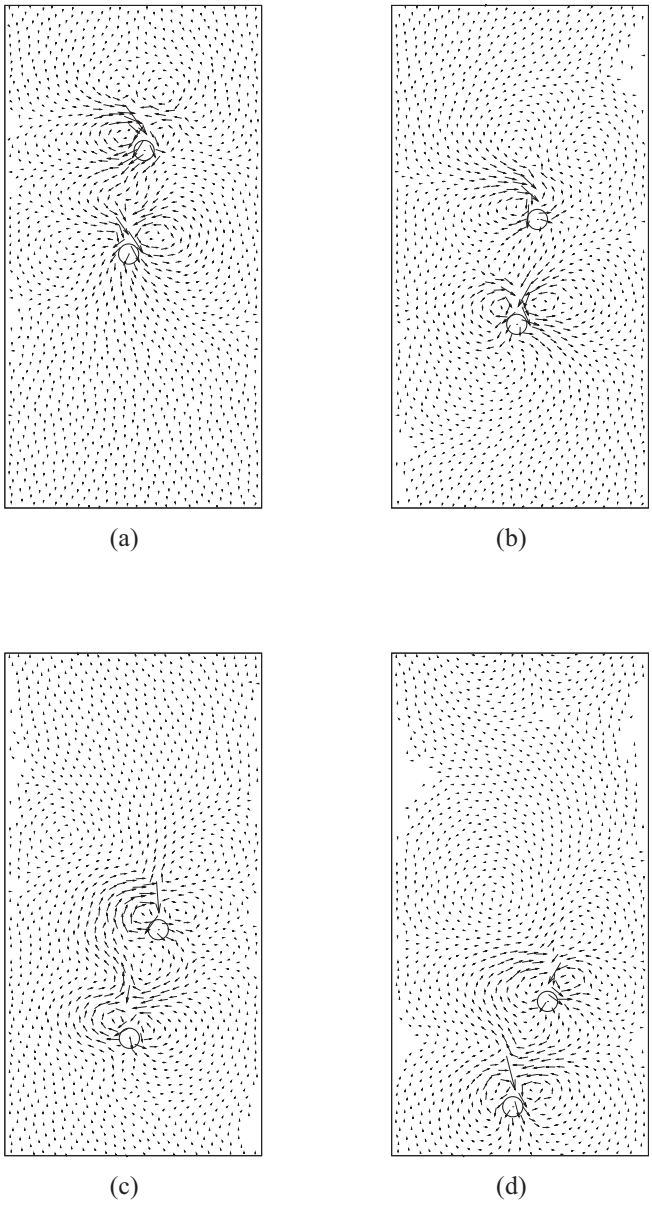

Figure 5.7: The bubble displacement field for foam A when two discs sediment in configuration 2 with an initial separation of $8.35d_b$. The discs have area $4A_b$ and weight 10 and the liquid fraction of the foam is 3.7×10^{-3} as before. Bubble centre points are recorded every 20 iterations and their displacement during this period is given by arrows. The displacement fields shown are for (a) 40 – 60 iterations, (b) 80 – 100 iterations, (c) 120 – 140 iterations and (d) 160 – 180 iterations. The interaction between the two discs is minimal as their separation is greater than the critical separation d_2^c. This minimal interaction is due to the fact that the flow field imposed by either disc does not intercept the other. In this case the discs sediment separately and stay far apart or move further apart, depending on the local structure of the foam near to each disc.

foam as the discs sediment. It was found that for the dry foam considered here, most T1s occur within a distance of $2d_b$ to a disc of size $4A_b$ (see §3.5.2). However, this is not uniform in every direction from the disc and is dependent on how the bubbles are elongated or squeezed.

The T1s occur mainly in two regions relative to the disc as it descends through the foam. These are directly below the disc where bubbles are squeezed and forced to move out of the discs' paths or in the wake where bubbles detach after becoming elongated. The elongation of bubbles in the wake results in T1s occurring frequently at a distance that is slightly greater than $2d_b$ from the disc. In effect, an elongated bubble at the wake of the disc can stretch so that it is of length up to roughly $2d_b$; therefore the first two layers of bubbles in the disc's wake can stretch $4d_b$ from the disc (see figure 3.6). In this case, the frequent T1s at the wake of the discs take place within a range of $0 - 4d_b$ from the disc boundary. Frequent T1s also occur in the range $0 - 2db$ in front of the trailing disc. In this case, the plastic fluidized region between two discs sedimenting one above the other would be as one if the discs are separated by up to roughly $6d_b$.

The positions of T1 events as two discs sediment in configuration 2 at initial separations below and above the critical separation are shown in figures 5.8 and 5.9 respectively. The discs in figure 5.8 are initially separated by $3.66d_b$ and are therefore interacting with each other during sedimentation. This is demonstrated by the fact that the distribution of T1 positions during sedimentation shows one large fluid region surrounding the two discs.

In figure 5.9 the discs are initially separated by $8.35d_b$ and the fluidized regions surrounding the discs are completely separate. Since the fluidized wake of the leading disc does not extend to the fluidized region in front of the trailing disc, each fluid region is separated by an unyielded foam. This part of the foam has previously been disturbed by the leading disc, but has now relaxed and is not under great stress. This elastic region of the foam hides the fluidized regions created by each disc from each other. As a result, the discs sediment independently.

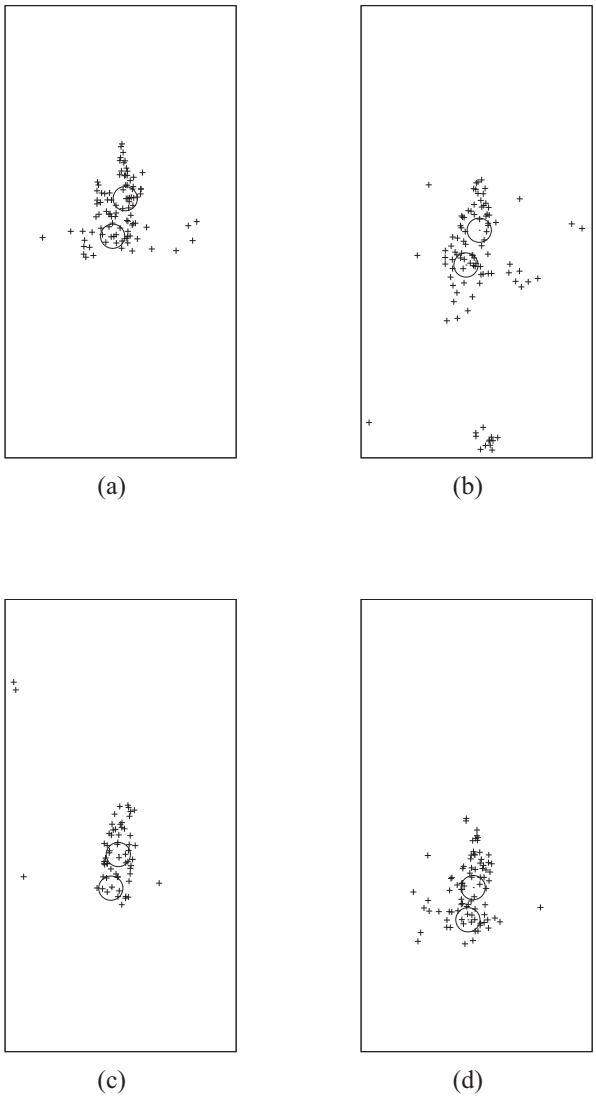

Figure 5.8: The positions of T1s in foam A (with $\Phi_l = 3.7 \times 10^{-3}$) are recorded at each iteration as two discs sediment in configuration 2. The discs have area $4A_b$, weight 10 and are initially separated by $d_2^{init} = 3.66d_b$. The T1 positions are shown for the intervals (a) 40 – 60 iterations, (b) 80 – 100 iterations, (c) 120 – 140 iterations and (d) 160 – 180 iterations. The discs are separated by less than the critical separation d_2^c and therefore the fluidized region imposed by each disc intercept the other. In this case the resulting fluid region surrounds the two discs as one, enabling the discs to interact.

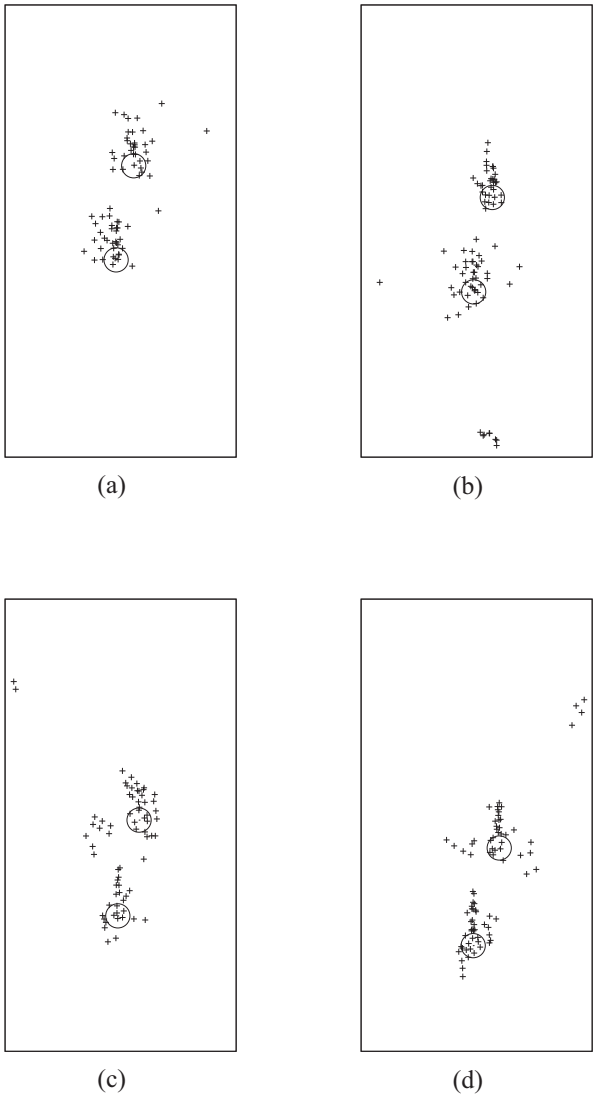

Figure 5.9: The positions of T1s in foam A are recorded by each iteration as two discs initially separated by $d_2^{init} = 8.35d_b$ sediment in configuration 2. The discs have area $4A_b$, weight 10 and the liquid fraction of the foam is $\Phi_l = 3.7 \times 10^{-3}$. Each plot represents the T1 positions for then intervals (a) 40−60 iterations, (b) 80−100 iterations, (c) 120 − 140 iterations and (d) 160 − 180 iterations. Here, the discs are further apart than the critical separation d_2^c and therefore the fluidized region imposed by each disc are separate. In this case the discs sediment independently of each other and do not interact.

5.4.3 Bubble Pressure

As in section 4.4.3 the pressure field of the foam is represented by colouring the bubbles relative to the values of their pressure compared to a reference bubble (that is far from the discs). The bubble pressure field yields information about how far a disc influences the surrounding foam flow.

Figure 5.10 demonstrates the pressure field within the foam when two discs sediment in configuration 2 at an initial separation of $d_2^{init} = 3.66d_b$. The pressure field every 50^{th} iteration is shown. As for two discs in configuration 1 (§4.4.3) there exist regions of high pressure under the discs and regions of low pressure in the wake of the two disc system. The two discs are interacting and the pressure field that arises yields visual evidence of this interaction. The pressure field is such that there is a region of high pressure below the leading disc and in the region directly between the discs. A region of low pressure exists in the wake of the trailing disc which stretches vertically for roughly $5d_b$. This implies that the motion of the trailing disc is dependent on the motion of the leading disc.

The bubble pressure field for the foam when the discs are separated by $d_2^{init} = 8.35d_b$ is shown in figure 5.11. In this case, the discs are further apart than the critical separation d_2^c, whence do not interact. The pressure fields surrounding each disc is as would be expected for one disc sedimenting in a foam channel (see §3.5.3). The region of high pressure in front of the trailing disc is not influenced by the low pressure region of the leading discs' wake as they are too far apart. In this case each disc descends within a pressure field that remains unaffected by the field imposed by the other disc. Thus, the discs are so far apart that the foam shields the deformation caused by one disc from the other. Therefore they sediment independently in their own flow fields.

5.5 Variation of Disc Area

It was shown in section 4.7 that for discs in configuration 1, the size of the disc is a decisive factor in determining the critical separation. Larger discs apply greater stress on

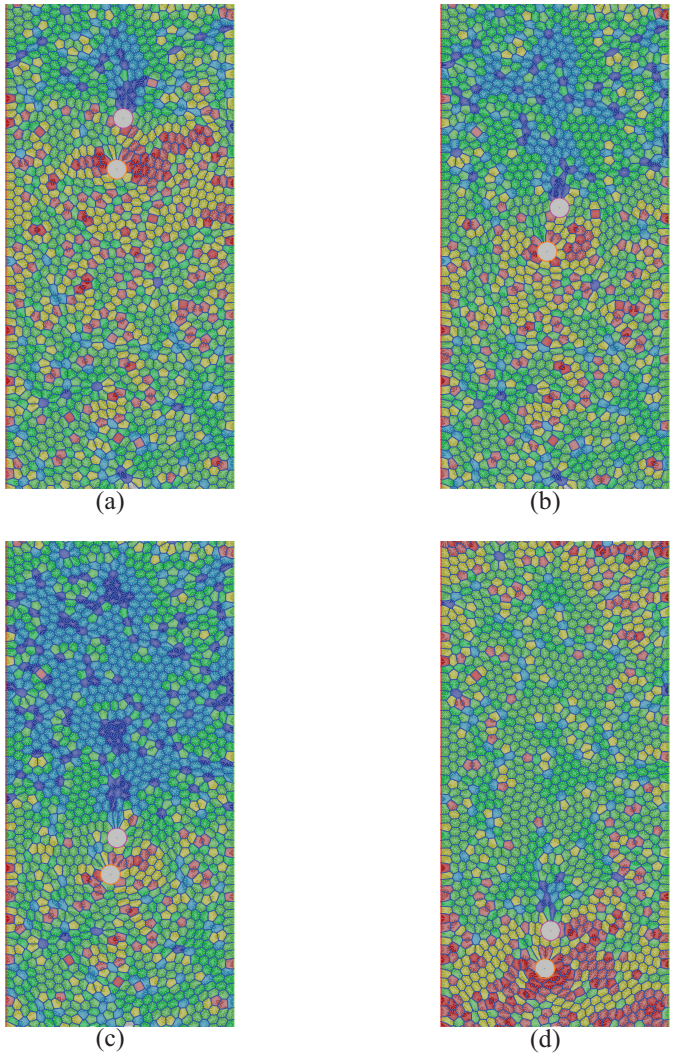

Figure 5.10: The bubble pressure field when two discs sediment in configuration 2 at an initial separation of $d_2^{init} = 3.66d_b$. The bubbles are colour coded depending on their pressure comparable to a reference bubble chosen to be in a region far from the disc (so that it is relatively undeformed). Here the pressure increases with the order dark blue, light blue, green, light green, light red to red. Each figure represent the pressure field for the (a) 50^{th} iteration, (b) 100^{th} iteration, (c) 150^{th} iteration and the (d) 200^{th} iteration. Here, the discs interact, moving closer together during sedimentation until they are terminally separated by $1d_b$ to $2d_b$. The pressure field imposed by the trailing disc is impacting the pressure field imposed by the leading disc.

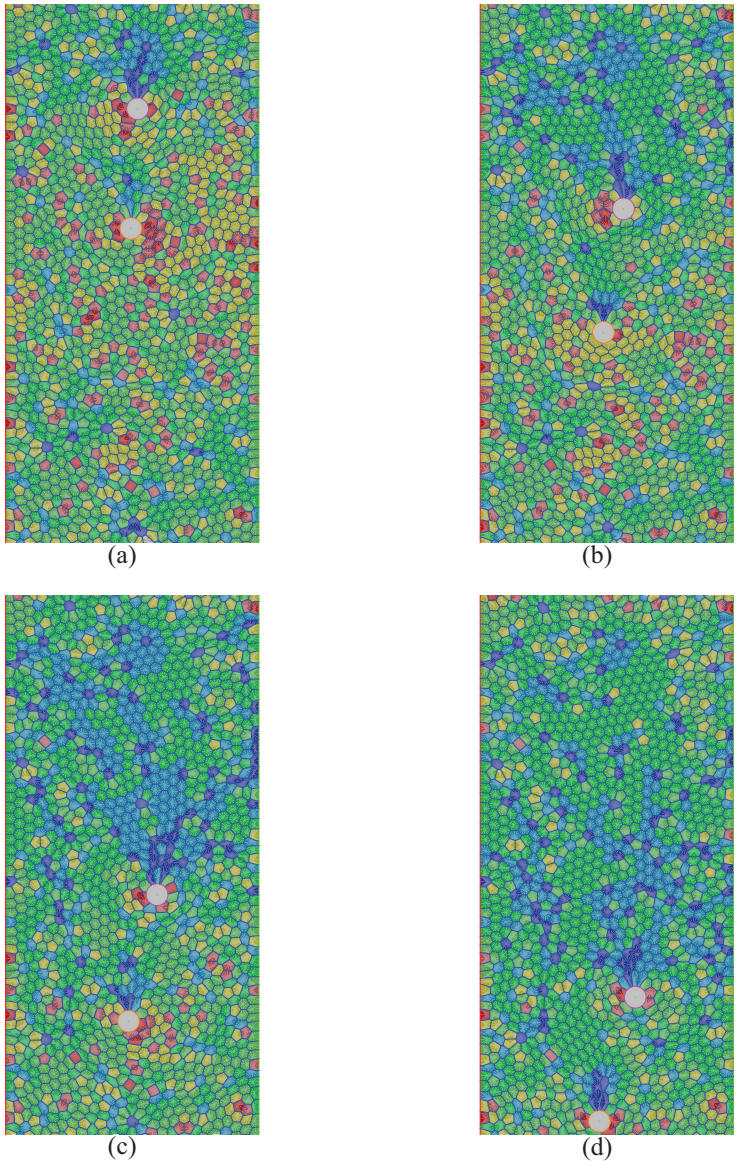

Figure 5.11: The bubble pressure field when two discs sediment in configuration 2 at an initial separation of $d_2^{init} = 8.35d_b$. The bubbles are colour coded depending on their pressure compared to that of a reference bubble (chosen to be in a region far from the disc). Here the pressure increases with the order dark blue, light blue, green, light green, light red to red. Each figure shows the pressure fields for the (a) 40^{th} iteration, (b) 90^{th} iteration, (c) 140^{th} iteration and the (d) 190^{th} iteration. The interaction between the discs is minimal because they are further apart than the critical separation d_2^c. In this case the pressure field imposed by one disc is unaffected by the pressure field imposed by the other disc.

the foam, resulting in a bigger fluidized region around the disc. In this case the critical separation for discs in configuration 1 was found to increase affinely with disc area. In this section, it is demonstrated that the same can be said for the critical separation (d_2^c) for discs positioned in configuration 2.

In this case, the initial separation (d_2^{init}) between the discs in configuration 2 is varied for discs of areas $2A_b$, $6A_b$, $8A_b$ and $10A_b$. The weight of the discs is fixed at $mg = 10$ and the liquid fraction of the foam is $\Phi_l = 3.7\times10^{-3}$. As for discs of area $4A_b$ (§5.3), the interaction is quantified by looking at whether they move together so that they become terminally separated by one or two bubbles. As before, the interaction between the discs can be demonstrated clearly by calculating the difference in average drag force exerted on each disc (ΔF_y) during sedimentation (see equation (5.3)). Discs move closer together if $\Delta F_y > 0$, move further apart when $\Delta F_y < 0$ and stay at a constant separation if $\Delta F_y \approx 0$.

Figures 5.12 and 5.13 shows how ΔF_y varies with initial separation between discs of area $2A_b$, $6A_b$, $8A_b$ and $10A_b$ that sediment in configuration 2. It can be seen that the relation between the drag force difference ΔF_y and initial separation between the discs d_2^{init} follows the same pattern as for the discs of area $4A_b$ (figure 5.5). When the discs are initially close together ($0 \leq d_2^{init} \leq 2d_b$), their motion is stable as the separation between them remains fairly constant. In this case the difference in the drag force exerted on both discs is minimal. When the discs are separated by more than $2d_b$ but less than the critical separation d_2^c, ΔF_y is clearly positive. In this case, the drag force on the leading disc is greater than that on the trailing disc, thus they move closer together during sedimentation. When the discs are separated by more than d_2^c the drag force differences are scattered about zero. This indicates that the discs are not interacting with each other.

The critical separation (d_2^c) between the discs is again found to increase affinely with disc area A_d, as seen in figure 5.14. Thus, the critical separations between discs follows a similar relationship with disc size for both initial configurations (1 and 2). The size of the disc influences the flow field imposed in the foam as it sediments. A large disc applies a stress on a larger region of the foam than a smaller disc. It is proposed as a

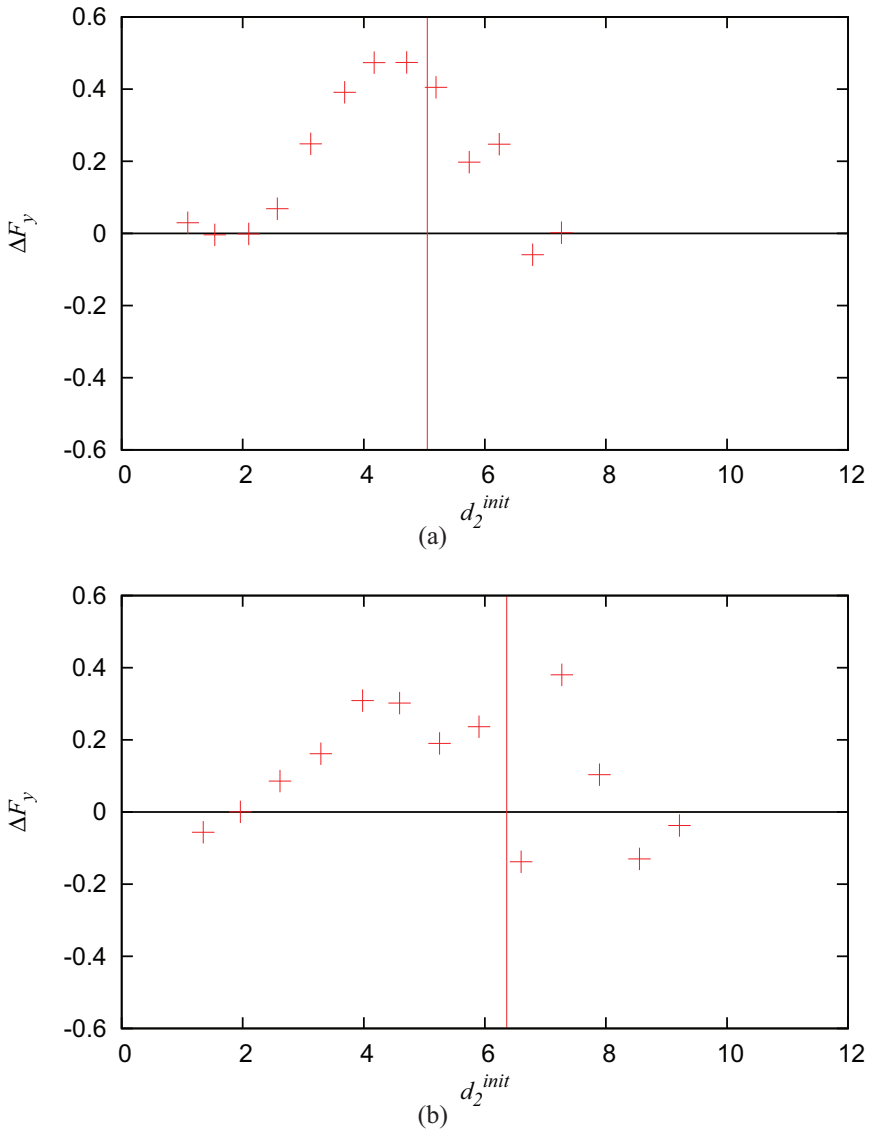

Figure 5.12: The difference between the drag force exerted on each disc (ΔF_y) sedimenting in configuration 2 as the initial separation d_2^{init} between them is varied. The discs considered are of size (a) $2A_b$ and (b) $6A_b$. A critical separation d_2^c, which determines whether the two discs interact or not exists in both case. For consistency, the value for the critical separation is calculated as the average of two factors. These are values for d_2^{init} where (i) the gradient of ΔF_y changes from positive to negative and (ii) the final clearly positive value for ΔF_y before it becomes scattered about zero. In this case, d_2^c is taken to be the average value of (i) and (ii) for all disc sizes. The critical separation is denoted in each plot by a vertical dashed line. Here it can be seen that the critical separation is greater for the discs of size $6A_b$ than the discs of size $2A_b$.

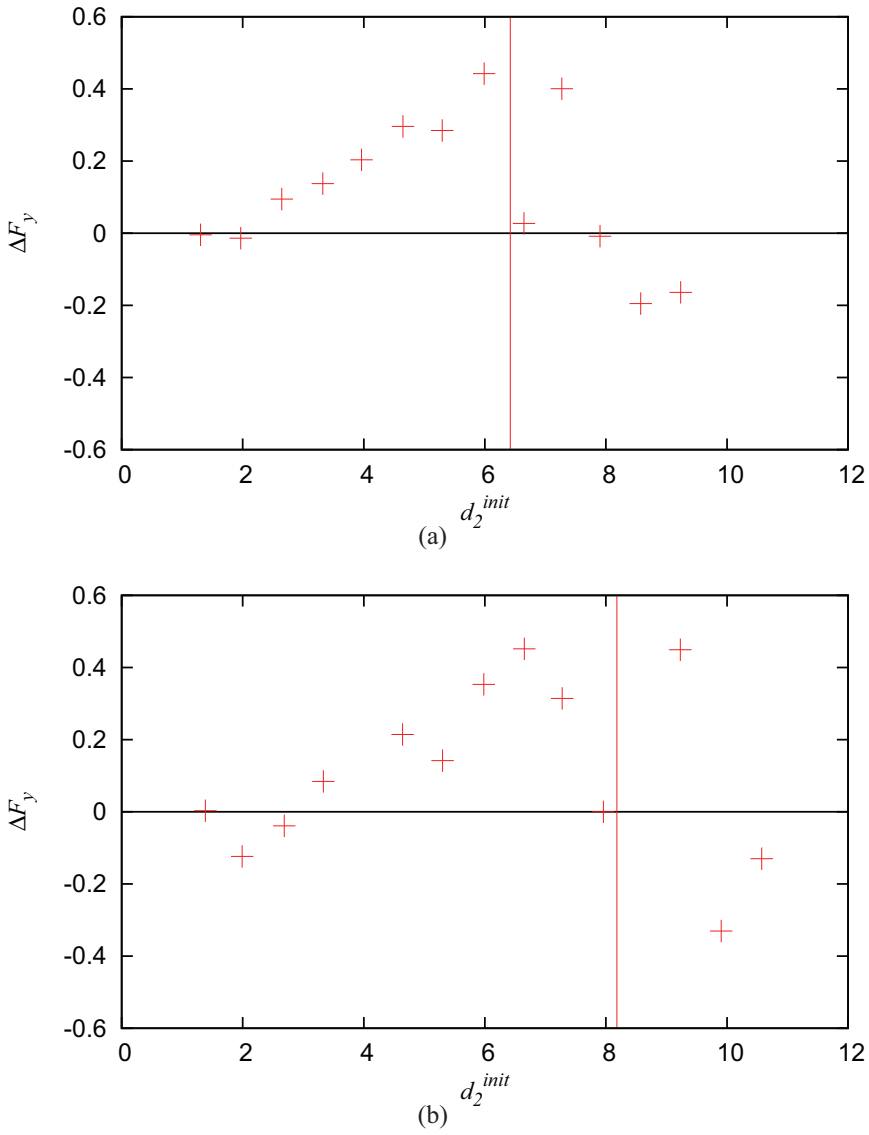

Figure 5.13: The differences between the drag force (ΔF_y) exerted on each disc (as they sediment in configuration 2) versus the initial separation d_2^{init} between them. The discs are of size (a) $8A_b$, (b) $10A_b$. The critical separation d_2^c (see figure 5.12 for details) is denoted in each plot by a vertical dashed line. Again, the critical separation is seen to increase with disc size.

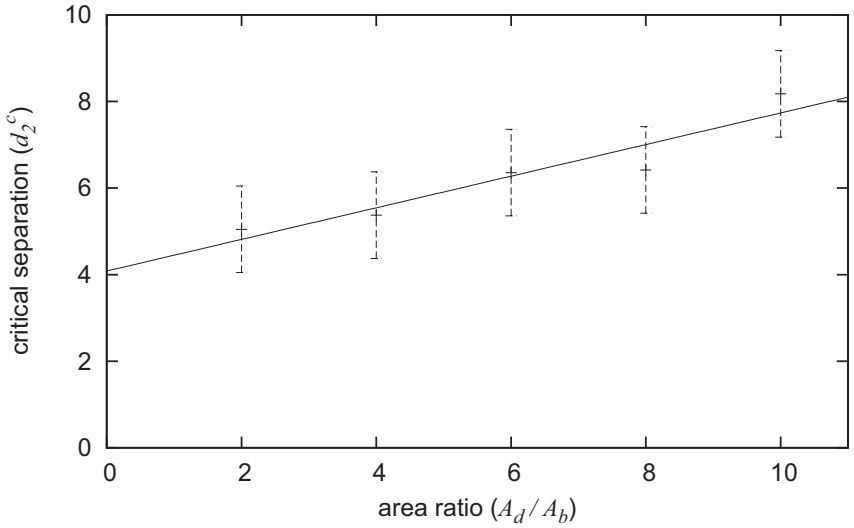

Figure 5.14: The critical separation d_2^c versus disc area A_d (with $1d_b$ error bars). As in configuration 1, the critical separation that determines whether the two discs interact or not increases affinely with disc area.

result of the linear dependence of the critical separation with disc size that the vertical length of the fluidized region surrounding a disc increases affinely with disc area. The critical separation between the discs in the vertical direction (d_2^c) is larger than that found in the horizontal direction (d_1^c). This is due to the fact that the fluidized region surrounding a disc in a dry foam is not circular. Its range is greater in the vertical direction than the horizontal due to the elongated bubbles in the wake of each disc.

5.6 Discussion

The effect that the separation between discs and their size has on the interaction between them during sedimentation in configuration 2 has been classified in sections 5.3 and 5.5 respectively. These control parameters are considered to have the greatest influence on disc-to-disc interaction for this orientation. However, it is also of interest to consider the effect other control parameters such as disc weight and the liquid fraction of the foam may have on the interaction described in these previous sections.

5.6.1 Variation of the Disc Weight

The fluidized region surrounding a disc is dependent on the applied stress exerted by a nearby object. Its size is dependent on the shape and size of this object. For the range of disc weights that can be considered to work within the quasi-static limit, the fluidized region surrounding the disc is considered to be independent of the disc weight and totally dependent on the geometry of the obstacle.

The work presented in this chapter is limited to a disc weight of $mg = 10$. This was chosen so that the resulting motion of the discs in the foam is steady and slow. Lighter discs sediment at an unsteady rate and are often brought to a halt by the foam. This was shown to be the case when testing the maximum disc weight a foam could support in section 3.2. Decreasing the weight of the disc would not prove interesting when looking at the interaction between two discs in configuration 2. However, it is expected that the position of light discs relative to each other may decide whether they are supported in the foam or not. If they are positioned close together (co-existing in one fluidized region of the foam) they will sediment steadily, as the maximum weight the foam can support is suppressed by the fact that the total weight of the two discs contributes to deform the foam. This was shown to be the case in a highly plastic fluid [58]. Non-interacting lighter discs are expected to prove neutrally buoyant as in the one disc case (§3.2).

Heavier discs (weighing more than $mg = 10$) descend a greater distance during each iteration. When considering the sedimentation and interaction between two discs, increasing the rate at which the discs descend through the foam is undesirable. Apart from numerical problems that may arise, longer foam channels would be required. It was decided that the weight of each disc should be limited to $mg = 10$, and increasing the discs weight above this value is not considered to be interesting or beneficial in improving the prediction of a 2D foam's response.

5.6.2 Variation of Liquid Fraction

Increasing the liquid fraction changes the rheology of the foam, thus it would greatly affect the nature of interaction between two discs in configuration 2. The fluidized region

of the foam surrounding either disc would become less prominent as the T1s become more scattered throughout the foam. In other words, increasing the liquid fraction of the foam reduces its elasticity, and its plasticity becomes dominant [106]. The method used for these simulations is limited to the dry limit of foam wetness. By increasing the critical length (l_c) that triggers T1s, one could practically perform the simulations presented in this chapter for liquid fraction in the range $0 < \Phi_l \leq 2\%$. In this case, the interaction process is expected to follow a similar pattern as in section 5.3.

As for configuration 1, it is predicted that the transition between strong interaction and no interaction between the discs when increasing disc-to-disc separation becomes smoother as Φ_l is increased. It is also predicted that the critical separation between the discs decreases with increasing liquid fraction of the foam.

Increasing the liquid fraction further would require a different method for simulating. Actual Plateau borders would have to be incorporated into the simulations, as in the PLAT code of Bolton and Weaire [91]. Although looking at the interaction of discs in wet foams would be computationally expensive compared to the simulations presented here, I believe that they would provide interesting results. The response of the foam to sedimenting objects for different foam liquid fractions would provide valuable insight into its rheology.

It could also be of interest in future work to directly measure the local stress in the foam as an object sediments. The texture tensor, used by Dollet and Graner [51] in a similar experiment could be used to compare the stress in the foam as the aforementioned control parameters are varied.

5.7 Concluding Remarks

When two discs sediment directly one above the other (i.e. in configuration 2) in a dry 2D foam, the discrete nature of the foam controls the degree to which they interact. As for configuration 1, the initial separation between the discs is an important parameter that determines whether the discs interact or not. A critical separation d_2^c of roughly 5 to 6 bubble diameters exists between the discs when they sediment in a dry foam.

When discs are closer together than this critical separation, they move together during their descent so that they become terminally separated by roughly $1 - 2d_b$. The critical separation d_2^c increases affinely with disc area A_d.

When discs interact the flow field imposed by the upper disc intercepts that imposed by the lower disc. In this case, the upper disc experiences less drag than the leading disc, thus it moves into the wake of the lower disc. As discs move close to a separation of $1 - 2d_b$, the drag force on both is equal and therefore they move at the same rate. At this point the bubbles directly between the discs have high pressure and they stay positioned between the discs.

However, if the initial separation is greater than the critical separation of $6d_b$, the drag force exerted on each disc is independent. In this case, the flow field imposed by each disc do not intercept the other, whence the discs don't interact.

The motion of the discs is stable when their line of centres is parallel to the direction of gravity and separated by one to two bubbles. Although this is reminiscent of elastic fluids, the plasticity of the foam plays an important role: the T_1 events behind the discs as bubbles lose contact change the local structure of the foam and allow the upper disc in the wake to move more quickly. The discrete nature of the foam means that objects don't interact if they are separated by more than d_1^c horizontally or d_2^c vertically.

Chapter 6

Sedimentation of an Elliptical Object in a 2D Dry Foam

6.1 Introduction

Here, the rheology of foam is probed further by considering the sedimentation of an elliptical object in a two-dimensional channel. The symmetry of the ellipse is less than that of the circle since it is longer in one direction than the other. Thus, it is expected to experience non-zero torque during its descent in the foam. It is predicted that a stable orientation for a sedimenting elliptical object is such that its major axis lies parallel to the direction of gravity. This prediction is related to the stable orientation found for two circular discs. It was shown in chapter 5 that two discs sedimenting with their line of centres parallel to the direction of gravity remained in the same orientation throughout their descent. It was also shown in chapter 4 that two discs initially side by side rotated about each other into this stable orientation. A similar rotation is expected in the case of an elliptical object.

Objects such as ellipses have long been used to probe the rheology of complex fluids. Investigations of the falling motion of long objects in yield stress fluids dates back to the 1960s [61, 63, 62]. These showed that the fluidized region surrounding the long object is highly dependent on its orientation.

The theoretical work of Leal [65] and Brunn [66] used material tensors to show that rod-like particles turn parallel to gravity when falling through viscoelastic fluids or into the flow in shear flows. They proposed that the rotation of a rod-like particle so that it becomes parallel to gravity as it sediments occurred due to the elasticity of the fluid.

The work of Joseph and Liu [67] proposed that the tilt angle of a long body falling in a viscoelastic liquid is determined by the competition between viscous, viscoelastic and inertial effects. Their three-dimensional experiments of the settling of a cylindrical rod in a viscoelastic fluid looked at the competition between fluid viscoelasticity and inertial effects by varying the weight of the particle under consideration. They found that for light particles, the viscoelasticity of the fluid dominates, whence turning the long body such that its major axis is parallel to gravity. In contrast, when a heavy particle was allowed to settle, minimal rotation of the long object was seen.

The three-dimensional simulations of Wang and Joseph [68] also show that it is the viscoelasticity of the fluid that controls the orientation of long objects in pressure driven flow so that their broadside is parallel to the net flow. In this case, an ellipse would rotate so that its major axis became parallel to the pressure driven flow. It was previously noted by Joseph and Feng [113] that the turning of long objects into the general flow of a viscoelastic fluid is due to normal forces that are compressive.

In this chapter, the sedimentation of a free rotating elliptical object is simulated in 2D using the Surface Evolver [78]. The elliptical object with centre (x_0, y_0) considered has an area A_e (which is an integer multiple of bubble area A_b in this work), eccentricity e_c and weight mg. Its boundary is described by

$$\frac{1}{e_c^2}\left((y-y_0)\cos\phi-(x-x_0)\sin\phi\right)^2+e_c^2\left((y-y_0)\sin\phi+(x-x_0)\cos\phi\right)^2=r_0^2\,. \quad (6.1)$$

The major axis of the ellipse denotes the maximum value for its diameter; when $e_c < 1$ this length is equal to $2r_0/e_c$ where r_0 denotes the average radius of the ellipse. Similarly the minor axis of the ellipse denotes the minimum value for the diameter which is equal to $2r_0e_c$ when $e_c < 1$. These parameters are described in figure 6.1.

It was shown by Dollet *et al.* [69] that a free rotating ellipse with its centre fixed

in a pressure driven flow of foam rotates so that its major axis is parallel to the flow. Therefore, for the work presented in this chapter, the ellipse is expected to rotate so that its major axis is parallel to gravity as it sediments. The role of the foam's elasticity and plasticity on the motion of the ellipse is discussed throughout.

The simulation method used for this chapter is described in detail in section 2.4. As in previous chapters discussing the sedimentation of circular discs, the motion of the ellipse and the forces it experiences during sedimentation are studied. Recall that the forces exerted on the object as it descends through the foam are due to the pull of the foam films (network force F^n) and bubble pressure (pressure force F^p). These forces contribute towards the drag (vertical force that opposes the descent of the object) and lift force (horizontal force that leads to lateral motion) exerted on the object as it descends through the foam under its own weight mg. Due to the asymmetry of the elliptical object these network and pressure forces contribute towards a non-zero torque being exerted on the object; denoted as τ^n and τ^p respectively. The method used to calculate these forces is detailed in section 2.4.3. To gather qualitative results on the rotating motion of the ellipse it is required to model its motion by defining two separate effective time scales for downward and rotational motion. These time scales are described in section 2.4.3 and the limitations of the model are discussed later in this chapter (§6.4.3).

Some preliminary work in which the orientation of the ellipse is fixed as it sediments through the foam is presented in section 6.2. The orientation in which the ellipse has its major axis parallel or perpendicular to gravity is discussed in section 6.2.1. The orientation of the ellipse is then changed so that its major axis lies at an acute angle to the horizontal axis. This scenario is described in section 6.2.2. The forces exerted on ellipses with these fixed orientations are compared with the case of a circular disc, described in chapter 3. The asymmetry of the ellipse provides a tool for studying the rheology of the foam it descends through.

A rotation of the ellipse is incorporated into the simulations and presented in section 6.3. Here, the motion of an ellipse from various initial orientations is discussed (§6.3.3) as well as the flow fields imposed on the foam during the process (§6.3.2). The importance of control parameters such as the area of the ellipse, its eccentricity and its

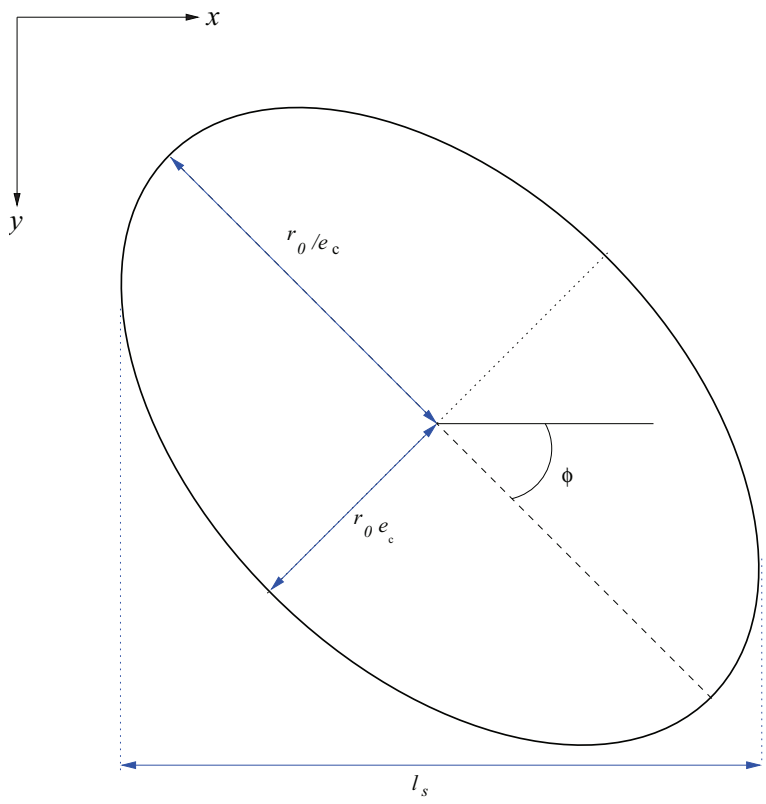

Figure 6.1: The shape parameters of the ellipse that sediments through a two-dimensional dry foam. It has area A_e, an average radius r_0 and eccentricity e_c. The angle to which the ellipse's major axis is inclined under the horizontal line is denoted by ϕ. The initial orientation of the ellipse in a typical simulation has an angle of inclination ϕ_{init}. The elliptical object is left to sediment through the foam under its own weight mg.

weight are discussed in sections 6.3.4, 6.3.5 and 6.3.6 respectively. Further to this, the importance of foam liquid fraction and bubble area dispersity are discussed in section 6.4.

6.2 Sedimentation of an Ellipse with Fixed Orientation

In this section, the ellipse is left to sediment under its own weight but is not allowed to rotate during sedimentation. The orientation of the ellipse is fixed at $\phi = 0$ or $\phi = \pi/2$ in section 6.2.1 whence its major axis is perpendicular or parallel to the direction of gravity. The orientation of the ellipse is then changed so that it is tilted at an acute angle either in the clockwise ($0 < \phi < \pi/2$) or anticlockwise ($-\pi/2 < \phi < 0$) direction to the horizontal x-axis as it sediments. This fixed tilted orientation of the ellipse is considered in section 6.2.2.

6.2.1 Major Axis Parallel or Perpendicular to the y-axis

In this section, an ellipse defined by equation 6.1 with fixed orientation $\phi = 0$ is left to sediment through a 2D foam with liquid fraction $\Phi_l = 4 \times 10^{-3}$ under its own weight ($mg = 10$). Thus, depending on the value of the ellipse's eccentricity e_c, the major axis is either parallel or perpendicular to the horizontal x-axis. An ellipse with eccentricity $e_c < 1$ and $\phi = 0$ is oriented such that its major axis is parallel to the horizontal x-axis and perpendicular to gravity. Similarly, an ellipse with eccentricity $e_c > 1$ and $\phi = 0$ is oriented such that its major is perpendicular to the horizontal x-axis and parallel to gravity. The foam used for the simulation is foam E (see table 2.1).

As for the work presented on the sedimentation of a circular disc, the motion of the ellipse is dependent on the drag (F_y) and lift force (F_x) exerted by the foam films and bubble pressures. In this section, the eccentricity (e_c) and area (A_e) of the ellipse are varied and the dependence of network and pressure contributions to the drag exerted on the ellipse (denoted by F_y^n and F_y^p respectively) by the foam on these parameters is quantified. The ellipse sediments from a central position at the top of the foam channel,

whence the lift force it experienced is negligible. This was shown to be the case for a circular disc in section 3.3 and it is also shown to be the case for an ellipse oriented so that its major axis is either parallel or perpendicular to the direction of gravity (see figure 6.8(a)).

Let us first consider the sedimentation of an ellipse of area $A_e = 4A_b$ from a central position at the top of the foam channel. It is interesting to compare the network and pressure contributions to the total drag force exerted on the ellipse when its major axis is perpendicular and parallel to gravity. In this case, two equivalent ellipses are chosen for simulation. These two ellipses have eccentricities $e_c^1 = 0.8$ and $e_c^2 = \frac{1}{e_c^1} = 1.25$. In this case, the shape of the ellipses is the same. The first ellipse is oriented such that its major axis is perpendicular to gravity while the second ellipse is oriented such that its major axis is parallel to gravity. The variations of the network and pressure contributions to the total drag force exerted on the two equivalent ellipses as they sediment separately in a foam are shown in figure 6.2. It can be seen that these forces fluctuate in the same manner as they did when a circular disc of area $A_d = 4A_b$ was left to sediment from a similar position in a foam (see §3.3). The fluctuations in these forces are described for the circular disc (see figures 3.6 and 3.7) and are a result of bubbles rearranging and T1 events near to the sedimenting object.

During the sedimentation of a circular disc of area $A_d = 4A_b$ in a foam with the same liquid fraction as considered here, the network contribution to the drag was roughly four times the pressure contribution (see figure 3.5 in section 3.3). When the ellipse is oriented with its major axis parallel to the x-axis, the network contribution to the drag is roughly twice the value of the pressure contribution to the drag (as shown in figure 6.2(a). Conversely, when the ellipse is oriented such that its major axis is parallel to the y-axis, both the network and pressure contributions to the drag force exerted on the obstacle by the foam are greatly reduced (see figure 6.2(b)). In this case, the pressure contribution to the drag is almost reduced to zero.

In this case, changing the shape of the sedimenting object so that it is slightly longer in the horizontal direction increases both the network and pressure contributions to the total drag force exerted by the foam. The effect is greater for the pressure contribution.

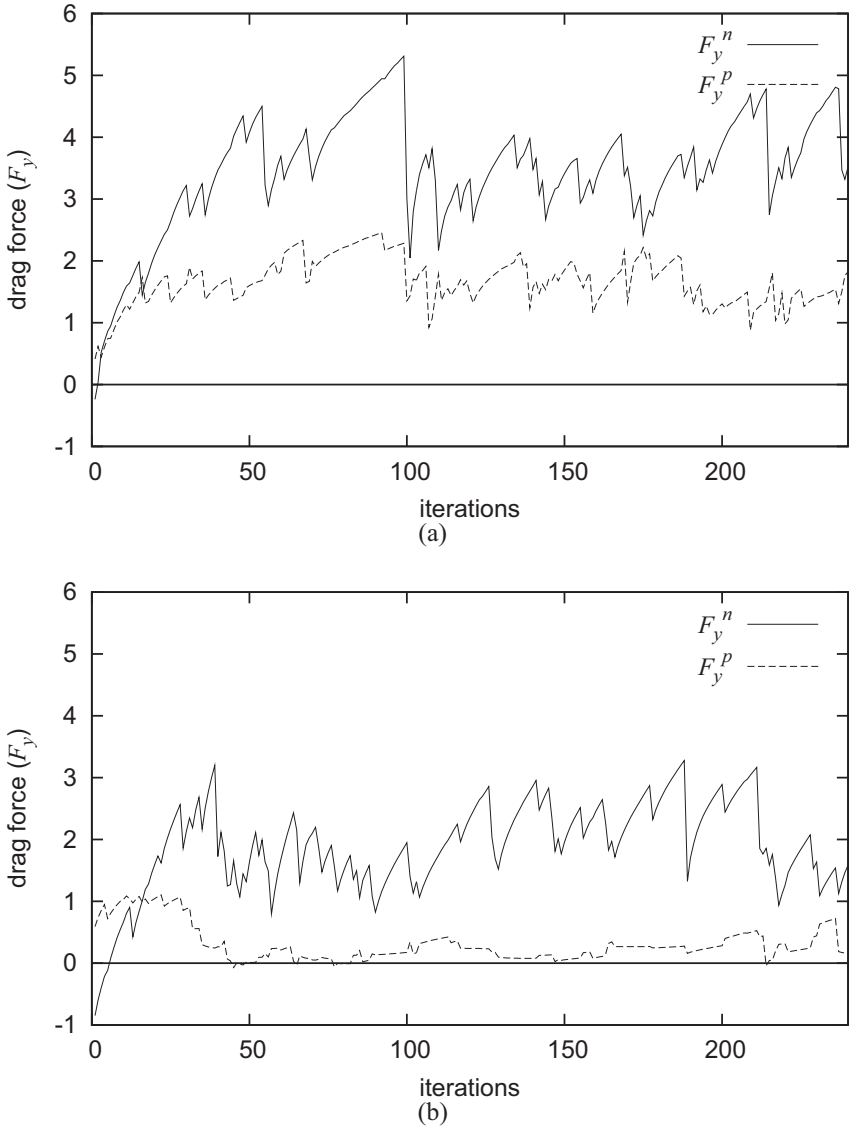

Figure 6.2: The network (F_y^n) and pressure (F_y^p) contributions to the total drag force (F_y) exerted on an ellipse of area A_e and weight $mg = 10$ as it sediments through the foam oriented such that its major axis is (a) perpendicular to the direction of gravity ($\phi = 0$ and $e_c = 0.8$) and (b) parallel to gravity ($\phi = 0$ and $e_c = 1.25$). It can be seen that both contributions to the drag force are higher when the ellipse is oriented such that its major axis is perpendicular to the direction of gravity. In this case the network contribution to the total drag is roughly twice the order of the pressure contribution. When the ellipse is oriented such that its major axis is directed parallel to gravity, the drag is minimized. In this case the pressure contribution to the total drag force becomes minimal while the network contribution has been halved.

This is a result of more bubbles being squeezed under the ellipse as it sediments with its major axis parallel to the x-axis; thus a greater amount of bubbles have greater pressure directly beneath the sedimenting ellipse. The amount of bubbles with low pressures directly above the ellipse are also greater for an ellipse oriented in this way as its wake is wider (see figure 6.3(a)). As a result the pressure contribution to the drag is greatly increased when a long object such as an ellipse sediments with its major axis perpendicular to the direction of gravity. Similarly, the network contribution to the drag is also greater for the ellipse oriented in this way compared to the circular disc. This is a result of more foam films bunching along the top of the ellipse due to its greater spanwise width l_s compared to the circular disc. The increase in this network contribution is less dramatic than for the pressure contribution as there is a limit to how bunched up the films can become before T1s are triggered above the object.

In the case where the major axis of the ellipse is parallel to the y-axis, both contributions to the drag are less than experienced for the circular disc and the ellipse with its major axis perpendicular to the y-axis. When the ellipse is oriented in this manner, its spanwise width l_s is minimized whence less bubbles are squeezed as the ellipse descends through the foam (see figure 6.3(c)). As a result the region of high pressure usually seen below the descending object is minimized as bubbles can easily move out of the ellipse's way as it descends. Thus, the pressure force contribution to the total drag force exerted on the ellipse is minimal when the ellipse is oriented in this way. Similarly, the network drag is also minimized as less films bunch up in the wake of the ellipse.

In this case, the two contributions to the drag force depend on the spanwise width of the ellipse. For an ellipse with its major axis parallel to the direction of gravity, its width is small. In this case, it is the films network that controls the motion of the ellipse. The pressure contributes more prominently when the ellipse has a greater horizontal width.

6.2.1.1 Vary Ellipse Area

Simulation of the sedimentation of an ellipse oriented parallel or perpendicular to the direction of gravity is continued for ellipses of different areas. In this case, the area

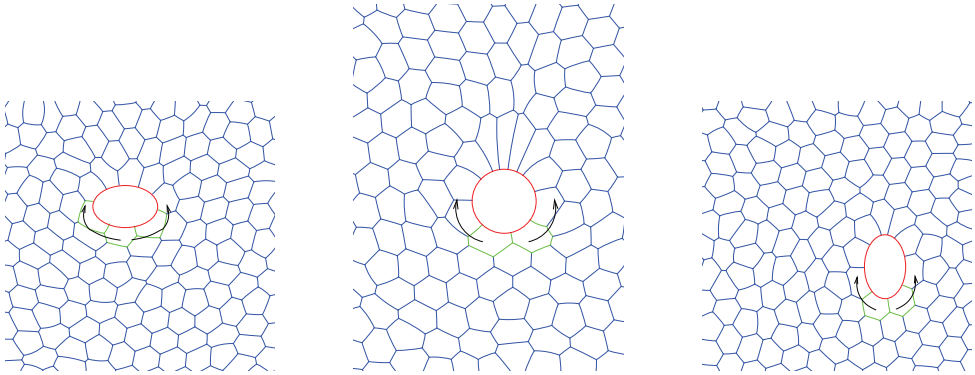

Figure 6.3: The difference in the pressure contribution to the drag force exerted on an sedimenting object by the foam is highly dependent on the object's shape. In the case of an ellipse, it was found that this contribution was at its greatest when the ellipse is oriented such that its major axis is perpendicular to gravity, shown in (a). The pressure contribution to the drag was slightly lower for a circular disc (b) and minimal for an ellipse oriented such that its major axis is parallel to gravity (c). The pressure contribution is dependent on how many bubbles are forced to move laterally by the descending object. Thus, an ellipse sedimenting as in (a) enforces the bubbles with their edges coloured green to move greater lateral distances than the other objects. In this case, these bubbles are squeezed to a greater extent than in the other two case ((b) and (c)) and therefore apply a greater pressure force upwards on the ellipse. The arrows show the amount of lateral motion required for the squeezed bubbles in each case.

of the ellipse (A_e) is varied between $2A_b$ and $8A_b$ and the variations in the network and pressure drag force exerted are recorded. The angle ϕ is fixed at zero throughout the simulation and the weight of the ellipse is always chosen to be $mg = 10$. This weight was shown to be sufficient for the descending motion of circular discs of similar sizes to be steady (see §3.2) and is assumed to be the case for the elliptical objects considered here. The eccentricity of the ellipse is fixed at either $e_c = 0.8$ (i.e. major axis perpendicular to gravity) or $e_c = 1.25$ (i.e. major axis parallel to gravity). Finally, recall that the liquid fraction of the foam is kept fixed at $\Phi_l = 4 \times 10^{-3}$ throughout.

The work of Raufaste *et al.* [77] predicted a affine increase in network drag force on a circular object in foam flow as the size of object is increased. It was shown in section 3.7.1 that both the network and pressure contribution to the drag force exerted on a circular disc sedimenting through a foam increase affinely with disc diameter. For a monodisperse foam with the same liquid fraction considered in this section, the network

drag increased with disc diameter d_0 with a slope of 0.75 and the pressure contribution increased with a slope of 0.46. It is investigated here whether the shape of the sedimenting object changes the nature of the relationship between the two contributions to the drag force and the object's size. This is done by considering the relationship between the forces and the spanwise width l_s of the ellipse. Since $\phi = 0$, the spanwise width is equal to $2r_0/e_c$.

Figure 6.4 shows that both the network and pressure contribution to the drag force increases affinely with the ellipse's spanwise width when it is oriented such that its major axis is either perpendicular or parallel to the direction of gravity. When the ellipse is oriented such that its major axis is perpendicular to gravity, both contributions increase with spanwise width with the same slope of 0.79. Conversely, when the ellipse is oriented such that its major axis is parallel to gravity, the network drag increases with spanwise width with a slope of 1.12 while the pressure contribution increases with a slope of only 0.17. Thus, the dependence of each contribution to the drag force on spanwise width differs for the two orientations of the ellipse considered.

In this case, changing the shape of the sedimenting object slightly has a noticeable effect on the forces exerted on that object. It can be seen that for both fixed orientations of the ellipse considered here, the network force contribution to the drag force is always greater than the pressure contribution exerted. This network force increases affinely with object width with nearly the same relation for the three objects considered (the circular disc and ellipses oriented such that their major axis are perpendicular or parallel to gravity).

However, the same affine relation was not seen between the pressure contribution to the drag force and spanwise width for the three objects. It was seen that the pressure force increased at a greater rate with object width when the ratio between the object's width and height is greater. In this case, the ellipse oriented so that its major axis is perpendicular to gravity experiences the greatest pressure contribution to the drag force. The affine increase of this pressure contribution with spanwise width is also at its greatest for this orientation. This is a consequence of the flow field imposed by the object as it sediments in the foam. An ellipse oriented in this way imposes

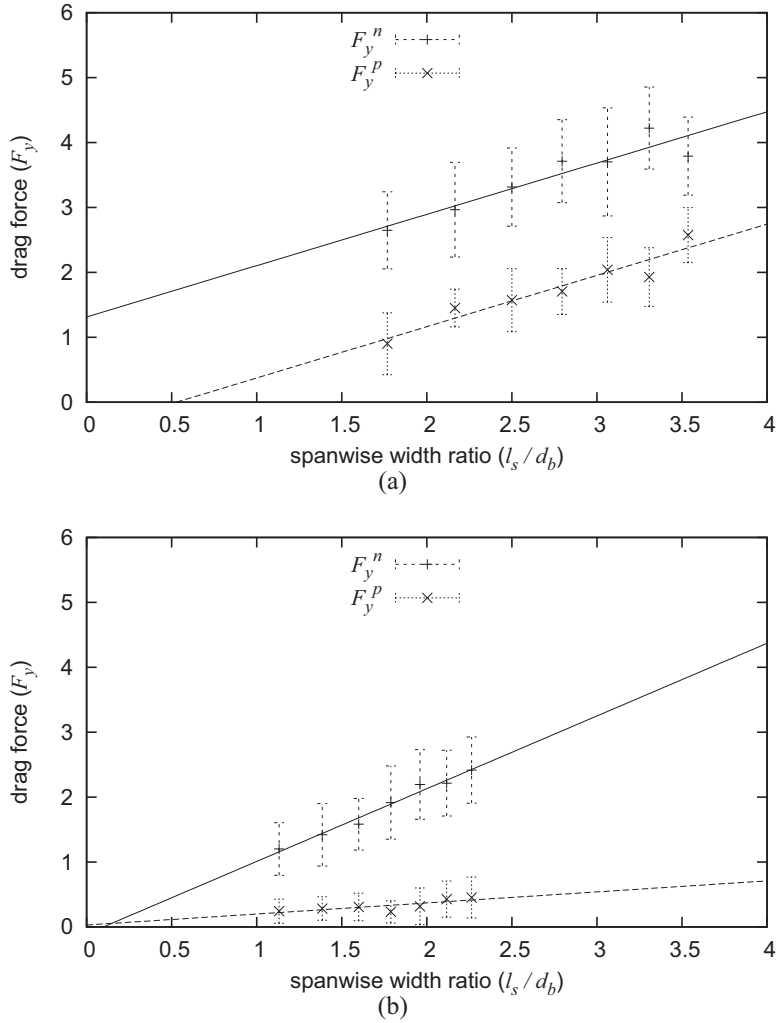

Figure 6.4: The dependence of the network and pressure contributions to the drag force on the spanwise width of an ellipse sedimenting such that its major axis is either (a) perpendicular ($e_c = 0.8$, $\phi = 0$) or (b) parallel ($e_c = 1.25$, $\phi = 0$) to the direction of gravity. The average values of the contributions are taken (ignoring a transient stage of each simulation) and they are accompanied by standard deviation error bars. Both the network and pressure contributions to the drag increase affinely with the spanwise width of the ellipse in each case. The affine relations between the size of the ellipse and the separate contributions to the drag force are given in each case by (a) $F_y^n = 0.79 l_s/d_b + 1.31$, $F_y^p = 0.79 l_s/d_b - 0.42$ (b) $F_y^n = 1.12 l_s/d_b - 0.11$, $F_y^p = 0.17 l_s/d_b + 0.03$. When the ellipse is oriented such that its major axis is perpendicular to the direction of gravity (i.e. $e_c = 0.8$), the affine increase of each contribution to the drag with the ellipse's spanwise width is the same. However, when the ellipse is oriented such that its major axis is parallel to gravitational pull (i.e. $e_c = 1.25$), the affine increase of the pressure contribution to the drag force is less inclined than for the network contribution.

greater deformation on the foam as it sediments. It can be seen in figure 6.12 that more lateral motion of the bubbles occurs when the ellipse has its major axis perpendicular to gravity. It can also be seen in figure 6.13 that the regions of high pressure in front and low pressure behind the ellipse are maximized when the ellipse is oriented such that its major axis is perpendicular to gravity. As a result, the pressure contribution to the drag force is at its greatest when the ellipse is oriented in this manner (see figure 6.7).

6.2.1.2 Vary Ellipse Eccentricity

The relation between the network and pressure contributions to the drag force and the sedimenting object's shape is probed further by considering further variations of the ellipse shape by varying its eccentricity. In this case, the ellipse area is kept constant at $4A_b$ and ellipse eccentricities of $e_c \in \{0.7, 0.8, 0.9, 1, 1.11, 1.25, 1.43\}$ are used. These eccentricities represent three ellipses with their major axis perpendicular to gravity ($e_c \in \{0.7, 0.8, 0.9\}$), the circle ($e_c = 1$) and three equivalent ellipses with their major axis parallel to gravity ($e_c \in \{1.11, 1.25, 1.43\}$). As in the previous section, the ellipses sediment from a central position at the top of the channel through foam E (see table 2.1) with liquid fraction $\Phi_l = 4 \times 10^{-3}$ under their own weight ($mg = 10$).

Figure 6.5 shows how the network and pressure contributions to the drag force vary with ellipse eccentricity. It can be seen that the network contribution to the drag force decreases affinely as the eccentricity of the ellipse is increased from $e_c = 0.7$ to $e_c = 1.43$. As shown in the previous section (6.2.1.1), the network drag is at its greatest when a long, thin ellipse ($e_c = 0.7$) is oriented such that its major axis is perpendicular to gravity. The minimum value for the network contribution to the drag force occurs when the same shaped ellipse is oriented such that its major axis is parallel to gravity (i.e. $e_c = 1.43$).

The pressure contribution to the drag force has a non-linear relationship with ellipse eccentricity. For the ellipses oriented such that their major axes are perpendicular to gravity ($e_c \in \{0.7, 0.8, 0.9\}$), the pressure component of the drag decreases steadily with increasing eccentricity. However, this decrease in the pressure contribution of the drag force lessens when the ellipse eccentricity is increased so that its major axes is

parallel to gravity ($e_c \in \{1.11, 1.25, 1.43\}$). In this case, the pressure contribution of the drag tends to a constant value close to zero. The data showing the relation between the pressure contribution to the drag force and ellipse eccentricity is best described by a power-law relation with a coefficient of -3.66 (see figure 6.5). It has been shown already in section 6.2.1.1 that the pressure contribution to the drag force is much more prominent when the ellipse is oriented such that its major axis is perpendicular to gravity ($e_c \in \{0.7, 0.8, 0.9\}$). This was proposed to be the result of more bubbles being squeezed underneath the ellipse, applying a greater pressure drag force. Conversely, when an ellipse is oriented so that its major axis is parallel to gravity ($e_c \in \{1.11, 1.25, 1.43\}$), less bubbles are squeezed by the descending ellipse and the pressure contribution to the drag is minimal. The transition of the shape of the ellipse between these two extremes greatly affect the flow field imposed in the foam; this is investigated in detail in section 6.3.2 for a free rotating ellipse.

By considering these two specific orientations of the ellipse sedimenting in foam, the nature of the network and pressure contributions to the drag force has been exposed. It has been shown that the network contribution to the drag, exerted by the foam films, is dependent on the size of the obstacle and its orientation. It is shown in the next section 6.2.2 that the network contribution to the drag force is dependent only on the spanwise width of the ellipse, which is a function of the ellipse area, eccentricity and orientation defined by equation 6.2. The relation between the pressure contribution of the drag force and ellipse area and eccentricity has been shown to be slightly more complex.

6.2.2 Major Axis at a Acute Angle to the x-axis

In this section, the orientation of the ellipse during sedimentation is kept fixed so that its major axis makes an acute angle ϕ with the horizontal line (see figure 6.6). This angle of orientation is varied in the range $-\pi/2 < \phi < \pi/2$. Thus, for the range $0 \leq \phi < \pi/2$ the major axis has been rotated clockwise an amount ϕ from the horizontal line (see figure 6.6(a)); similarly when $-\pi/2 < \phi < 0$, it has been rotated an amount ϕ in an anticlockwise direction to the horizontal line (see figure 6.6(b)). The dependence of the

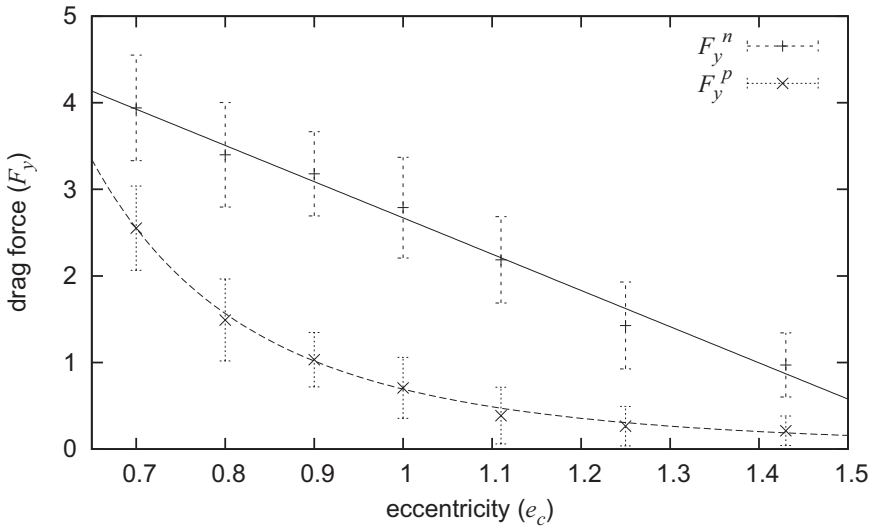

Figure 6.5: The average network and pressure contributions (with standard deviation error bars) to the drag force exerted on a sedimenting ellipse of area $A_e = 4A_b$, weight $mg = 10$ and of different eccentricities. In all, the eccentricities used are $e_c \in \{0.7, 0.8, 9, 1, 1.11, 1.25, 1.43\}$. In this case, the first three ellipses ($e_c \in \{0.7, 0.8, 0.9\}$) are oriented such their major axes are perpendicular to the direction of gravity. The fourth ellipse ($e_c = 1$) represents a circular disc. The last three ellipses ($e_c \in \{1.11, 1.25, 1.43\}$) are equivalent to the first three, but their major axes are directed parallel to the direction of gravity. Increasing the ellipse eccentricity in this manner leads to a affine decrease in the network contribution to the drag force. The pressure contribution decreases with a non-linear relationship with the ellipse eccentricity. In this case, the data relating the pressure contribution to the drag force and ellipse eccentricity is best fitted by the power-law relation $F_y^p = 0.69 e_c^{-3.66}$.

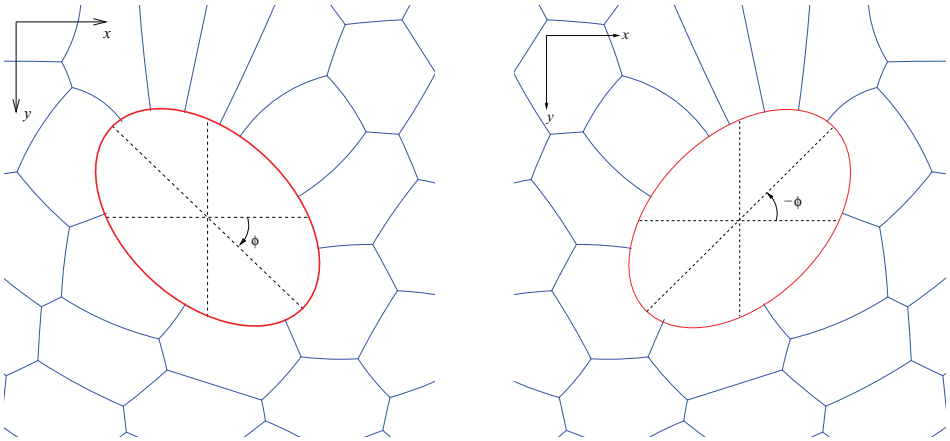

(a) (b)

Figure 6.6: The angle of orientation ϕ (i.e. the angle between the ellipse's major axis and the horizontal line) is varied in (a) the clockwise (positive) direction and (b) the anticlockwise (negative) direction.

drag and lift force, as well as the torque exerted on the ellipse with its orientation is investigated here.

The drag and lift force exerted on an ellipse of area $A_e = 4A_b$, eccentricity $e_c = 0.8$ and weight mg sedimenting in foam E (see table 2.1) with liquid fraction $\Phi_l = 4 \times 10^{-3}$ for different angles of orientation is shown in figure 6.7. It can be seen that the network and pressure contributions to the drag force are at their largest when the ellipse is oriented such that its major axis is close to being perpendicular to gravity (i.e. ϕ is close to zero). These contributions decrease affinely as the angle for the ellipse's orientation is increased in either direction. Both contributions to the drag are minimized when the ellipse is oriented so that the major axis is parallel to gravity. This is expected to be the case, since the drag force depends on the spanwise width (the cross-sectional width perpendicular to the direction of motion, as shown in figure 6.1) of the ellipse, defined by

$$l_s = 2r_0 \sqrt{\frac{1}{e_c^2} \cos^2 \phi + e_c^2 \sin^2 \phi} \, . \tag{6.2}$$

As the angle of orientation is increased, the spanwise width (l_s) of the ellipse decreases (for $e_c < 1$, the opposite is true when $e_c > 1$), whence the drag force it experiences decreases as well. Dollet *et al.* [69] calculated the forces exerted on an ellipse in a

2D pressure driven flow of foam. Their experiment had the ellipse fixed to a base by an elastic fibre and it was free to rotate due to the torque applied by the foam. It was shown in this work that a drag force increased affinely with the ellipse's spanwise width. A similar result is expected when an ellipse of fixed orientation is allowed to sediment under its own weight in the foam. Figure 6.7(b) shows that the drag force exerted on an ellipse of area $4A_b$ increases affinely with spanwise width l_s for ellipses of eccentricities $e_c = 0.8$ and $e_c = 0.7$. It can be seen that the eccentricity of the ellipse has a small effect on the relationship between drag and spanwise width as the slope of the fitted data changes slightly. In this case, the drag force increases at a slightly greater rate with spanwise width for the ellipse of eccentricity 0.8 (i.e. the most round shape) than that with eccentricity 0.7. In this case, the drag force exerted on the obstacle falling through the foam is dependent on the spanwise width and shape of the object.

Previously, the lift force exerted on an ellipse sedimenting from a central position was shown to be negligible (see figure 6.8(a)). This is only the case when the ellipse sediments with fixed orientations such that its major axis is either parallel or perpendicular to gravity. In this case, the ellipse is symmetric about the central vertical line of the foam channel. Thus, the resulting flow of the foam as the ellipse descends is also symmetric about the centre line of the channel. Wall effects on the forces exerted on the ellipse are deemed to be negligible when the sedimentation occurs from a central position in the foam channel, as shown for a circular disc (see §3.3). However, when an ellipse is oriented such that its major axis makes a non-zero angle with the horizontal line, the symmetry is broken. In this case, the lift force exerted on the ellipse by the foam may be non-zero.

This lift force for a tilted ellipse (with $A_e = 4A_b$ and $e_c = 0.8$) is shown in figure 6.8(a). When the angle of orientation is zero, the average lift exerted on the ellipse is close to zero. In this case the ellipse has its major axis perpendicular to the direction of gravity, an orientation which is shown to be metastable for the ellipse in section 6.3.3. The lift force is also close to zero when the angle of orientation is close to $\pi/2$; in this case the ellipse has its major axis directed parallel to gravity. This orientation is shown to be the stable orientation for the ellipse when it sediments through the foam

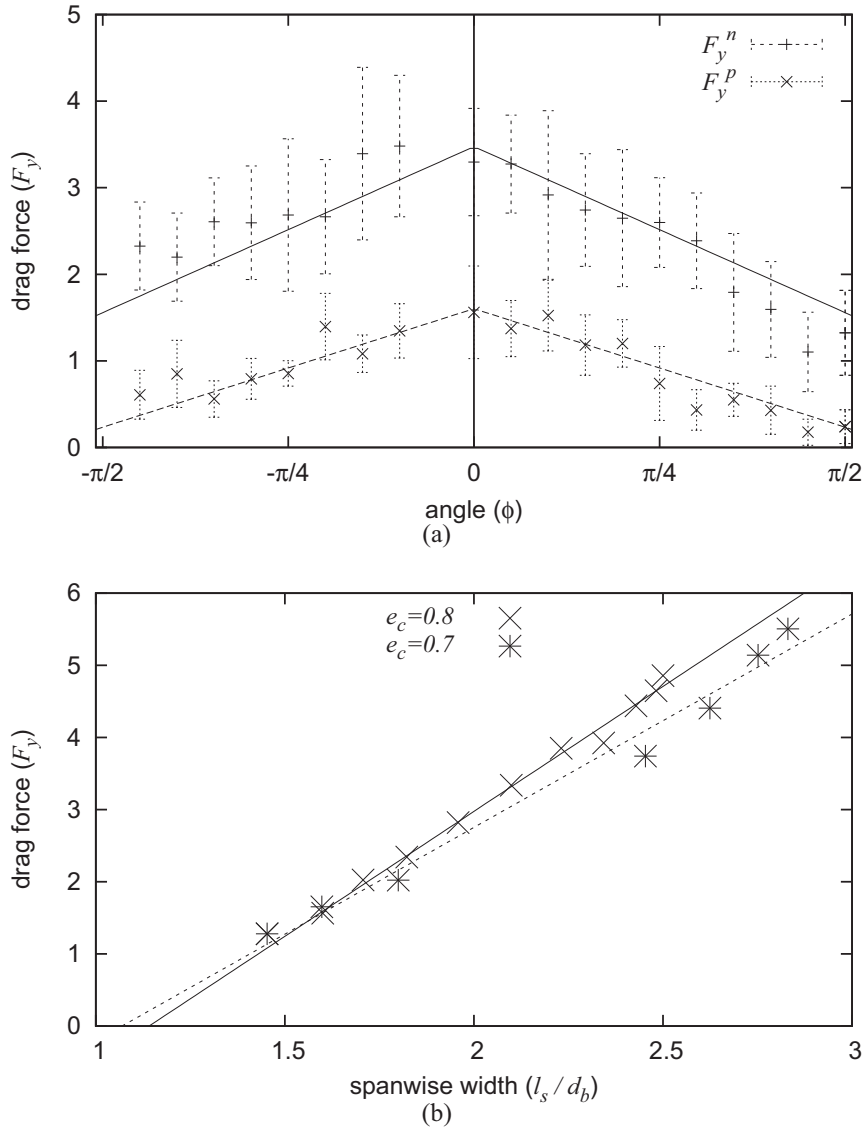

Figure 6.7: (a) The relationship between both the network and pressure contributions to the drag force exerted on the ellipse and its orientation. In this case, the ellipse has area $4Ab$, eccentricity 0.8 and weighs $mg = 10$. It sediments in foam E (see table 2.1) with liquid fraction 4×10^{-3}. The average values of the network and pressure contributions are taken after a transient stage of the simulation and are accompanied by standard deviation error bars. Both contributions of the drag force decrease affinely as the orientation of the ellipse is increased from $\phi = 0$ in the clockwise and anticlockwise direction. The affine decrease of the network contribution with ϕ has a slope of -1.22; this slope is -0.87 for the pressure contribution. (b) The total drag force increases affinely with the spanwise width l_s of the ellipse (which is varied by changing the angle ϕ), for eccentricities of $e_c \in \{0.7, 0.8\}$ as found in the work of Dollet *et al.* [69]. The rate of this affine increase is dependent on the shape of the ellipse; the slope is 2.96 when $e_c = 0.7$ and 3.46 when $e_c = 0.8$.

in section 6.3.3. For angles of orientations other than these two values, the average lift force exerted on the ellipse is non-zero (but small). The direction of the lift force applied is dependent on the direction to which the ellipse is oriented relative to the horizontal direction. Thus, a positive lift (directed to the right) is exerted when the ellipse's orientation lies in the range $0 < \phi < \pi/2$ and is negative (to the left) when the ellipse is oriented such that $-\pi/2 < \phi < 0$. This means that the lift force is directed in the same direction as the front of the ellipse is tilted, in which case the ellipse drifts laterally in this direction during sedimentation. The overall motion of the ellipse is however, still downwards as the lift force is much less than the weight and drag exerted on the ellipse.

The orientation of the ellipse is expected to affect the amount of torque exerted on it by the foam. For the stable and metastable orientations, ($\phi = 0$ or $\phi = \pi/2$) the torque experienced by the ellipse is close to zero. This is shown to be the case in figure 6.8(b). Tilting the ellipse so that its major axis makes an acute angle with the horizontal line, results in non-zero torque. Evidence for this is shown in figure 6.8(b); the torque exerted on the ellipse peaks when it is oriented between $\phi = 0.2\pi$ and $\phi = 0.3\pi$ in the clockwise or anticlockwise direction. The value for the torque when the ellipse is oriented such that $0.2\pi < \phi < 0.3\pi$ is positive, meaning that the ellipse wants to rotate in the foam in a clockwise direction so that its major axis becomes parallel to the direction of gravity. Similarly, when the ellipse is oriented such that $-0.3\pi < \phi < -0.2\pi$, the torque is negative meaning that the ellipse wants to rotate in the anticlockwise direction (so that its major axis becomes parallel to gravity). As seen for the network and pressure contributions to the drag and lift forces, the network contribution to the torque is greater than the pressure contribution.

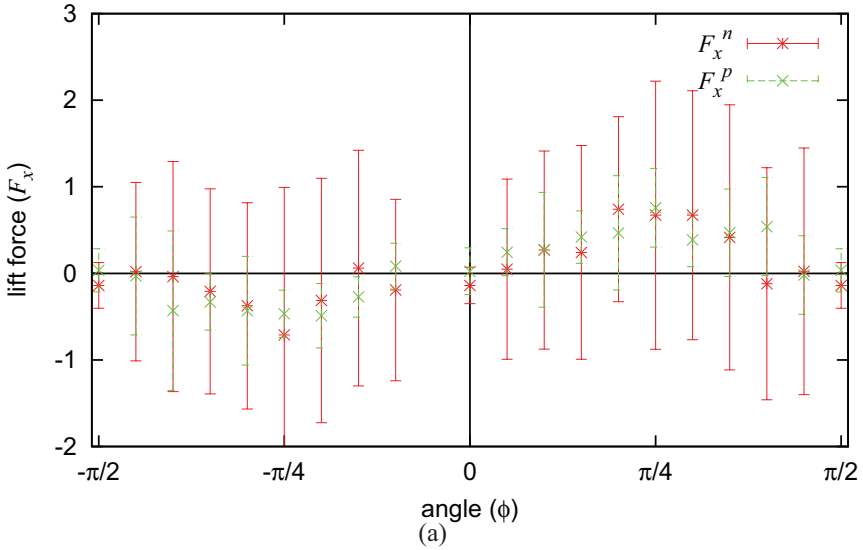

(a)

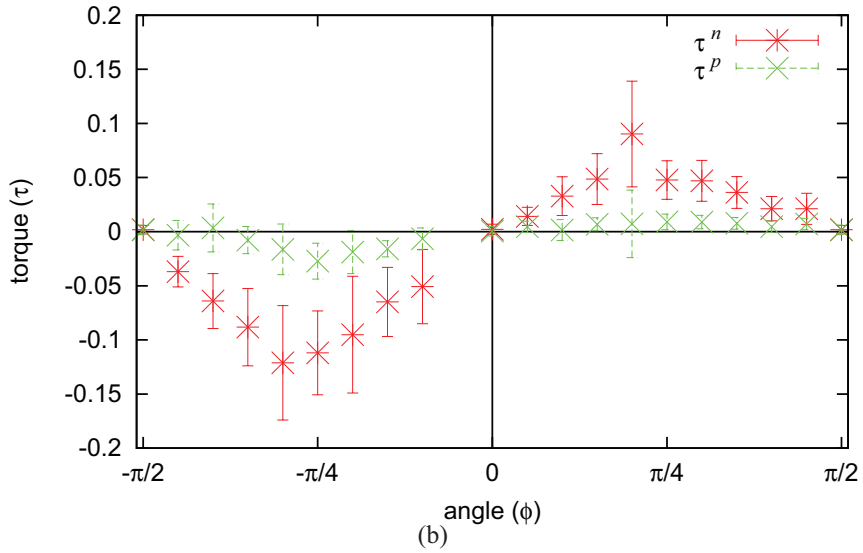

(b)

Figure 6.8: The average network and pressure contributions (with standard deviation error bars) to the (a) lift force F_x and (b) torque τ exerted on an ellipse of area $A_e = 4A_b$, eccentricity $e_c = 0.8$ and weight $mg = 10$ as its angle of orientation ϕ is varied (but kept fixed during a single simulation). The lift and torque are clearly non-zero for values of ϕ close to $\pm\frac{\pi}{4}$. The lift pushes an ellipse that is oriented in this way sideways as it sediments through the foam while the torque applied would rotate the ellipse such that its major axis becomes parallel to gravity. The torque when the orientation of the ellipse is such that its major axis is perpendicular to the direction of gravity (i.e. when $\phi = 0$) is close to zero. This is shown in further sections of this chapter to be a metastable orientation of the ellipse. Similarly, the torque is near to zero when the orientation of the ellipse is such that its major axis is in the direction of gravitational pull (i.e. when $\phi = \frac{\pi}{2}$). Note that the variation with orientation of the pressure contribution to the torque is less apparent than that seen for the network contribution.

6.3 Sedimentation of a Freely Rotating Ellipse in a 2D Dry Foam

In this section, the ellipse is allowed to rotate during sedimentation. This rotation is dependent on the torque exerted on the ellipse by the foam. The stable orientation for the ellipse is found to be such that its major axis is parallel to the direction of gravity. In this section, an example of a simulation where an ellipse rotates from a metastable orientation to the stable orientation is discussed in detail (§6.3.1). The foam fields during the sedimentation and rotation of this ellipse are studied in section 6.3.2. The initial orientation of the ellipse is then varied and its effect on the motion of the ellipse discussed in section 6.3.3. Variation of control parameters such as ellipse area (§6.3.4), eccentricity (§6.3.5) and weight 6.3.6 yields more information about the foam's response and the reasons for the rotation of the ellipse.

6.3.1 Metastable to Stable Orientation

In this section, an ellipse of area $A_e = 4A_b$, weight $mg = 10$, eccentricity $e_c = 0.8$ is left to sediment freely from a central position at the top of the foam channel for foam F. It is initially oriented so that its major axis is perpendicular to gravity, in which case $\phi_{init} = 0$.

Figure 6.9(a) shows how the ellipse rotates into a stable orientation of $\phi = \pi/2$, in which case its major axis is parallel to the direction of gravity. Notice that the increase in the angle of orientation ϕ is initially very slow and the ellipse remains close to its initial orientation for the first 50 iterations. It was shown in section 6.2.2 that the torque exerted on an ellipse sedimenting with a fixed orientation such as this is minimal; whence this initial orientation of the ellipse is metastable. It requires a fluctuation in force exerted on the ellipse to trigger any rotation. Such a fluctuation can occur at any stage of the simulation due to the disordered nature of the foam; it occurred after nearly 30 iterations in the example shown here. Once the rotation of the ellipse has begun, the major axis rotates until it is parallel to the direction of gravity. After reaching this

orientation, the ellipse motion is stable and only slight fluctuations in the orientation occur. Figure 6.9(b) shows that the ellipse drifts laterally as it descends through the foam. This lateral motion reduces as the ellipse reaches its stable orientation.

The rotation occurs as the ellipse sediments due to the positioning of the foam films and the deformation of bubbles along the boundary of the ellipse. It can be seen in figure 6.10 that the foam films bunch up at the highest point of the ellipse as it sediments. The bunching up of the films on the ellipse boundary when it is oriented close to the metastable orientation (see figure 6.10(a)) can occur at a position on the ellipse boundary that is off-centre. This results in a non-zero network torque being applied on the ellipse by the foam. The films can be seen to bunch up slightly to the left of the ellipse's centre of mass, applying a clockwise torque that rotates the ellipse such that its major axis becomes parallel to the direction of gravity. Once the ellipse is oriented in this stable orientation, the films are more evenly distributed around the ellipse boundary. At the same time the distribution and shape of the bubbles that surround the ellipse become less deformed when the ellipse is in the stable configuration. When the ellipse is oriented so that its major axis is perpendicular to gravity, bubbles in its wake are highly elongated and the bubbles beneath are squeezed. However, when the ellipse is in the stable orientation, the elongation and squeezing of the bubbles is less apparent.

The network and pressure contributions to the drag, lift and torque exerted on the ellipse are therefore minimized when the ellipse is oriented such that its major axis is parallel to gravity. Figure 6.11 shows how these contributions vary during the sedimentation of the ellipse from the metastable to the stable orientation. It can be seen that during the rotation of the ellipse, both contributions to the drag force decrease. It was shown in section 6.2.2 that the magnitude of the network and pressure contributions to the drag force were dependent on the spanwise width l_s of the ellipse. This width is decreasing as the ellipse rotates, whence both contributions to the drag force decrease.

The variations of the network and pressure contributions to the lift force exerted on the ellipse are shown in figure 6.11(b). It can be seen that the network and pressure lift exerted on the ellipse is maximized when it is oriented so that its major axis is far from being parallel or perpendicular to the direction of gravity. This non-zero lift forces the

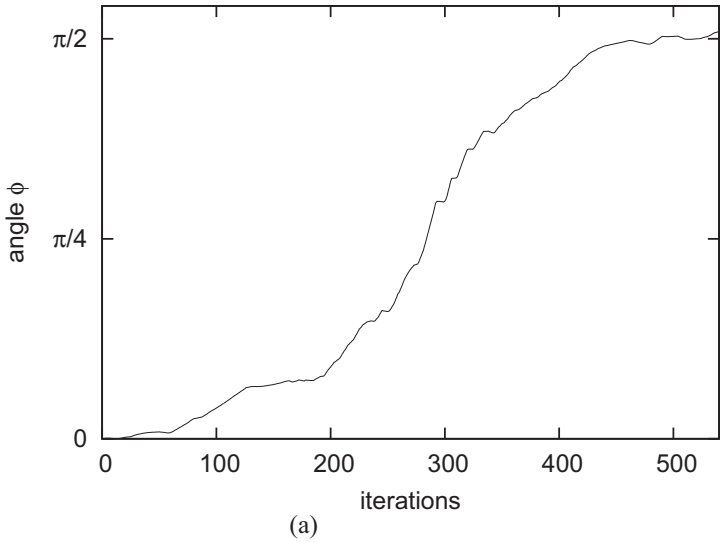

(a)

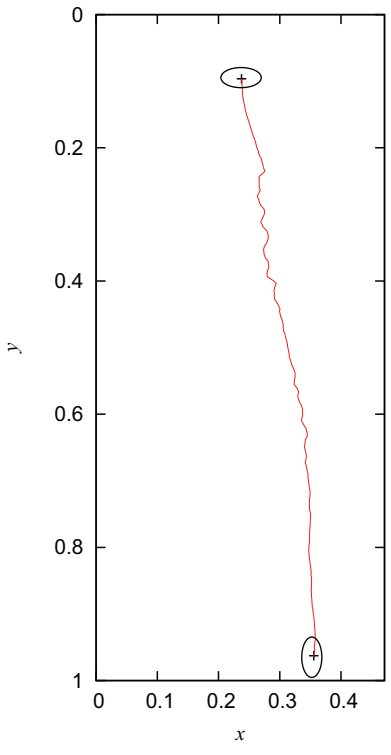

(b)

Figure 6.9: An ellipse of area $4A_b$, eccentricity 0.8 and weight 10 is left to sediment freely from being initially oriented such that its major axis is perpendicular to gravity (i.e. $\phi_{init} = 0$). (a) In this case, the angle of orientation increases until the ellipse is oriented such that its major axis is parallel to gravity. This orientation proves to be stable for the elliptical object. (b) Tracking the ellipse as it descends through the foam shows that it drifts laterally in the channel as it rotates towards a stable orientation. This lateral motion stops once the ellipse's major axis is parallel to gravity.

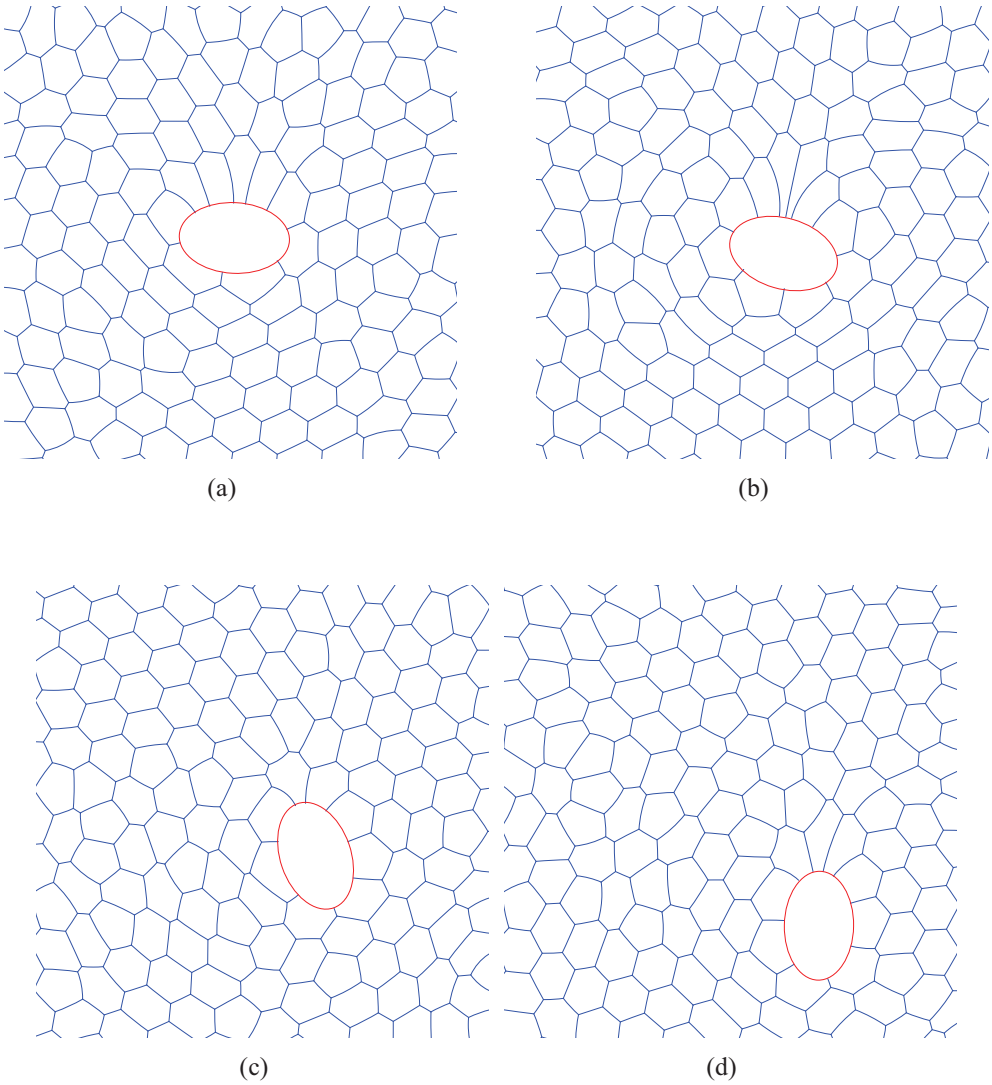

Figure 6.10: The position of an ellipse of area $A_e = 4A_b$, eccentricity $e_c = 0.8$ and weight $mg = 10$ sedimenting in foam F from being initially oriented such that its major axis was perpendicular to gravity (i.e. $\phi_{init} = 0$). (a) The position of the ellipse at the $50th$ iteration. The ellipse is oriented so that its major axis is close to being perpendicular to the direction of gravity. This is a metastable orientation that requires a fluctuation in the force exerted on the ellipse by the foam to trigger rotation. (b) The position of the ellipse at the $150th$ iteration. Its orientation has begun to rotate as a result of films beginning to bunch up in the wake of the ellipse slightly to the left of its centre of mass. This results in a torque being applied in the clockwise direction; whence the ellipse rotates. (c) The ellipse's orientation for the $250th$ iteration. Further rotation of the ellipse has occurred by this stage. (d) The ellipse's orientation is stable by the $350th$ iteration. In this case, the major axis of the ellipse is close to being parallel to the direction of gravity.

ellipse to move laterally during sedimentation. However, this lateral drift does not occur for long as the angle of orientation increases so that the ellipse becomes oriented in its stable configuration. Both contributions to the lift force fluctuate around the value zero when the ellipse reaches its stable orientation. The contributions to the lift are much smaller than the difference between the total force and the ellipse weight, ensuring that the downward motion of the ellipse is greater than any lateral motions at all time.

The variation in the network and pressure contributions to the torque experienced by the elliptical object as it sediments is shown in figure 6.11(c). It can be seen that both contributions to the torque are minimal when the ellipse is in both the metastable and stable orientation (i.e. the beginning and the end of the simulation). However, both have small non-zero values during the majority of the sedimentation where rotation of the ellipse is seen. Both the network and pressure torque fluctuate during the sedimentation of the ellipse. The torque applied by the foam films (network) is greater than the pressure torque at all times. Both contributions are in the clockwise direction, ensuring that rotation of the ellipse is clockwise in this case.

6.3.2 Foam Fields

As for the circular disc case, understanding of the rheology of the foam by looking at the sedimentation of such objects requires visualization of the foam fields during this process. Here, the bubble displacement and pressure fields of the foam as well as the positions of T1 events yield more information about the role that the elasticity and plasticity of the foam play during the sedimentation of an elliptical object.

6.3.2.1 Bubble Displacement

The displacement of the bubbles over intervals of 30 iterations while the ellipse sediments from being initially in the metastable orientation is presented in figure 6.12. The initial orientation of the ellipse is metastable and the flow of the bubbles in the earliest interval demonstrated (figure 6.12(a)) is relatively symmetric around the object. The asymmetry of the flow of the foam is broken as the ellipse rotates from the metastable

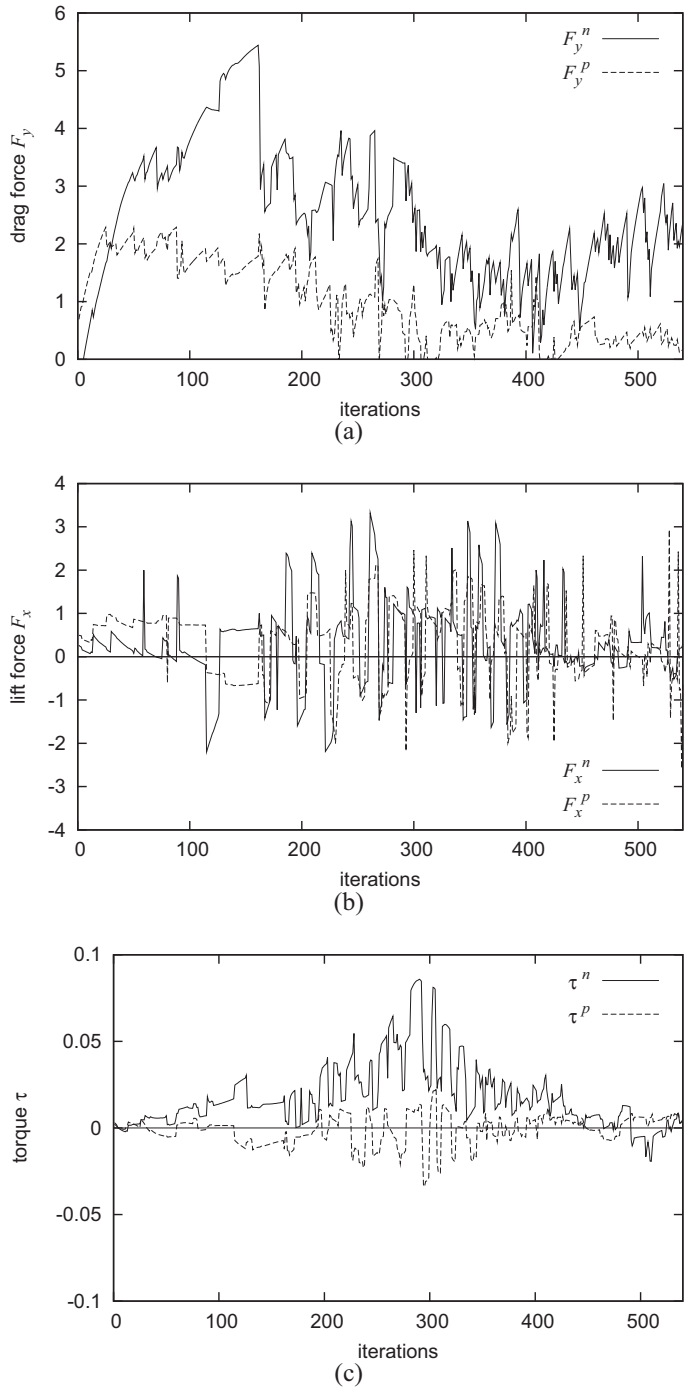

Figure 6.11: The network and pressure contributions to the (a) drag force, (b) lift force and (c) torque exerted on the ellipse of area $4A_b$, eccentricity 0.8 and weight 8 as it sediments (in foam F with $\Phi_l = 4 \times 10^{-3}$) from an initial metastable orientation (ϕ_{init}) to a stable orientation ($\phi \approx \pi/2$). The variation of these contributions is analysed in the text of section 6.3.1.

orientation (see figures 6.12(b) and 6.12(c)). In this case, the semi-circular pattern for the bubble displacements previously seen either side of the object becomes exaggerated to the left of the ellipse while the flow to the right is reduced. This proves to be the case as the ellipse is oriented such that its leading point is to the right of its centre of mass; thus the bubbles slip along the underside of the ellipse to the left. The symmetry of the flow is recovered as the ellipse moves into its stable orientation where its major axis is parallel to gravity (see figure 6.12(d)).

6.3.2.2 Bubble Pressure Field

The bubble pressure field directly affects the motion of the ellipse through the foam. As in previous chapters studying the sedimentation of circular discs through the foam, the bubbles can be colour-coded with respect to their relative pressure compared to a specific bubble.

Figure 6.13 demonstrates how the pressure field of the foam varies when the ellipse sediments from its initial metastable orientation into the stable orientation. The region of high pressure that is expected directly below the ellipse is at its most prominent when the ellipse has its major axis perpendicular to the direction of gravity. This is the orientation of the ellipse where the bubble pressure contributes the most to the drag force exerted on the ellipse. As the ellipse rotates into the stable orientation, this region of high pressure is reduced. This results in a smaller contribution to the drag force from bubble pressures. During rotation, the region of high pressure is slightly to the left of the ellipse's centre of mass. Thus, the region of high pressure is contributing to the torque that is applied on the ellipse in the clockwise direction, resulting in the rotation to the stable orientation. Meanwhile, the region of low pressure in the wake has a greater width when the ellipse sediments in the metastable orientation than when it reaches the fully stable orientation.

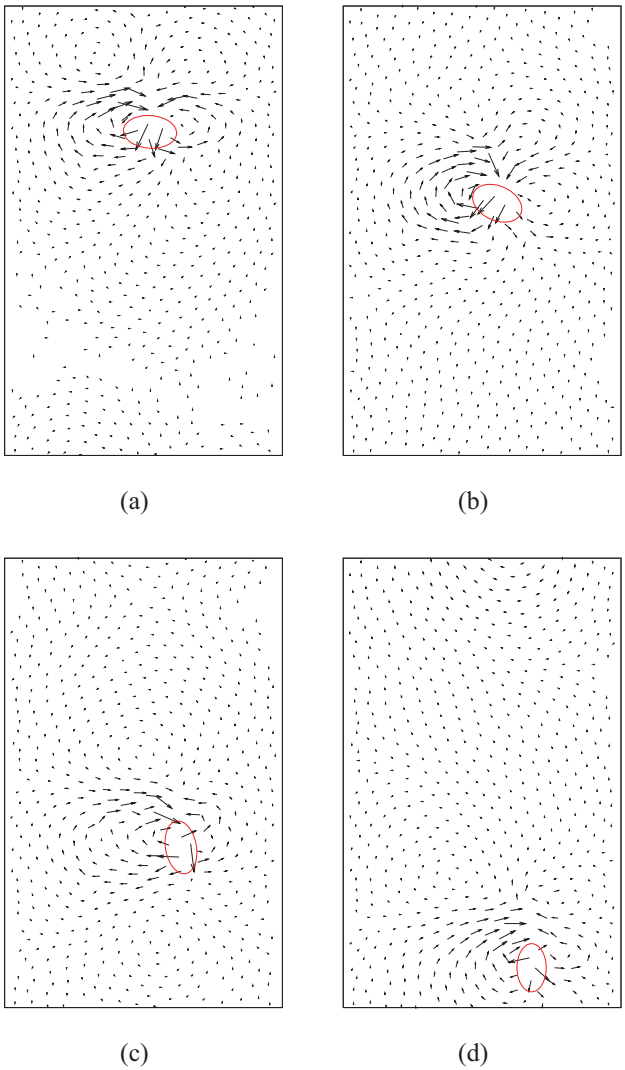

Figure 6.12: The bubble displacement field of foam F when an ellipse with eccentricity $e_c = 0.8$, area $A_e = 4A_b$ and weight $mg = 10$ sediments from being initially oriented such that its major axis is perpendicular to gravity (i.e. $\phi_{init} = 0$). Bubble centre points are recorded every 30 iterations and their displacement during this period is denoted by arrows. The fields shown represent the intervals (a) 60 – 90 iterations, (b) 150 – 180 iterations, (c) 240 – 270 iterations and (d) 330 – 360 iterations. The movement of bubbles is highest very close to the ellipse. The first plot (a) demonstrates the foam flow field when the ellipse is still in its metastable orientation. In this case the flow field is symmetric and a negative wake can be seen above the ellipse. The second and third plot (b and c) demonstrate intervals in the simulation where the ellipse is in the process of rotating. In this case the foam flow is not symmetric. The last plot (d) demonstrates an interval in the simulation when the ellipse has fully rotated into its stable orientation. In this case the flow symmetry is recovered.

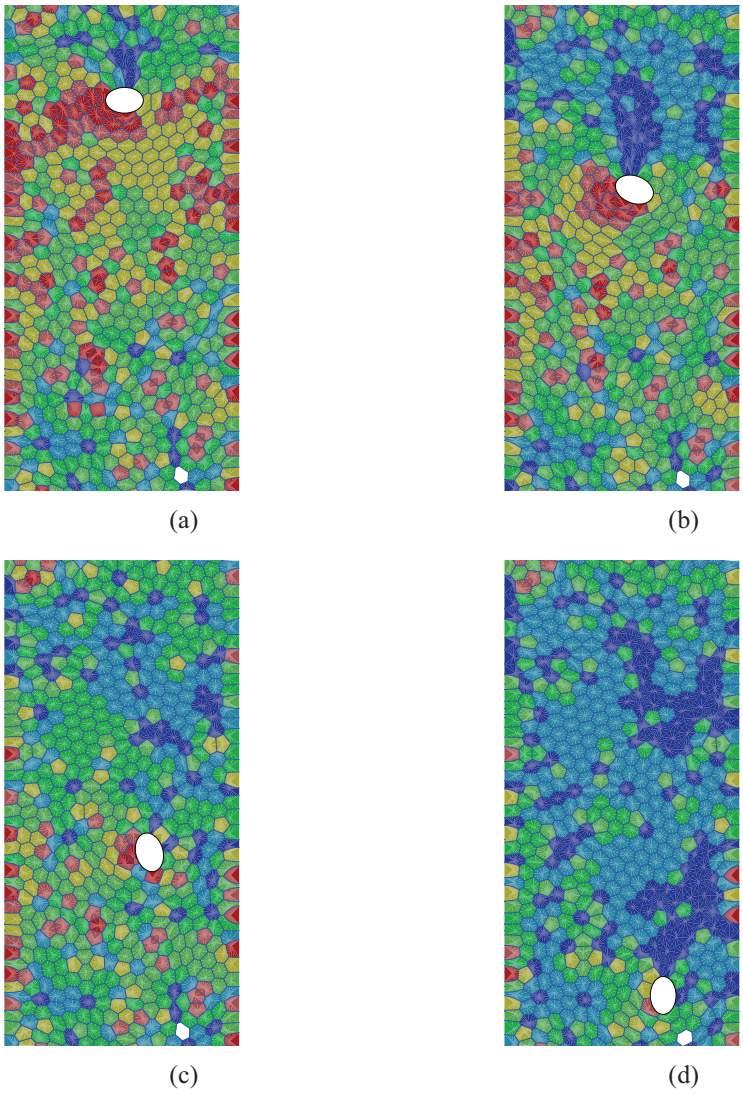

Figure 6.13: Bubble pressure field within a foam when an ellipse with eccentricity $e_c = 0.8$ and area $A_e = 4A_b$ sediments from being initially oriented such that its major axis is perpendicular to gravity (i.e. $\phi_{init} = 0$). Bubble pressures are colour coded with the pressure increasing with the order dark blue, light blue, green, light green, light red to red. The pressure field for the (a) 50^{th} iteration, (b) 150^{th} iteration, (c) 250^{th} iteration and (d) 350^{th} iteration are shown.

6.3.2.3 T1 Positions

The distribution of T1 events as the ellipse sediments and rotates yields information on the role that the foam plasticity has on the motion of the object. As for the circular disc (see §3.5), the yielding of the foam occurs mainly in the first 2 to 3 bubble layers surrounding the object. It is of interest to investigate the positions of T1 events as the ellipse sediments through the foam. In this case, the position of a T1 event which occurs at (x_i, y_i) relative to the ellipse's centre (x_0, y_0) is investigated in terms of the angle θ_{T1} which is defined as

$$\theta_{T1} = \arctan\left(\frac{x_i - x_0}{y_i - y_0}\right), \tag{6.3}$$

and shown in figure 6.14(a).

The positions of T1s in terms of θ_{T1} as the ellipse sediments through the foam is given in figure 6.14(b). It can be seen that during the sedimentation and rotation of the ellipse, the T1s are scattered around the ellipse. However, they are more concentrated for values of θ_{T1} close to $\pm\pi$ and zero. These represent the regions of the foam directly above and below the ellipse respectively. The T1s at $\theta_{T1} = \pm\pi$ occur as a result of elongated bubbles detaching from the object as it sediments. Conversely, T1s occurring at $\theta_{T1} = 0$ are a result of rearrangements where bubbles attach to the object as other bubbles move laterally out of the ellipse's way.

Figure 6.14(b) shows that the manner in which the T1s are scattered about the elliptical object seems independent of the orientation of the ellipse. The orientation of the object as it sediments through the foam has been shown to affect the deformation of the foam. The deformation is minimized when the ellipse is oriented so that its major axis is parallel to gravity. It is therefore to be expected that the number of T1s is reduced when the ellipse is oriented in this way. However, this is not the case for the simulation presented here.

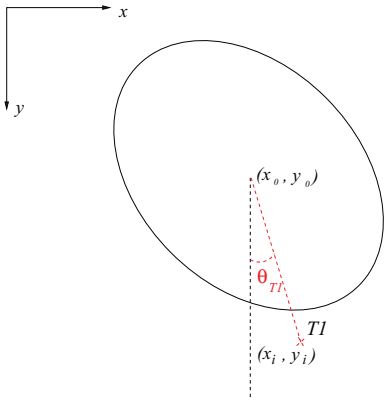

(a)

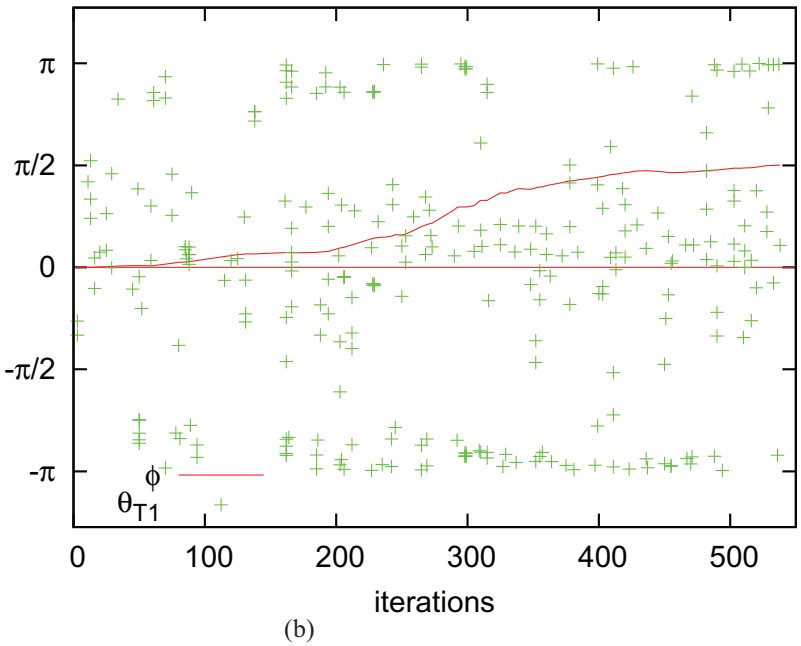

(b)

Figure 6.14: (a) A T1 event occurs at (x_i, y_i). Thus, the angle θ_{T1} (defined by $\tan\theta_{T1} = (x_i - x_0)/(y_i - y_0)$) yields information of how the T1s are scattered relative to the centre point (x_0, y_0) of the ellipse. (b) The distribution of θ_{T1} when an ellipse (of area $4A_b$, eccentricity 0.8 and weight 10) sediments from an initial metastable orientation to a stable orientation is considered. The scattered nature for the distribution of T1s is relatively independent of the orientation of the ellipse. In this case, the distribution of T1s is similar when $\phi = 0$ and when $\phi = \pi/2$.

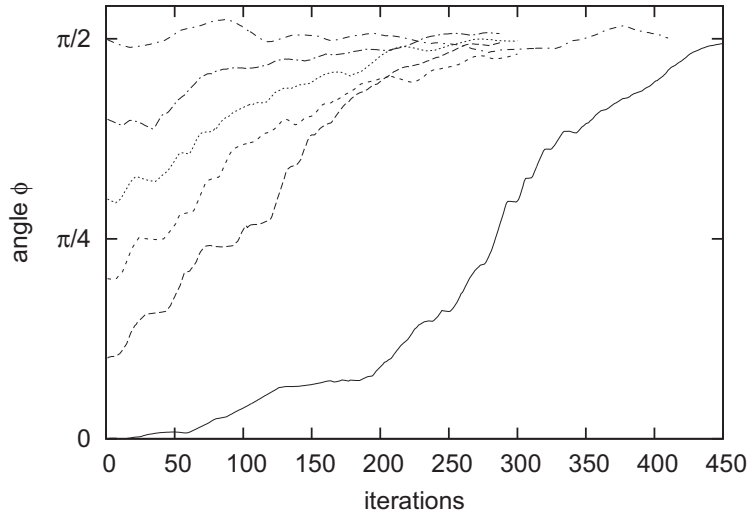

Figure 6.15: Variation of the angle of orientation (ϕ) as the ellipse (with $A_e = 4A_b$ and $e_c = 0.8$) descends through the foam from different initial orientations ($\phi_{init} \in \{0, 0.1\pi, 0.2\pi, 0.3\pi, 0.4\pi, 0.5\pi\}$). In all cases, the orientation of the ellipse rotates such that its major axis becomes parallel to the direction of gravity. In other words, $\phi \rightarrow \frac{\pi}{2}$ when $0 \leq \phi_{init} \leq \frac{\pi}{2}$. The rate of rotation is dependent on the angle of orientation and the maximum values for the gradients of the lines occur when ϕ is close to $\pi/4$. The stability of the orientation where $\phi = \pi/2$ is confirmed here as all the ellipses rotate so that $\phi \rightarrow \pi/2$ after which the rotation is minimal.

6.3.3 Variation of the Initial Orientation of the Ellipse

In this section, the simulation described in section 6.3.1 is repeated for different initial orientations ϕ_{init} of the ellipse. The initial orientations of the ellipse chosen are $\phi_{init} \in \{0.1\pi, 0.2\pi, 0.3\pi, 0.4\pi, 0.5\pi\}$. These are confined to the range $0 \leq \phi_{init} \leq \pi/2$ so that the rotation towards the stable orientation occurs in a clockwise direction. It is assumed by the symmetry of the torque applied on ellipses sedimenting with fixed orientations varied between $-\pi/2$ and $\pi/2$ in section 6.2.2 that the rotational motion of ellipses that are initially oriented so that $\phi_{init} \in \{-0.1\pi, -0.2\pi, -0.3\pi, -0.4\pi\}$ is equivalent but in the opposite direction. The rotational motion of the ellipses sedimenting from these initial orientations is compared to that of the ellipse sedimenting from the metastable orientation (i.e. $\phi_{init} = 0$) in figure 6.15.

It is seen here that the initial orientation of the ellipse only affects the rate to which the ellipse rotates. An ellipse initially oriented in the metastable orientation requires

more iterations to rotate into the stable orientation than for other values of ϕ_{init}. It is also shown that the rate of rotation is at its maximum when ϕ is close to $\pi/4$ since the torque is maximum here.

6.3.4 Varying the Ellipse Area

The process in which the ellipse rotates into a stable orientation is investigated further by varying the area of the ellipse under consideration. In this case, the ellipse eccentricity is kept constant at $e_c = 0.8$ as well as the initial orientation of $\phi_{init} = 0$. Ellipses of area $A_e \in \{2A_b, 4A_b, 6A_b, 8A_b, 10A_b\}$ are left to sediment under their own (fixed) weight $mg = 8$ from a central position in foam F with a liquid fraction of $\Phi_l = 4 \times 10^{-3}$.

The variation in the orientation of these ellipses within the foam during sedimentation is presented in figure 6.16. It is clear that the ellipses of all areas rotate into the stable orientation during the simulation. The initial rotation of an ellipse from the metastable orientation is shown to be dependent on ellipse area. In this case, the smallest ellipse ($A_e = 2A_b$) begins to rotate slightly earlier in the simulation than the others as it has greater mobility, i.e. it is more easily affected by a small perturbation. This ellipse has a spanwise width that is roughly of the same length as a bubble diameter. In this case, an event such as a T1 near the ellipse is more likely to result in a small rotation of the ellipse than for larger ellipses which are in contact with many bubbles.

Once the rotation of the ellipses has begun, the amount they rotate during each iteration is dependent of the ellipse size. It can be seen that the gradients of the graphs of ϕ versus number of iterations in figure 6.16 are greater for larger ellipses. The smallest ellipse considered here ($A_e = 2A_b$) rotates the least during each iteration and doesn't reach its stable orientation within the foam channel. The amount rotated during each simulation increases with ellipse size. Thus, the larger ellipses reach the stable orientation earliest during their descent through the channel (as shown in figure 6.16(b)). As well as experiencing a greater torque than smaller ellipses (see figure 6.17), they are less dense (since the weight is fixed for this section) and therefore descend through the foam at a lesser rate than small ellipses. In this case, the rotation into the stable orientation

occurs further up in the foam channel for the larger ellipses (see figure 6.16(b)).

Here it is shown that the torque exerted on an ellipse as it sediments freely from an initial metastable orientation is highly dependent on its size. The torque exerted on the large ellipse ($A_e = 10A_b$) peaks at roughly three times the maximum value of the torque exerted on the smallest ellipse ($A_e = 2A_b$) when they are in an unstable orientation. The torque exerted on the larger ellipses ($A_e \in \{6A_b, 10A_b\}$) have a distinct peak value where the rate of rotation will be at its greatest. However, the torque exerted on the smaller ellipse does not have an extreme peak value as it is consistently smaller throughout the sedimentation of the ellipse. Therefore the rotation of the small ellipse towards the stable orientation is slower and smoother than for bigger ellipses.

The network and pressure contributions to the total torque exerted on ellipses of size $2A_b$ and $10A_b$ are shown in figure 6.18. Here, it becomes clear that the network contribution to the total torque is greater than the pressure contribution for both the ellipses. The torque applied by the foam films is much larger for a bigger ellipse. This is to be expected as a bigger ellipse is in contact with much more foam films than the smaller ellipse. This is the case as more films are likely to bunch up in a slightly off-centre position in the wake of the bigger ellipse as it descends through a foam (see figure 6.10). It can also be seen that the torque exerted due to the pressure contribution opposes the network contribution during most of the simulation. The rotation of the ellipse is driven by the network contribution to the torque as it has a greater magnitude than the pressure contribution. Therefore, the bubbles that are squeezed by the rotating motion of the ellipse apply a pressure force that opposes the rotational motion. This resistive torque is small in comparison with the network force.

6.3.5 Varying the Eccentricity of the Ellipse

Another parameter that is expected to have an effect on how the ellipse sediments through the foam is its eccentricity. Long, thin objects are expected to rotate at a greater rate than rounded objects. The bunching up of films in the wake of round objects is more likely to occur at a position which is close to the object's centre of mass. However, films

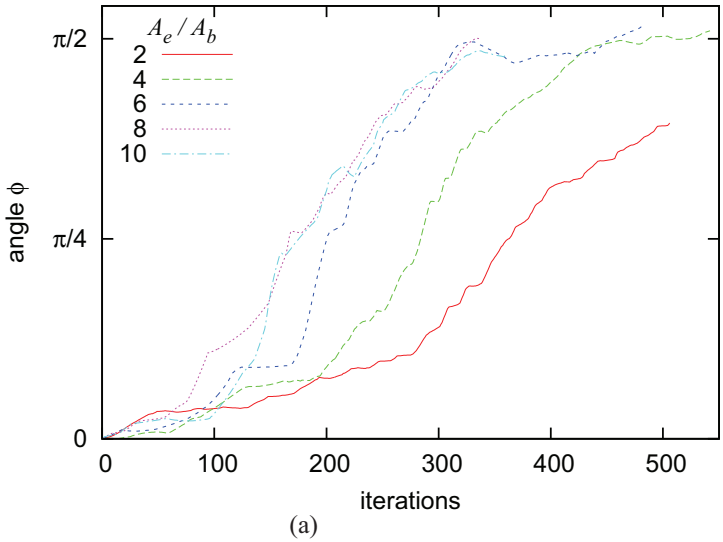

(a)

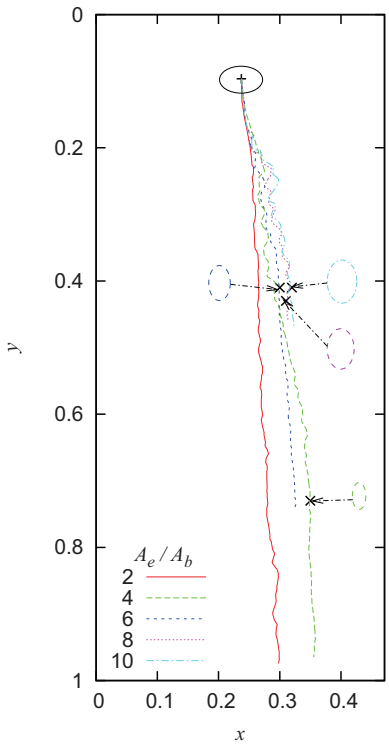

(b)

Figure 6.16: (a) Variation in orientation of ellipses with area $2A_b, 4A_b, 6A_b, 8A_b, 10A_b$ as they sediment through a foam from the metastable orientation. The rate at which the ellipses rotate towards a stable orientation is dependent on their size. (b) The ellipses are tracked during their descent in the foam. They can be seen to drift laterally in a period where they are also rotating towards the stable orientation. The rotation of larger ellipses into the stable orientation occurs higher in the foam channel. These tendencies are discussed in greater detail in the section 6.3.4.

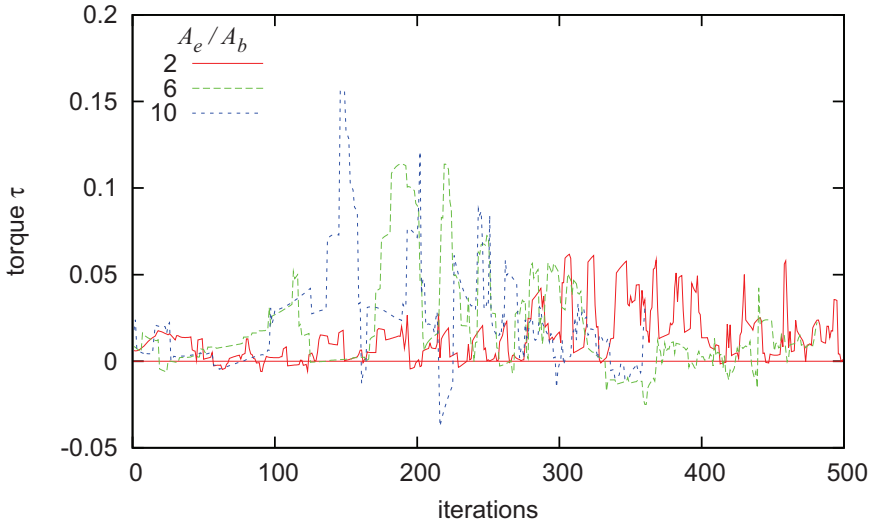

Figure 6.17: The torque exerted on ellipses of area $2A_b$, $6A_b$ and $10A_b$ as they sediment from the metastable orientation (i.e. $\phi_{init} = 0$) towards a stable orientation ($\phi = \pi/2$). The torque exerted during the sedimentation process is dependent on the size of the ellipse. The maximum torque exerted on the ellipse of area $10A_b$ is roughly three times the value for the maximum torque exerted on the ellipse of area $2A_b$. The torque exerted on the smaller ellipse is consistently non-zero throughout the simulation but is of a small magnitude. Thus, the rotation of the small ellipse is more gradual than for the bigger ellipses which rotate at a greater rate whence reaching the stable orientation higher up in the foam. It was found that for all ellipse sizes considered in section 6.3.4, the maximum value for the torque occurred when the ellipse is oriented so that ϕ lies within $\pi/4 - 0.1 \leq \phi \leq \pi/4 + 0.1$.

can bunch up at a position that is far from a long thin object's centre of mass; resulting in a greater network torque being exerted by the foam. The deformation of the bubbles is also greater when a long thin object sediments from a metastable orientation than for round objects (see figure 6.3), whence rotational forces exerted on the object by the foam is greater.

Here, three ellipses of eccentricities $e_c \in \{0.8, 0.85, 0.9\}$, area $A_e = 4A_b$ and weight $mg = 8$ sediment separately in foam F from an initial orientation of $\phi_{init} = 0.1$. The liquid fraction of the foam is again $\Phi_l = 4 \times 10^{-3}$.

The variation in orientation of the three ellipses as they sediment through the foam is shown in figure 6.19(a). It can be seen here that the most eccentric ellipse (i.e. $e_c = 0.8$) rotates in larger steps, thus it reaches the stable orientation higher up in the channel

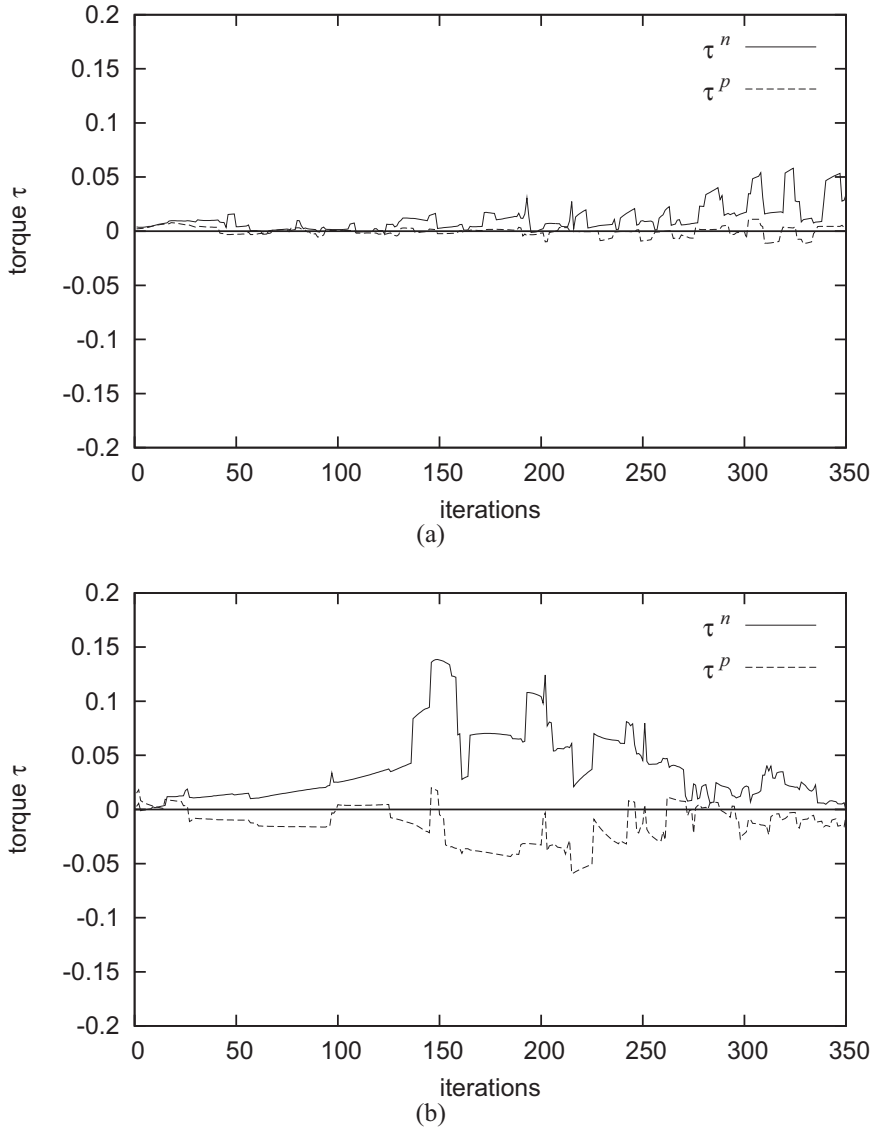

Figure 6.18: Variation in network and pressure contributions (denoted τ^n and τ^p respectively) to the torque exerted during the free sedimentation of ellipses with area (a) $2A_b$ and (b) $10A_b$ from the metastable orientation $\phi_{init} = 0$. It is noticeable that both contributions to the total torque are large in magnitude for the bigger ellipse. The torques exerted due to each contribution opposes each other. The network torque is greater in magnitude than the pressure torque. In this case, the rotational motion of the ellipse is driven by the network contribution to the torque while it is resisted by the pressure contribution.

than the other two ellipses considered (see figure 6.19(b)). The least eccentric ellipse ($e_c = 0.9$) is the ellipse that takes the longest to rotate to the stable orientation. It is also the ellipse that rotates the least between simulation steps. This is the most rounded of the three ellipses and is not far off being a circle ($e_c = 1$). For these simulations, a circular disc experiences zero torque and would not rotate at all.

The importance of the shape of the ellipse on the rate of rotation into the stable orientation is clarified by the amount of torque the ellipse experiences during sedimentation (as seen in figure 6.20). Both the network and pressure contributions of the torque exerted is clearly demonstrated to be greater for a more eccentric ellipse when sedimenting into the stable orientation. This proves to be the case since the angle at which films pull (and bubbles push) the object relative to the centre coordinates of that object is smaller when the object is round. In this case, the rate of rotation of an object decreases as $e_c \to 1$.

6.3.6 Varying the Weight of the Ellipse

In this section, the importance of an ellipse's weight on its motion through the foam is studied. Ellipses that weigh $mg \in \{6, 8, 10, 12\}$ are left to sediment from an initial orientation where $\phi_{init} = 0.1$. Their size is fixed at $A_e = 4A_b$ and they have an eccentricity of $e_c = 0.8$. They sediment in foam F with liquid fraction $\Phi_l = 4 \times 10^{-3}$.

Figure 6.21(a) shows how the orientation of the ellipses of different weight vary as they sediment through the foam. The weights chosen are adequate to ensure that the ellipses descend to the bottom of the foam channel and are not brought to a halt by the network and pressure forces exerted by the foam. The amount of iterations required for these ellipses to rotate to the steady orientation where $\phi = \frac{\pi}{2}$ is similar in all three cases. It is to be expected that the rate at which the ellipses rotate in terms of iterations is independent of ellipse weight. This is the case since the torque exerted by the foam is not dependent on the weight of the object (see figure 6.22). The difference in the motion of the ellipses considered here is that the point in the foam channel where they reach the stable orientation is dependent on their weight. Thus, a heavy object reaches

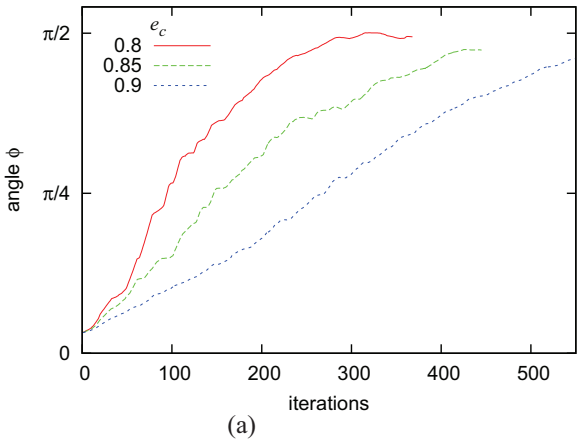

(a)

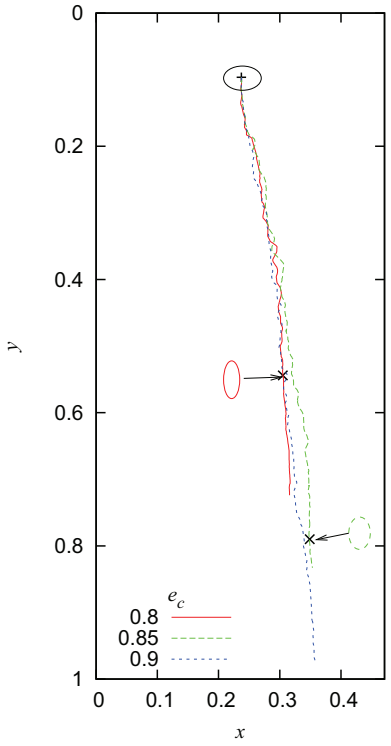

(b)

Figure 6.19: (a) The sedimentation and rotation of ellipses with eccentricities $e_c \in \{0.8, 0.85, 0.9\}$, area $4A_b$ and weight 8, from the initial orientation ($\phi_{init} = 0.1$) into the stable orientation. It can be seen that the ellipse with eccentricity $e_c = 0.8$ rotates at a greater rate to the others. The rate that ϕ increases per iteration decreases with increasing e_c as the ellipse becomes more rounded. (b) The ellipse is tracked during sedimentation. The height in the channel at which the ellipses reach their stable orientation decreases as the ellipses become more rounded. The ellipse with eccentricity $e_c = 0.9$ does not fully rotate to this orientation; a longer channel is required for this to happen.

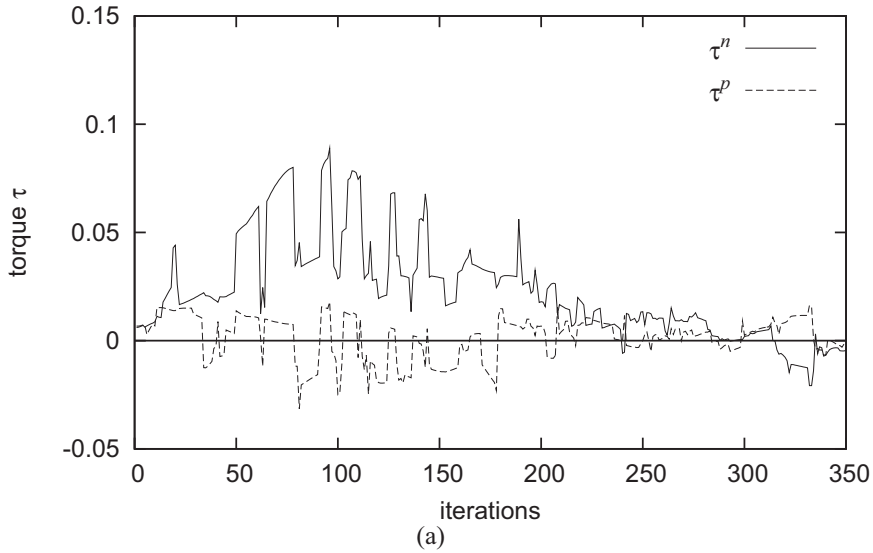

(a)

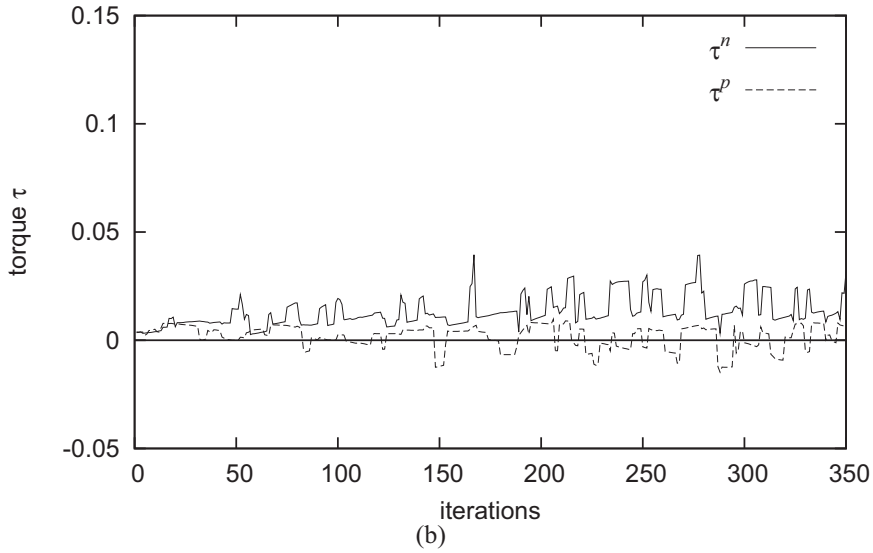

(b)

Figure 6.20: The network and pressure contributions to the torque exerted on an ellipse (of area $4A_b$ and weight $mg = 8$) with eccentricity (a) $e_c = 0.8$ and (b) $e_c = 0.9$ during sedimentation through foam F. The network torque applied on the most eccentric ellipse $e_c = 0.8$ is much greater than that applied on the more round ellipse $e_c = 0.9$. This is also the case for the resistive pressure torque exerted. The smaller values for the torque exerted on the round object are a result of the pull of films and push of bubbles being exerted at a smaller angle to the centre coordinate of the ellipse.

its stable orientation lower in the channel than a light object (see figure 6.21(b)).

6.4 Discussion

In this chapter, the effect that varying control parameters such as the ellipse's area, eccentricity, weight as well as its initial orientation has on its motion through the foam has been studied. Let's consider other factors that may have an effect on how the ellipse descends through the foam.

6.4.1 Varying the Liquid Fraction

The liquid fraction of the foam was kept fixed at $\Phi_l = 4 \times 10^{-3}$ throughout the work presented in this chapter. Looking at the rotation of similar ellipses in a wetter foam could be of interest for future work. I expect that increasing the wetness of the foam would result in slower rotation of the ellipse from a metastable orientation towards its stable orientation.

It was shown in section 6.3 that the rotation of the object towards the stable orientation is driven by the network force exerted due to the foam films bunching up at the back of the ellipse. When the ellipse is inclined in an unstable orientation, the force exerted on it by the high concentration of films that have bunched up is to the left (or right) of its centre of mass. This results in a rotation of the ellipse so that its major axis becomes parallel to gravity. In this case, it is the deformation and distribution of the foam films along the boundary of the object that is the driving force behind the rotation of the ellipse.

Increasing the liquid fraction of the foam would result in less films bunching up behind the ellipse as T1s would be triggered before they become stretched. Thus, the main force that drives the ellipse rotation would be stifled for very wet foam. Work on varying the liquid fraction of the foam would require a different simulation method (as we are confined to the dry limit here).

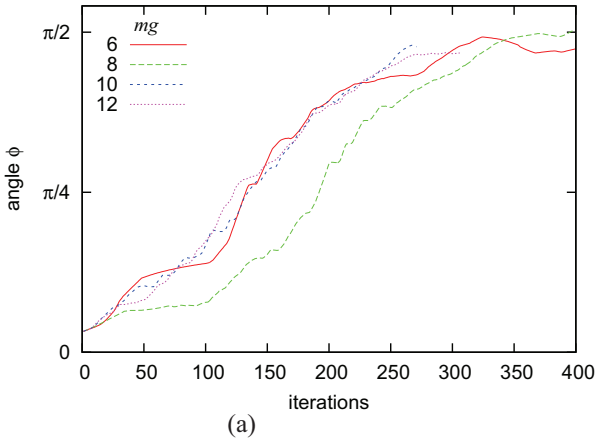

(a)

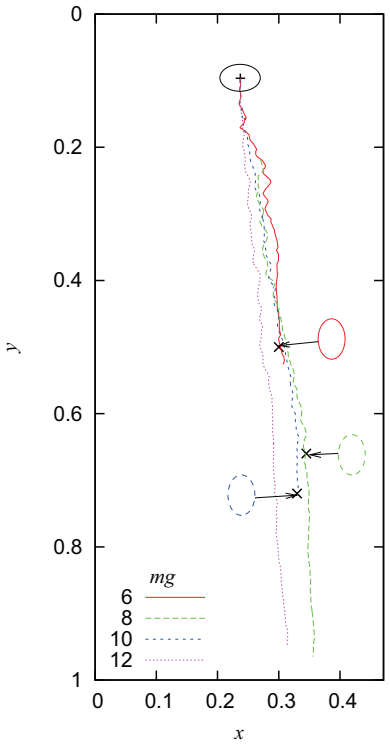

(b)

Figure 6.21: (a) The rotation of an ellipse of eccentricity $e_c = 0.8$ and area $A_e = 4A_b$ from an initial orientation where $\phi_{init} = 0.1$ towards a stable orientation for ellipses that weigh $mg \in \{6, 8, 10, 12\}$. These weights ensure that the objects cannot be supported by the foam. The rate of rotation in terms of iterations is similar for all the different ellipses since the torque exerted by the foam on an object is independent of its weight. (b) The ellipses are tracked and the position at which they reach the stable orientation is shown. The weight of the object determines how much the downward motion dominates the rotational motion of the ellipse.

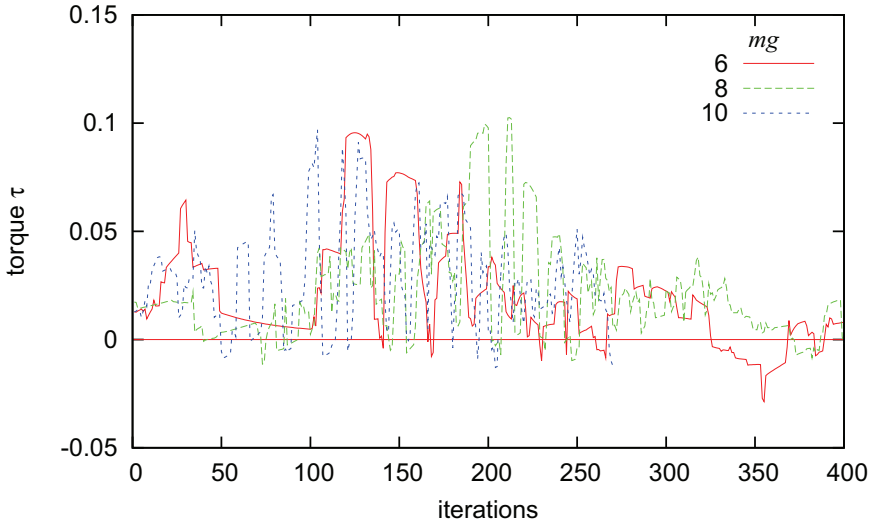

Figure 6.22: The total torque exerted on ellipses of different weight ($mg \in \{6, 8, 10\}$) but a fixed area of $A_e = 4A_b$ and eccentricity $e_c = 0.8$, as they sediment through foam F with liquid fraction $\Phi_l = 4 \times 10^{-3}$. The torque exerted is shown to be independent of the ellipse weight.

6.4.2 Variation of Bubble Area Dispersity

The simulations presented in this chapter are confined to the use of monodisperse foams. In previous chapters on the sedimentation of circular discs, the polydispersity of the foam was considered an insignificant factor in the motion of the objects in the foam. I believe this to be the case also for a sedimenting ellipse. As long as the foam is dry enough, films should bunch up behind the ellipse. In this case, the greater dispersity in bubble area results in films of different lengths bunching up behind the ellipse. In this case, the elastic force that drives the rotation of the ellipse would be more varied during the sedimentation of an ellipse in a polydisperse foam. However, on average, this force would be similar to that exerted in the monodisperse foam. Therefore, the polydispersity of the foam would not affect the overall rotation motion of the ellipse during its sedimentation through a dry foam.

6.4.3 Time-Scales for Ellipse Motion

It was shown in section 2.4.3 that the motion of the ellipse through the foam is governed by two different effective time-scales. In this case, the amount an ellipse is moved in the downward (or lateral) direction relative to the network and pressure forces exerted by the foam is governed by a small constant ϵ_1. However, since the torque applied on the ellipse by the foam is so small, using the same effective time scale for its rotational motion would result in the requirement of very long channels for obtaining any qualitative results. In this case, the amount an ellipse is rotated during a single iteration is controlled by another small constant ϵ_2. The two constants are related by $\epsilon_2 = 500\epsilon_1$. In this case, the simulations presented here show the sedimentation of an ellipse through the foam with its response to the torque applied being exaggerated.

In an ideal situation, the motion of the ellipse would be defined by one effective time scale. It can be seen from figures 6.16(b), 6.19(b) and 6.21(b) that for the simulations presented in this chapter, this would require channels that are at least a 100 times longer than the length of foam E. This is a huge foam channel that would not be feasible to use for simulation using the current techniques available. The channel length required would be reduced slightly by the incorporation of some viscous drag between the foam films and the sedimenting object. The network torque exerted on the object would be slightly greater. However, introducing such a drag would again increase the computational expense of any simulations.

The simulation results presented in this chapter, using two different time scales for downward and rotational motion of the objects, does however satisfy the main aim of the work. This was to provide qualitative results on how a foam responds to the sedimentation of long objects such as ellipses. Information on the network and pressure forces exerted on such shaped objects was gained as well as visual descriptions of 2D foam flow during the sedimentation process.

6.4.4 Concluding Remarks

The sedimenting motion of an elliptical object in a dry foam has been discussed as a probe to the foam's rheology. It was found that the ellipse rotates to a stable orientation where its major axis is parallel to the direction of gravity independently of its initial orientation. The size and eccentricity of the ellipse were shown to affect the rate of rotation during sedimentation. This rotation to the stable orientation corresponds to the results presented for the interaction between two sedimenting discs in chapters 4 and 5.

The rotation of the objects into a stable orientation is a result of the local structure of the foam and the positioning of the films along the ellipse boundary. It was shown that the rotation process is driven by the bunching up of highly stretched films in the wake of the ellipse at an off-centre position to its centre of mass.

Chapter 7

Conclusions

The sedimentation of circular and elliptical objects through a two-dimensional foam has been studied using a quasi-static model for simulation. The main assumption of this model is that the motion of the object is so slow that the viscous effects of the foam can be neglected. This is justified as the rate at which the foam is deformed by the motion of the object is much slower than the relaxation rate of the foam after events such as T1s. Thus, the foam is modelled as an elasto-plastic fluid. The response of the foam and the role that the elasticity and plasticity has on the motion of the sedimenting objects was studied.

The sedimentation of one circular disc through the foam was considered in chapter 3. Here, the maximum disc weight a foam can support was shown to increase affinely with disc size and decrease with the liquid fraction of the foam. It was ensured that the weight of the objects chosen for the rest of the work was adequate for steady motion through the foam.

The drag force exerted on the object by the foam was shown to fluctuate as a result of the rearrangements of bubbles and films around its boundary. Similarly, the lift force exerted on the disc fluctuated about zero when it was positioned centrally in the foam channel. However, the lift force was shown to be non-zero when the disc was placed closer to either wall. An attractive force towards the nearest wall was exerted on the disc when it was positioned within a critical separation of the wall. This attractive force

vanished if the disc was positioned too close to (or too far from) the wall. These wall effects were shown to be a consequence of the flow symmetry around the sedimenting object being broken by the disc's proximity to the wall. As a result it was ensured that objects were positioned centrally in the foam for the rest of the work, so that their motion was not affected by either wall.

Details of the foam's response to the sedimenting motion of the object were provided by visualization of the bubble displacement and pressure fields as well as the positions of T1 events. The object sedimented within a fluidized region of the foam where the motion of the bubbles was at its greatest, and T1 events were highly concentrated. For a disc of area $4A_b$, sedimenting in a foam of liquid fraction $\Phi_l = 3.7 \times 10^{-3}$, this fluidized region consists of the first few layers of bubbles surrounding the disc. The shape of the fluidized region of the foam was not uniformly circular as a result of the bubbles in the wake of the disc being highly elongated and those in front being squeezed. A negative wake was seen for large discs as a result of bubbles detaching from the disc. In this case, an upward motion of bubbles was seen in the wake of a disc that was moving downwards.

The disc area and the liquid fraction of the foam were varied and their effect on the drag force exerted by the foam quantified. It was seen that the average value for both the network and pressure contributions to the drag force (after a transient build up) increased affinely with disc diameter. The network drag force was shown to decrease when increasing the foam's liquid fraction with a power-law relation equivalent to that found in the experiments of Raufaste *et al.* [77]. However, the pressure contribution to the drag force was shown to stay relatively constant when increasing the liquid fraction.

A second disc was then introduced in the foam for chapters 4 and 5. The interaction between two discs placed initially side by side (configuration 1) or one above the other (configuration 2) was of interest. Discs initially positioned in configuration 1 interact if within 3 or 4 bubbles of each other. In this case, they rotate about one another into configuration 2. Discs initially positioned in configuration 2 interact if separated by less than 5 or 6 bubbles. In this case, they move closer together until becoming terminally separated by 1 or 2 bubbles. The critical separations for interaction relate to the size

of the fluidized region surrounding each disc in the foam. Configuration 2 is the stable orientation for the discs as they sediment through the foam.

In relation to the stable orientation of two discs relative to each other, the sedimentation of an ellipse through a 2D foam was considered (chapter 6). The orientation of the ellipse was initially kept fixed during sedimentation. The drag, lift and torque exerted on the ellipse by the foam were investigated. The drag force was shown to increase affinely with the spanwise width of the ellipse. It was shown that a non-zero torque is applied on the ellipse when it is oriented so that its major axis made an acute angle with the horizontal x-axis. The torque was shown to increase with ellipse size and eccentricity. Whenever the major axis was parallel or perpendicular to gravity, the torque applied by the foam was minimal.

By considering the sedimentation of a freely rotating ellipse in the foam, it was shown that the stable orientation was such that the ellipse had its major axis parallel to gravity. The orientation where the major axis of the ellipse is perpendicular to gravity was shown to be metastable. The rotation of the ellipse towards the stable orientation is shown to be driven by the distribution of films along its boundary. The films move along the ellipse's boundary, becoming bunched up at an off-centre position in its wake, thus forcing the ellipse to turn so that its major axis becomes parallel to gravity. Increasing the liquid fraction of the foam results in T1 events being triggered earlier, as films bunch up in the wake of the ellipse. In this case, the bubbles in the wake are less elongated during the sedimentation of the ellipse and fewer films pull the ellipse from an off-centre position. Thus, the network contribution to the torque is minimized in wet foams.

The sedimenting motion of the ellipse through the foam was modelled to be slow and steady. The rotating motion and downward motion proceeded at different time scales. In this case, as the torque applied on the ellipse by the foam is much smaller than the drag and lift forces, its rotating motion is set to be over responsive to the torque. This ensured that qualitative results on the stable orientation of the ellipse were obtained.

7.1 Outlook and Future Work

A limitation of the simulations presented in this work is that viscous dissipation has not been included. Only the role of plasticity and elasticity in the foam's response to sedimenting objects is considered. It was decided that obtaining a realistic structure for the foam during the sedimentation of objects was of prime importance for our simulation model. Visualization of the foam structure during the descent of the objects ensured that the response of the foam could be understood and predicted. However, viscous effects of the foam are important when considering its overall rheology. It is a target of future work to incorporate viscosity into the model. This could involve introducing a viscous drag (friction) between foam films and the boundary of objects. In this case, even circular discs could be liable to rotation during sedimentation. The viscous froth model of Kern *et al.* [100] could be used to introduce a normal viscous drag on the foam's films. This would however, increase the computational expense of simulations and only incorporates a normal viscous drag force on the foam films.

It is also of interest to compare the simulation results presented in this thesis with experimental data. Thus, consideration of an equivalent experiment would be interesting. In this case, one would require a monolayer of bubbles bounded between two vertical glass plates. Circular and elliptical objects of similar width to the gap between the glass plates would then be released into the foam and their descending motion and the response of the foam could be visualized and reproduced using image analysis techniques. The challenges of such an experiment include choosing an object weight that will not break the foam as it descends. The width of the object must be close to the gap between the glass plates so that no foam films can slip in between the object and plate. The friction between the object and the glass plates needs to be minimized so that it does not affect the descending motion of such an object through the foam.

It would be of interest in future work to extend the argument of Dollet *et al.* [77] that predicts the relation between the network contribution to the drag force exerted on a circular obstacle and the foam's liquid fraction, to predict the equivalent relation for the pressure contribution to the drag. This was shown in section 3.7.2 to remain

relatively unaffected by the foam's liquid fraction. One would attempt to predict the relationship using a similar argument to that of Dollet *et al.*. Thus, the pressures of bubbles in contact with the object would be required as a function of the ortho-radial angle along the object's boundary, as done in the experiments of Dollet and Graner [51]. Compared with Dollet's argument for the network force, it is predicted that bubble pressure as a function of the ortho-radial angle along the boundary of the object is relatively unaffected when increasing the foam's liquid fraction.

It would also be of interest for future work to extend this argument to predict the relationship between the network and pressure contributions to the drag exerted on an elliptical object and the liquid fraction of the foam. This should be possible for an ellipse that is oriented such that its major axis is parallel or perpendicular to gravity as the symmetry of the object is retained in this case.

Apart from considering the sedimentation of discs and elliptical objects in a 2D foam, it would be interesting to look at other shaped objects. One could look at how a cambered airfoil or a square object might sediment in a dry foam. It would be interesting to see how a cambered airfoil rotates during sedimentation through a dry foam. It is expected that it will rotate so that its long axis becomes parallel to gravity as shown for the ellipse in this work.

It is natural to consider the interaction that occurs between more than two objects as they sediment in a foam. For example, one could investigate the sedimentation and interaction between three circular discs through a foam. Preliminary work investigating the interaction between three discs positioned side-by-side in the foam channel is shown in figure 7.1. The discs are close together and therefore interact in the same manner as two discs. In this case, they rotate about one another so that they are directly above one another. Two discs have interacted more with each other as one disc is left trailing further behind during sedimentation. It is proposed that considering the sedimentation of two discs yields all the interesting results on a foam's response to sedimenting objects. Including more objects increases the computational time of simulations and doesn't yield any more information that will improve the prediction of foam response.

This work also needs to be extended to 3D in the future for both simulation and ex-

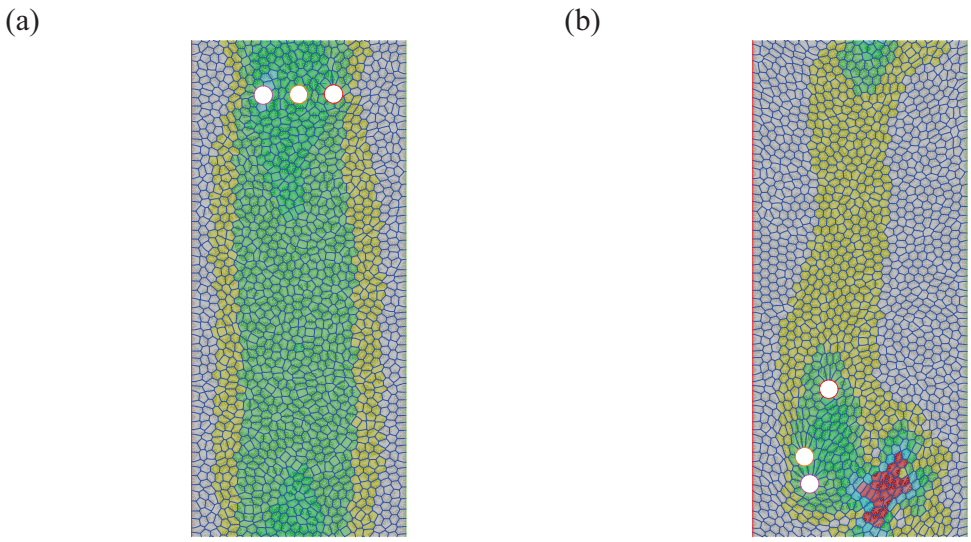

Figure 7.1: The sedimentation and interaction between three circular discs in a 2D dry foam could be considered as future work. A preliminary simulation where the discs are initially positioned side-by-side along the top of the channel, each separated by less than a bubble diameter from the next is shown. The discs are shown to interact in a similar way to that seen for two discs; they rotate about one another so that they form a vertical chain. (The bubbles are coloured by their displacement in this case. Thus the bubble displacement increases from grey to yellow to green to blue to red.)

periment. 3D simulations are much more computationally expensive than the 2D case. They must be an aim for future work since foams are in reality 3D, thus 3D simulations will improve the prediction of foam response. Three-dimensional experiments provide challenges in visualization techniques, making validation with simulations more difficult. However, the friction between objects and a bounding surface is not a problem in this case. A 3D experiment provides a more realistic method for studying foam's response to the sedimentation and interaction between spherical or long objects.

The work presented in this thesis provides valuable insight into the response of a 2D dry foam to the sedimentation of objects. The response of the foam and its influence on the interaction between circular objects and the rotation of an elliptical object has provided details on the role of its plasticity and elasticity. The results contribute to improving the prediction of a dry foam's response.

Bibliography

[1] D. Weaire and S. Hutzler. *The Physics of Foams*. Oxford University Press, 2000.

[2] R. K. Prud'homme and S. A. Khan, editors. *Foams: Theory, Measurements and Applications*. CRC Press, 1996.

[3] J. J. Bikerman. *Foams: Theory and Industrial Applications*. Reinhold Publishing Corporation, New York, 1953.

[4] *"Pint of Guiness". [online image] Available from http://www.pdphoto.org/PictureDetail.php?mat=&pg=8748 [Accessed 25 September 2009]*.

[5] *"Aluminium Foam" [online image]. Available from: http://en.wikipedia.org/wiki/File:Aluminiumfoam.jpg [Accessed 25 September 2009]*.

[6] W. R. Rossen. Foams in enhanced oil recovery. In R. K. Prud'homme and S. A. Khan, editors, *Foams: Theory, Measurements and Applications*. CRC Press, 1996.

[7] R. K. Prud'homme and G. G. Warr. Foams in mineral flotation and separation processess. In R. K. Prud'homme and S. A. Khan, editors, *Foams: Theory, Measurements and Applications*. CRC Press, 1996.

[8] S. J. Neethling and J. J. Cilliers. Solids motion in flowing froths. *Chem. Eng. Sci.*, 57:607–615, 2002.

[9] H. T. Lee, S. J. Neethling, and J. J. Cilliers. Particle and liquid dispersion in foams. *Colloids Surf. A*, 263:320–329, 2005.

[10] H. A. Barnes and K. Walters. The yield stress myth? *Rheol. Acta*, 24:323–326, 1985.

[11] H. A. Barnes. The yield stress - a review. *J. Non-Newtonian Fluid Mech.*, 81:133–178, 1999.

[12] Y. Jiang, P. J. Swart, A. Saxena, M. Asipauskas, and J. A. Glazier. Hysteresis and avalanches in two-dimensional foam rheology simulations. *Phys. Rev. E*, 59:5819–5832, 1999.

[13] S. J. Cox, D. Weaire, and J. A. Glazier. The rheology of two-dimensional foams. *Rheol Acta*, 43:442–448, 2004.

[14] *POLYFLOW, Fluent Inc., www.fluent.com/software/polyflow*.

[15] D. M. A. Buzza, C.-Y. D. Lu, and M. E. Gates. Linear shear rheology of incompressible foams. *J. Phys II France*, 5:37–52, 1995.

[16] B. S. Gardiner, B. Z. Dlugogorski, G. J. Jameson, and R. P. Chhabra. Yield stress measurements of aqueous foams in the dry limit. *J. Rheol.*, 42:1437–1450, 1998.

[17] F. Bolton and D. Weaire. Rigidity loss transition in a disordered 2D froth. *Phys. Rev. Lett.*, 65:3449–3451, 1990.

[18] R. D. MacPherson and D. J. Srolovitz. The von Neumann relation generalized to coarsening of three-dimensional microstructures. *Nature*, 446:1053–1055, 2007.

[19] D. Weaire, N. Pittet, and S. Hutzler. Steady-state drainage of an aqueous foam. *Phys. Rev. Lett.*, 71:2670 – 2673, 1993.

[20] S. A. Koehler, H. A. Stone, M. P. Brenner, and J. Eggers. Dynamics of foam drainage. *Phys. Rev. E*, 58:2097–2106, 1998.

[21] S. Hutzler, S. J. Cox, and G. Wang. Foam drainage in two dimensions. *Colloids Surf. A*, 263:178–183, 2005.

[22] G. Verbist, D. Weaire, and A. M. Kraynik. The foam drainage equation. *J. Phys.: Condens. Matter*, 8:3715–3731, 1996.

[23] P. R. Garrett. Recent developments in the understanding of foam generation and stability. *Chem. Eng. Sci.*, 48:367–392, 1993.

[24] G. G. Stokes. On the effect of the inertial friction of fluids on the motion of pendulums. *Trans. Camb. Phil. Soc.*, IX:8–149, 1850.

[25] D. A. Cygan and B. Caswell. Precision falling sphere viscometry. *J. Rheol. Volume*, 15:663–683, 1971.

[26] J. L. Sutterby. Falling sphere viscometry. I. Wall and inertial corrections to Stokes' law in long tubes. *J. Rheol.*, 17:559–573, 1973.

[27] A. Einstein. On the movement of small particles suspended in stationary liquids required by the molecular-kinetic theory of heat. *Ann. Phys*, 17:549–560, 1905.

[28] N. A. Bennani, A. Fujiwara, S. Takagi, and Y. Matsumoto. Coarse particles sedimentation within a quasi two-dimensional rising foam. *Colloids Surf. A*, 309:7–12, 2007.

[29] A. N. Beris, J. A. Tsamopoulos, R. C. Armstrong, and R. A. Brown. Creeping motion of a sphere through a Bingham plastic. *J. Fluid Mech.*, 158:219–244, 1985.

[30] M. Beaulne and E. Mitsoulis. Creeping motion of a sphere in tubes filled with HerschelBulkley fluids. *J. Non-Newtonian Fluid Mech.*, 72:55–71, 1997.

[31] J. Blackery and E. Mitsoulis. Creeping motion of a sphere in tubes filled with a Bingham plastic material. *J. Non-Newtonian Fluid Mech.*, 70:59–77, 1997.

[32] T.C. Papanastasiou. Flow of materials with yield. *J. Rheol.*, 31:385–404, 1987.

[33] D. D. Atapattu, R. P. Chhabra, and P. H. T. Uhlherr. Creeping sphere motion in Herschel-Bulkley fluids: Flow field and drag. *J. Non-Newtonian Fluid Mech.*, 59:245–265, 1995.

[34] B. D. de Besses, A. Magnin, and P. Jay. Sphere drag in a viscoplastic fluid. *AIChE J*, 50:2627–2629, 2004.

[35] H. Tabuteau, P. Coussot, and J. R. de Bruyn. Drag force on a sphere in steady motion through a yield-stress fluid. *J. Rheol.*, 51:125–137, 2007.

[36] H. Tabuteau, F. K. Oppong, J. R. de Bruyn, and P. Coussot. Drag on a sphere moving through an aging system. *EPL*, 78:68007, 2007.

[37] D. D. Joseph, J. Y. Liu, M. Poletto, and J. Feng. Aggregation and dispersion of spheres falling in viscoelastic liquids. *J. Non-Newtonian Fluid Mech.*, 54:45–86, 1994.

[38] J. A. Tatum, M. V. Finnis, N. J. Lawson, and G. M. Harrison. 3D particle image velocimetry of the flow field around a sphere sedimenting near a wall. Part 1. Effects of Weissenberg number. *J. Non-Newtonian Fluid Mech.*, 141:99–115, 2007.

[39] G.M. Harrison, N.J. Lawson, and D.V. Boger. The measurement of the flow around a sphere settling in a rectangular box using 3-dimensional particle image velocimetry. *Chem. Eng. Commun.*, 188:143, 2001.

[40] Y. Liu, J. Nelson, J. Feng, and D. D. Joseph. Anomalous rolling of spheres down an inclined plane. *J. Non-Newtonian Fluid Mech.*, 50:305–329, 1993.

[41] P. Singh and D. D. Joseph. Sedimentation of a sphere near a vertical wall in an Oldroyd-B fluid. *J. Non-Newtonian Fluid Mech.*, 94:179–203, 2000.

[42] R. I. Tanner. End effects in falling-ball viscometer. *J. Fluid Mech.*, 17:161, 1963.

[43] L. E. Becker, G. H. McKinley, and H. A. Stone. Sedimentation of a sphere near a plane wall: Weak non-Newtonian and inertial effects. *J. Non-Newtonian Fluid Mech.*, 63:201 233, 96.

[44] J. Feng, P. Y. Huang, and D. D. Joseph. Dynamic simulation of sedimentation of solid particles in an Oldroyd-B fluid. *J. Non-Newtonian Fluid Mech.*, 63:63–88, 1996.

[45] H. Binous and R. J. Phillips. The effect of sphere-wall interactions on particle motion in a viscoelastic suspension of FENE dumbbells. *J. Non-Newtonian Fluid Mech.*, 85:63–92, 1999.

[46] J. A. Tatum, M. V. Finnis, N. J. Lawson, and G. M. Harrison. 3-D particle image velocimetry of the flow field around a sphere sedimenting near a wall. Part 2. Effects of distance from the wall. *J. Non-Newtonian Fluid Mech.*, 127:95–106, 2005.

[47] R. P. Chhabra. *Bubbles, Drops, and Particles in Non-Newtonian Fluids*. CRC Press, 2007.

[48] O. Hassager. Negative wake behind bubbles in non-Newtonian liquids. *Nature*, 29:402, 1979.

[49] M. T. Arigo and G. H. McKinley. An experimental investigation of negative wakes behind spheres settling in a shear-thinning viscoelastic fluid. *Rheol. Acta*, 37:307–327, 1998.

[50] O. G. Harlen. The negative wake behind a sphere sedimenting through a viscoelastic fluid. *J. Non-Newtonian Fluid Mech.*, 108:411–430, 2002.

[51] B. Dollet and F. Graner. Two-dimensional flow of foam around a circular obstacle: local measurements of elasticity, plasticity and flow. *J. Fluid Mech.*, 585:181–211, 2007.

[52] K. O. L. F. Jayaweera, B. J. Mason, and G. W. Slack. The behaviour of clusters of spheres falling in a viscous fluid. Part 1. Experiment. *J. Fluid Mech.*, 20:121–128, 1964.

[53] A. J. Goldman, R. G. Cox, and H. Brenner. The slow motion of two identical arbitrarily oriented spheres through a viscous fluid. *Chem. Eng. Sci.*, 21:1151–1170, 1966.

[54] J. Feng, H. H. Hu, and D. D. Joseph. Direct simulation of initial value problems for the motion of solid bodies in a Newtonian fluid Part 1. Sedimentation. *J. Fluid Mech.*, 261:95–134, 1994.

[55] J. Michele, R. Patzold, and R. Donis. Alignment and aggregation effects in suspension of spheres in non-Newtonian media. *Rheol. Acta*, 16:317–321, 1977.

[56] S. Daugan, L. Talini, B. Herzhaft, and C. Allain. Aggregation of particles settling in shear-thinning fluids. Part 1: Two-particle aggregation. *Eur. Phys. J. E*, 7:73–81, 2002.

[57] E. Verneuil, R. J. Phillips, and L. Talini. Axisymmetric two-sphere sedimentation in a shear thinning viscoelastic fluid: Particle interactions and induced fluid velocity fields. *J. Rheol.*, 51:1343, 2007.

[58] O. Merkak, L. Jossic, and A. Magnin. Spheres and interactions between spheres moving at very low velocities in a yield stress fluid. *J. Non-Newtonian Fluid Mech.*, 133:99–108, 2006.

[59] B. T. Liu, S. J. Muller, and M. M. Denn. Interactions of two rigid spheres translating collinearly in creeping flow in a Bingham material. *J. Non-Newtonian Fluid Mech.*, 113:49–67, 2003.

[60] B. Gueslin, L. Talini, B. Herzhaft, Y. Peysson, and C. Allain. Aggregation behavior of two spheres falling through an aging fluid. *Phys. Rev. E 74*, 74:042501, 2006.

[61] G. Boardman and R. L. Whitmore. Yield stress exerted on a body immersed in a Bingham fluid. *Nature*, 187:50–51, 1960.

[62] G. Boardman and R. L. Whitmore. 'Response to Rae D.'. *Nature*, 194:272, 1962.

[63] D. Rae. Yield stress exerted on a body immersed in a Bingham fluid. *Nature*, 194:272, 1962.

[64] P. Y. Huang, J. Feng, and D. D. Joseph. The turning couples on an elliptic particle settling in a vertical channel. *J. Fluid Mech.*, 271:1–16, 1994.

[65] L. G. Leal. The slow motion of slender rod-like particles in a second-order fluid. *J. Fluid Mech.*, 69:305–337, 1975.

[66] P. Brunn. The slow motion of a rigid particle in a second-order fluid. *J. Fluid Mech.*, 82:529–550, 1977.

[67] D. D. Joseph and Y. J. Liu. Orientation of long bodies falling in a viscoelastic liquid. *J. Rheol.*, 37:961–983, 1993.

[68] J. Wang and D. D. Joseph. Potential flow of a second-order fluid over a sphere or an ellipse. *J. Fluid Mech.*, 511:201–215, 2004.

[69] B. Dollet, M. Durth, and F. Graner. Flow of foam past an elliptical obstacle. *Phys. Rev. E*, 73:061404, 2006.

[70] S. J. Cox, M. D. Alonso, S. Hutzler, and D. Weaire. The Stokes Experiment in a Foam. In P. Zitha, J. Banhart, and G. Verbist, editors, *Foams, Emulsions and their Applications*, pages 282–289. MIT-Verlag, Bremen, 2000.

[71] I. Cantat and O. Pitois. Mechanical probing of liquid foam ageing. *J. Phys. Condens. Matter*, 17:S3455–S3461, 2005.

[72] I. Cantat and O. Pitois. Stokes experiment in a liquid foam. *Phys. Fluids*, 18:083302, 2006.

[73] J. R. de Bruyn. Transient and steady-state drag in a foam. *Rheol. Acta.*, 44:150–159, 2004.

[74] J. R. de Bruyn. Age dependence of the drag force in an aqueous foam. *Rheol. Acta*, 45:801–811, 2005.

[75] B. Dollet, F. Elias, C. Quilliet, A. Huillier, M. Aubony, and F. Graner. Two-dimensional flows of foam: drag exerted on circular obstacles and dissipation. *Colloids Surf. A*, 263:101–110, 2005.

[76] B. Dollet, F. Elias, C. Quillet, C. Raufaste, M. Aubony, and F. Graner. Two-dimensional flow of foam around an obstacle: Force measurements. *Phys. Rev. E*, 71:031403, 2005.

[77] C. Raufaste, B. Dollet, S. Cox, Y. Jiang, and F. Graner. Yield drag in a two-dimensional foam flow around a circular obstacle: Effect of liquid fraction. *Euro. Phys. J. E.*, 23:217–228, 2007.

[78] K. Brakke. The Surface Evolver. *Exp. Math.*, 1:141–152, 1992.

[79] M. Asipauskas, M. Aubouy, J. A. Glazer, G. Graner, and Y. Jiang. A texture tensor to quantify deformations: the example of two dimensional flowing foams. *Granular Matter*, 5:67–74, 2003.

[80] P. Marmottant, C. Raufaste, and F. Graner. Discrete rearranging disordered patterns. Part II: 2D plasticity, elasticity and flow of a foam. *Eur. Phys. J. E*, 25:371–384, 2008.

[81] M. Aubouy, Y. Jiang, J. A. Glazier, and F. Graner. A texture tensor to quantify deformations. *Granular Matter*, 5:67–70, 2003.

[82] S. Courty, B. Dollet, F. Elias, P. Heining, and F. Graner. Two-dimensional shear modulus of a Langmuir foam. *Europhys. Lett.*, 64:709–715, 2003.

[83] S. J. Cox, B. Dollet, and F. Graner. Foam flow around an obstacle: Simulations of obstacle-wall interaction. *Rheol. Acta.*, 45:403–410, 2006.

[84] Q. Sun and S. Hutzler. Studying localized bubble rearrangements in 2D liquid foams using a hybrid lattice gas model. *Colloids Surf. A*, 263:27–32, 2005.

[85] B. Dollet, M. Aubouy, and F. Graner. Anti-inertial lift in foams: A signature of the elasticity of complex fluids. *Phys. Rev. Lett.*, 95:168303, 2005.

[86] I. Cantat and R. Delannay. Dynamical transition induced by large bubbles in two-dimensional foam flows. *Phys. Rev. E*, 67:031501, 2003.

[87] A. Wyn, I. T. Davies, and S. J. Cox. Simulations of two-dimensional foam rheology: Localization in linear Couette flow and the interaction of settling discs. *Eur. Phys. J. E*, 26:81–89, 2008.

[88] I. T. Davies and S. J. Cox. Sedimenting discs in a two-dimensional foam. *Coll. Surf. A*, 344:8–14, 2009.

[89] J. P. Kermode and D. Weaire. 2D-FROTH: a program for the investigation of 2-dimensional froths. *Comp Phys Com*, 60:75–109, 1990.

[90] K. A. Brakke. 200,000,000 Random Voronoi Polygons. www.susqu.edu/brakke, 1986.

[91] F. Bolton and D. Weaire. The effects of Plateau borders in the two-dimensional soap froth. ii. General simulations and analysis of rigidity loss transition. *Phil. Mag. B*, 65:473–487, 1992.

[92] D. A. Reinelt and A. M. Kraynik. Large elastic deformations of three-dimensional foams and highly concentrated emulsions. *J Colloid Interface Sci*, 159:460–470, 1993.

[93] D. A. Reinelt and A. M. Kraynik. Simple shearing flow of a dry kelvin soap foam. *J Fluid Mech*, 311:327–342, 1996.

[94] Q. Sun and S. Hutzler. Lattice gas simulations of two-dimensional liquid foams. *Rheol Acta*, 43:567–574, 2004.

[95] T. Okuzono, K. Kawasaki, and T. Nagai. Rheology of random foams. *J. Rheol.*, 37:571–586, 1993.

[96] T. Okuzono and K. Kawasaki. Intermittent flow behavior of random foams: A computer experiment on foam rheology. *Phys. Rev.E*, 51:1246–1253, 1995.

[97] D. J. Durian. Foam mechanics at the bubble scale. *Phys Rev Lett*, 75:4870, 1995.

[98] V. J. Langlois, S. Hutzler, and D. Weaire. Rheological properties of the soft-disk model of two-dimensional foams. *Phys. Rev. E*, 78:021401, 2008.

[99] D. J. Durian. Bubble-scale model of foam mechanics: Melting, nonlinear behavior, and avalanches. *Phys Rev E*, 55:1739, 1997.

[100] N. Kern, D Weaire, A. Martin, S. Hutzler, and S. J. Cox. Two-dimensional viscous froth model for foam dynamics. *Phys Rev E*, 70:041411, 2004.

[101] I. Cantat, N. Kern, and R. Delannay. Dissipation in foam flowing through narrow channels. *Europhys. Lett.*, 65:726–732, 2004.

[102] S. J. Cox. A viscous froth model for dry foams in the Surface Evolver. *Coll. Surf. A*, 263:81–89, 2005.

[103] X. Li, H. Zhou, and C. Pozrikidis. A numerical study of the shearing motion of emulsions and foams. *J. Fluid Mech.*, 286:379–404, 1995.

[104] *J. L. Higdon, http://chbe.illinois.edu/Faculty/higdon.php*.

[105] *Personal communication with S. J. Cox*.

[106] A. Saint-Jalmes and D. J. Durian. Vanishing elasticity for wet foams: Equivalence with emulsions and role of polydispersity. *J. Rheol.*, 43:1411–1422, 1999.

[107] E. Mitsoulis. On creeping drag flow of a viscoplastic fluid past a circular cylinder: wall effects. *Chemical Engineering Science*, 59:789–800, 2004.

[108] S. J. Cox, F. Graner, and M.F. Vaz. Screening in dry two-dimensional foams. *Soft Matter*, 4:1871–1878, 2008.

[109] R. J. Phillips and L. Talini. Chaining of weakly interacting particles suspended in viscoelastic fluids. *J. Non-Newtonian Fluid Mech.*, 147:175–188, 2007.

[110] G. Gheissary and B.H.A.A. van den Brule. Unexpected phenomena observed in particle settling in non-Newtonian medial. *J. Non-Newtonian Fluid Mech.*, 67:1–18, 1996.

[111] R. Scirocco, J. Vermant, and J. Mewis. Effect of the viscoelasticity of the suspending fluid on structure formation in suspensions. *J. Non-Newtonian Fluid Mech.*, 117:183–192, 2004.

[112] E. T. G. Bot, M. A. Hulsen, and B. H. A. A van den Brule. The motion of two spheres falling along their line of centres in a Boger fluid. *J. Non-Newtonian Fluid Mech.*, 79:191–212, 1998.

[113] D. D. Joseph and J. Feng. A note on the forces that move particles in a second-order fluid. *J. Non-Newtonian Fluid Mech.*, 64:299–302, 1996.

Chapter 8

Appendix A - Published Work

Presented here are the two published papers [87, 88] that contain work presented in this thesis. A section in the first paper is devoted to the results presented in chapters 4 and 5 while the second paper concentrates fully on my work probing the discrete nature of a dry 2D foam's response to the sedimentation of circular discs.

EPJ manuscript No.
(will be inserted by the editor)

Simulations of two-dimensional foam rheology: localization in linear Couette flow and the interaction of settling discs

A. Wyn[1], I.T. Davies[1], and S.J. Cox[1,2] [a]

[1] Institute of Mathematical and Physical Sciences, Aberystwyth University, Ceredigion SY23 3BZ, Wales, UK
[2] UMR 5588 – Laboratoire Spectrométrie Physique, B.P. 87, F-38402 St. Martin d'Hères Cedex, France.

January 30, 2008

Abstract. Surface Evolver simulations of flowing two-dimensional foams are described. These are used for two purposes. Firstly, to extract the location of the T_1s, the changes in bubble topology that occur during plastic flow. It is shown that the T_1s are localized in space, becoming more so as the polydispersity of the foam decreases. Secondly, the sedimentation of two circular discs through a foam under gravity is studied. If the discs are sufficiently close, they begin to interact and one moves behind the other during their descent.

PACS. 47.57.Bc Foams and Emulsions – 83.80.Iz Emulsions and Foams

1 Introduction

Liquid foams are familiar from domestic use and important in industrial applications including ore-separation and enhanced oil recovery [1, 2]. They are elasto-visco-plastic complex fluids with a highly nonlinear response to applied forces: at low strain they deform elastically, like a solid, while above a yield stress they flow like a viscous liquid [3]. Of all complex fluids, liquid foams provide one of the most experimentally accessible systems for study, since bubbles are objects that can have millimetric dimensions. Moreover, Plateau's laws [4] mean that the internal structure of a foam is well understood, at least at the level of the network of films. Foams thus provide a prototypical complex fluid.

[a] email: foams@aber.ac.uk

However, given the degree of disorder within the foam structure and the complex response, it makes sense to first consider two-dimensional (2D) foams, such as can be made by squeezing a foam between parallel glass plates until it consists of a single layer of bubbles [5]. Other realizations of a 2D foam include the bubble raft of Bragg and Nye [6], promoted recently by Dennin and co-workers [7, 8, 9], and the hybrid method of Cyril Stanley Smith [10] and Fortes and co-workers [11, 12]. A theme of current research is exploring the different responses of each of these experimental setups [13, 14], requiring an understanding in particular of the effects of liquid content.

The mathematical idealization of a two-dimensional foam is, however, clear: a dry 2D foam at equilibrium consists of bubbles with fixed areas surrounded

by films that are circular arcs meeting threefold at angles of 120° (figure 1). These rules are consequences of minimization of energy [15], which is in this case the total film length multiplied by surface tension. This model, and various approximations to it, have long been used for simulation [16, 17, 18, 19, 20, 21]. Here, we use the Surface Evolver software [22] to simulate with high accuracy foams consisting of many hundreds of bubbles, to predict the plastic response of 2D foams.

At low strain a foam responds as an elastic medium. That is, the shear stress, given as a sum of surface tension contributions in the films [23, 24], increases linearly with strain. As the strain increases, the foam begins to yield and bubbles begin to slide past each other in plastic events known as T_1 topological changes (figure 1) [25]. These occur when a film shrinks to zero length and a fourfold vertex is formed. Such a vertex is unstable, and immediately dissociates into two threefold vertices with the connecting film now perpendicular to the vanishing one. In the notation of Wang et al. [9], two bubbles that were nearest-neighbours become next-nearest neighbours, and *vice versa*. Each T_1 event contributes a drop in both total film length and stress.

Localization of T_1 events, also referred to as shear banding, has been described in experiments in an annular wide-gap Couette viscometer [26]. After an initial transient, the majority of T_1 events occur close to the inner moving wall. Similar results have been found in simulations [27]. In linear Couette shear between parallel side-walls, there is also localization of T_1s. In this geometry, since the shear stress should be homogeneous there is no preferred location for the localized region based upon the boundary conditions, confirmed by Potts model [28] and Surface Evolver [19] simulations.

The presence of phenomena such as shear localization presents a non-trivial obstacle to the development of continuum models for foam rheology [29, 30]. Approaches such as the theory of shear transformation zones [31] also require that the local dynamics is first understood.

In §2 we predict the *width* of the localized region in linear Couette shear, and its dependence on the area disorder of the foam. This is, in effect, a prediction of the degree to which the foam is fluidized under shear. In the limit of zero area disorder - a monodisperse foam - T_1 events tend to occur in a very narrow band and shear-induced crystallization is evident. We show here that making a foam more polydisperse widens the localized region and can thus reduce the amount of static foam present.

We characterize the polydispersity, or volumetric disorder, of a foam by the second moment of the distribution of bubble areas A:

$$\mu_2(A) = \left\langle \frac{(A - \langle A \rangle)^2}{\langle A \rangle^2} \right\rangle \qquad (1)$$

where $\langle\rangle$ denotes an average over the whole foam. In contrast to the disorder in the number of sides n of each bubble, $\mu_2(n) = \langle (n-6)^2 \rangle$, which varies in time due to T_1s, the area disorder is fixed in each of our simulations. That is, we exclude inter-bubble gas diffusion (coarsening) and film collapse. The elastic response of a foam is characterized by the shear modulus [32], which decreases by up to 10% at both high topological and high volumetric disorder [23].

In a further effort to understand the response of a foam, we consider a geometry in which we know approximately where the T_1s will occur, and ask what is the interaction between the foam flow and an embedded object (§3).

A number of authors have studied the flow of a 2D foam past a fixed object, with both experiments [12, 33, 34, 35] and simulations [36, 35]. The drag and lift forces on the object are due to a number of contributions. At low velocity the dominant ones are the force from the tensions in the films attached to the object and the pressures in the bubbles that touch it. For a circular object in the centre of a channel the drag force increases with object diameter [36, 37] and decreases with increasing liquid fraction [35]. For asymmetric objects such as an aerofoils [12], and for circular objects

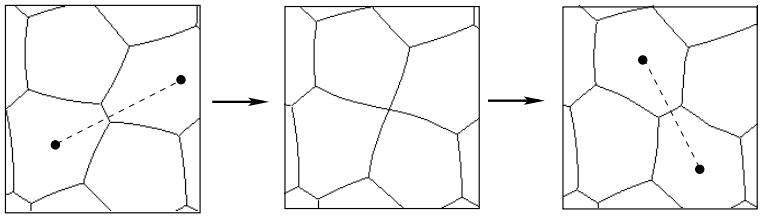

Fig. 1. An ideal 2D foam consists of films that are circular arcs, meeting at 120°. The sequence of images shows a T_1 topological change. The intermediate step with the fourfold vertex is energetically unstable. The orientation of a T_1 is characterized by the lines joining bubble centres adjacent to the deleted and created films, marked by dashed lines.

close to one of the walls of the channel, there is in addition a lift force. For an aerofoil this is a negative lift [12], while for the circular object it points away from the wall [36].

Related work in three dimensions is concerned with single spheres, with a diameter larger than the bubble size, being pulled [38, 39, 40] or dropped [41, 42] through a foam.

In §3 we examine the the interaction between two circular discs falling through a foam under their own weight. We aim to answer questions such as the conditions under which two objects falling through a foam are mutually attracted or repelled, as has been done for a number of viscoelastic fluids [43, 44, 45]. The answers will give guidance in determining the effect of a wake in a discretized elasto-plastic fluid.

To guide our intuition we recall work on the flow of a foam past an ellipse: Dollet et al. [46] found that the only stable orientation of an ellipse was with its long axis parallel to the direction of flow. This is a feature of elastic fluids [47]. Is it therefore the case that the plastic events are not significant in determining this aspect of the foam response, and we can treat it as an elastic liquid?

2 The localization of topological changes in linear Couette shear

We describe simulations of the slow linear Couette shear of a 2D foam confined between parallel walls (figure 2). The area dispersity $\mu_2(A)$ is varied to determine how the width of the localized region depends upon this parameter.

2.1 Method

We use the Surface Evolver [22] in a mode in which each film is represented as a circular arc. We use foams of $N = 1120$ bubbles, in a channel of width $W = 3.2$ and length $L = 8.0$, giving an average bubble size of $\langle A \rangle = 0.0229$ and about 21 bubbles between the walls. The value of surface tension, which should be thought of as a line tension with units of energy per unit length, is taken equal to one throughout. A realistic foam structure is found by minimizing the total film length subject to the prescribed bubble areas. For some parameter values we doubled the number of bubbles in the $x-$ direction to ensure that the results were not affected by the possibility of system-wide avalanches of T_1 events (data not shown).

The simulation procedure is as follows. A Voronoi construction [48] is first used to generate a fully periodic tessellation of the plane. Bubbles at the top and bottom are sequentially deleted until the required number of bubbles remains. This structure is imported into the Surface Evolver and peripheral films constrained to one of the two side-walls, a distance W apart. New bubble areas are determined randomly from a Weibull distribution:

$$f(A;\beta,\lambda) = \frac{\beta}{\lambda}\left(\frac{A}{\lambda}\right)^{\beta-1} e^{-(A/\lambda)^{\beta}}. \quad (2)$$

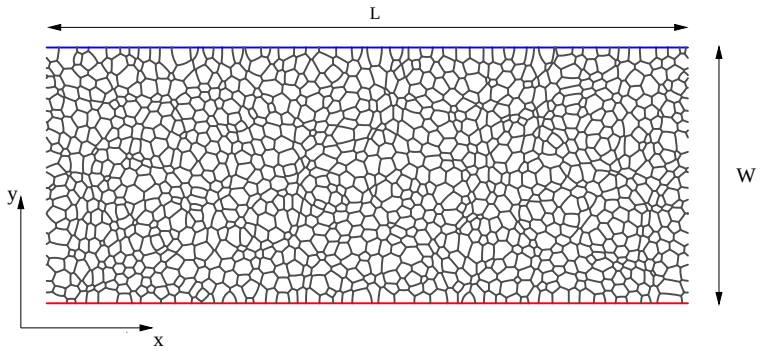

Fig. 2. An example of the foams used to simulate linear Couette shear in a channel, with $\mu_2(A) = 0.175$. The channel is periodic in the x direction. To shear the foam the side-wall at the top of the image is moved to the right (positive x-direction) in small increments $d\epsilon$. Those films that meet the side-walls have their ends pinned to the wall (no-slip condition).

The parameter $\beta > 1$ determines the area dispersity and the parameter λ is chosen as $\lambda = 1.115\langle A\rangle$ (so that the peak of the distribution is close to $A = \langle A\rangle$). The second moment of this distribution is

$$\mu_2(A) = \frac{\Gamma\left(1+\frac{2}{\beta}\right)}{\Gamma\left(1+\frac{1}{\beta}\right)^2} - 1 \qquad (3)$$

where Γ is the Gamma function. The limit $\beta \to \infty$ corresponds to a monodisperse foam ($\mu_2(A) = 0$); decreasing β leads to increasingly polydisperse foams. Note that since our foam sample is finite, the value of β chosen for each simulation can lead to slightly different values of $\mu_2(A)$.

The initial structure for each simulation is found by reducing the total film length to a local minimum. During this minimization T_1s are triggered by deleting each film that shrinks below a certain length l_c and allowing a new films to form to complete the process. The critical length l_c is a measure of liquid fraction ϕ [36], but we keep it small enough here ($l_c = 0.005$ throughout, corresponding to $\phi = 2.6 \times 10^{-4}$) that it should not affect the results [27].

To shear the foam, a small step in strain is applied by moving one of the confining walls a distance $d\epsilon$, moving all vertices affinely, and then reducing the film length to a minimum. In this way, the foam passes through a sequence of equilibrium states, appropriate to an applied strain with strain rate much lower than the rate of equilibration after T_1s. The value $d\epsilon = 0.0078$ was used throughout, and the foam sheared up to a total strain of at least $\epsilon = 5$.

2.2 Position of T_1s

Figure 3 shows the T_1 positions in foams at three representative values of $\mu_2(A)$. Plotting the y position of a T_1 against strain, or the number of iterations, indicates that for each value of $\mu_2(A)$ there is an initial transient that lasts up to approximately unit strain. In the monodisperse case shown in figure 3(a), the T_1s mostly occur close to the moving wall. Although this is not the case for all of our simulations in the monodisperse limit, we found that monodisperse foams usually localize near one of the walls (see figure 4(a)). As the polydispersity increases, the width of the localized region increases and it often occurs further from the walls (figure 4(a)). At large values of polydispersity (small β) the T_1s occur almost throughout the channel. For the intermediate value of $\mu_2(A)$ shown in figure 3(b), we note that plotting the data on y *vs* x axes illustrates a slight undulation in the localized region.

We measure the width l_w of the localized region as follows. After the tran-

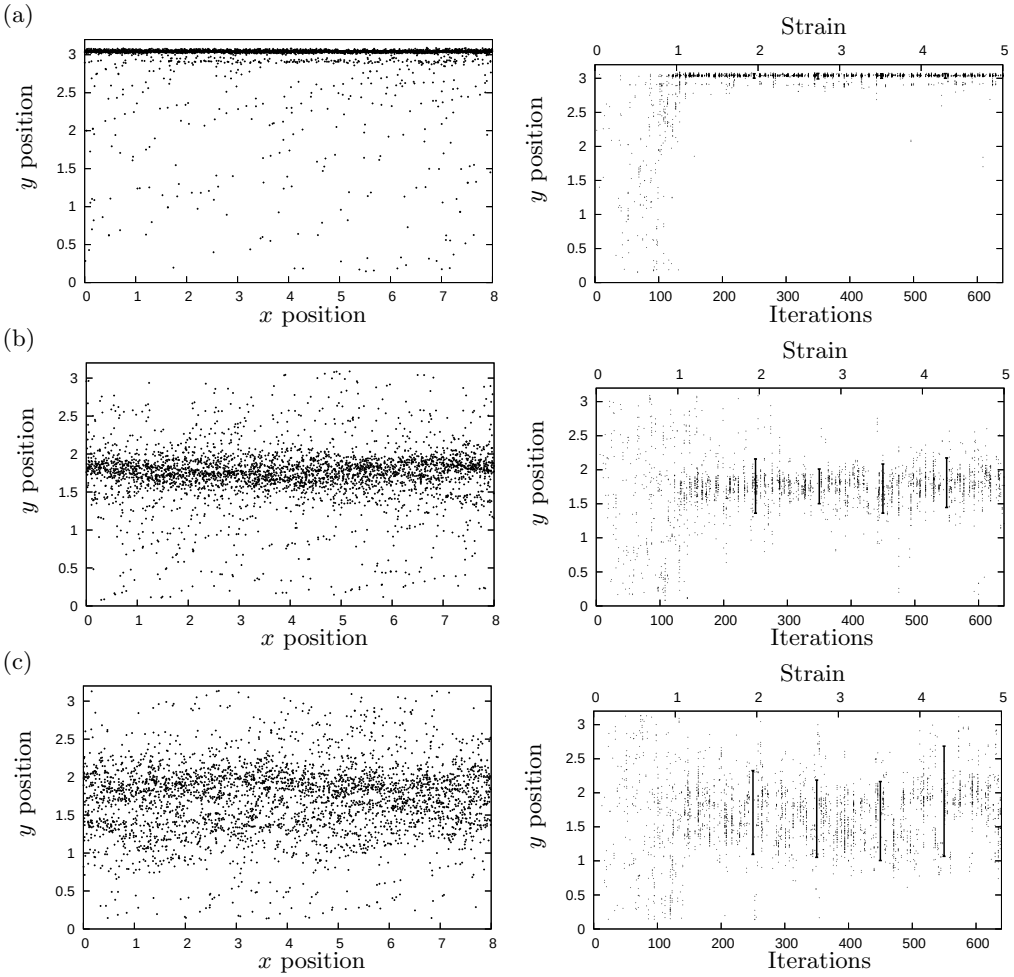

Fig. 3. Locations of topological changes in simulations at three values of $\mu_2(A)$, shown on y *vs* x axes (left-hand column) and on y *vs* γ (strain or number of iterations) axes (right hand column). (a) Monodisperse ($\mu_2(A) = 0, \beta \to \infty$). (b) Moderately polydisperse (the foam in figure 2, $\mu_2(A) = 0.175$). (c) Highly polydisperse ($\mu_2(A) = 0.561$). The vertical bars show the position and width of the localized region after the transient; they are centred at the average y position of the T_1s, averaged in groups of $N_s = 100$ iterations, and their total height encompasses the foam width within which 90% of T_1s occur.

sient, taken to be the first 200 iterations, we find the mean y position of the T_1s in bins of N_s iterations. The localisation width w_l is the interval in y position within which 90% of T_1s are found. We find that $N_s = 100$ gives the best measure of w_l, that is, it balances the need to have many points in each bin with the desire to accurately reflect the width of the evolving localization.

Figure 4(b) shows the increase of localisation width w_l/W with disorder. It is clear that at high disorder, and for narrow (low W foams), the localized region may encompass the whole foam. At low disorder, crystallization is more frequent, and localization usually occurs in a narrow band. We find the following rule of thumb:

$$\frac{w_l}{W} \approx \sqrt{\mu_2(A)}. \qquad (4)$$

On a few occasions (data not shown) we found that two narrow localized regions persisted up to strains of about 3.

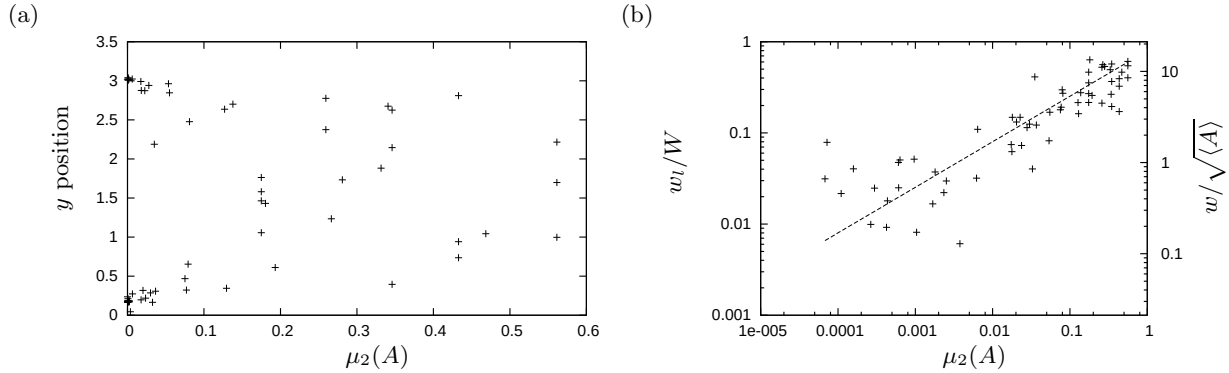

Fig. 4. (a) The position of the centre of the localized region, given as the average of the mean y position of the T_1s in each group of $N_s = 100$ iterations after the transient. Each point corresponds to one full simulation. As the foam becomes less disordered, the T_1s localize closer to the walls, but without showing a preference for either the stationary or moving wall. (b) The width of the localized region w_l/W, given as the width of foam within which 90% of T_1s occur after the transient, increases with area disorder $\mu_2(A)$. Note the log axes. The right-hand axis indicates the localization width in terms of bubble diameters. The straight line has slope one-half: $w_l/W = 0.8\sqrt{\mu_2(A)}$.

2.3 Angular dependence of T_1s

Wang et al. [9] recorded the orientation of the disappearing film and the newly-created film during each T_1 event in their experiments on a sheared bubble raft. This is done by drawing a line between the centres of the bubbles neighbouring each film, in consecutive images bracketing the T_1 event, as in figure 1. The distributions of angles show peaks at angles of about 45° and 135° respectively to the walls of the channel. The height of the peak increases with shear-rate, and at low shear rate a small "knee" appears at about 90°, i.e. parallel to the direction of shear.

From our simulations we can extract the same data, in the limit of low shear-rate. Figure 5 shows these distributions, with data obtained after the transient in each simulation. We find the same peak for the films that disappear, but the most probable orientation for new films is at 30°. Moreover, no detail is seen around 90°. We therefore believe that this discrepancy is due to the high liquid content in the bubble raft experiments, unattainable with the methods described here.

Although we do not probe the effect of shear-rate on the height of the peak (as could be done with the Viscous Froth Model [49]), we see that it is strongly affected by polydispersity: monodisperse foams exhibit a much higher peak. This is perhaps suggestive of hexagonal ordering, although we did not test this explicitly (e.g. by measuring $\mu_2(n)$, with n the number of sides of a bubble).

2.4 Other predictions

Our ultimate goal is to predict the region of a foam where localization will occur from the initial structure. Given that there are many T_1s throughout the foam during the transient, this is difficult. To begin, we seek ways of characterizing the foam structure, and then following these characterizations through each simulation to detect robust changes when the foam localizes. In particular, these methods should be able extractable from a single image of a foam at a given time, rather than requiring the tracking of bubbles from video analysis.

Our structural measures extract the distribution of various quantities as a function of y. In particular, we seek to characterize the area distribution of a foam. Five methods were investigated:

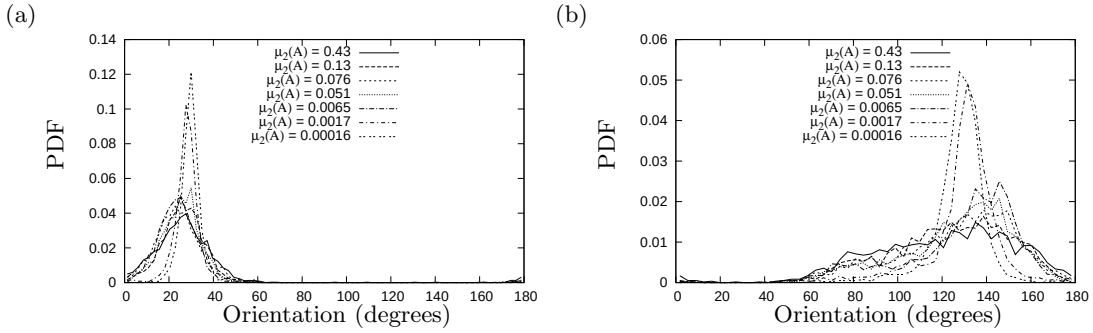

Fig. 5. The distribution of the angle made with the x axis by a line joining the centres of the two bubbles neighbouring a film that (a) disappears and (b) is created during a T_1 event. The former peaks at around 30° and the latter at 135°.

1. we find the centre (x_c, y_c) of each bubble by averaging the coordinates of its vertices, and calculate the histogram of y_c in 20 bins;
2. for each value of $y_0 \in [0, W]$ we calculate the average area $\mathcal{A}_y$ of those bubbles that intersect the line $y = y_0$;
3. we find the centre (x_c, y_c) of each bubble by averaging the coordinates of its vertices, and calculate the local foam disorder $\mu_2(A)$, from (1), in 20 bins based upon y_c;
4. for each value of $y_0 \in [0, W]$ we calculate the average length $\mathcal{L}_y$ of the line $y = y_0$ that is covered by each bubble, sometimes referred to as the linear intercept method [50];
5. we calculate the texture tensor [51] based upon bubble centres in 20 bins.

Figure 6 shows these structural measures for the foam in figures 2 and 3(b) at the beginning and end of the simulation, i.e. before and after localization has occurred. All measures are uniform at the beginning of the simulation, suggesting that it is not possible to predict where a foam will localize.

Method 4, $\mathcal{L}_y$, is the only 1D structural measure to give a clear indication that the foam has localized. Note that it does have the disadvantage that large fluctuations are observed for ordered structures.

The texture tensor, method 5, is the tensorial equivalent of $\mathcal{L}_y$. It is more sensitive than the latter but more difficult to extract from the data. We shall return to it in future work, in addition to other measures such as the local stress in the foam.

3 Movement of discs through a foam

We describe simulations that probe the interaction between macroscopic objects falling through a foam. The system under study consists of two circular discs, whose diameters are equal and larger than the bubble size. Recall that an elliptical object tries to align itself with the foam flow [46]. Here, we show that when the discs are sufficiently close, one of them moves behind the other.

The discs' motion is commenced from a position near the top of a monodisperse foam. They descend under the action of three forces, defined in figure 7: (i) gravity; (ii) the resultant tension force F^n due to the network of films that contact each obstacle; (iii) the resultant pressure force F^p from the bubbles that touch each obstacle. The films touching the discs are not uniformly distributed around the circumference: as figure 8(a) shows, they bunch up behind the obstacle. It is this inhomogeneity that leads to the resultant network and pressure forces.

For each disc the network force is a sum over those films j that touch the disc. Each film meets the disc perpendicularly, and makes an angle θ with the

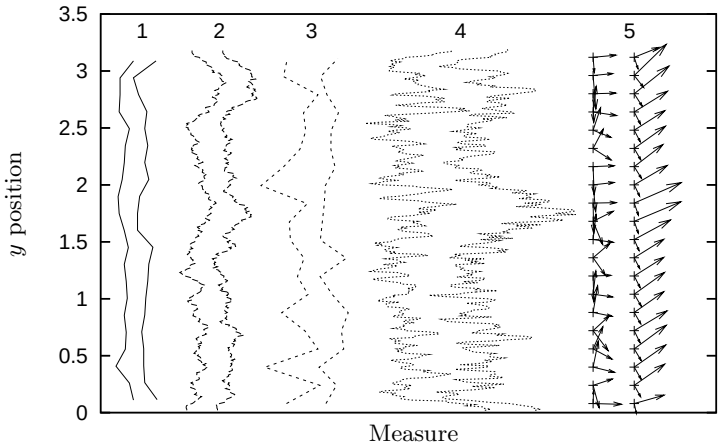

Fig. 6. The five measures of foam structure are shown from left to right for the foam in figure 3(b), both at the beginning and the end of the simulation. It is clear that the foam is initially fairly isotropic, and that none of the methods 1 to 3 indicate that any structural change has occurred during the evolution. In contrast, the peak around $y \approx 1.7$ in $\mathcal{L}_y$ (method 4) corresponds to the region where the T_1s have localized. The tensorial texture tensor (method 5) also shows this feature, as well as indicating that the bubbles are more closely aligned (cf. figure 5).

y direction [36]. Thus:

$$\underline{F}^n = \gamma \sum_{\text{films}j} (\sin\theta_j, \cos\theta_j). \qquad (5)$$

The pressure force is a sum over all bubbles touching the obstacle:

$$\underline{F}^p = \sum_{\text{bubbles}k} p_k l_k (\sin\theta_k, \cos\theta_k). \qquad (6)$$

where p_k is the pressure inside the bubble, l_k is the length of contact, and θ_k is the angle that the inward normal at the midpoint of the line of contact makes with the y-direction.

3.1 Method

We perform quasi-static simulations as described in §2.1, using a foam with $N = 727$ bubbles, width $W = 0.792$ and length $L = 1$. The bubble size is therefore $A \approx 1 \times 10^{-3}$ (it shrinks slightly in proportional to the disc size, since the total area of the foam and two disc system is constant). The cut-off length for T_1 events is $l_c = 0.002$, corresponding to a dry foam with $\phi \approx 1 \times 10^{-3}$. The channel is periodic in the y direction, parallel to the direction of gravity, and we stop the simulations before either of the discs returns to the top of the foam. Films that meet the side-walls have that end fixed throughout each simulation (no-slip condition). The ends of films that touch the discs are free to slide, so as to be able to make an equilibrium 90° angle (slip condition).

Our dimensionless units are chosen so that the line tension γ has the value 1. We choose the discs to have equal areas in the range $2A$ to $7A$ and equal weights of $w = 10$ irrespective of their size. We first ensured that this value of weight is large enough that the discs are not brought to a halt by the opposing forces due to film tensions and bubble pressures.

Two starting configurations are chosen, as shown in figure 8. The disc centres are initially separated by a distance d_i, either horizontally ($i = 1$) or vertically ($i = 2$). In the first configuration, there is a possibility of a small lift force due to, and perpendicular to, the walls [36], acting to push the discs together; we quantify this in §3.2 and show that

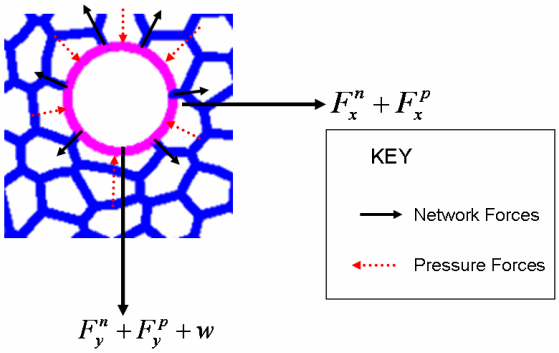

Fig. 7. The position of each disc evolves under the gravitational, tension and pressure forces shown.

the discs are far enough from the wall that it is negligible. The second case has the advantage that the lift force on each disc should be zero on average.

The simulations proceed as follows. A foam containing the two discs in their starting positions is relaxed to equilibrium, using the method described in [35]. At each iteration, the resultant forces on each disc in the x and y directions are calculated and the disc centres moved according to

$$\begin{aligned} \Delta x &= \epsilon \left(F_x^n + F_x^p\right), \\ \Delta y &= \epsilon \left(F_y^n + F_y^p + w\right), \end{aligned} \tag{7}$$

where the subscripts denote the x and y components of the forces. The parameter $\epsilon = 5 \times 10^{-4}$ measures how far the centres are moved at each iteration. The foam perimeter (energy) is then brought back to a local minimum with the discs fixed. This comprises one iteration, which is repeated until a disc reaches the bottom of the simulation cell. Representative paths of two discs are shown in figure 9.

3.2 Wall effects

To estimate the effect to which the lateral movement observed is due to the wall, we ran simulations for each configuration with and without one of the discs present. For a simulation of configuration 1 in which the discs are far enough apart that they do not interact, in contrast to figure 9(a), figure 10(a) shows that the motion of the left-hand disc changes little when the right-hand disc is removed. We therefore surmise that the wall has no influence on the motion of the discs here.

In configuration 2, figure 10(b) shows that the lower disc perturbs the foam in such a way that the upper disc moves more quickly than if it were not present. Neither disc moves sideways to a great extent.

3.3 Varying disc size

We now fix the initial centre-to-centre separation of the discs and measure how the separation evolves during the descent for discs of different size. For configuration 1, figure 11 shows that, in general, the area of the discs makes little difference. In all but one case one of the discs falls behind the other one. That our system always chooses the left-hand disc is probably an artefact due to the foam creation step.

Fixing the initial centre-to-centre separation of the discs in configuration 2 leads to the result, shown in figure 12, that the distance between the discs is reduced more quickly when the discs are smaller. This can be attributed to the fact that smaller discs experience a smaller drag force [36], and are therefore more affected by small changes in the foam structure in the wake of another disc.

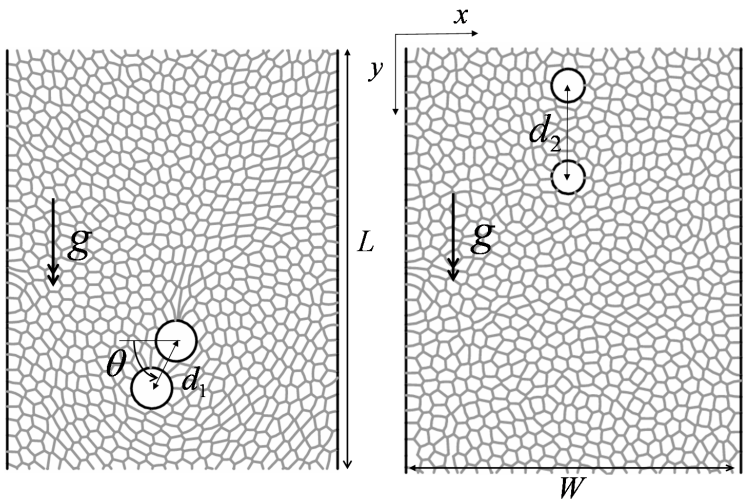

Fig. 8. Two discs in a monodisperse 2D foam confined in a channel of width W. (a) Configuration 1, in which the discs start side-by-side, with a distance d_1 between their centres and an angle θ made by the line joining their centres. (b) Configuration 2, in which the discs start one above the other a distance d_2 apart.

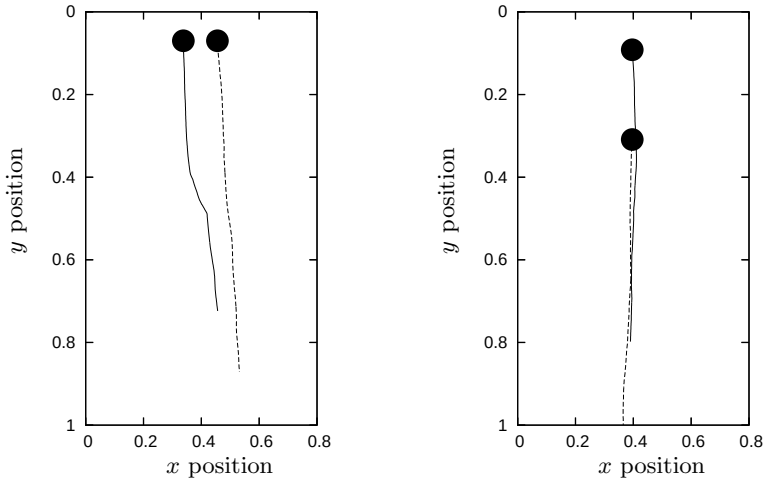

Fig. 9. The motion of the disc centres in two typical simulations. Disc area is $4.5A$. (a) Configuration 1, with $d_1 = 0.08$. Here, both discs move a small distance to the right, and the disc that began on the left of the foam advances more slowly and moves behind the right-hand disc. (b) Configuration 2, with $d_2 = 0.2$. The discs barely deviate to the sides, but the higher disc moves slightly faster in the wake of the lower one.

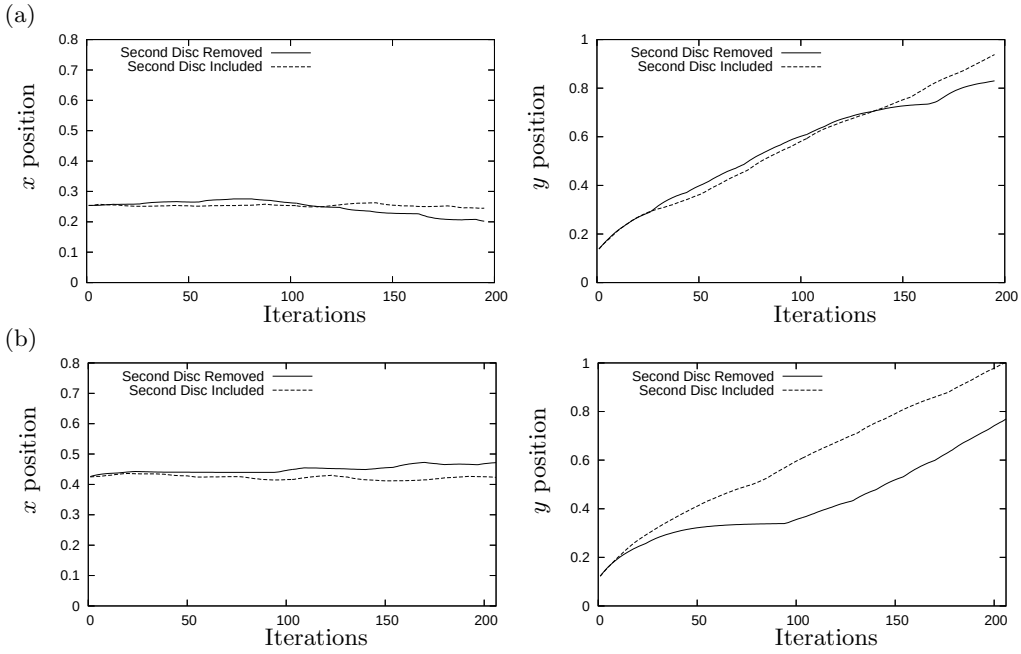

Fig. 10. The position of the disc centres with disc area $3.5A$. (a) In configuration 1, the presence of the right-hand disc (with $d_1 = 0.24$) does not affect the descent of the left-hand one. (b) In configuration 2, the upper disc descends more quickly when the lower disc (a distance $d_2 = 0.2$ away) is present, but they do not deviate sideways.

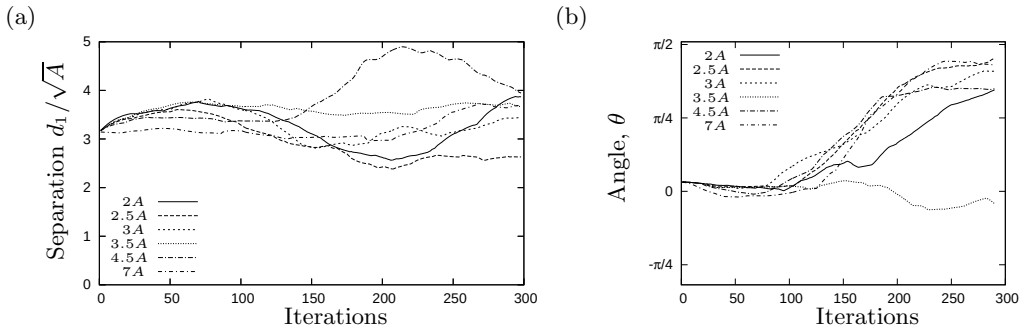

Fig. 11. (a) The separation, measured in bubble widths, of the disc centres in configuration 1 for a range of disc areas, expressed in multiples of the bubble area. The initial separation is close to 3 bubble widths. On average there is a slight increase in the separation between the discs, and no clear trend with disc size. (b) The angle θ made by the line joining the disc centres. In all but one case the left-hand disc moves behind the right-hand one.

3.4 Varying disc separation

The results for configuration 1 in figure 11 may be difficult to interpret because the distance between the edges of the discs varies as well as their areas. This means that there are a different number of bubbles between the discs in each case. We now fix the disc size and vary the initial separation between the edges of the discs. Figure 13 emphasizes that discs which start closer together are more likely to interact, and for one to move behind the other.

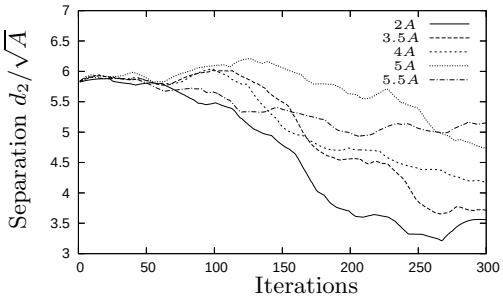

Fig. 12. The separation, measured in bubble widths, of the two discs in configuration 2. The upper disc "catches up" the lower disc, and it does so more quickly if the discs are smaller.

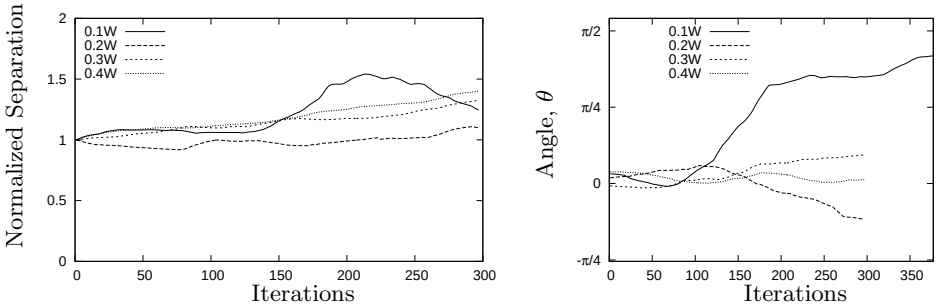

Fig. 13. The separation, normalized by the initial separation, and the angle made by the line joining the centres of the two discs in Configuration 1. The initial separations in the key are given in terms of the width W of the foam. For the closest discs, the left-hand disc moves behind the right-hand one, while for the next closest pair the reverse occurs.

4 Conclusion

We have shown that localization in the linear Couette shear of a 2D foam is highly dependent on the polydispersity in bubble areas. At high dispersity, the localized region can extend throughout the foam, with the width of this region dependent upon the square-root of the second moment of area disorder, $\mu_2(A)$. A signature of the localization is given by a 1D measure of the polydispersity, $\mathcal{L}_y$, enabling us to probe how bubbles readjust to the shear and allow T_1s to collect in specific regions of the foam.

The results begin to explain why the simulations of Kabla and Debregeas [52] indicate that T_1s occur close to the walls: the area dispersity is low in their case, so that we expect the localised region to be near a wall.

Our simulations of two discs descending through a foam probe the interactions between falling objects. We have shown that small particles move faster in the wake of another, and that for sufficiently close pairs of particles one is attracted into the wake of the other. Given the elastic nature of the interaction, and the discrete nature of the foam which allows single bubbles to detach from the disc and possibly move upwards, we are currently working towards extracting the bubble displacement field to test for the phenomenon of a "negative wake" [53].

It remains to investigate the effects of a polydisperse foam, although we expect these to be small, and the interaction between more particles/discs. We are currently pursuing an experimental realization of this system, to ascertain the applicability of the results given here.

For both systems studied here, and indeed for foam research in general, the influence of liquid is important. Extending this work to wet foams presents a

challenge to simulation, although this is itself overshadowed by the demands of three-dimensional calculations on wet foams.

Acknowledgements

We thank K. Brakke for developing, distributing and supporting the Surface Evolver and for providing the script to generate Voronoi input. This work benefited from discussions with D. Weaire, K. Krishan and F. Graner. Financial support is gratefully acknowledged from EPSRC (EP/D048397/1, EP/D071127/1) and the British Council Alliance programme.

References

1. J.J. Bikerman. *Foams: Theory and Industrial Applications*. Reinhold, New York, 1953.
2. R.K. Prud'homme and S.A. Khan, editors. *Foams: Theory, Measurements and Applications*, volume **57** of *Surfactant Science Series*. Marcel Dekker, New York, 1996.
3. D. Weaire and S. Hutzler. *The Physics of Foams*. Clarendon Press, Oxford, 1999.
4. J.A.F. Plateau. *Statique Expérimentale et Théorique des Liquides Soumis aux Seules Forces Moléculaires*. Gauthier-Villars, Paris, 1873.
5. C.S. Smith. The Shape of Things. *Scientific American*, **190**:58–64, 1954.
6. L. Bragg and J.F. Nye. A dynamical model of a crystal structure. *Proc. R. Soc. Lond.*, A**190**:474–481, 1947.
7. J. Lauridsen, M. Twardos, and M. Dennin. Shear-induced stress relaxation in a two-dimensional wet foam. *Phys. Rev. Lett.*, **89**:098303, 2002.
8. M. Twardos and M. Dennin. Comparison between step strains and slow steady shear in a bubble raft. *Phys. Rev. E*, **71**:061401, 2005.
9. Y. Wang, K. Krishan, and M. Dennin. Statistics of microscopic yielding in sheared aqueous foams. *Phil. Mag. Letts.*, **87**:125–133, 2007.
10. C.S. Smith. Grain shapes and other metallurgical applications of topology. In *Metal Interfaces*, pages 65–108. American Society for Metals, Cleveland, OH, 1952.
11. M.E. Rosa and M.A. Fortes. Development of bamboo structure in a 2D liquid foam. *Europhys. Lett.*, **41**: 577–582, 1998.
12. B. Dollet, M. Aubouy, and F. Graner. Inverse Lift: a signature of the elasticity of complex fluids. *Phys. Rev. Lett.*, **95**:168303, 2005.
13. M.F. Vaz and S.J. Cox. Two-bubble instabilities in quasi-two-dimensional foams. *Phil. Mag. Letts.*, **85**:415–425, 2005.
14. Y. Wang, K. Krishan, and M. Dennin. Impact of boundaries on velocity profiles in bubble rafts. *Phys. Rev. E*, **73**:031401, 2006.
15. J.E. Taylor. The structure of singularities in soap-bubble-like and soap-film-like minimal surfaces. *Ann. Math.*, **103**:489–539, 1976.
16. D. Weaire and J.P. Kermode. Computer simulation of a two-dimensional soap froth I. Method and motivation. *Phil. Mag. B*, **48**: 245–249, 1983.
17. F. Bolton and D. Weaire. The effects of Plateau borders in the two-dimensional soap froth. II. General simulation and analysis of rigidity loss transition. *Phil. Mag. B*, **65**: 473–487, 1992.
18. T. Okuzono, K. Kawasaki, and T. Nagai. Rheology of Random Foams. *J. Rheol.*, **37**:571–586, 1993.
19. S.J. Cox, D. Weaire, and J.A. Glazier. The rheology of two-dimensional foams. *Rheol. Acta*, **43**: 442–448, 2004.
20. I. Cantat and R. Delannay. Dynamical transition induced by large bubbles in two-dimensional foam flows. *Phys. Rev. E*, **67**:031501, 2003.
21. S.J. Cox. The mixing of bubbles in two-dimensional foams under exten-

sional shear. *J. Non-Newtonian Fl. Mech.*, **137**:39–45, 2006.
22. K. Brakke. The Surface Evolver. *Exp. Math.*, **1**:141–165, 1992.
23. S.J. Cox and E.L. Whittick. Shear modulus of two-dimensional foams: The effect of area dispersity and disorder. *Eur. Phys. J. E*, **21**:49–56, 2006.
24. A.M. Kraynik, D.A. Reinelt, and F. van Swol. The structure of random monodisperse foam. *Phys. Rev. E*, **67**:031403, 2003.
25. D. Weaire and N. Rivier. Soap, cells and statistics–random patterns in two dimensions. *Contemp. Phys.*, **25**:59–99, 1984.
26. G. Debrégeas, H. Tabuteau, and J.M. di Meglio. Deformation and flow of a two-dimensional foam under continuous shear. *Phys. Rev. Lett.*, **87**:178305, 2001.
27. S.J. Cox. Simulations of Two-Dimensional Foam under Couette Shear (preprint), 2007. http://hdl.handle.net/2160/323.
28. Y. Jiang, P.J. Swart, A. Saxena, M. Asipauskas, and J.A. Glazier. Hysteresis and Avalanches in two-dimensional foam rheology simulations. *Phys. Rev. E*, **59**:5819–5832, 1999.
29. E. Janiaud, D. Weaire, and S. Hutzler. Two dimensional foam rheology with viscous drag. *Phys. Rev. Lett.*, **97**:038302, 2006.
30. P. Marmottant and F. Graner. An elastic, plastic, viscous model for slow shear of a liquid foam. *Euro. Phys. J. E*, **23**:337–347, 2007.
31. M.L. Falk and J.S. Langer. Dynamics of viscoplastic deformation in amorphous solids. *Phys. Rev. E*, 57:7192–7205, 1998.
32. N.P. Kruyt. On the shear modulus of two-dimensional liquid foams: a theoretical study of the effect of geometrical disorder. *J. Appl. Mech.*, **74**:560–567, 2007.
33. B. Dollet, F. Elias, C. Quilliet, C. Raufaste, M. Aubouy, and F. Graner. Two-dimensional flow of foam around an obstacle: Force measurements. *Phys. Rev. E*, **71**:031403, 2005.
34. B. Dollet and F. Graner. Two-dimensional flow of foam around a circular obstacle: local measurements of elasticity, plasticity and flow. *J. Fl. Mech.*, **585**:181–211, 2006.
35. C. Raufaste, B. Dollet, S. Cox, Y. Jiang, and F. Graner. Yield drag in a two-dimensional foam flow around a circular obstacle: Effect of liquid fraction. *Euro. Phys. J. E*, **23**: 217–228, 2007.
36. S.J. Cox, B. Dollet, and F. Graner. Foam flow around an obstacle: simulations of obstacle-wall interaction. *Rheol. Acta.*, **45**:403–410, 2006.
37. B. Dollet, F. Elias, C. Quilliet, A. Huillier, M. Aubouy, and F. Graner. Two-dimensional flows of foam: drag exerted on circular obstacles and dissipation. *Coll. Surf. A*, **263**:101–110, 2005.
38. J.R. de Bruyn. Transient and steady-state drag in foam. *Rheol. Acta*, **44**:150–159, 2004.
39. I. Cantat and O. Pitois. Mechanical probing of liquid foam ageing. *J. Phys.: Condens. Matter*, **17**:S3455–S3461, 2005.
40. I. Cantat and O. Pitois. Stokes experiment in a liquid foam. *Phys. Fluids*, **18**:083302, 2006.
41. S.J. Cox, M.D. Alonso, S. Hutzler, and D. Weaire. The stokes experiment in a foam. In P. Zitha, J. Banhart and G. Verbist, editor, *Foams, emulsions and their applications*, pages 282–289. MIT-Verlag, Bremen, 2000.
42. H. Tabuteau, F.K. Oppong, J.R. de Bruyn, and P. Coussot. Drag on a sphere moving through an aging system. *Europhys. Lett.*, **78**:68007, 2007.
43. J. Feng, P.Y. Huang, and D.D. Joseph. Dynamical simulation of sidementation of solid particles in an oldroyd-b fluid. *J. non-Newt. Fl. Mech.*, **63**:63–88, 1996.
44. S. Daugan, L. Talini, B. Herzhaft, and C. Allain. Aggregation of particles settling in shear-thinning fluids. Part 1. Two-particle aggrega-

tion. *Euro. Phys. J. E*, **7**:73–81, 2002.
45. B. Gueslin, L. Talini, B. Herzhaft, Y. Peysson, and C. Allain. Aggregation behavior of two spheres falling through an aging fluid. *Phys. Rev. E*, **74**:042501, 2006.
46. B. Dollet, M. Durth, and F. Graner. Flow of foam past an elliptical obstacle. *Phys. Rev. E*, **73**:061404, 2006.
47. J. Wang and D.D. Joseph. Potential flow of a second-order fluid over a sphere or an ellipse. *J. Fl. Mech.*, **511**:201–215, 2004.
48. K. Brakke. 200,000,000 Random Voronoi Polygons. `www.susqu.edu/brakke/papers/voronoi.htm`, 1986. Unpublished.
49. N. Kern, D. Weaire, A. Martin, S. Hutzler, and S.J. Cox. Two-dimensional viscous froth model for foam dynamics. *Phys. Rev. E*, **70**: 041411, 2004.
50. L. Arnaud, J. Weiss, M. Gay, and P. Duval. Shallow-ice microstructure at Dome Concordia, Antarctica. *Ann. Glaciol.*, **30**:8–12, 2000.
51. M. Aubouy, Y. Jiang, J.A. Glazier, and F. Graner. A texture tensor to quantify deformations. *Granular Matter*, **5**:67–70, 2003.
52. A. Kabla and G. Debregeas. Quasi-static rheology of foams. part 1. oscillating strain. *J. Fluid Mech.*, **587**: 23–44, 2007.
53. O. Hassager. Negative wake behind bubbles in non-Newtonian liquids. *Nature*, **279**:402–403, 1979.

Sedimenting discs in a two-dimensional foam

I. T. Davies, S. J. Cox

Institute of Mathematics and Physics, Aberystwyth University, Ceredigion SY23 3BZ, UK

Abstract

The sedimentation of circular discs in a dry two-dimensional, monodisperse foam is studied. This, a variation of the classical Stokes experiment, provides a prototype experiment to study a foam's response. The interaction between two circular particles of equal size and weight is investigated as they fall through the foam under their own weight. Their positions are tracked and the lift and drag force measured in numerical calculations using the Surface Evolver. The initial placements of the discs are varied in each of two different initial configurations, one in which the discs are side by side and the second in which the discs are one above the other. It is shown that discs that are initially side by side rotate as a system during the descent in the foam. In the second scenario, the upper disc falls into the wake of the lower, after which the discs sediment as one with a constant non-zero separation. We present evidence that the foam screens this interaction for specific initial separations between the discs in both configurations. The force between a channel wall and a nearby sedimenting disc is also investigated.

Key words: Surface Evolver, discs, sedimentation, interaction
PACS:

1 Introduction

Liquid foams are familiar materials used domestically and in industrial processes such as ore-separation and enhanced oil recovery [1–3]. They are characterised as elasto-visco-plastic complex fluids due to their highly non-linear response to applied stresses. At low stresses they can be considered elastic solids, while increasing the applied stress results in plastic events. Plasticity in a foam is described by topological changes T1s, where a neighbour-swapping of bubbles occurs in response to the applied stress. Increasing the applied stress above a foam's yield stress results in viscous liquid-like behaviour [4]. Thus, foams provide a prototype complex fluid with which it is possible to work at a macroscopic bubble scale instead of the usual molecular scale.

We use a variation of the classical Stokes' experiment [5], originally used to measure the viscosity of a fluid through which a sphere is dropped, to describe and understand these elasto-visco-plastic transitions in foam rheology.

Existing work on experiments in which a constant force is applied to a particle in a foam is limited to a single sphere [6]. Other work where foam flow is probed by a fixed sphere uses the variation in drag force on the particle to quantify the foam response [7,8]. This scenario has proved useful in describing foam ageing [9,10].

Two-dimensional foams can be thought of as a monolayer of bubbles squeezed between two glass plates. We choose to probe the foam response by dropping circular obstacles of greater size than the bubbles into a foam channel. Existing work on smaller particles in foam concentrates on the dispersion of particles within the Plateau borders that constitute the liquid network of the foam [11,12]. Two-dimensional experiments using circular obstacles to probe foam response are a simplification of the 3D case but provide a clearer description. The drag force on a circular obstacle due to the foam has been measured through image analysis [13,14] and it was found to increase with obstacle size and decrease with bubble size while the roughness of the obstacle was not important. Confinement in two dimensions means that images of the foam during such experiments provide information on foam deformation fields as well as bubble velocity and pressure fields [15]. Combining such experiments with simulation has proved beneficial in showing that the drag force on a circular obstacle is also inversely correlated with the liquid fraction of the foam [16]. Combining the work of [13] and [16], the drag force on a circular obstacle of diameter d_0 is approximately $\phi^{-\frac{1}{4}} d_0/\sqrt{A_b}$ where A_b is the bubble area in a two dimensional foam and ϕ its effective liquid fraction.

Experiments investigating the flow of foam past different shaped obstacles such as a cambered airfoil [17] and an ellipse [18] has enhanced the understanding of foam response. An inverse lift force was observed for the cambered airfoil when placed in foam flow while the ellipse rotated so that its axis was parallel with the foam flow for every initial placement. This is known to be a feature of elastic fluids [19]. Thus, we aim to answer the question of whether the plasticity of foam is significant in determining the way in which particles sediment within a foam, and can we therefore treat the foam as an elastic liquid? Moreover, does a foam screen the interaction between particles as it does for the effects of topological changes within its structure [20]?

We choose to work in two dimensions for the reasons stated. We use the Surface Evolver [21] to simulate the sedimentation and interaction of two circular discs falling under their own weight. We look at the position of the discs as they descend and analyse the time-varying forces on them. The resultant force is split into two; the drag contribution that is parallel to the direction of

gravity and the lift force that's perpendicular to gravity. We consider the low velocity limit, in which we expect that the dominant contributions to these forces to come from the tensions of the soap films (network force) and the pressures of the bubbles (pressure force) – see figure 1. We aim to understand the conditions under which two objects falling through a foam are mutually attracted or repelled, as has been done for a number of purely viscoelastic fluids [22–25].

2 Method

We simulate disc sedimentation in a 2D dry foam by tracking the motion of two discs commencing from a position near the top of a foam channel [26]. Particles descend in a foam under the actions of four forces, (i) weight, (ii) the resultant tension force F^n due to the network of films pulling each obstacle; (iii) the resultant pressure force F^p due to the pressure of bubbles contacting each obstacle; (iv) the viscous force $\vec{F}^\eta$ on the circumference of the discs. Note that the films that are in contact with the obstacle are not uniformly distributed around the circumference – they bunch up behind the obstacle, as shown in figure 2 – so that the resultant forces are usually non-zero.

Newton's second law applied to each disc of mass m gives

$$m\frac{d^2\vec{x}(t)}{dt^2} = mg\hat{y} - \lambda\frac{d\vec{x}(t)}{dt} - \vec{F}^p - \vec{F}^n - \vec{F}^\eta, \tag{1}$$

where $\vec{x}(t)$ denotes the position of the disc at time t, g is the acceleration due to gravity, and $\hat{y}$ is the unit vector in the vertical direction. λ is a friction coefficient due to the interaction of the plane faces of the discs with the bounding surfaces and.

We assume that the motion is slow and steady, so that we may neglect the acceleration term and the viscous forces. Thus, only three forces are controlling the motion of the discs through the foam 1. The model simplifies to the following evolution equation:

$$\frac{1}{\epsilon}\frac{d\vec{x}(t)}{dt} = mg\hat{y} - \vec{F}^p - \vec{F}^n, \tag{2}$$

where $\epsilon = 1/\lambda$ sets the effective time scale of the motion.

For each disc the resultant network force is the sum of the force due to those films j that touch the disc. Since viscous drag around the disc is neglected,

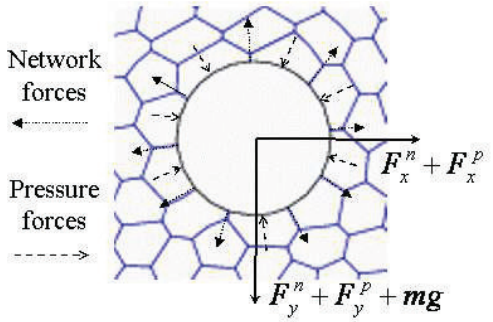

Fig. 1. The positions of the discs evolve under the gravitational, tension and pressure forces shown. Each force is resolved into its horizontal and vertical (the direction in which gravity acts) components.

each film meets the disc perpendicularly [27] and makes an angle θ_j with the positive y direction. Thus

$$\vec{F}^n = \gamma \sum_{\text{films } j} (\sin\theta_j, \cos\theta_j) \tag{3}$$

where γ represents the line tension of the foam. The pressure force is a sum over all the bubbles k touching the obstacle

$$\vec{F}^p = \sum_{\text{bubbles } k} p_k l_k (\sin\theta_k, \cos\theta_k) \tag{4}$$

where p_k is the pressure inside the bubble, l_k is the length of the contact line of the bubble with the disc and θ_k is the angle that the inward normal at the midpoint of l_k makes with the positive $y-$direction.

The simulation proceeds from a Voronoi construction [28] which is used to generate a fully periodic tessellation of the plane. Bubbles at the top and bottom of the structure are sequentially deleted until the required number remains. The structure is then imported to Surface Evolver [21] and the peripheral films are constrained to one of the two side walls. Using the Surface Evolver in a mode in which each film is represented as a circular arc, we perform quasi-static simulations. We use three different foams in a channel of length $L = 1$: the first has $N_1 = 727$ bubbles contained within a channel of width $W_1 = 0.792$. We work with monodisperse foams, so the bubble area is $A_b \approx 1 \times 10^{-3}$ (A_b shrinks slightly in proportion to the disc size, since the total area of the foam and two-disc system is constant). The second foam has $N_2 = 746$ bubbles, channel width $W_2 = 0.805$ and bubble area $A_b \approx 1.1 \times 10^{-3}$. The cut-off length [27,16] for T_1 events is $l_c = 0.002$ for both of these foams, corresponding to a dry foam with liquid fraction $\phi < 0.1\%$. The third foam has $N_3 = 1500$ bubbles in a channel of width $W_3 = 0.432$ and bubble area

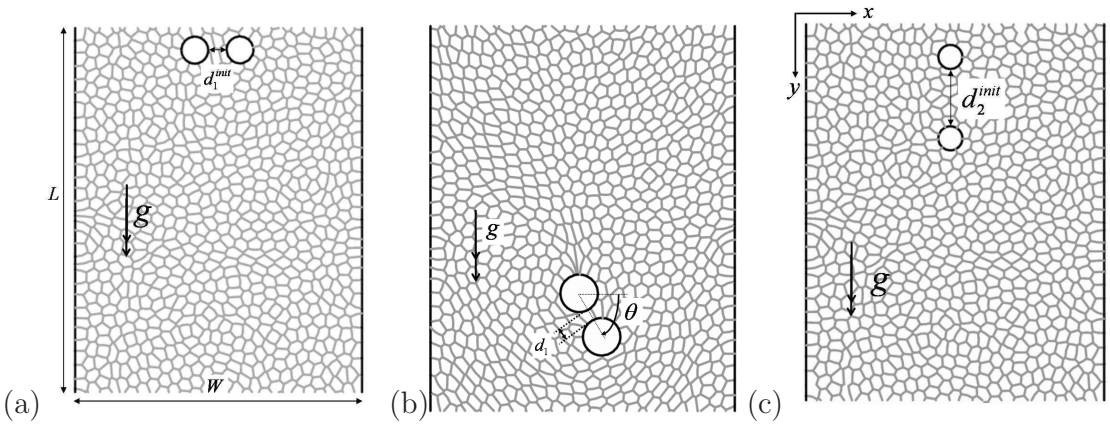

Fig. 2. Two discs sedimenting in a monodisperse foam contained in a channel of width W and length L. (a) Configuration 1, in which the discs start side by side, with a distance d_1^{init} between their centres. (b) If the discs rotate about one another we measure an angle θ between the positive x-direction and the line between the discs' centres. (c) Configuration 2, in which the discs start one above the other, a distance d_2^{init} apart.

$A_b \approx 2.9 \times 10^{-4}$. In this case the cut-off length for T_1 events is set to $l_c = 0.001$ so that the effective liquid fraction is consistent with that of the previous two foams. In all three cases the channel is periodic in the $y-$direction, parallel to the direction of gravitational acceleration. The simulations are stopped before either of the discs return to the top of the foam channel. We set a no-slip condition at the channel wall: the foam films that touch the walls have fixed vertices. The films that are in contact with the discs are free to slip. In addition, the no slip condition at the walls was relaxed in simulations by fixing only one vertex at each wall. In this case the foam moves (fluctuates) only slightly at the wall and does not seem to affect our results. Thus, the work presented here is all with no slip at the wall.

We choose dimensionless units such that the line tension γ has value 1 throughout. We keep the disc size and weight fixed throughout our simulations at $4A_b$ and $mg = 10$ respectively. It was ensured that this disc weight was sufficiently large that the discs were not brought to a halt by the foam.

The simulations proceed as follows: a foam containing the two discs in their starting positions is relaxed to equilibrium, using the method described in [16]. The resultant forces on the discs in the x and y directions are calculated and the disc centres moved according to

$$\Delta x = \epsilon(F_x^n + F_x^p) \tag{5}$$
$$\Delta y = \epsilon(F_y^n + F_y^p + mg) \tag{6}$$

where the subscripts denote the x and y components of the forces. The param-

eter ϵ measures how far the centres move at each iteration ($\epsilon = 5 \times 10^{-4}$ for N_1 and N_2, and $\epsilon = 2 \times 10^{-4}$ for N_3). The foam perimeter is then brought back to a local minimum with the discs fixed. This comprises one iteration, which is repeated until a disc reaches the bottom of the foam channel. The discs' centres are tracked as demonstrated in figure 5. The computational time is dependent upon the number of bubbles: the simulations take about 50 hours for the two smaller foams and more than 120 hours for the large foam.

We first examine the sedimentation of a single disc in the foam to quantify the wall effects and check that the rest of the simulations will be independent of such effects (Section 3.1). We then choose two main initial configurations for our two disc sedimentation simulation, as shown in figure 2. The disc centres are initially separated by a distance d_i^{init}, either horizontally $i = 1$ or vertically $i = 2$.

3 Results

3.1 Single disc falling near a vertical wall

We first ran simulations of one disc and varied the initial placement of this disc at the top of the channel so that the effects of the wall on the motion of the disc could be ascertained in the hope of being able to neglect it when considering the interaction of two discs. We track the disc motion for nine different initial placements, the first being $0.1W$ away from the left wall in increments of $0.1W$, the last being $0.1W$ from the right wall. This is done for the two smaller foams.

It was found that for a fixed obstacle placed in a flow of foam in a similar channel the wall repels the obstacle [27], while sedimenting particles in viscoelastic fluids are attracted to walls [28]. Figure 3 demonstrates the drag and lift forces on a disc as it falls through the foam. There is an initial transient during which the forces rise; they then saturate but fluctuate greatly. The sudden drops in each force occur when a bubble detaches from the back of a disc. We therefore take average values for the forces after the transient, shown as horizontal lines.

Figure 4(a) demonstrates the variation in average drag force on the discs as they fall from different positions along the top of the foam channel. We deduce that a disc's proximity to the walls does not have an effect on the drag force exerted by the foam. Figure 4(b) shows the average lift force on a disc as it descends through the foam. It can be seen that for discs that are released close to either of the walls, there is a small lift force that is in the direction

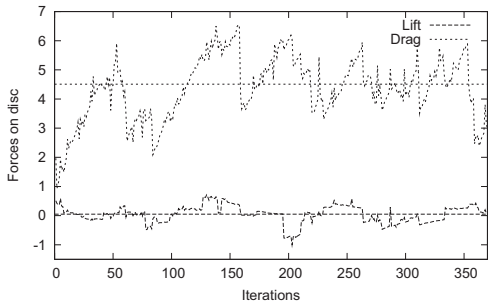

Fig. 3. The variation in drag and lift force on one disc (placed in the centre of the channel) as it descends through the foam. The plots are non-smooth due to the foam structure; jumps in the force appear when T1s occur. Note that a transient stage occurs for roughly the first 100 iterations. We take the average values for the drag and lift force after this transient.

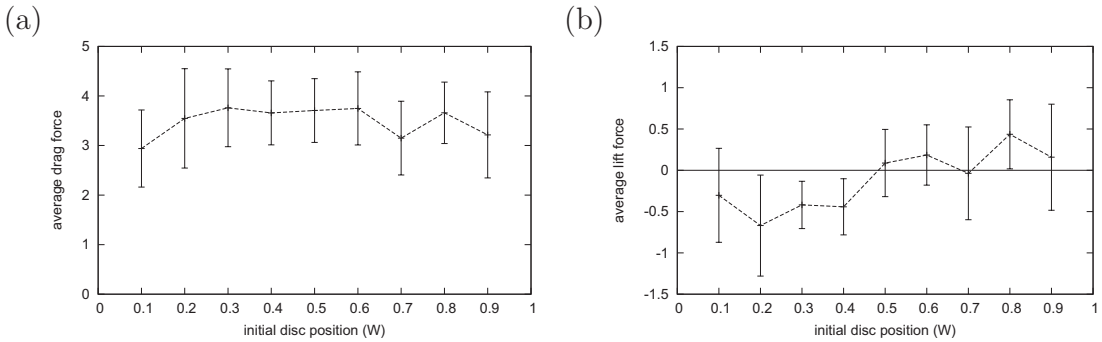

Fig. 4. (a) The variation of the average drag force on a disc (with standard deviation error bars) as it descends through the foam from different positions along the top of the channel. The disc is placed in nine positions at equal intervals of $0.1W$. The average drag force on a disc doesn't differ greatly even when the descent happens close to the walls. (b) The variation of the average lift force on a disc for the same initial placements as (a). The positive direction of the force is to the right. Thus lift is negative when the disc falls from $0.1W$ (close to the left wall) and positive when falling from $0.9W$ (close to the right wall) therefore an attractive force on the disc from the walls exists.

of those walls. For example, a negative lift on the left hand side of the plot demonstrates that the force is to the left and *vice versa*. These forces are considerably smaller and fluctuate less than the drag force. The attractive force between a disc and a nearby wall, although small, appears robust with respect to different foams.

3.2 Two discs in configuration 1

We investigate the interaction of two discs placed side by side within the centre of the foam channel, where we can neglect wall effects. For our simulations, we work in the region $0.3W$ to $0.7W$ of the foam channel where the wall effects

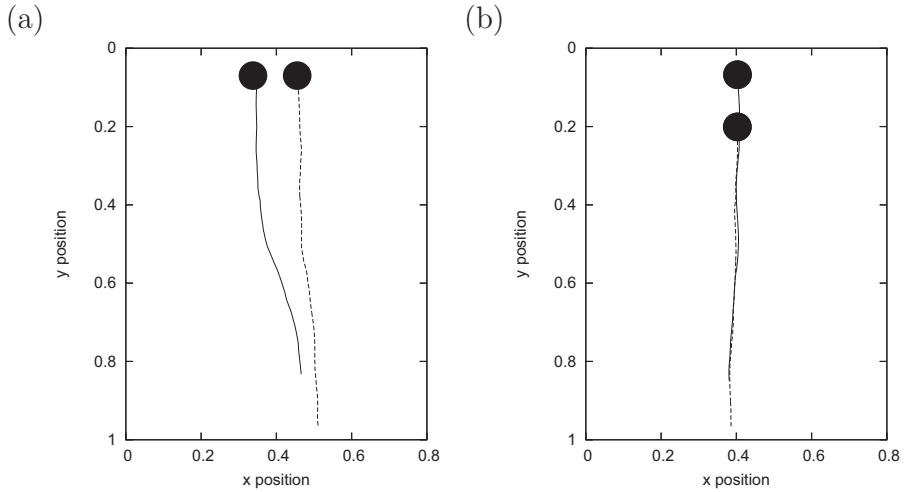

Fig. 5. Tracking the motion of the discs' centres in two typical simulations. Left: Configuration 1, with $d_1^{init} = 0.08$. Here, both discs move a short distance to the right, and the disc initially on the left advances more slowly and moves behind the right-hand disc. Right: Configuration 2, with $d_2^{init} = 0.2$. The discs barely deviate to the sides, but the upper disc moves slightly faster into the lower disc's wake.

have been shown to be negligible. The initial separation between the discs is varied and we investigate whether the discrete nature of the foam screens [20] the interaction between the discs. This is done for the three foams described. For each simulation, we record at each iteration the disc positions (figure 5) and the drag and lift forces on each one.

3.2.1 Disc Position

It has been shown that in a viscoelastic fluid circular particles in this configuration rotate about one another as they sediment [22–25]. We find the same rotation in foams (figure 5(a)): figure 6(a) shows the variation of the angle between the discs as they descend in the foam. The rotation of the disc system can occur in either a clockwise or an anticlockwise manner. Thus the plasticity of the material doesn't change the sedimenting motion of the particles greatly.

In figure 6(a) it is clearly seen that the discs that are initially close together rotate until they reach a plateau value at $|\theta| = \frac{\pi}{2}$. In this case the discs have rotated from being initially in configuration 1 so that they are finally oriented in configuration 2. The plateau at the positive and negative values for $\frac{\pi}{2}$ demonstrates that once the discs are directly above one another, they stay in this configuration. Notice that there are some simulations which don't reach these plateau values: those in which θ doesn't change dramatically are the ones where the discs were initially more than $4d_b$ apart, where d_b is the average bubble diameter. Others are those in which the foam was too short for the plateau to be reached.

(a) (b)

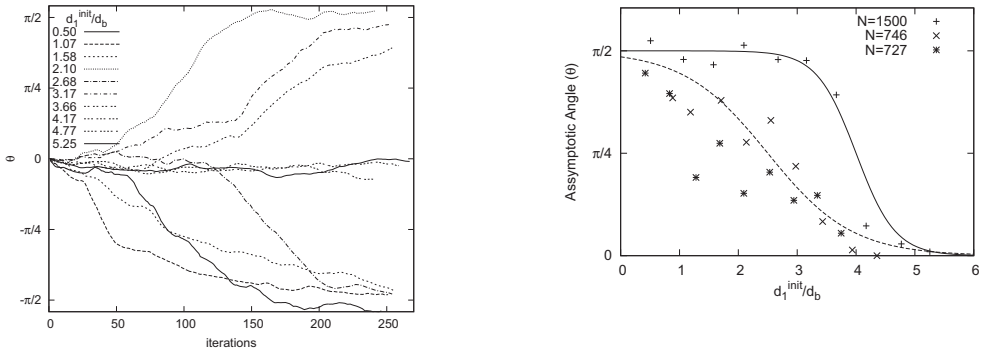

Fig. 6. (a) The angle θ between the discs' centres in configuration 1 with $N_3 = 1500$ for a range of initial separations d_1, demonstrates rotation of the discs as θ increases in either a clockwise and anticlockwise direction. The discs rotate, if close enough, into configuration 2 and stay in this configuration. (b) The settling angle of the discs (θ at the bottom of the channel). The data for the large foam and the two smaller foams are fitted to a tanh function (7). It is clear that the foam screens the interaction of the discs if they are initially 4 or more bubble diameters apart and that the lesser slope for the smaller foams is due to the foam being too short for the full rotation to occur.

There is a strong relationship between the initial separation of the discs and the settling angle (the angle between the discs after reaching the bottom of the foam). Discs that are initially far apart rotate less. We look more closely at this trend by fitting the data for the settling angle for the three foams (figure 6b) to the following model:

$$\theta = \frac{\pi}{4} \times \left(1 + \tanh\left(\kappa \frac{(d_{1c} - d_1^{init})}{d_b}\right)\right), \tag{7}$$

where $d_{1c} = (4 \pm 1)d_b$ and the slope here is $\kappa = N/1000$ which measures the extent to which the plateau has been reached. Thus, if the discs initially have more than four bubbles in between them then they don't interact and rotate. When the discs are closer than this then they will rotate until they reach configuration 2 in which they are one above the other.

The variation of disc separation is also important when looking at their motion. In figure 7 we see that this is highly dependent on their initial separation. For discs that are initially close ($0 < d_1^{init} < 4d_b$), there is a tendency for them to move together so that they are separated by $1 - 2d_b$. (There is one case here where the discs have moved so close together during sedimentation that they are touching, but they then separate and follow the same pattern.) Discs that are initially placed further apart than the screening value ($d_1^{init} > 4d_b$) don't move closer in the same manner. In some cases, the discs move away from each other. These are the discs that are so far apart that they don't rotate about each other and therefore don't interact as much. It was observed

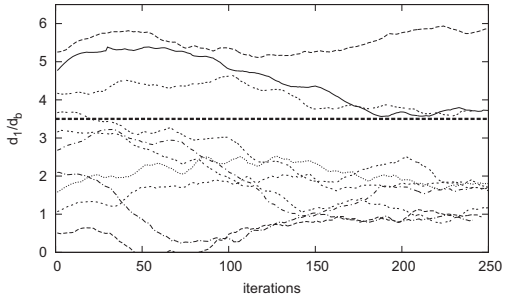

Fig. 7. The separation between disc edges, measured in bubble diameters, as they fall through the foam in configuration 1 with $N_3 = 1500$. There is a general tendency for the discs to move together so that they are separated by one to two bubbles if they are initially placed sufficiently close together. The horizontal line represents a screening value above which the interaction between the discs is negligible.

in simulations that any increase in separation arose from fluctuations in the vertical displacement rates for the two discs. Differences in the local foam structure around the two discs mean that they don't descend at exactly the same rate through the foam. A lateral fluctuation in their motion was found to be minimal as shown by our study for one disc in section 2. Recall that the lift force on the discs was shown to be negligible within the region of the channel under consideration here.

3.2.2 Forces on the Discs

We look at how the forces on the discs affect this interaction between the discs. Figure 8 shows the drag and lift forces from two different simulations in the $N = 1500$ foam. The first is for two initially close discs that rotate and the second is for two discs that are too far apart to interact. When the discs are initially close together, the drag force is seen to overshoot for one of the discs. This results in slower downward motion of this disc and it is left trailing. An increase in the lift force is seen for this disc at this stage and it is directed so that the disc moves into the wake of the other disc. Thus, the discs begin to rotate so that the resistance to their downward descent is minimized. After rotation has occurred it can be seen that the drag and lift forces on both discs become very similar, at which point the motion of the discs becomes more stable. For the discs that were initially further apart no such overshoots are seen as they don't interact (figure 8(c) and (d)). This is further clarified by figure 9 which demonstrates the cross-correlation between the lift and drag force on each disc when they are initially close and further apart. When the discs are sufficiently close for interaction, it is apparent that the lift and drag forces on the discs are correlated. This correlation between the forces occurs for the same disc which experienced a sudden increase in the forces applied by the foam. The forces on the other disc seem uncorrelated. As expected, when the discs are further apart and interaction between them is minimal,

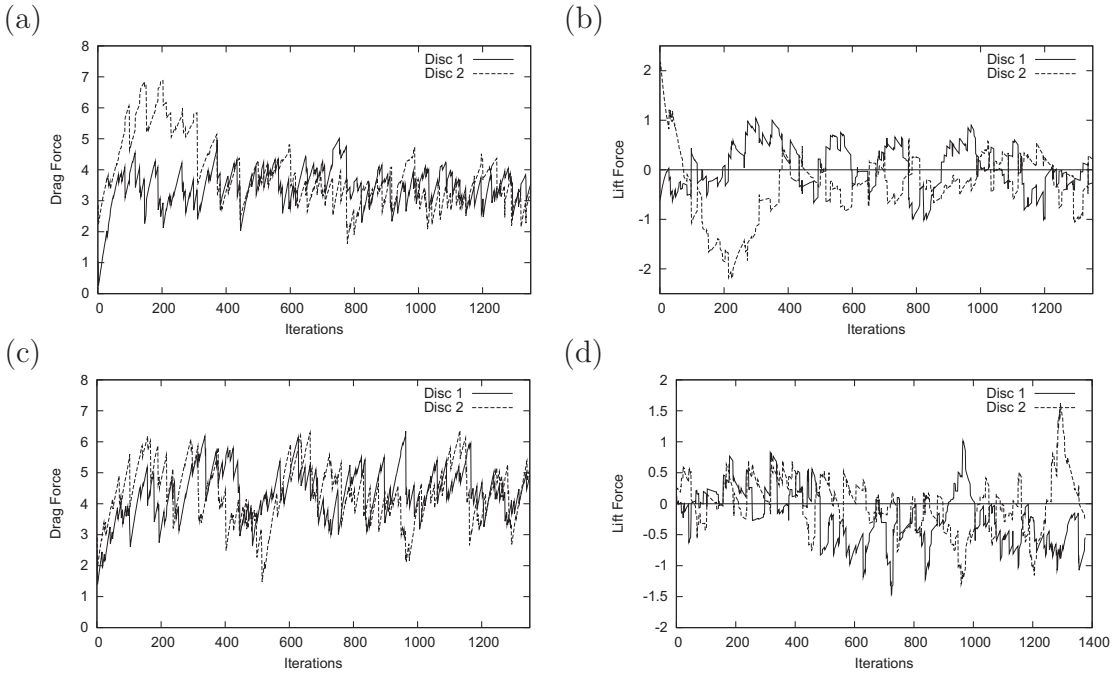

Fig. 8. Fluctuating forces on two discs in configuration 1. (a) drag force on both discs for ${d_1}^{init} = 0.64d_b$, (b) lift force on the discs when ${d_1}^{init} = 0.64d_b$. It can be seen that there is an overshoot in the drag for disc 1 in (a) and then an overshoot in the lift on disc 1 in (b). Thus, they interact and rotate about one another. (c) and (d) Same data for two discs that start further apart (${d_1}^{init} = 4.20d_b$). Here the drag and lift forces are very similar for both discs and follow the same pattern as would be expected on one disc falling in the foam. Thus, the discs don't interact in this case.

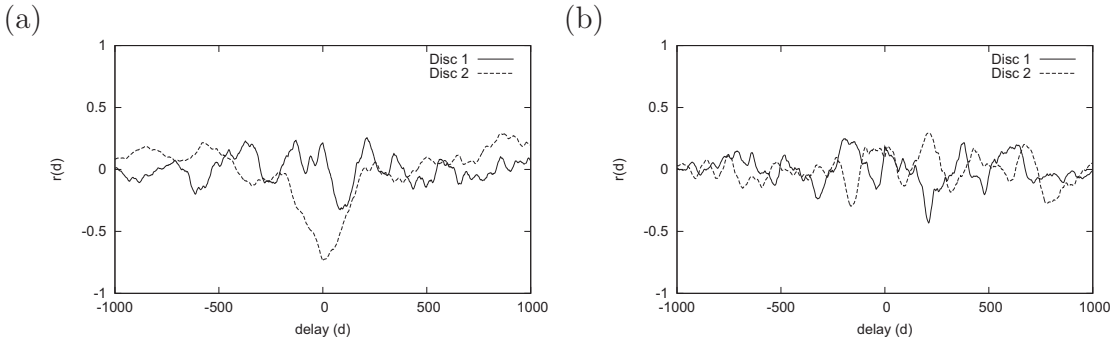

Fig. 9. The cross-correlation between the drag and lift forces on the two discs as they sediment in the foam. (a) The discs are close together (${d_1}^{init} = 0.64d_b$), whence they rotate. It can be seen that the forces are strongly correlated at a delay close to zero for one of the discs. The correlation between the forces on the second disc is less apparent. (b) The discs are further apart (${d_1}^{init} = 4.20d_b$), whence they don't interact by rotating about one another. As expected the correlation between the forces on each disc is minimal in this case.

the correlation between the forces on each disc is minimal.

(a) (b)

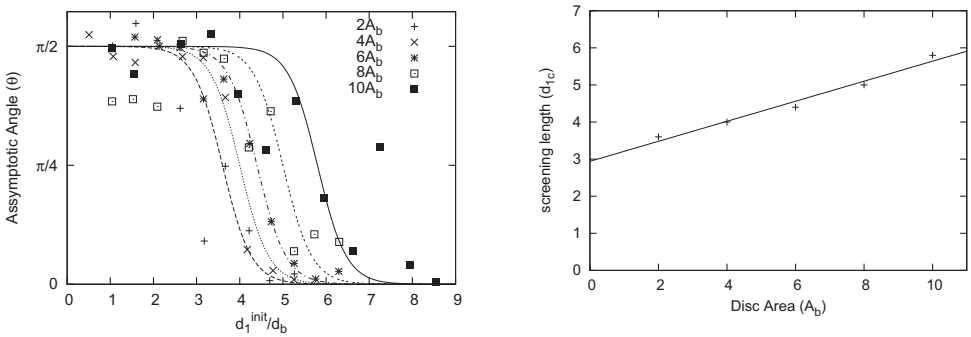

Fig. 10. The variation of the screening length with different sized discs. (a)The data for the asymptotic angle between the discs of areas $2A_b$, $4A_b$, $6A_b$, $8A_b$, and $10A_b$ is fitted to the tanh model 7. The bigger discs rotate about each other at a slower rate and require a longer foam for complete rotation into Configuration 2, whence a foam with N=2200 bubbles is used. (b) The variation of the critical screening length with disc size. It is clear that the screening length increases linearily with disc size.

3.3 Variation of the screening length with the disc size

The region of the foam affected by the sedimentation process of the two discs is logically dependent of the size of the discs. Thus it is to be expected that the screening length described increases with disc area. We look at the sedimentation of discs with areas of 2, 4, 6, 8 and 10 times the bubble area in configuration 1. It was experienced in simulation that bigger discs rotated at a slower rate, whence a longer foam is required for convergence of results. Thus a foam with $N = 2200$ bubbles (with consistent liquid fraction to previous foams) is used to simulate the sedimentation of discs with areas $8A_b$ and $10A_b$. Figure 10 demonstrates the variation in the critical screening length for the different sized discs. It is seen that this screening length increases linearly with the disc size. It is clear that the relative motion between the discs follows the same rotation pattern as described previously, but that bigger discs interact at a greater separation.

3.4 Two discs falling in configuration 2

We consider two discs descending in the foam one above each other, working with the same size discs as before. We vary the initial separation between the discs to interpret how the discs interact when they are oriented in this way (figure 5(b)).

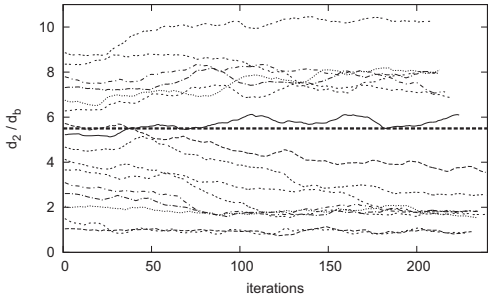

Fig. 11. The separation, measured in bubble diameters, between two discs falling through a foam in configuration 2 with $N_3 = 1500$. It can be seen that for discs initially separated by up to 2 d_b, the discs descend in the foam at a constant separation. If the discs are initially separated by 2 to 6 d_b, then they move closer together until they eventually reach a separation of 1 to 2 d_b, after which the motion is stable. If the initial separation is greater than 6 d_b then the variation in separation is less and they stay far apart. Here the yielded region above the lower disc (the wake) plays an important role in the interaction of the discs.

3.4.1 Disc Position

The discs move closer together as they descend in the foam until they have moved so close that only one or two bubbles separate them, after which they move at a constant separation. In contrast to configuration 1, when the discs are initially further apart than $4d_b$ they will still move closer together, albeit at a slower rate. This is illustrated in figure 11. The wake of the lower disc is a yielded region of the foam and it is this that determines how the discs interact. The data suggests that the wake stretches back roughly $5-6d_b$ from this disc. If the upper disc is initially within this distance from the lower disc then it is able to move closer into the wake until the constant separation of one to two bubble diameter separation is reached. If the upper disc is initially above the yielded region in the lower discs' wake then the interaction is less apparent and the discs separation remains constant.

3.4.2 Forces on the discs

The role that the drag force plays in this interaction pattern is described in figure 12. The lift force is assumed to be negligible as the discs are placed at the centre of the foam channel. To clarify the effect that varying the initial separation has on the drag force differences on both discs, the plot in figure 12 needs to be split into three regions where the interaction between the discs differs. For initially close discs ($d_2^{init} < 2d_b$) the drag force difference between the discs is negligible, whence they will move through the foam at constant separation. However, when the discs are initially separated by a larger distance, $2d_b < d_2^{init} < 6d_b$, the difference between the drag forces on the discs increases. The drag on the lower disc is always greater than that on the upper

disc so they will move closer together as the upper disc moves into the other disc's wake. When the discs are even further apart (more than $6d_b$ separation) the drag force differences become less in magnitude. In some cases there is a greater drag force on the upper disc, but in general there is limited interaction between the two discs.

The tendency for the obstacles to move closer together for a particular range of initial separations suggest that the yielded region of the wake of the lower disc extends up to five or six bubble diameters above the disc. Thus, if the initial separation is more than the length of this region the interaction becomes minimal. This is further evidence of the foam screening the interaction between the two objects.

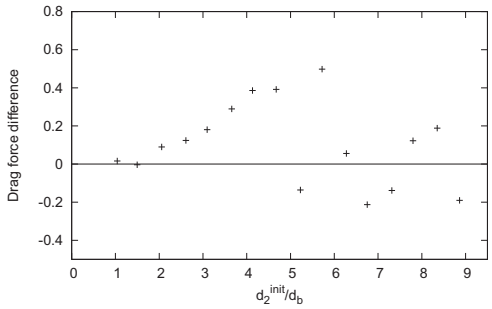

Fig. 12. Variation of the difference in average drag force of both discs falling in configuration 2 as the initial separation between them is varied. The difference in drag is measured by subtracting the drag force on the upper disc from the drag force on the lower disc. We see that when the discs are close together ($0 < {d_2}^{init}/d_b < 2$), the difference between the drag force is close to zero, whence negligible. By increasing the initial separation ($2 < {d_2}^{init}/d_b < 5$) we see that the differences in drag force between the discs increases. Here, the drag on the lower disc is greater than that of the upper disc. In this case the upper disc descends more quickly than the lower disc and moves into its wake. Increasing the initial separation further (${d_2}^{init}/d_b > 6$) leads to the differences in the drag force on both discs becoming scattered in a random manner, revealing that the discs don't interact

.

4 Conclusions

The interaction between a sedimenting disc and a wall was found to be minimal, although a small attractive force exists when the disc was in close proximity to the wall. Thus for our simulations of two sedimenting discs, we worked far enough away from the wall so that we could neglect these effects.

In the case of two discs sedimenting initially side-by-side, a rotation towards a configuration in which they are one above the other is evident. The rate of rotation is dependent on the initial separation between the discs and the

size of the discs. It was found that for discs sized at $4Ab$, this interaction only occurred if the initial separation between the discs is less than 3 to 4 bubble diameters. When the initial separation was greater than 4 bubble diameters the foam screens the interaction and the motion of each disc is determined by variations in the local structure of the foam. This critical screening length increases linearly with disc size.

For the case in which two discs above each other sediment, further evidence of screening was apparent. The initial separation of the discs was again an important parameter that determined their interaction. If the discs were placed less than $6d_b$ apart then they move closer together due to the drag force on the lower disc being greater than that of the upper disc. In this case the upper disc is sedimenting in the yielded region of the foam behind the lower disc, whence it moves into the wake of the lower disc. If the discs move close to a separation of $1 - 2d_b$, the drag force on both is equal and therefore they move at the same rate. However, if the initial separation is increased above $6d_b$ then the drag force on each disc is independent, whence the discs don't interact.

Thus the motion of the discs is stable when their line of centres is parallel to the direction of gravity and separated by one to two bubbles. Although this is reminiscent of elastic fluids, the plasticity of the foam plays an important rôle: the T_1 events behind the discs as bubbles lose contact change the local structure of the foam and allow the upper disc in the wake to move more quickly. The discrete nature of the foam means that objects don't interact if they are separated by more than $4d_b$ horizontally or $6d_b$ vertically.

It remains to be seen whether these results extend to objects of different dimensions (weight) or shape (e.g. ellipses), and to what extent material parameters such as the bubble area dispersity and the liquid fraction of the foam dictate the dynamics of sedimentation.

Inclusion of the viscous forces on the discs may lead to increased rotation of the discs, and simulations that do are likely to provide a better comparison with experiment.

References

[1] D. Weaire and S. Hutzler. *The Physics of Foams.* Oxford University Press, 2000.

[2] R. K. Prud'homme and S.A. Khan, editors. *Foams: Theory, Measurements and Applications.* CRC Press, 1996.

[3] J. J. Bikerman. *Foams: Theory and Industrial Applications.* Reinhold Publishing Corporation, New York, 1953.

[4] R. Hhler and S. Cohen-Addad. Topical review - rheology of liquid foam. *J. Physics: Condensed Matter*, 17:R1041–R1069, 2005.

[5] G. G. Stokes. On the effect of the inertial friction of fluids on the motion of pendulums. *Trans. Camb. Phil. Soc.*, IX:8–149, 1850.

[6] S. J. Cox, M. D. Alonso, S. Hutzler, and D. Weaire. The Stokes Experiment in a Foam. In P. Zitha, J. Banhart and G. Verbist, editor, *Foams, Emulsions and their Applications*, pages 282–289. MIT-Verlag, Bremen, 2000.

[7] I. Cantat and O. Pitois. Stokes experiment in a liquid foam. *Phys. Fluids*, 18, 2006.

[8] J.R. de Bruyn. Transient and steady-state drag in a foam. *Rheol. Acta.*, 44: 150–159, 2004.

[9] J.R. de Bruyn. Age dependence of the drag force in an aqueous foam. *Rheol. Acta*, 45:801–811, 2005.

[10] I. Cantat and O. Pitois. Mechanical probing of liquid foam ageing. *J. Phys. Condens. Matter*, 17:S3455–S3461, 2005.

[11] S. J. Neethling and J. J. Cilliers. Solids motion in flowing froths. *Chemical Engineering Science*, 57:607–615, 2002.

[12] H.T. Lee, S.J. Neethling, and J.J. Cilliers. Particle and liquid dispersion in foams. *Colloids Surf. A*, 263:320–329, 2005.

[13] B. Dollet, F. Elias, C. Quilliet, A. Huillier, M. Aubony, and F. Graner. Two-dimensional flows of foam: drag exerted on circular obstacles and dissipation. *Colloids Surf. A*, 263:101–110, 2005a.

[14] B. Dollet, F. Elias, C. Quillet, C. Raufaste, M. Aubony, and F. Graner. Two-dimensional flow of foam around an obstacle: Force measurements. *Phys. Rev. E*, 71:031403, 2005b.

[15] B. Dollet and F. Graner. Two-dimensional flow of foam around a circular obstacle: local measurements of elasticity, plasticity and flow. *J. Fluid Mech.*, 585:181–211, 2007.

[16] C. Raufaste, B. Dollet, S. Cox, Y. Jiang, and F. Graner. Yield drag in a two-dimensional foam flow around a circular obstacle: Effect of liquid fraction. *Euro. Phys. J. E.*, 23:217–228, 2007.

[17] B. Dollet, M. Aubouy, and F. Graner. Anti-inertial lift in foams: A signature of the elasticity of complex fluids. *Phys. Rev. Lett.*, 95, 2005c.

[18] B. Dollet, M. Durth, and F. Graner. Flow of foam past an elliptical obstacle. *Phys. Rev. E*, 73, 2006.

[19] J. Wang and D. D. Joseph. Potential flow of a second-order fluid over a sphere or an ellipse. *J. Fluid Mech.*, 511:201–215, 2004.

[20] S.J. Cox, F. Graner, and M.F. Vaz. Screening in two-dimensional foams. *Soft Matter*, (Accepted):1871–1878, 2008.

[21] K. Brakke. The Surface Evolver. *Exp. Math.*, 1:141–152, 1992.

[22] S. Daugan, L. Talini, B. Herzhaft, and C. Allain. Aggregation of particles settling in shear-thinning fluids. *Eur. Phys. J. E*, 7:73-81, 2002.

[23] B. Gueslin, L. Talini, B. Herzhaft, Y. Peysson, and C. Allain. Aggregation behaviour of two spheres falling through an aging fluid. *Phys. Rev. E 74*, 74, 2006.

[24] J. Feng, P. Y. Huang, and D. D. Joseph. Dynamic simulation of sedimentation of solid particles in an Oldroyd-b fluid. *J. Non-Newtonian Fluid Mech.*, 63: 63–88, 1996.

[25] D. D. Joseph, J. Y. Liu, M. Poletto, and J. Feng. Aggregation and dispersion of spheres falling in viscoelastic liquids. *J. Non-Newtonian Fluid Mech.*, 54:45–86, 1994.

[26] A. Wyn, I. T. Davies, and S. J. Cox. Simulations of two-dimensional foam rheology: Localization in linear Couette flow and the interaction of settling discs. *Eur. Phys. J. E*, 26:81–89, 2008.

[27] S.J. Cox, B. Dollet, and F. Graner. Foam flow around an obstacle: simulations of obstacle-wall interaction. *Rheol. Acta.*, 45:403–410, 2006.

[28] D. D. Joseph and J. Feng. A note on the forces that move particles in a second-order fluid. *J. Non-Newtonian Fluid Mech.*, 64:299–302, 1996.

[28] K. Brakke. 200,000,000 Random Voronoi Polygons. *www.susqu.edu/brakke/papers/voronoi.htm*, 1986, unpublished.